UNIVERSITÀ
DEGLI STUDI
DI PADOVA

UNIVERSITÁ DEGLI STUDI DI PADOVA

DIPARTIMENTO DI TECNICA E GESTIONE
DEI SISTEMI INDUSTRIALI
SCUOLA DI DOTTORATO IN INGEGNERIA
MECCATRONICA E INNOVAZIONE MECCANICA DEL
PRODOTTO
CICLO XXVI

LINEAR AND NON-LINEAR STRUCTURAL ANALYSIS OF NOTCHED COMPONENTS WITH LOCAL ENERGY APPROACHES

Direttore della Scuola: Ch.mo Prof. Alessandro Persona
Supervisore: Ch.mo Prof. Paolo Lazzarin

Dottorando: Christian Marangon

Alla mia famiglia,

ai miei amici,

a Chiara.

Contents

Abstract

In engineering practice, mechanical components are weakened by a wide range of sharp or blunt notches and their presence has to be accurately taken into account in the design. In fact near notches a strong stress gradient is always induced when a far field loading is applied.

Aiming to investigate the integrity of notched components subjected to different loading histories, for many years to nowadays a lot of stress and strain based damage criteria have been proposed. However, in the last years, some energy based criteria have been introduced and successfully applied on notched members proving to be powerful damage prediction tools.

In particular the averaged strain energy density criterion (Lazzarin and Zambardi 2001) has been developed and used in order to assess the strength of notched components with various notch geometries subjected to different types of loading.

The aim of this work is to extend the validity of the averaged SED criterion to the three-dimensional effects arising in the vicinity of a notch and to the problems induced by the application of multiaxial static and cyclic loadings.

Taking advantage of some results obtained from multiaxial cyclic analyses, the effect of the phase displacement between the applied loads has been addressed presenting a new proposal based on the maximum tangential stress averaged over an entire loading cycle.

Finally, a dedicated software based on the cyclic plasticity theory has been developed in order to obtain the stress/strain distributions at the tip of a rounded notch subjected to uniaxial and multiaxial low cycle fatigue. A particular link between the plastic hysteresis energy at the notch tip and the averaged SED has been found representing the first potential step for a future extension of the averaged SED criterion to cyclic plasticity.

Sommario

Nella pratica ingegneristica, i componenti meccanici sono sovente indeboliti da discontinuità geometriche di diversa forma e dimensione, i quali devono essere tenuti in considerazione in fase di progettazione al fine di evitare malfunzionamenti o collassi strutturali.

Con l'obiettivo di valutare l'integrità strutturale di componenti indeboliti da intagli soggetti a sollecitazioni di diversa natura, numerosi criteri di cedimento sono stati sviluppati considerando lo stato di tensione e/o di deformazione all'apice dell'intaglio o nelle immediate vicinanze di quest'ultimo. Inoltre, negli ultimi anni, sono stati sviluppati approcci di tipo energetico, i quali hanno dimostrato un'ottima attitudine alla previsione del cedimento di componenti intagliati. In particolare, il criterio basato sulla densità di energia di deformazione (SED) mediata all'interno di un volume strutturale è stato presentato da Lazzarin e Zambardi (2001) al fine di valutare la resistenza di componenti intagliati soggetti a diverse sollecitazioni.

L'obiettivo del primo filone di ricerca di questa tesi è quello di estendere e validare il criterio SED considerando sia i modi accoppiati che si generano per effetto Poisson in componenti tridimensionali, sia problemi legati all'applicazione di sollecitazioni di modo misto e di fatica multiassiale.

Prendendo spunto da alcuni risultati ottenuti nel caso di sollecitazioni cicliche, il secondo filone di ricerca ha riguardato lo studio di una proposta in grado di discriminare l'effetto dello sfasamento tra le sollecitazioni su provini intagliati a spigolo vivo soggetti a fatica multiassiale.

Il terzo filone di ricerca ha riguardato l'implementazione di un software in grado di fornire le tensioni e le deformazioni elasto-plastiche all'apice di un intaglio raccordato sottoposto a fatica oligociclica. Infine, è stato possibile trovare un coefficiente di correlazione tra l'area del ciclo di isteresi all'apice dell'intaglio ed il valore della densità di energia di deformazione elasto-plastica all'interno di un volume strutturale.

Introduction

Geometrical discontinuities in mechanical components and structures induce more or less localized perturbations of the stress fields. The knowledge of the stress distributions in the vicinity of the stress raisers is fundamental in order to accurately design a mechanical component.

For a long time, problems related to notches were addressed evaluating first the peak stress value and only subsequently the whole stress field. Over the years, the specialized literature promoted some new expressions able to obtain the stress concentration factors of notches body basing the research on the series expansion of Airy biharmonic potential functions (Neuber 1958). With another approach, Williams (1952) presented stress and strain displacement fields near V-notches in the form of eigenfunction series expansions. When a non zero notch tip radius is considered, solutions have been, instead, determined by Creager and Paris (1967). With the aim of evaluating the stress fields problem in general terms, for cracked, sharp notched or blunt notched components, Lazzarin and Tovo (1996) presented some new solutions based on the complex potential functions according to Muskelishvili's method. The problem of sharp V-shaped notches in round bars under antiplane shear was solved by Seweryn and Molski (1996) and Qian and Hasebe (1997). Recently the elastic stress fields ahead of different types of circumferential notches in infinite and finite size round bars under torsion were reported by Lazzarin et al. (2007) and Zappalorto et al. (2008-2010).

In order to find a complete solution of the elastic stress fields in notched bodies Hartranft and Sih (1969) introduce some new expressions considering the whole three-dimensional nature of the problem. Following, the three-dimensional crack stress fields have been obtained by Yang and Freund (1985) by using the simplified assumption tied to Kane and Mindlin (1956). More recently, some extensions of the linear elastic three-dimensional solutions were given by

Kotousov and Lew (2006) and Zappalorto and Lazzarin (2013). Chapter 1 of this work briefly introduces the above mentioned linear elastic solutions.

Chapter 2 of this work focuses on the introduction of the main concepts at the basis of the criterion based on the evaluation of the strain energy density (SED) over a control volume surrounding the tip of a sharp or rounded notch presented and accurately described in some recent contributions by Lazzarin and Zambardi (2001) and Lazzarin and Berto (2005a). The strength properties of brittle components weakened by different types of notch were uniquely obtained both in the case of static and cyclic loading. The definition of this particular approach represents the starting point of the following chapters of this dissertation, in fact the principal aim of this work is to verify the validity of the SED approach and to extend it, if possible, to particular three-dimensional notch effects or problems related to different uniaxial or multiaxial, static or cyclic loading conditions.

Chapters 3 and 4 are related to three-dimensional problems of notched components. In particular Chapter 3 discusses the main features of the out-of-plane induced mode dealing with three-dimensional plates weakened by blunt notches. Some results from blunt V-notches, circular and elliptic holes are discussed in detail and presented. The main key-point highlighted in this Chapter is that always three-dimensional effects exist in finite thickness plates, because mode I, II and III cannot exist in isolation. The importance of induced modes varies from case to case and depends on the geometry of the component and on the externally applied load. These effects cannot be neglected *a priori* even if, in some cases, they may be negligible. Applying some particular boundary conditions on pointed V-notches, Chapter 4 remarks that the application of a far field mode II loading generates a coupled out-of-plane singular mode. The effect of free-fixed boundary conditions along the notch edges in three dimensional plates weakened by pointed V-notches has been investigated. A synthesis of the magnitude of the stress state through the plate thickness is carried out by using the mean value of the strain energy density (SED) over a given control volume embracing the notch tip. The capability of the SED to capture all the combined effects due to the out-of-plane mode make it a powerful parameter.

The validity of the SED criterion has been investigated in Chapter 5 dealing with an experimental and numerical study of U-notched samples subjected to mixed mode loading considering different combinations of the notch radius and the tilt angle of the notch.

The averaged SED, in conjunction with the equivalent local mode I concept, has been used not only to assess the static strength of the graphite specimens but also to determine the damage initiation point along the notch profile. Good agreement has been found between experimental data and theoretical predictions based on the constancy of the mean strain energy density over the control volume.

Chapter 6 makes use of the energy based criterion in order to assess the strength of sharp and blunt notched components subjected to proportional and non-proportional multiaxial fatigue. The results from multiaxial tests have been discussed together with those obtained under pure tension and pure torsion loading from notched specimens with the same geometry. Altogether more than 120 new fatigue data has been summarised in Chapter 6, corresponding to a one-year of testing programme.

All fatigue data has been re-analysed in terms of the mean value of the strain energy density evaluated over a given, crescent shape volume embracing the stress concentration region. For the examined steel, the radius of the control volume is found to be independent of the loading mode.

Taking advantage of some results obtained on the previous chapter, and in particular from in-phase and out-of-phase multiaxial loadings, Chapter 7 focuses on the effect of the phase angle on sharp V-notches subjected to multi-axial fatigue loading. A new proposal based on the maximum shear stress averaged over an entire fatigue cycle has been presented. The formulation revealed to be applicable to the whole different opening angles ranging to 0° to 180°.

Some interesting considerations on the effect of the phase angle have been drawn and in particular the main conclusion is that the phase angle is found to play a non-negligible effect on the fatigue strength of pointed notches. This effect, that is found to be dependent on the biaxiality ratio, should be considered together with the non linear effects acting on the region closed to the notch tip.

The last Chapter (8) presents a comprehensive theoretical and numerical study on the cyclic elastic-plastic notch stress and strain distributions. The incremental cyclic plasticity theory has been extended to the study of the three dimensional effects at the tip of rounded notches in plates of finite thickness. Different notch geometries and loading configurations have been investigated, such as plane specimens with finite thickness weakened by circular holes, U-notches and rounded V-notches subjected to cyclic mode I and mode II loadings. Theoretical results based on the incremental cyclic plasticity theory have been compared with time-consuming elastic-plastic finite element analyses carried out with a commercial FE code showing a satisfactory agreement. In addition, an interesting link between the SED criterion and the plastic hysteresis energy calculated at the notch tip has been obtained for high amplitudes of load. This could represent the starting point for a future extension of the SED criterion to cyclic plasticity.

1

On the local behaviour of mechanical components weakened by notches

1.1 Introduction

This chapter is aimed to recall the basic concepts concerning the evaluation of the state of stress in the vicinity of a geometrical discontinuity weakening a mechanical component. Linear elastic solutions regarding sharp and blunt notches will be recall after a brief introduction on continuum mechanics and on the theory of elasticity.

1.2 Equations of continuum mechanics

In this work one refers on continuous, homogeneous and isotropic bodies. A continuous body maintains its continuity even at infinitesimal scale, an homogenous body does not change abruptly its material properties and, finally, an isotropic body does not vary its properties with directions.

1.2.1 Equilibrium equations

Let assume to consider a body subjected to a generic state of stress. According to the classical theory of elasticity, the effect of body forces or inertia will be neglected on the following argumentation.

By considering the above mentioned conditions, the following system of equations describes a state of equilibrium of the body:

$$\begin{aligned} \frac{\partial \sigma_{xx}}{\partial x} + \frac{\partial \tau_{xy}}{\partial y} + \frac{\partial \tau_{xz}}{\partial z} = 0 \\ \frac{\partial \tau_{xy}}{\partial x} + \frac{\partial \sigma_{yy}}{\partial y} + \frac{\partial \tau_{yz}}{\partial z} = 0 \\ \frac{\partial \tau_{xz}}{\partial x} + \frac{\partial \tau_{yz}}{\partial y} + \frac{\partial \sigma_{zz}}{\partial z} = 0 \end{aligned} \qquad (1.2.1)$$

In order to ensure a state of equilibrium, the mutuality condition of the shear stresses has to be satisfied, namely:

$$\tau_{ij} = \tau_{ji} \tag{1.2.2}$$

This assumption reduces the number of stresses to be determined from nine to six.

1.2.2 Traction vector and principal stresses

On the surface of a body, the stresses produce a force per unit of area called traction **T**, whose components can be expressed in a matrix form:

$$\mathbf{T} = \begin{bmatrix} \sigma_{xx} & \tau_{xy} & \tau_{xz} \\ \tau_{xy} & \sigma_{yy} & \tau_{yz} \\ \tau_{xz} & \tau_{yz} & \sigma_{zz} \end{bmatrix} \begin{Bmatrix} n_x \\ n_y \\ n_z \end{Bmatrix} \tag{1.2.3}$$

where n_i are the components of an outward normal unit vector of the surface.
Considering an elementary cubic body, the axes of the Cartesian coordinate system can be rotated at any point such that all the shear stresses will be equal to zero. The value of stress at this particular point is characterised by three normal stresses (σ_1, σ_2, σ_3), acting collinear to the three principal axes.
Knowing that a plane is called principal only when the traction vector T acts in the same direction of the outward unit normal vector n, let assume the magnitude of the traction equal to σ. On the principal plane, it can be stated that: $\mathrm{T} = \sigma \mathrm{n}$.
In matrix notation:

$$\begin{bmatrix} \mathrm{t}_1 \\ \mathrm{t}_2 \\ \mathrm{t}_3 \end{bmatrix} = \sigma \begin{bmatrix} \mathrm{n}_1 \\ \mathrm{n}_2 \\ \mathrm{n}_3 \end{bmatrix}. \tag{1.2.4}$$

Where ***T*** and ***n*** are vectors, while σ is a scalar representing the magnitude of the principal stress.

The traction vector can be thought as equal to the stress matrix times the normal vector:

$$\begin{bmatrix} \sigma_{11} & \sigma_{12} & \sigma_{13} \\ \sigma_{21} & \sigma_{22} & \sigma_{23} \\ \sigma_{31} & \sigma_{32} & \sigma_{33} \end{bmatrix} \begin{bmatrix} n_1 \\ n_2 \\ n_3 \end{bmatrix} = \sigma \begin{bmatrix} n_1 \\ n_2 \\ n_3 \end{bmatrix}. \tag{1.2.5}$$

This represents an eigenvalue problem. When the stress state is known, i.e., the stress matrix is given, it is possible to solve an eigenvalue problem in order to determine the eigenvalue σ and the eigenvector ***n***. The eigenvalue σ represents the principal stress, while the eigenvector ***n*** represents the principal direction.

Because the stress tensor is a 3 by 3 symmetric matrix, one can always find three real eigenvalues, i.e., principal stresses, $\sigma_a, \sigma_b, \sigma_c$, distinguishing three different cases:

a. If the three principal stresses are unequal, the three principal directions are orthogonal (e.g., pure shear state).
b. If two principal stresses are equal, but the third is different, the two equal principal stresses can be in any directions in a plane, and the third principal direction is normal to the plane (e.g., pure tensile state).
c. If all the three principal stresses are equal, any direction is a principal direction. This stress state is called hydrostatic state.

The magnitude of the maximum shear stress, τ_{max}, can be obtained by:

$$\left|\tau_{max}\right| = \frac{\max\left|\sigma_\alpha - \sigma_\beta\right|}{2} \tag{1.2.6}$$

where $\max\left|\sigma_\alpha - \sigma_\beta\right|$ is the greatest difference between principal stresses. τ_{max} acts on a plane with the normal vector 45° from the principal directions.

1.2.3 Displacement field

A displacement is a vector by which a material particle moves relative to its position in the reference configuration. If all the material particles in the body move by the same displacement vector, the body moves by a rigid-body translation. If instead the material particles in the body move relative to one another, the body deforms.

Let assume each material particle by its coordinates (x, y, z) in the reference configuration. At time *t*, the material particle (x, y, z) has the displacement $u(x, y, z, t)$ in the *x*-direction, $v(x, y, z, t)$ in the *y*-direction and $w(x, y, z, t)$ in the *z*-direction. A function of spatial coordinates is known as a field. The displacement field is a time-dependent vector field.

1.2.4 Strain field

For a given displacement field, it is always possible to calculate the respective strain field. Let consider two generic material particles in the reference configuration: particle A at (x, y, z) and particle B at $(x + dx, y, z)$, the two particles are far *dx* one to another. At a given time *t*, the two particles move to new locations. The *x*-component of the displacement of particle A is $u(x, y, z, t)$, and that of particle B is $u(x + dx, y, z, t)$. Consequently, the distance between the two particles elongates by $u(x + dx, y, z, t) - u(x, y, z, t)$. The axial strain in the *x*-direction is equal to:

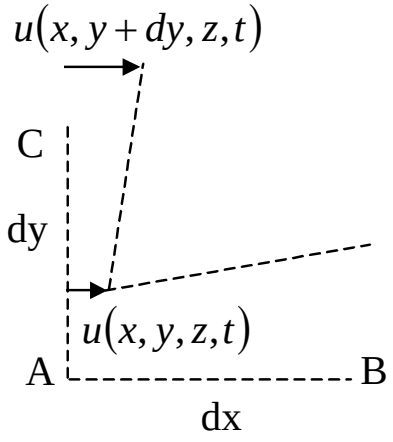

Figure 1.2.2. Schematic representation of deformation

$$\varepsilon_x = \frac{u(x+dx, y, z, t) - u(x, y, z, t)}{dx} = \frac{\partial u}{\partial x}. \tag{1.2.30}$$

This is a strain of material particles in the vicinity of (x, y, z) at time *t*. The function $\varepsilon_x(x, y, z, t)$ is a component of the strain field of the body.

The shear strain is defined as follows. Consider two lines of material particles. In the reference configuration, the two lines are perpendicular one to another. The deformation changes the angle between the two lines by a certain amount. This change in the angle defines the shear strain, γ. Let assume to translate this definition into a strain-displacement relation. Consider three material particles A, B, and C. In the reference configuration, their coordinates are $A(x, y, z)$, $B(x+dx, y, z)$, and $C(x, y+dy, z)$. In the deformed configuration, in the *x*-direction, particle A moves by $u(x, y, z, t)$ and particle C by $u(x, y+dy, z, t)$. Consequently, the deformation rotates line AC about axis *z* by an angle

$$\frac{u(x, y+dy, z, t) - u(x, y, z, t)}{dy} = \frac{\partial u}{\partial y}. \tag{1.2.31}$$

Similarly, the deformation rotates line AB about axis *z* by an angle

$$\frac{v(x+dx, y, z, t) - v(x, y, z, t)}{dx} = \frac{\partial v}{\partial x}. \tag{1.2.32}$$

Consequently, the shear strain in the *xy* plane is the net change in the included angle:

$$\gamma_{xy} = \frac{\partial u}{\partial y} + \frac{\partial v}{\partial x}. \tag{1.2.33}$$

For a body in the three-dimensional space, the strain state of a material particle is described by a total of six components. The strains are linked to the displacements as follows:

$$\varepsilon_x = \frac{\partial u}{\partial x}, \quad \varepsilon_y = \frac{\partial v}{\partial y}, \quad \varepsilon_z = \frac{\partial w}{\partial z}$$
$$\gamma_{xy} = \frac{\partial u}{\partial y} + \frac{\partial v}{\partial x}, \quad \gamma_{yz} = \frac{\partial v}{\partial z} + \frac{\partial w}{\partial y}, \quad \gamma_{zx} = \frac{\partial w}{\partial x} + \frac{\partial u}{\partial z} \tag{1.2.34}$$

The shear strain can also be written in the following form: $\varepsilon_{xy} = \gamma_{xy}/2$. This new definition permits to write the six strain-displacement relations as follows:

$$\varepsilon_{ij} = \frac{1}{2}\left(\frac{\partial u_i}{\partial x_j} + \frac{\partial u_j}{\partial x_i}\right). \tag{1.2.35}$$

In general six equation of compatibility must be satisfied in order to obtain a single-valued displacement field:

$$\frac{\partial^2 \varepsilon_{xx}}{\partial y^2} + \frac{\partial^2 \varepsilon_{yy}}{\partial x^2} - \frac{\partial^2 \gamma_{xy}}{\partial x \partial y} = 0$$
$$\frac{\partial^2 \varepsilon_{xx}}{\partial z^2} + \frac{\partial^2 \varepsilon_{zz}}{\partial x^2} - \frac{\partial^2 \gamma_{xz}}{\partial x \partial z} = 0$$
$$\frac{\partial^2 \varepsilon_{yy}}{\partial z^2} + \frac{\partial^2 \varepsilon_{zz}}{\partial y^2} - \frac{\partial^2 \gamma_{yz}}{\partial y \partial z} = 0$$
$$\frac{\partial^2 \varepsilon_{xx}}{\partial y \partial z} = \frac{\partial^2 \varepsilon_{xy}}{\partial x \partial z} - \frac{\partial^2 \varepsilon_{yz}}{\partial x^2} + \frac{\partial^2 \varepsilon_{zx}}{\partial y \partial x} = 0 \tag{1.2.36}$$
$$\frac{\partial^2 \varepsilon_{yy}}{\partial x \partial z} = \frac{\partial^2 \varepsilon_{xy}}{\partial y \partial z} + \frac{\partial^2 \varepsilon_{yz}}{\partial y \partial x} - \frac{\partial^2 \varepsilon_{zx}}{\partial y^2} = 0$$
$$\frac{\partial^2 \varepsilon_{zz}}{\partial x \partial y} = -\frac{\partial^2 \varepsilon_{xy}}{\partial z^2} + \frac{\partial^2 \varepsilon_{yz}}{\partial x \partial z} + \frac{\partial^2 \varepsilon_{zx}}{\partial y \partial z} = 0$$

1.2.5 Equations in Cylindrical Coordinates (r, θ, z)

Suppose *u, v, w* are the displacement components in the radial, circumferential and axial directions, respectively. Equations of Equilibrium become:

$$\frac{\partial \sigma_r}{\partial r}+\frac{1}{r}\frac{\partial \sigma_{r\theta}}{\partial \theta}+\frac{\partial \sigma_{rz}}{\partial z}+\frac{\sigma_r-\sigma_\theta}{r}=0$$
$$\frac{\partial \sigma_{r\theta}}{\partial r}+\frac{1}{r}\frac{\partial \sigma_\theta}{\partial \theta}+\frac{\partial \sigma_{\theta z}}{\partial z}+\frac{2\sigma_{r\theta}}{r}=0 \qquad (1.2.37)$$
$$\frac{\partial \sigma_{rz}}{\partial r}+\frac{1}{r}\frac{\partial \sigma_{\theta z}}{\partial \theta}+\frac{\partial \sigma_z}{\partial z}+\frac{\sigma_{rz}}{r}=0$$

$$\varepsilon_r=\frac{\partial u}{\partial r} \qquad \varepsilon_{\theta z}=\frac{1}{2}\left(\frac{\partial v}{\partial z}+\frac{1}{r}\frac{\partial w}{\partial \theta}\right)$$
$$\varepsilon_\theta=\frac{1}{r}\left(\frac{\partial v}{\partial \theta}+u\right) \qquad \varepsilon_{zr}=\frac{1}{2}\left(\frac{\partial w}{\partial r}+\frac{\partial u}{\partial z}\right) \qquad (1.2.38)$$
$$\varepsilon_z=\frac{\partial w}{\partial z} \qquad \varepsilon_{r\theta}=\frac{1}{2}\left(\frac{1}{r}\frac{\partial u}{\partial \theta}+\frac{\partial v}{\partial r}-\frac{v}{r}\right)$$

1.3 Equations of elasticity

Linear relations between the components of stress and the components of strain are known generally as Hooke's law:

$$\varepsilon_{ij}=\frac{\sigma_{ij}}{2G}-\frac{\nu}{E}\sigma_{kk}\delta_{ij} \qquad (1.3.1)$$

In more details, every Cartesian strain component can be written as follows:

$$\varepsilon_{xx}=\frac{1}{E}\left[\sigma_{xx}-\nu(\sigma_{yy}+\sigma_{zz})\right] \qquad \gamma_{xz}=\frac{\tau_{xz}}{G}$$
$$\varepsilon_{yy}=\frac{1}{E}\left[\sigma_{yy}-\nu(\sigma_{xx}+\sigma_{zz})\right] \qquad \gamma_{yz}=\frac{\tau_{yz}}{G} \qquad \textbf{(1.3.2)}$$
$$\varepsilon_{zz}=\frac{1}{E}\left[\sigma_{zz}-\nu(\sigma_{yy}+\sigma_{xx})\right] \qquad \gamma_{xy}=\frac{\tau_{xy}}{G}$$

1.3.1 Plane problems of elasticity theory

The plane problems of elasticity are generally designated as plane strain and plane stress problems.

Plane strain conditions are typically met by thick plates that are loaded in the plane. The loading is invariant along the *z*-direction. Consequently, the

displacement field takes the form $u(x,y),\ v(x,y),\ w=0$.

Considering the strain displacement relations, only the three in-plane strains are nonzero: $\varepsilon_{xx}(x,y), \varepsilon_{yy}(x,y), \gamma_{xy}(x,y)$. The three out-of-plane strains, instead, vanish: $\varepsilon_{zz}=\gamma_{xz}=\gamma_{yz}=0$. This implies that $\tau_{xz}=\tau_{yz}=0$. From $\varepsilon_{zz}=0$ instead, it is possible to obtain:

$$\sigma_{zz}=\nu(\sigma_{xx}+\sigma_{yy}) \tag{1.3.3}$$

On the other hand, if a thin plate is loaded by forces applied at the boundary, parallel to the plane of the plate and distributed uniformly over the thickness, the non-zero components in its plane are $\sigma_{xx}, \sigma_{yy}, \tau_{xy}$, and the components out of the plane vanish:

$$\sigma_{zz}=\tau_{xz}=\tau_{yz}=0. \tag{1.3.4}$$

For both cases the stress field in the plane is described by three functions $\sigma_{xx}(x,y),\ \sigma_{yy}(x,y),\ \tau_{xy}(x,y)$. Then, in light of the simplified stress states the equilibrium equations reduce to:

$$\frac{\partial\sigma_{xx}}{\partial x}+\frac{\partial\tau_{xy}}{\partial y}=0,\quad \frac{\partial\tau_{xy}}{\partial x}+\frac{\partial\sigma_{yy}}{\partial y}=0 \tag{1.3.5}$$

while compatibility of strains requires:

$$\frac{\partial^2\varepsilon_{xx}}{\partial y^2}+\frac{\partial^2\varepsilon_{yy}}{\partial x^2}=\frac{\partial^2\gamma_{xy}}{\partial x\partial y} \tag{1.3.6}$$

The stress-strain relationships for plane stress are then:

$$
\begin{aligned}
\varepsilon_{xx} &= \frac{\sigma_{xx}}{E} - \nu\frac{\sigma_{yy}}{E} \\
\varepsilon_{yy} &= \frac{\sigma_{yy}}{E} - \nu\frac{\sigma_{xx}}{E} \\
\gamma_{xy} &= \frac{2(1+\nu)}{E}\tau_{xy} \\
\varepsilon_{zz} &= -\frac{\nu}{E}(\sigma_{xx}+\sigma_{yy}) \\
\gamma_{xz} &= \gamma_{yz} = 0
\end{aligned}
\tag{1.3.7}
$$

While for plane strain one has:

$$
\begin{aligned}
\varepsilon_{xx} &= \frac{1}{E}(\sigma_{xx} - \nu\sigma_{yy} - \nu\sigma_{zz}) = \frac{1-\nu^2}{E}\left(\sigma_{xx} - \frac{\nu}{1-\nu}\sigma_{yy}\right) \\
\varepsilon_{yy} &= \frac{1}{E}(\sigma_{yy} - \nu\sigma_{xx} - \nu\sigma_{zz}) = \frac{1-\nu^2}{E}\left(\sigma_{yy} - \frac{\nu}{1-\nu}\sigma_{xx}\right) \\
\gamma_{xy} &= \frac{2(1+\nu)}{E}\tau_{xy}
\end{aligned}
\tag{1.3.8}
$$

1.4 The Airy stress function

Consider two different functions $f(x,y)$ and $g(x,y)$ satisfying:

$$
\frac{\partial \mathrm{f}}{\partial \mathrm{x}} = \frac{\partial \mathrm{g}}{\partial \mathrm{y}} \tag{1.4.1}
$$

Cauchy-Schwarz conditions assures that there exists a function $A(x,y)$:

$$
\mathrm{f} = \frac{\partial \mathrm{A}}{\partial \mathrm{y}}, \quad \mathrm{g} = \frac{\partial \mathrm{A}}{\partial \mathrm{x}}. \tag{1.4.2}
$$

Considering the equilibrium condition:

$$
\frac{\partial \sigma_{xx}}{\partial x} + \frac{\partial \tau_{xy}}{\partial y} = 0 \tag{1.4.3}
$$

It is possible to state that a function $A(x,y)$ exists and the components of stress can be written as:

$$\sigma_{xx} = \frac{\partial A}{\partial y}, \quad \tau_{xy} = -\frac{\partial A}{\partial x} \tag{1.4.4}$$

From:

$$\frac{\partial \tau_{xy}}{\partial x} + \frac{\partial \sigma_{yy}}{\partial y} = 0 \tag{1.4.5}$$

A function $B(x,y)$ exists and the components of stress can be written as:

$$\sigma_{yy} = \frac{\partial B}{\partial x}, \quad \tau_{xy} = -\frac{\partial B}{\partial y} \tag{1.4.6}$$

Finally, from the properties

$$\frac{\partial A}{\partial x} = \frac{\partial B}{\partial y} \tag{1.4.7}$$

Made use of this last property, a function $\phi(x,y)$ can exists, such that:

$$A = \frac{\partial \phi}{\partial y}, \quad B = \frac{\partial \phi}{\partial x} \tag{1.4.8}$$

The function $\phi(x,y)$ is known as the Airy stress function (1862). The three different components representing the stress field can be written as a function of $\phi(x,y)$:

$$\sigma_{xx} = \frac{\partial^2 \phi}{\partial y^2}, \quad \sigma_{yy} = \frac{\partial^2 \phi}{\partial y^2}, \quad \tau_{xy} = -\frac{\partial^2 \phi}{\partial y \partial x} \tag{1.4.9}$$

Using the stress-strain relations, the three components of strain field can be obtain

in terms of the Airy stress function:

$$\varepsilon_{xx} = \frac{1}{E}\left(\frac{\partial^2\phi}{\partial y^2} - \nu\frac{\partial^2\phi}{\partial x^2}\right)$$
$$\varepsilon_{yy} = \frac{1}{E}\left(\frac{\partial^2\phi}{\partial x^2} - \nu\frac{\partial^2\phi}{\partial y^2}\right) \qquad (1.4.10)$$
$$\gamma_{xy} = -\frac{2(1+\nu)}{E}\frac{\partial^2\phi}{\partial x\partial y}$$

In this manner, the compatibility equation can be written as follows:

$$\frac{\partial^4\phi}{\partial x^4} + 2\frac{\partial^4\phi}{\partial x^2\partial y^2} + \frac{\partial^4\phi}{\partial y^4} = 0 \qquad (1.4.11)$$

Or, equally:

$$\left(\frac{\partial^2}{\partial x^2} + \frac{\partial^2}{\partial y^2}\right)\left(\frac{\partial^2\phi}{\partial x^2} + \frac{\partial^2\phi}{\partial y^2}\right) = 0 \qquad (1.4.12)$$

This is the so-called biharmonic equation.

Thus, a procedure to solve a plane problem of elasticity is to solve for $\phi(x,y)$ from the above partial differential equation, and then calculate stresses and strains. After the strains are obtained, the displacement field can be obtained by integrating the strain-displacement relations.

1.4.1 Equations in polar coordinates

The Airy stress function can be expressed also in polar coordinates, $\phi(r,\theta)$. Following all the stress components will be presented in terms of polar coordinate system:

$$\sigma_{rr} = \frac{\partial^2 \phi}{r^2 \partial \theta^2} + \frac{1}{r}\frac{\partial \phi}{\partial r}$$
$$\sigma_{\theta\theta} = \frac{\partial^2 \phi}{\partial r^2} \qquad (1.4.13)$$
$$\tau_{r\theta} = -\frac{\partial}{\partial r}\left(\frac{\partial \phi}{r \partial \theta}\right)$$

The new biharmonic equation can be written as:

$$\left(\frac{\partial^2}{\partial r^2} + \frac{\partial}{r\partial r} + \frac{\partial^2}{r^2\partial\theta^2}\right)\left(\frac{\partial^2 \phi}{\partial r^2} + \frac{\partial \phi}{r\partial r} + \frac{\partial^2 \phi}{r^2 \partial \theta^2}\right) = 0 \qquad (1.4.14)$$

The stress-strain relations can be thus written as follows:

$$\varepsilon_{rr} = \frac{\sigma_{rr}}{E} - \nu\frac{\sigma_{\theta\theta}}{E}$$
$$\varepsilon_{\theta\theta} = \frac{\sigma_{\theta\theta}}{E} - \nu\frac{\sigma_{rr}}{E} \qquad (1.4.15)$$
$$\gamma_{r\theta} = \frac{2(1+\nu)}{E}\tau_{r\theta}$$

The strain-displacement relations are

$$\varepsilon_{rr} = \frac{\partial u_r}{\partial r}$$
$$\varepsilon_{\theta\theta} = \frac{u_r}{r} + \frac{\partial u_\theta}{r\partial\theta} \qquad . \qquad (1.4.16)$$
$$\gamma_{r\theta} = \frac{\partial u_r}{r\partial\theta} + \frac{\partial u_\theta}{\partial r} - \frac{u_\theta}{r}$$

1.4.2 Mushkelisvili- Kolosov's equations

The Mushkelisvili-Kolosov's formulation of plane problems of elasticity follows the equations reported below:

$$\sigma_{xx} + \sigma_{yy} = 4\,\mathrm{Re}\,\psi'(z)$$
$$\sigma_{xx} - \sigma_{yy} - 2i\tau_{zy} = 2\left[z\overline{\psi}''(\bar{z}) + \overline{\chi}''(\bar{z})\right] \qquad (1.4.17)$$

where, as is well known, ψ and χ are two holomorphic functions that have to be determined.

1.5 Linear elastic stress distributions on classic notches using the Airy stress function: plane problems

In this section the most relevant linear elastic solutions of notched problems will be listed in order to better describe the state of the art dealing with this particular problems.

1.5.1 Circular hole in an infinite sheet under remote tension

A classic problem dealing with a component weakened by a notch is the Kirsch problem (1898). Let consider an infinite sheet subjected by a remote pure tension loading, namely: $\tau_{xy} = \sigma_{yy} = 0$ and $\sigma_{xx} = S$.

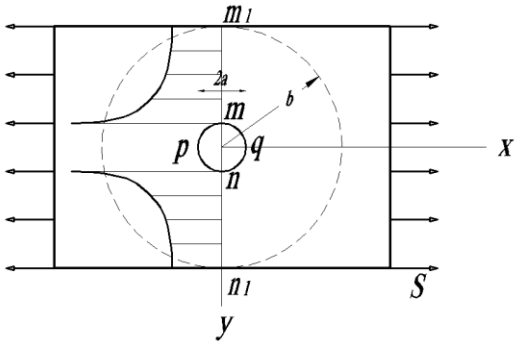

Figure 1.5.1. A circular hole in an infinite sheet under remote tension

The remote state of stress can be expressed in polar coordinates:

$$\sigma_{rr} = \frac{S}{2}(1+\cos 2\theta)$$
$$\sigma_{\theta\theta} = \frac{S}{2}(1-\cos 2\theta) \qquad (1.5.1)$$
$$\tau_{r\theta} = -\frac{S}{2}\sin 2\theta$$

The stress field can be considered as the superposition of two distinct stress fields:

- A symmetric stress field about an axis, which does not depend on the polar coordinate θ, object of the study of Timoshenko and Goodier.

- A non symmetric stress field, which depends on the polar coordinate θ.

The first, symmetric solution, depends only on the radial distance r, so that $\phi = \phi(\mathrm{r})$. The biharmonic equation can be written as follows:

$$\left(\frac{\mathrm{d}^2}{\mathrm{dr}^2} + \frac{1}{\mathrm{r}}\frac{\mathrm{d}}{\mathrm{dr}}\right)\left(\frac{\mathrm{d}^2\phi}{\mathrm{dr}^2} + \frac{1}{\mathrm{r}}\frac{\mathrm{d}\phi}{\mathrm{dr}}\right) = 0 \qquad (1.5.2)$$

This is an equi-dimensional equation, whose solutions can be sought in the form $\phi = r^m$.

Inserting $\phi = r^m$ into the biharmonic equation, one can obtain the algebraic equation $\mathrm{m}^2(\mathrm{m}-2)^2 = 0$ .Consequently, the general solution is:

$$\phi(\mathrm{r}) = \mathrm{A}\log\mathrm{r} + \mathrm{Br}^2\log\mathrm{r} + \mathrm{Cr}^2 + \mathrm{D}. \qquad (1.5.3)$$

where *A, B, C* and *D* are four unknowns constants related to the problem..
The components of the stress field can be written as follows:

$$\sigma_{rr} = \frac{\partial^2 \phi}{r^2 \partial \theta^2} + \frac{1}{r}\frac{\partial \phi}{\partial r} = \frac{A}{r^2} + B(1 + 2\log r) + 2C$$
$$\sigma_{\theta\theta} = \frac{\partial^2 \phi}{\partial r^2} = -\frac{A}{r^2} + B(3 + 2\log r) + 2C \qquad (1.5.4)$$
$$\tau_{r\theta} = -\frac{\partial}{\partial r}\left(\frac{\partial \phi}{r \partial \theta}\right) = 0$$

By using the expression $\varepsilon_r = d(r\varepsilon_\theta)/dr$ in combination with the Hooke's law:

$$\begin{aligned} E\varepsilon_r &= [\sigma_r - \nu\sigma_\theta] \\ E\varepsilon_\theta &= [\sigma_\theta - \nu\sigma_r] \end{aligned} \qquad (1.5.5)$$

One obtains the following equation:

$$\sigma_r(1+\nu) - \sigma_\theta(1+\nu) - r\left(\frac{\partial \sigma_r}{\partial r} - \nu\frac{\partial \sigma_\theta}{\partial r}\right) = 0 \qquad (1.5.6)$$

Substituting into Eq. (1.5.6) the expressions for stresses, Eqs. (1.5.4), one obtains B=0. Then the complete stress field can be re-written in the well-known formulation:

$$\begin{aligned} \sigma_{rr} &= C_1 + \frac{C_2}{r^2} \\ \sigma_{\theta\theta} &= C_1 - \frac{C_2}{r^2} \end{aligned} \qquad (1.5.7)$$

From these equation it is possible to obtain the case of a hole of radius *a* in an infinite sheet subject to a remote biaxial stress *S*. The stress field in the sheet is equal to:

$$\sigma_{rr} = \frac{S}{2}\left[1-\left(\frac{a}{r}\right)^2\right]$$
$$\sigma_{\theta\theta} = \frac{S}{2}\left[1+\left(\frac{a}{r}\right)^2\right] \qquad (1.5.8)$$
$$\tau_{r\theta} = 0$$

Dealing with the non symmetric solution, the stress function has to be imposed in the form $\phi(\mathrm{r},\theta) = \mathrm{f}(\mathrm{r})\cos 2\theta$. Under this circumstances, the biharmonic equation can be re-rewritten as:

$$\left(\frac{d^2}{dr^2}+\frac{d}{rdr}-\frac{4}{r^2}\right)\left(\frac{\partial^2 f}{\partial r^2}+\frac{\partial f}{r\partial r}-\frac{4f}{r^2}\right)=0 \qquad (1.5.9)$$

and the solution is:

$$\phi(\mathrm{r},\theta)=\left(\mathrm{Ar}^2+\mathrm{Br}^4+\frac{\mathrm{C}}{\mathrm{r}^2}+\mathrm{D}\right)\cos 2\theta \qquad (1.5.10)$$

Then:

$$\sigma_{rr} = \frac{\partial^2\phi}{r^2\partial\theta^2}+\frac{1}{r}\frac{\partial\phi}{\partial r} = -\left(2A+\frac{6C}{r^4}+\frac{4D}{r^2}\right)\cos 2\theta$$
$$\sigma_{\theta\theta} = \frac{\partial^2\phi}{\partial r^2} = \left(2A+12Br^2+\frac{6C}{r^4}\right)\cos 2\theta \qquad (1.5.11)$$
$$\tau_{r\theta} = -\frac{\partial}{\partial r}\left(\frac{\partial\phi}{r\partial\theta}\right) = \left(2A+6Br^2-\frac{6C}{r^4}-\frac{2D}{r^2}\right)\sin 2\theta$$

The four-needed boundary conditions are:

Remote from the hole, namely, $r\to\infty$, $\sigma_{\mathrm{rr}} = \frac{\mathrm{S}}{2}\cos 2\theta$, $\tau_{\mathrm{r}\theta} = -\frac{\mathrm{S}}{2}\sin 2\theta$, giving $\mathrm{A} = -\mathrm{S}/4,\ \mathrm{B} = 0$.

On the surface of the hole, namely, $r = a$, $\sigma_{rr} = 0$, $\tau_{r\theta} = 0$, giving $\mathrm{D} = \mathrm{Sa}^2/2$ and $\mathrm{C} = -\mathrm{Sa}^4/4$.

Then stress fields take the form:

$$\sigma_{rr} = \frac{S}{2}\left[1+3\left(\frac{a}{r}\right)^4 - 4\left(\frac{a}{r}\right)^2\right]\cos 2\theta$$
$$\sigma_{\theta\theta} = -\frac{S}{2}\left[1+3\left(\frac{a}{r}\right)^4\right]\cos 2\theta \qquad (1.5.12)$$
$$\tau_{r\theta} = -\frac{S}{2}\left[1-3\left(\frac{a}{r}\right)^4 + 2\left(\frac{a}{r}\right)^2\right]\sin 2\theta$$

Adding the solution for the two sub-problems, one can obtain the complete solution.

$$\sigma_{rr} = \frac{S}{2}\left[1+3\left(\frac{a}{r}\right)^4 - 4\left(\frac{a}{r}\right)^2\right]\cos 2\theta + \frac{S}{2}\left[1-\left(\frac{a}{r}\right)^2\right]$$
$$\sigma_{\theta\theta} = -\frac{S}{2}\left[1+3\left(\frac{a}{r}\right)^4\right]\cos 2\theta + \frac{S}{2}\left[1+\left(\frac{a}{r}\right)^2\right] \qquad (1.5.13)$$
$$\tau_{r\theta} = -\frac{S}{2}\left[1-3\left(\frac{a}{r}\right)^4 + 2\left(\frac{a}{r}\right)^2\right]\sin 2\theta$$

1.5.2 Williams' solution for sharp V-notches under Mode I and Mode II

Williams, in his pioneering work, addressed for the first time the problem of stress distributions resulting from re-entrant corners using an Airy stress function composed by two separated variables (Williams 1952):

$$\phi(r,\theta) = r^{\lambda+1}\cdot f(\theta) \qquad (1.5.14)$$

By knowing the representation of the stress components in terms of polar coordinates it is possible to write those related to the Williams problem:

$$\sigma_{rr} = \frac{\partial^2 \phi}{r^2 \partial \theta^2} + \frac{1}{r}\frac{\partial \phi}{\partial r} = r^{\lambda-1}\left[\frac{d^2 f(\theta)}{d\theta^2} + (\lambda+1)\cdot f(\theta)\right]$$
$$\sigma_{\theta\theta} = \frac{\partial^2 \phi}{\partial r^2} = r^{\lambda-1}\left[\lambda\cdot(\lambda+1)\cdot f(\theta)\right] \qquad (1.5.15)$$
$$\tau_{r\theta} = -\frac{\partial}{\partial r}\left(\frac{\partial \phi}{r\partial \theta}\right) = r^{\lambda-1}\left[-\lambda\cdot\frac{df(\theta)}{d\theta}\right]$$

The bi-harmonic equation can be expressed as follows:

$$\left(\frac{\partial^2 \phi}{\partial r^2} + \frac{\partial \phi}{r\partial r} + \frac{\partial^2 \phi}{r^2 \partial \theta^2}\right) = \sigma_{rr} + \sigma_{\theta\theta} =$$
$$r^{\lambda-1}\left[\frac{\partial^2 f(\theta,\lambda)}{\partial \theta^2} + (\lambda+1)\cdot f(\theta)\right] + r^{\lambda-1}\left[\lambda\cdot(\lambda+1)\cdot f(\theta)\right] \qquad (1.5.16)$$

Substituting in the bi-harmonic equations, the following equation can be written:

$$\frac{\partial^4 f}{\partial \theta^4} + \left[(\lambda-1)^2 + (\lambda+1)^2\right]\frac{\partial^2 f}{\partial \theta^2} + \left[(\lambda-1)^2\cdot(\lambda+1)^2\right] f = 0 \qquad (1.5.17)$$

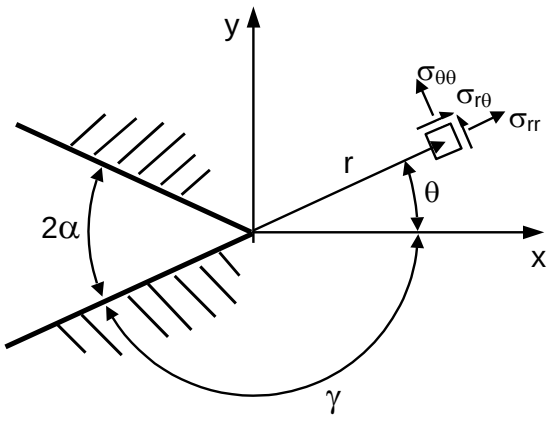

Figure 1.5.2. Polar coordinate system at the tip of a sharp V-notch.

Eq. (1.5.17) can be satisfied if function f(θ) holds the following form:

$$f(\theta) = b_1 \sin(\lambda+1)\theta + b_2 \cos(\lambda+1)\theta + b_3 \sin(\lambda-1)\theta + b_4 \cos(\lambda-1)\theta \qquad (1.5.18)$$

With reference to the fig. 1.5.2, the boundary conditions of the free edge of the notch can be written as follows :

$$\sigma_{\theta\theta}(\pm\gamma) = \tau_{r\theta}(\pm\gamma) = 0 \qquad (1.5.19)$$

That in terms of f turn to:

$$f(\pm\gamma, \lambda) = \frac{\partial f(\pm\gamma, \lambda)}{\partial \theta} = 0 \qquad (1.5.20)$$

Substituting Eq.(1.5.18) in Eq.(1.5.19) one can obtain:

$$\begin{aligned} &\pm b_1 \sin(\lambda+1)\gamma + b_2 \cos(\lambda+1)\gamma \pm b_3 \sin(\lambda-1)\gamma + b_4 \cos(\lambda-1)\gamma = 0 \\ &+ b_1(\lambda+1)\cdot\cos(\lambda+1)\gamma \pm b_2(\lambda+1)\cdot\sin(\lambda+1)\gamma + \\ &+ b_3(\lambda-1)\cdot\cos(\lambda-1)\gamma \pm b_4(\lambda-1)\cdot\sin(\lambda-1)\gamma = 0 \end{aligned} \qquad (1.5.21)$$

Now it is possible to consider two different contributions on the problem, one related to the symmetric mode (Mode I) and the other tied to the skew-symmetric one (Mode II), respectively:

$$\begin{cases} + b_2 \cos(\lambda_1+1)\gamma + b_4 \cos(\lambda_1-1)\gamma = 0 \\ + b_2(\lambda_1+1)\cdot\sin(\lambda_1+1)\gamma + b_4(\lambda_1-1)\cdot\sin(\lambda_1-1)\gamma = 0 \end{cases} \qquad (1.5.22)$$

$$\begin{cases} + b_1 \sin(\lambda_2+1)\gamma + b_3 \sin(\lambda_2-1)\gamma = 0 \\ + b_1(\lambda_2+1)\cdot\cos(\lambda_2+1)\gamma + b_3(\lambda_2-1)\cdot\cos(\lambda_2-1)\gamma = 0 \end{cases} \qquad (1.5.23)$$

The eigenvalues of the problem can be determined providing the following two equations:

$$\begin{aligned} &(\lambda_1-1)\cdot\sin(\lambda_1-1)\gamma\cdot\cos(\lambda_1+1)\gamma + \\ &-(\lambda_1+1)\cdot\cos(\lambda_1-1)\gamma\cdot\sin(\lambda_1+1)\gamma = 0 \end{aligned} \qquad (1.5.24)$$

$$(\lambda_2+1)\cdot\sin(\lambda_2-1)\gamma\cdot\cos(\lambda_2+1)\gamma+ \\ -(\lambda_2-1)\cdot\cos(\lambda_2-1)\gamma\cdot\sin(\lambda_2+1)\gamma=0 \tag{1.5.25}$$

which can also be rewritten in the following form:

$$\sin 2\lambda_1\gamma+\lambda_1\cdot\sin 2\gamma=0 \tag{1.5.26}$$

$$\sin 2\lambda_2\gamma-\lambda_2\cdot\sin 2\gamma=0 \tag{1.5.27}$$

In the case of Mode I and Mode II, respectively. Solutions of the two above reported equations are plotted in Figure 1.5.3.

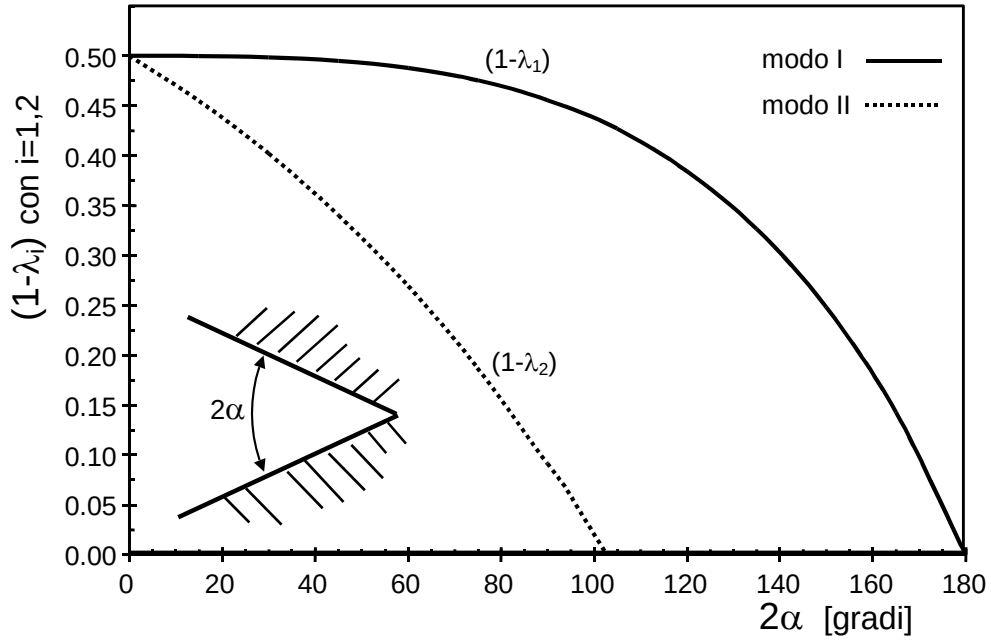

Figure 1.5.3. Plotting of Williams' eigeinvalues.

The smallest but positive roots related to each loading mode have to be determined. This choice has been made in order to keep the strain energy density close to the tip equal to a finite value.

The remaining parameters can be determined as follows:

$$b_2=-b_4\frac{(\lambda_1-1)}{(\lambda_1+1)}\cdot\frac{\sin(\lambda_1-1)\gamma}{\sin(\lambda_1+1)\gamma}=b_4\frac{(\lambda_1-1)}{(\lambda_1+1)}\cdot\chi_1 \tag{1.5.28}$$

where χ_1 satisfies:

$$\chi_1 = \frac{\sin(\lambda_1 - 1)\gamma}{\sin(\lambda_1 + 1)\gamma} = -\frac{\sin(1-\lambda_1)\gamma}{\sin(1+\lambda_1)\gamma} \tag{1.5.29}$$

And:

$$b_1 = -b_3 \frac{\sin(\lambda_2 - 1)\gamma}{\sin(\lambda_2 + 1)\gamma} = -b_3 \cdot \chi_2 \tag{1.5.30}$$

Where:

$$\chi_2 = \frac{\sin(\lambda_2 - 1)\gamma}{\sin(\lambda_2 + 1)\gamma} = -\frac{\sin(1-\lambda_2)\gamma}{\sin(1+\lambda_2)\gamma} \tag{1.5.31}$$

Finally, the expressions for stress distributions in the case of Mode I loading are:

$$\begin{aligned}
\sigma_{\theta\theta}(r,\theta) &= \lambda_1 r^{\lambda_1 - 1} b_4 \left[(1+\lambda_1)\cos(1-\lambda_1)\theta + \chi_1(1-\lambda_1)\cos(1+\lambda_1)\theta\right] \\
\sigma_{rr}(r,\theta) &= \lambda_1 r^{\lambda_1 - 1} b_4 \left[(3-\lambda_1)\cos(1-\lambda_1)\theta - \chi_1(1-\lambda_1)\cos(1+\lambda_1)\theta\right] \\
\tau_{r\theta}(r,\theta) &= \lambda_1 r^{\lambda_1 - 1} b_4 \left[(1-\lambda_1)\sin(1-\lambda_1)\theta + \chi_1(1-\lambda_1)\sin(1+\lambda_1)\theta\right]
\end{aligned} \tag{1.5.32}$$

And in the case of Mode II loading:

$$\begin{aligned}
\sigma_{\theta\theta}(r,\theta) &= \lambda_2 r^{\lambda_2 - 1} b_3 \left[(1+\lambda_2)\sin(1-\lambda_2)\theta + \chi_2(1+\lambda_2)\sin(1+\lambda_2)\theta\right] \\
\sigma_{rr}(r,\theta) &= \lambda_2 r^{\lambda_2 - 1} b_3 \left[(3-\lambda_2)\sin(1-\lambda_2)\theta - \chi_2(1+\lambda_2)\sin(1+\lambda_2)\theta\right] \\
\tau_{r\theta}(r,\theta) &= \lambda_2 r^{\lambda_2 - 1} b_3 \left[(1-\lambda_2)\cos(1-\lambda_2)\theta + \chi_2(1+\lambda_2)\cos(1+\lambda_2)\theta\right]
\end{aligned} \tag{1.5.33}$$

Stress fields are defined as a function of two unknown parameters which can be linked to the geometry and to the far fields applied load through the notch stress intensity factors defined by Gross and Meldenson (1972):

$$K_1^N = \sqrt{2\pi} \lim_{r \to 0} \left[r^{1-\lambda_1} \sigma_{\theta\theta}(r, \theta = 0) \right] \tag{1.5.34}$$

$$K_2^N = \sqrt{2\pi} \lim_{r \to 0} \left[r^{1-\lambda_2} \sigma_{r\theta}(r, \theta = 0) \right] \tag{1.5.35}$$

In this manner, the equations representing the stress components become, in the case of Mode I:

$$\begin{aligned}
\sigma_{\theta\theta}(r,\theta) &= \frac{1}{\sqrt{2\pi}} \frac{r^{\lambda_1 - 1} \cdot K_1^N}{(1+\lambda_1) + \chi_1 (1-\lambda_1)} \left[(1+\lambda_1)\cos(1-\lambda_1)\theta + \chi_1 (1-\lambda_1)\cos(1+\lambda_1)\theta \right] \\
\sigma_{rr}(r,\theta) &= \frac{1}{\sqrt{2\pi}} \frac{r^{\lambda_1 - 1} \cdot K_1^N}{(1+\lambda_1) + \chi_1 (1-\lambda_1)} \left[(3-\lambda_1)\cos(1-\lambda_1)\theta - \chi_1 (1-\lambda_1)\cos(1+\lambda_1)\theta \right] \\
\tau_{r\theta}(r,\theta) &= \frac{1}{\sqrt{2\pi}} \frac{r^{\lambda_1 - 1} \cdot K_1^N}{(1+\lambda_1) + \chi_1 (1-\lambda_1)} \left[(1-\lambda_1)\sin(1-\lambda_1)\theta + \chi_1 (1-\lambda_1)\sin(1+\lambda_1)\theta \right]
\end{aligned} \tag{1.5.36}$$

And in the case of Mode II:

$$\begin{aligned}
\sigma_{\theta\theta}(r,\theta) &= \frac{1}{\sqrt{2\pi}} \frac{r^{\lambda_2 - 1} \cdot K_2^N}{(1-\lambda_2) + \chi_2 (1+\lambda_2)} \left[(1+\lambda_2)\sin(1-\lambda_2)\theta + \chi_2 (1+\lambda_2)\sin(1+\lambda_2)\theta \right] \\
\sigma_{rr}(r,\theta) &= \frac{1}{\sqrt{2\pi}} \frac{r^{\lambda_2 - 1} \cdot K_2^N}{(1-\lambda_2) + \chi_2 (1+\lambda_2)} \left[(3-\lambda_2)\sin(1-\lambda_2)\theta - \chi_2 (1+\lambda_2)\sin(1+\lambda_2)\theta \right] \\
\sigma_{r\theta}(r,\theta) &= \frac{1}{\sqrt{2\pi}} \frac{r^{\lambda_2 - 1} \cdot K_2^N}{(1-\lambda_2) + \chi_2 (1+\lambda_2)} \left[(1-\lambda_2)\cos(1-\lambda_2)\theta + \chi_2 (1+\lambda_2)\cos(1+\lambda_2)\theta \right]
\end{aligned} \tag{1.5.37}$$

1.5.3 Lazzarin and Tovo's equations for blunt V and U shaped notches under Mode I and II

Lazzarin and Tovo (1996) made use of the Kolosoff-Muskhelishvili's method aiming to the determination of the stress components in the proximity of an open notch (which becomes a V-notch when the notch radius is equal to zero) under plane stress and plane strain conditions.

Following are reported the analytical functions used in the procedure:

$$\varphi(z) = a z^{\lambda} \qquad \psi(z) = b z^{\lambda} + c z^{\mu} \tag{1.5.38}$$

where coefficients a, b, c are complex numbers, while exponents λ and μ are real numbers, with the hypothesis stating that $\lambda > \mu$.

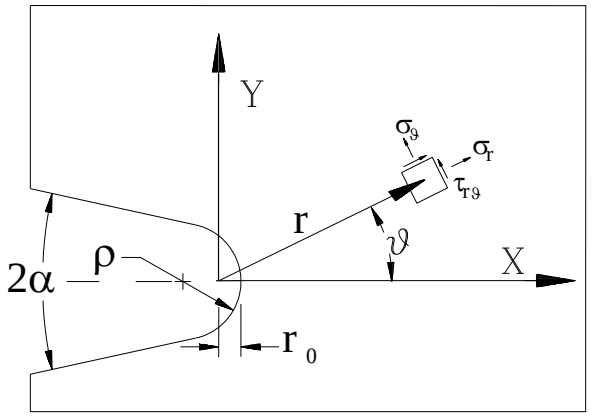

Figure 1.5.4. Coordinate system and symbols used for the stress field components (figure from Lazzarin and Tovo, 1996).

With reference to the figure 1.5.4, polar components of stresses can be written as follows:

$$\begin{aligned}
\sigma_\vartheta &= \lambda r^{\lambda-1}\left[a_1(1+\lambda)\cos(1-\lambda)\vartheta + a_2(1+\lambda)\sin(1-\lambda)\vartheta + b_1\cos(1+\lambda)\vartheta - b_2\sin(1+\lambda)\vartheta\right] + \\
&\quad + \mu r^{\mu-1}\left[c_1\cos(1+\mu)\vartheta - c_2\sin(1+\mu)\vartheta\right] \\
\sigma_r &= \lambda r^{\lambda-1}\left[a_1(3-\lambda)\cos(1-\lambda)\vartheta + a_2(3-\lambda)\sin(1-\lambda)\vartheta - b_1\cos(1+\lambda)\vartheta + b_2\sin(1+\lambda)\vartheta\right] + \\
&\quad + \mu r^{\mu-1}\left[-c_1\cos(1+\mu)\vartheta + c_2\sin(1+\mu)\vartheta\right] \\
\tau_{r\vartheta} &= \lambda r^{\lambda-1}\left[a_1(1-\lambda)\sin(1-\lambda)\vartheta - a_2(1-\lambda)\cos(1-\lambda)\vartheta + b_1\sin(1+\lambda)\vartheta + b_2\cos(1+\lambda)\vartheta\right] + \\
&\quad + \mu r^{\mu-1}\left[c_1\sin(1+\mu)\vartheta + c_2\cos(1+\mu)\vartheta\right]
\end{aligned} \tag{1.5.39}$$

In order to impose the boundary conditions, Lazzarin and Tovo (1996) made use of the Neuber's curvilinear coordinates u and v. The analytical link between the two coordinate systems can be written as follows:

$$x + iy = re^{i\vartheta} = z = w^q = (u + iv)^q \tag{1.5.40}$$

The parametric curve corresponding in the curvilinear system to the u=0 condition, describes in the (x,y) system a sharp angle equal to 2α where:

$$2\alpha = \pi(2-q) \tag{1.5.41}$$

Moreover the curve u = u_0, corresponding to the free edge of a generic smooth notch with notch root radius equal to:

$$\rho = \frac{q \cdot u_0^q}{(q-1)} = \frac{q \cdot r_0}{(q-1)} \tag{1.5.42}$$

Being $\beta = -\frac{\vartheta}{q}$ the angle between the principal directions of the polar and the curvilinear systems, the components of the stress field in the (u,v) curvilinear system can be obtained from the stress components expressions by imposing the rotation of the reference system above defined (Lazzarin and Tovo, 1996):

$$\begin{aligned}
\sigma_u &= \frac{1}{2}(\sigma_r + \sigma_\vartheta) + \frac{1}{2}(\sigma_r - \sigma_\vartheta)\cos\frac{2\vartheta}{q} - \tau_{r\vartheta}\sin\frac{2\vartheta}{q} \\
\sigma_v &= \frac{1}{2}(\sigma_r + \sigma_\vartheta) - \frac{1}{2}(\sigma_r - \sigma_\vartheta)\cos\frac{2\vartheta}{q} + \tau_{r\vartheta}\sin\frac{2\vartheta}{q} \\
\tau_{uv} &= \frac{1}{2}(\sigma_r - \sigma_\vartheta)\sin\frac{2\vartheta}{q} + \tau_{r\vartheta}\cos\frac{2\vartheta}{q}
\end{aligned} \tag{1.5.43}$$

The following boundary conditions have been imposed along the free edge of the notch:

$$\begin{aligned}
(\sigma_u)_{u=u_0} &= 0 \\
(\tau_{uv})_{u=u_0} &= 0
\end{aligned} \tag{1.5.44}$$

Authors focused the attention in two important considerations:

- The boundary conditions in Eq.(1.5.44) should be satisfied far away from the tip of the notch, where terms related to exponent "μ" are negligible;
- The stress field should be correct in the close neighbourhood of the tip. Hence the first two terms of the series expansions along the free edge, related to σ_u and τ_{uv} stresses, have to be zero.

Under these considerations, in the case of σ_u, the general boundary conditions become:

$$\left(\sigma_u\right)_{\substack{u=u_0\\ v>>u_0}} = 0 \quad \Rightarrow \quad \lim_{\substack{r\to\infty\\ \vartheta\to\pm\frac{q\pi}{2}}} \left(r^{1-\lambda}\sigma_\vartheta\right) = 0 \tag{1.5.45}$$

$$\left(\sigma_u\right)_{\substack{u=u_0\\ v=0}} = \left(\sigma_r\right)_{\substack{r=u_0{}^q\\ \vartheta=0}} = 0 \tag{1.5.46}$$

$$\left(\frac{\partial\sigma_u}{\partial v}\right)_{\substack{u=u_0\\ v=0}} = 0 \quad \Rightarrow \quad \left(\frac{\partial\sigma_r}{\partial\vartheta}\right)_{\substack{r=u_0{}^q\\ \vartheta=0}} - \frac{2}{q}\left(\tau_{r\vartheta}\right)_{\substack{r=u_0{}^q\\ \vartheta=0}} = \left(\frac{\partial\sigma_r}{\partial\vartheta}\right)_{\substack{r=u_0{}^q\\ \vartheta=0}} = 0 \tag{1.5.47}$$

In the same way, other three boundary conditions can be obtained for τ_{uv}.

Eq. (1.5.45) gives n-solutions (eigenvalues) that will be characterized by a second subscript n. Being the problem linear, the general solution can be given as a linear combination of particular solutions. The stress field defined by the lowest eigenvalue, however, represents the prevailing component and it will be later considered in the analyses. The values of the constants, associated to each eigenvalue, are following reported:

$$\begin{aligned} b_{1n} &= -a_{1n}\left(1+\lambda_{1n}\right)\frac{\cos\left(1-\lambda_{1n}\right)q\pi/2}{\cos\left(1+\lambda_{1n}\right)q\pi/2} = \\ &= -a_{1n}\left(1-\lambda_{1n}\right)\frac{\sin\left(1-\lambda_{1n}\right)q\pi/2}{\sin\left(1+\lambda_{1n}\right)q\pi/2} = a_{1n}\left(1-\lambda_{1n}\right)\chi_{1n} \end{aligned} \tag{1.5.48}$$

$$\begin{aligned} b_{2n} &= a_{2n}\left(1+\lambda_{2n}\right)\frac{\sin\left(1-\lambda_{2n}\right)q\pi/2}{\sin\left(1+\lambda_{2n}\right)q\pi/2} = \\ &= a_{2n}\left(1-\lambda_{2n}\right)\frac{\cos\left(1-\lambda_{2n}\right)q\pi/2}{\cos\left(1+\lambda_{2n}\right)q\pi/2} = -a_{2n}\left(1+\lambda_{2n}\right)\chi_{2n} \end{aligned} \tag{1.5.49}$$

where χ_{ik} are:

$$\chi_{ik} = -\frac{\sin\left(1-\lambda_{ik}\right)q\pi/2}{\sin\left(1+\lambda_{ik}\right)q\pi/2} \tag{1.5.50}$$

The remaining unknowns parameters can be obtained using the expression of the boundary conditions. Four expressions can be obtained for the real constants c_{1n} and c_{2n}:

$$\begin{aligned}&\mu_{1n} r_0^{\mu-\lambda}\left[\frac{1}{q}-\left(1+\mu_{1n}\right)\right]c_{1n} = \\ &= \lambda_{1n} a_{1n}\left[\left[\left(1-\lambda_{1n}\right)^2-\frac{\left(1+\lambda_{1n}\right)}{q}\right]+\chi_{1n}\left(1-\lambda_{1n}\right)\left[\left(1+\lambda_{1n}\right)-\frac{1}{q}\right]\right]\end{aligned} \tag{1.5.51}$$

$$\mu_{2n} r_0^{\mu-\lambda}\left[-\left(1+\mu_{2n}\right)\right]c_{2n} = \lambda_{2n} a_{2n}\left[\left[\left(3-\lambda_{2n}\right)\left(1-\lambda_{2n}\right)\right]-\chi_{2n}\left(1+\lambda_{2n}\right)^2\right] \tag{1.5.52}$$

The values of the parameter μ and of the real and imaginary components of the variable c can be obtained as follows for Mode I and Mode II:

$$\mu_{1n} = \frac{1}{q}-\left\{\frac{\left[\left(1-\lambda_{1n}\right)^2-\frac{\left(1+\lambda_{1n}\right)}{q}\right]+\chi_{1n}\left(1-\lambda_{1n}\right)\left[\left(1+\lambda_{1n}\right)-\frac{1}{q}\right]}{\left(3-\lambda_{1n}\right)-\chi_{1n}\left(1-\lambda_{1n}\right)}\right\}-1 \tag{1.5.53}$$

$$\mu_{2n} = -\left\{\frac{\left[\left(3-\lambda_{2n}\right)\left(1-\lambda_{2n}\right)\right]-\chi_{2n}\left(1+\lambda_{2n}\right)^2}{\left(1-\lambda_{2n}\right)+\chi_{2n}\left(1+\lambda_{2n}\right)}\right\}-1 \tag{1.5.54}$$

$$c_{1n} = \frac{\lambda_{1n}}{\mu_{1n}} r_0^{\lambda_{1n}-\mu_{1n}} a_{1n}\left[\left(3-\lambda_{1n}\right)-\chi_{1n}\left(1-\lambda_{1n}\right)\right] \tag{1.5.55}$$

$$c_{2n} = \frac{\lambda_{2n}}{\mu_{2n}} r_0^{\lambda_{2n}-\mu_{2n}} a_{2n}\left[\left(1-\lambda_{2n}\right)+\chi_{2n}\left(1+\lambda_{2n}\right)\right] \tag{1.5.56}$$

Stress field components in the neighbourhood of the notch tip, for Mode I and II respectively, are defined with an exception related to a single constant value:

$$\begin{Bmatrix}\sigma_\vartheta\\ \sigma_r\\ \tau_{r\vartheta}\end{Bmatrix}=\lambda_1 r^{\lambda_1-1}a_1\left\{\left[\begin{Bmatrix}(1+\lambda_1)\cos(1-\lambda_1)\vartheta\\ (3-\lambda_1)\cos(1-\lambda_1)\vartheta\\ (1-\lambda_1)\sin(1-\lambda_1)\vartheta\end{Bmatrix}+\chi_1(1-\lambda_1)\begin{Bmatrix}\cos(1+\lambda_1)\vartheta\\ -\cos(1+\lambda_1)\vartheta\\ \sin(1+\lambda_1)\vartheta\end{Bmatrix}\right]\right.$$
$$\left.+\left(\frac{r}{r_0}\right)^{\mu_1-\lambda_1}\left[(3-\lambda_1)-\chi_1(1-\lambda_1)\right]\begin{Bmatrix}\cos(1+\mu_1)\vartheta\\ -\cos(1+\mu_1)\vartheta\\ \sin(1+\mu_1)\vartheta\end{Bmatrix}\right\} \tag{1.5.57}$$

$$\begin{Bmatrix}\sigma_\vartheta\\ \sigma_r\\ \tau_{r\vartheta}\end{Bmatrix}=\lambda_2 r^{\lambda_2-1}a_2\left\{\left[\begin{Bmatrix}(1+\lambda_2)\sin(1-\lambda_2)\vartheta\\ (3-\lambda_2)\sin(1-\lambda_2)\vartheta\\ (1-\lambda_2)\cos(1-\lambda_2)\vartheta\end{Bmatrix}+\chi_2(1+\lambda_2)\begin{Bmatrix}\sin(1+\lambda_2)\vartheta\\ -\sin(1+\lambda_2)\vartheta\\ \cos(1+\lambda_2)\vartheta\end{Bmatrix}\right]+\right.$$
$$\left.-\left(\frac{r}{r_0}\right)^{\mu_2-\lambda_2}\left[(1-\lambda_2)+\chi_2(1+\lambda_2)\right]\begin{Bmatrix}\sin(1+\mu_2)\vartheta\\ -\sin(1+\mu_2)\vartheta\\ \cos(1+\mu_2)\vartheta\end{Bmatrix}\right\} \tag{1.5.58}$$

In the presence of a tension loading, the maximum stress at the notch tip can be obtained by imposing $r=r_0$ and $\vartheta=0$, so that:

$$a_1=\frac{\sigma_{max,tr}}{4\lambda_1 r_0^{\lambda-1}} \tag{1.5.59}$$

According to LEFM, stress components can also be linked to a field parameter, in such a way that this particular parameter will be equal to the stress intensity factors K_I and K_{II} as soon as the notch degenerates into a crack. ($\rho=0$, $2\alpha=0$); then such a parameter should be representative of the only main stress term, related to exponent λ. The equations representing the stress fields tied to Mode I and Mode II loadings, can be particularized by using the definitions given by Gross and Mendelson (1972) for open cracks:

$$K_1=\sqrt{2\pi}\lim_{r\to 0}\left(\sigma_\vartheta\right)_{\vartheta=0}r^{1-\lambda_1}\qquad K_2=\sqrt{2\pi}\lim_{r\to 0}\left(\tau_{r\vartheta}\right)_{\vartheta=0}r^{1-\lambda_2} \tag{1.5.60}$$

Applying these definitions as long as the component in μ related to the fillet

radius is equal to zero (so that also $c_{1,2}$=0), the real and imaginary parts of the complex constant a are:

$$a_1 = \frac{K_1}{\lambda_1\sqrt{2\pi}\left[\left(1+\lambda_1\right)+\chi_1\left(1-\lambda_1\right)\right]}$$
$$a_2 = -\frac{K_2}{\lambda_2\sqrt{2\pi}\left[\left(1-\lambda_2\right)+\chi_2\left(1+\lambda_2\right)\right]} \qquad (1.5.61)$$

On the basis of these last expressions, in presence of a tensile loading, the maximum stress at the notch tip can be linked to the field parameter by means of the notch radius and the opening angle.
Thus:

$$\sigma_{max,tr} = \frac{4K_1 r_0^{\lambda-1}}{\sqrt{2\pi}\left[\left(1+\lambda_1\right)+\chi_1\left(1-\lambda_1\right)\right]} \qquad (1.5.62)$$

1.6 Generalized stress intensity factors for rounded V-shaped notches: plane problems

The definitions of stress intensity factors given by Gross and Mendelson (1972) are valid only for ideal sharp V notches where Williams' solution exactly matches stress distributions, but these parameters were often used also in the presence of notch tip radii small but different from zero, by simply ignoring the presence of the radius. Lazzarin and Filippi (2005) suggest a generalized form of N-SIFs (Notch Stress Intensity Factors) capable of including the influence of the notch root radius and quantifying, in particular, the stress redistribution it involves.

Starting from the Lazzarin-Tovo's procedure, Filippi et al. (2002) added a new term to Eqs. (1.5.38) in order to obtain better precision and more flexibility of the stress field distributions. The new analytical functions used in the procedure are:

$$\varphi(z) = az^{\lambda} + dz^{\mu} \qquad \psi(z) = bz^{\lambda} + cz^{\mu} \qquad (1.6.1)$$

For the sake of shortness, the mathematical steps will be omitted, because of the procedure traces accurately that already explained in the previous section.
With reference to the polar coordinate system, the new stress distributions for Mode I and Mode II loading respectively can be obtained in the form of:

$$\begin{Bmatrix}\sigma_\theta\\ \sigma_r\\ \tau_{r\theta}\end{Bmatrix} = \lambda_1\, r^{\lambda_1-1} a_1 \left[\begin{Bmatrix}(1+\lambda_1)\cos(1-\lambda_1)\theta\\ (3-\lambda_1)\cos(1-\lambda_1)\theta\\ (1-\lambda_1)\sin(1-\lambda_1)\theta\end{Bmatrix} + \chi_{b_1}(1-\lambda_1) \begin{Bmatrix}\cos(1+\lambda_1)\theta\\ -\cos(1+\lambda_1)\theta\\ \sin(1+\lambda_1)\theta\end{Bmatrix} + \right.$$
$$\left. + \frac{q}{4(q-1)} \left(\frac{r}{r_0}\right)^{\mu_1-\lambda_1} \left(\chi_{d_1} \begin{Bmatrix}(1+\mu_1)\cos(1-\mu_1)\theta\\ (3-\mu_1)\cos(1-\mu_1)\theta\\ (1-\mu_1)\sin(1-\mu_1)\theta\end{Bmatrix} + \chi_{c_1} \begin{Bmatrix}\cos(1+\mu_1)\theta\\ -\cos(1+\mu_1)\theta\\ \sin(1+\mu_1)\theta\end{Bmatrix} \right) \right] \tag{1.6.2}$$

$$\begin{Bmatrix}\sigma_\theta\\ \sigma_r\\ \tau_{r\theta}\end{Bmatrix} = \lambda_2\, r^{\lambda_2-1} a_2 \left[\begin{Bmatrix}(1+\lambda_2)\sin(1-\lambda_2)\theta\\ (3-\lambda_2)\sin(1-\lambda_2)\theta\\ (1-\lambda_2)\cos(1-\lambda_2)\theta\end{Bmatrix} + \chi_{b_2}(1+\lambda_2) \begin{Bmatrix}\sin(1+\lambda_2)\theta\\ -\sin(1+\lambda_2)\theta\\ \cos(1+\lambda_2)\theta\end{Bmatrix} + \right.$$
$$\left. + \frac{1}{4(\mu_2-1)} \left(\frac{r}{r_0}\right)^{\mu_2-\lambda_2} \left(\chi_{d_2} \begin{Bmatrix}(1+\mu_2)\sin(1-\mu_2)\theta\\ (3-\mu_2)\sin(1-\mu_2)\theta\\ (1-\mu_2)\cos(1-\mu_2)\theta\end{Bmatrix} + \chi_{c_2} \begin{Bmatrix}-\sin(1+\mu_2)\theta\\ \sin(1+\mu_2)\theta\\ -\cos(1+\mu_2)\theta\end{Bmatrix} \right) \right] \tag{1.6.3}$$

All the parameters composing the equations can be determined with closed form expression. The only exceptions are a_1 and a_2 that need to be evaluated on the basis of the local stress distributions.
With reference only to Mode I stress distributions, a partial solution of the problem can be obtained by linking the generalized stress intensity factor to the maximum principal stress at the notch tip, σ_{max}, as follows (Filippi et al. 2002):

$$K^V_{\rho,\,I} = \sigma_{max}\ \sqrt{2\pi}\,\frac{r_0^{1-\lambda_1}}{1+\tilde{\omega}_1} = \sigma_{max}\ \frac{\sqrt{2\pi}}{1+\tilde{\omega}_1}\left(\frac{q-1}{q}\,\rho\right)^{1-\lambda_1} \tag{1.6.4}$$

With reference to figure 1.6.1, when the notch angle is null, q=2, $\tilde{\omega}_1$=1, $r_0 = \rho/2$, so that (1.6.4) immediately gives (Glinka, 1985):

$$K^{V}_{\rho,\,I} = \sigma_{max}\sqrt{\pi\rho}\,/\,2 \qquad (1.6.5)$$

Under Mode II conditions, instead, the procedure cannot be applied, because $\tau_{r\theta}$ at the notch tip is always zero.

In order to extend the solution on mixed mode loading configuration, and thus to formulate a more general approach, the maximum stress has been replaced by the components of stress ahead of the notch. The generalized N-SIFs can be written as follows:

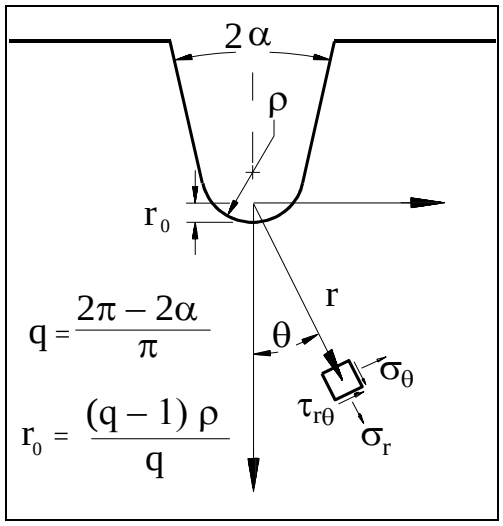

Figure 1.6.1. Coordinate systems and geometrical parameters (figure from Lazzarin and Filippi, 2005).

$$K^{V}_{\rho,I} = \sqrt{2\pi}\; r^{1-\lambda_1}\,\frac{(\sigma_\theta)_{\theta=0}}{1+\tilde{\omega}_1\left(\frac{r}{r_0}\right)^{\mu_1-\lambda_1}} \qquad (1.6.6)$$

$$K^{V}_{\rho,II} = \sqrt{2\pi}\; r^{1-\lambda_2}\,\frac{(\tau_{r\theta})_{\theta=0}}{1+\tilde{\omega}_2\left(\frac{r}{r_0}\right)^{\mu_2-\lambda_2}} \qquad (1.6.7)$$

where σ_θ and $\tau_{r\theta}$ are the stresses at the distance r from the local frame origin (see fig.1.6.1). These two equations represents the extension of the Gross and

Mendelson N-SIFs in the case of rounded notches. Solutions thus obtained are not expected to give a constant value for N-SIFs, in fact, they show a slightly oscillating value ahead of the notch tip. In order to eliminate the dependence on the notch tip distance, the mean values of generalized NSIFs might be used:

$$\overline{K}^{V}_{\rho,I} = \frac{1}{\eta\rho}\int_{r_0}^{r_0+\eta\rho}\left(K^{V}_{\rho,I}\right)dr \tag{1.6.8}$$

$$\overline{K}^{V}_{\rho,II} = \frac{1}{\eta\rho}\int_{r_0}^{r_0+\eta\rho}\left(K^{V}_{\rho,II}\right)dr \tag{1.6.9}$$

As soon as N-SIFs are determined, parameters a_1,a_2 in Eqs.(1.6.2)-(1.6.3) can be determined according to the following expressions:

$$a_1 = \frac{K^{V}_{\rho,I}}{\lambda_1\sqrt{2\pi}\left[1+\lambda_1+\chi_{b_1}(1-\lambda_1)\right]} \tag{1.6.10}$$

$$a_2 = \frac{K^{V}_{\rho,II}}{-\lambda_2\sqrt{2\pi}\left[1-\lambda_2+\chi_{b_1}(1+\lambda_2)\right]} \tag{1.6.11}$$

1.7 Linear elastic solutions for notches under torsion

1.7.1 Complex potentials in antiplane elasticity

The problem of an axisymmetric body weakened by a circumferential notch of a generic shape subjected to torsion loading has been taken into account by Lazzarin et al. (2007) and Zappalorto et al. (2008).

Referring to the Cartesian coordinate system in figure 1.7.1, let's consider a body loaded by a remote shear stress τ_∞, resulting only in displacements *w* along the z coordinate.

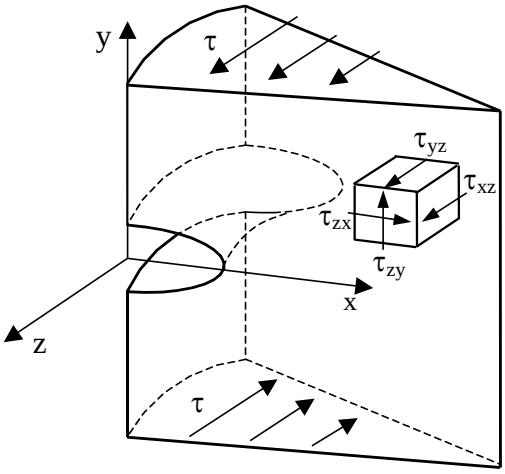

Figure 1.7.1. Axi-symmetric body weakened by a circumferential notch and subjected to antiplane shear stresses (figure from Zappalorto et al. 2008).

The only two components different from zero on the strain tensor are (Timoshenko and Goodier, 1970):

$$\gamma_{xz} = \frac{\partial w}{\partial x} \qquad \gamma_{yz} = \frac{\partial w}{\partial y}. \tag{1.7.1}$$

Since:

$$\gamma_{xz} = \frac{\tau_{xz}}{G} \qquad \gamma_{yz} = \frac{\tau_{yz}}{G} \tag{1.7.2}$$

The equilibrium condition in the *z* direction results in:

$$\frac{\partial \tau_{xz}}{\partial x} + \frac{\partial \tau_{yz}}{\partial y} = 0 \quad . \tag{1.7.3}$$

And thus:

$$\frac{\partial^2 w}{\partial x^2} + \frac{\partial^2 w}{\partial y^2} = 0 \tag{1.7.4}$$

and then *w* is an harmonic function.

A real function solution of Laplace's equation can be written as the real part of an analytical function:

$$H(z)+\overline{H}(\bar{z})=2Gw \tag{1.7.5}$$

Differentiating Eq.(1.7.5) with respect to *x* and *y*:

$$2G\frac{\partial w}{\partial x}=H'(z)+\overline{H}'(\bar{z}) \tag{1.7.6}$$

And

$$2G\frac{\partial w}{\partial y}=i\left(H'(z)-\overline{H}'(\bar{z})\right) \tag{1.7.7}$$

Re-arranging it is possible to obtain:

$$\tau_{xz}-i\tau_{yz}=H'(z). \tag{1.7.8}$$

Eq. (1.7.8) can also be re-written in polar coordinates

$$\tau_{rz}-i\tau_{\varphi z}=e^{i\varphi}H'(z). \tag{1.7.9}$$

1.7.2 Mode III loading solutions with hyperbolic-parabolic transformations

The problem of circumferential hyperbolic and parabolic notches subjected to torsion loading has been addressed by Zappalorto et al. (2008) in order to obtain the elastic stress distributions ahead of the notch. In this section the main concepts of the dissertation will be recalled.

Zappalorto et al. used an orthogonal curvilinear hyperbolic-parabolic coordinate system generate by the following transformation suggested by Neuber 1958 and Lazzarin and Tovo (1996) (See section 1.5.3):

$$z=w^{q} \tag{1.7.10}$$

where $z = x + iy$ and $w = u + iv$ are complex variables in the physical and the transformed planes, respectively, and q is a real number related to the opening angle of the curve 2α (see figure 1.7.2):

$$q = \frac{2\pi - 2\alpha}{\pi} = \frac{2\gamma}{\pi}. \tag{1.7.11}$$

Eq. (1.7.10) can be re-written as:

$$w^q = (u + iv)^q = re^{i\varphi} = r(\cos\varphi + i\sin\varphi) \tag{1.7.12}$$

and thus, coordinates u and v can be written as:

$$\begin{cases} u = r^{\frac{1}{q}} \cos\dfrac{\varphi}{q} \\ v = r^{\frac{1}{q}} \sin\dfrac{\varphi}{q} \end{cases} \tag{1.7.13}$$

The angle between the radial vector r and the normal vector n_u to the curve u=cost is equal to $-\frac{\varphi}{q}$ (see figure 1.7.2b).

System of equations (1.7.13) results in:

$$r = \left(u^2 + v^2\right)^{\frac{q}{2}} \tag{1.7.14}$$

The generic curve characterised by the coordinate u_0 intersects the x-axis at:

$$r_0 = (u_0)^q \tag{1.7.15}$$

So the parameter r_0 can be linked to the curvature radius by:

$$\rho = \frac{q\, u_0^{\,q}}{(q-1)} = \left(\frac{q\, r_0}{(q-1)}\right) \tag{1.7.16}$$

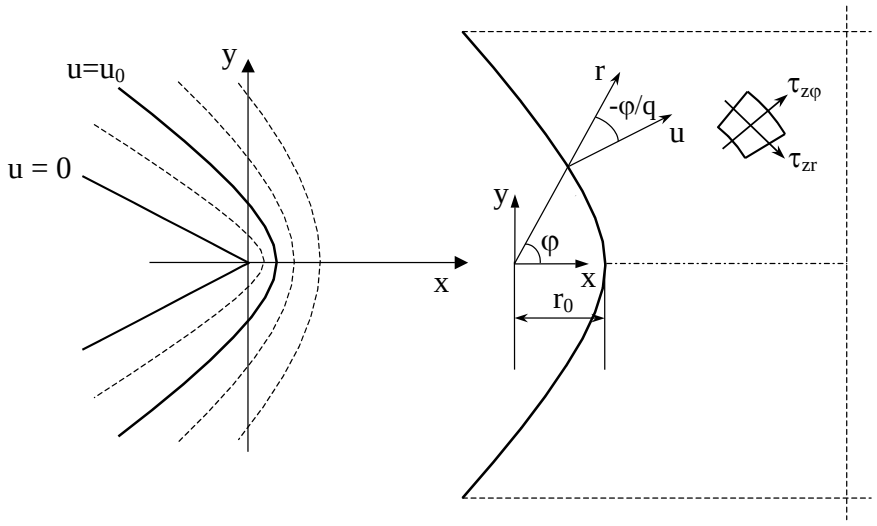

Figure 1.7.2. (a) Auxiliary system of curvilinear coordinates (*u*, *v*); (b) reference system adopted for the solution (figure from Zappalorto et al. 2008).

In order to address the problem, Zappalorto et al. suggested to consider the analytical function H as:

$$H(z) = Aw \tag{1.7.17}$$

where $A=A_1+iA_2$ is a complex coefficient.

The first derivative of the analytical function, after some mathematical manipulations (here omitted for sake of brevity), can be expressed as:

$$H'(z) = \frac{iA_2(u-iv)^{q-1}}{q(u^2+v^2)^{q-1}} = \frac{iA_2}{qr^{\frac{q-1}{q}}}\left[\cos\left(\frac{q-1}{q}\varphi\right) - i\sin\left(\frac{q-1}{q}\varphi\right)\right] \tag{1.7.18}$$

Stress components thus have been defined in terms of an unknown constant, A_2, which can be determined as a function of the external loading conditions:

$$\tau_{zx} = \frac{A_2}{qr^{\frac{q-1}{q}}} \sin\left(\frac{q-1}{q}\varphi\right)$$
$$\tau_{zy} = \frac{-A_2}{qr^{\frac{q-1}{q}}} \cos\left(\frac{q-1}{q}\varphi\right) \qquad (1.7.19)$$

In polar coordinates:

$$\tau_{zr} = \frac{-A_2}{qr^{\frac{q-1}{q}}} \sin\left(\frac{1}{q}\varphi\right)$$
$$\tau_{z\varphi} = \frac{-A_2}{qr^{\frac{q-1}{q}}} \cos\left(\frac{1}{q}\varphi\right) \qquad (1.7.20)$$

Authors stated that the same solution can be obtained using for H(z) the first analytical function already used dealing with the Lazzarin-Tovo's formulation (1996):

$$H(z) = A\, z^{\lambda} \qquad (1.7.21)$$

Thus the first derivative is equal to:

$$H'(z) = (A_1 + iA_2)\lambda\, z^{\lambda-1} \qquad (1.7.22)$$

Considering the polar reference system in figure 1.7.2b, the stress distributions have been written as:

$$\tau_{zr} = \mathrm{Re}\left\{e^{i\varphi}H'(z)\right\} = \lambda\, r^{\lambda-1}\left(-A_2 \sin\lambda\varphi + A_1 \cos\lambda\varphi\right) \qquad (1.7.23)$$
$$\tau_{z\varphi} = -\mathrm{Im}\left\{e^{i\varphi}H'(z)\right\} = \lambda\, r^{\lambda-1}\left(-A_1 \sin\lambda\varphi - A_2 \cos\lambda\varphi\right)$$

Coefficients A_i has been determined by imposing boundary conditions on the notch edge at infinity (see Zappalorto et al. 2008).

The following system can be written:

$$\begin{bmatrix} \sin\lambda\gamma & \cos\lambda\gamma \\ -\sin\lambda\gamma & \cos\lambda\gamma \end{bmatrix} \begin{Bmatrix} A_1 \\ A_2 \end{Bmatrix} = \underline{0}\,. \tag{1.7.24}$$

The following characteristic equation of the system can be obtained from Eq.(1.7.24):

$$2\sin\lambda\gamma\cos\lambda\gamma = \sin 2\lambda\gamma = 0\,. \tag{1.7.25}$$

The solution of the characteristic equation leads to the determination of the smaller positive value of λ_3 that is:

$$\lambda_3 = \frac{\pi}{2\gamma} = \frac{1}{q}\,. \tag{1.7.26}$$

Thus, the first equation of the system results in:

$$A_1 = -A_2 \cdot \frac{\cos\lambda_3\gamma}{\sin\lambda_3\gamma} = -A_2 \cdot \frac{\cos\,(\pi/2)}{\sin\,(\pi/2)} = 0 \tag{1.7.27}$$

Shear stress components can be finally re-written as:

$$\begin{Bmatrix} \tau_{zr} \\ \tau_{z\varphi} \end{Bmatrix} = -\lambda_3\, r^{\lambda_3 - 1} A_2 \begin{Bmatrix} \sin\lambda_3\varphi \\ \cos\lambda_3\varphi \end{Bmatrix} \tag{1.7.28}$$

Shear strain components can be determined as:

$$\begin{Bmatrix} \gamma_{zr} \\ \gamma_{z\varphi} \end{Bmatrix} = \begin{Bmatrix} \frac{\tau_{zr}}{G} \\ \frac{\tau_{z\varphi}}{G} \end{Bmatrix} = \frac{-\lambda_3\, r^{\lambda_3 - 1} A_2}{G} \begin{Bmatrix} \sin\lambda_3\varphi \\ \cos\lambda_3\varphi \end{Bmatrix}. \tag{1.7.29}$$

Stress, strain and displacement fields are defined in terms of an unknown constant, A_2, which can be determined as a function of the external loading conditions.

Authors extended the N-SIF definitions from the plane problems to the antiplane case writing:

$$K_{3\rho} = \sqrt{2\pi} \lim_{r \to r_o^+} \left[r^{1-\lambda_3} \tau_{z\varphi}(r, \varphi = 0) \right] \tag{1.7.30}$$

Substituting eq. (1.7.28) into eq. (1.7.30) and using limit properties:

$$A_2 = -\frac{K_{3\rho}}{\sqrt{2\pi}\lambda_3} \tag{1.7.31}$$

and thus stress and strain components and displacement w can be written as:

$$\begin{Bmatrix} \tau_{zr}(r,\varphi) \\ \tau_{z\varphi}(r,\varphi) \end{Bmatrix} = \frac{K_{3\rho}\, r^{\lambda_3 - 1}}{\sqrt{2\pi}} \begin{Bmatrix} \sin \lambda_3 \varphi \\ \cos \lambda_3 \varphi \end{Bmatrix} \tag{1.7.32}$$

$$\begin{Bmatrix} \gamma_{zr}(r,\varphi) \\ \gamma_{z\varphi}(r,\varphi) \end{Bmatrix} = \frac{K_{3\rho}\, r^{\lambda_3 - 1}}{G\sqrt{2\pi}} \begin{Bmatrix} \sin \lambda_3 \varphi \\ \cos \lambda_3 \varphi \end{Bmatrix} \tag{1.7.33}$$

$$w = \frac{K_{3\rho}}{G\sqrt{2\pi}\lambda_3} r^{\lambda_3} \sin \lambda_3 \varphi \,. \tag{1.7.34}$$

If the notch radius is different from zero, or not too small, the coefficient A_2 can be determined as a function of the maximum shear stress occurring at the notch tip:

$$A_2 = \frac{-\tau_{max}}{\lambda_3 r_0^{\lambda_3 - 1}} \tag{1.7.35}$$

And, in this case, stress and strain components and displacement w can be written as:

$$\begin{Bmatrix}\tau_{zr}(r,\varphi)\\ \tau_{z\varphi}(r,\varphi)\end{Bmatrix}=\tau_{max}\left(\frac{r}{r_0}\right)^{\lambda_3-1}\begin{Bmatrix}\sin\lambda_3\varphi\\ \cos\lambda_3\varphi\end{Bmatrix} \tag{1.7.36}$$

$$\begin{Bmatrix}\gamma_{zr}(r,\varphi)\\ \gamma_{z\varphi}(r,\varphi)\end{Bmatrix}=\frac{\tau_{max}}{G}\left(\frac{r}{r_0}\right)^{\lambda_3-1}\begin{Bmatrix}\sin\lambda_3\varphi\\ \cos\lambda_3\varphi\end{Bmatrix} \tag{1.7.37}$$

$$w=\frac{\tau_{max}}{G}\frac{r_0}{\lambda_3}\left(\frac{r}{r_0}\right)^{\lambda_3}\sin\lambda_3\varphi\,. \tag{1.7.38}$$

The case $2\alpha=0°$ and $\rho=0$ mm represents a circumferential edge crack. As $q=2$ $\lambda_3=1/q=0.5$, and, substituting K_3 with K_{III}, eq. (1.7.32) matches the well known equations of LEFM:

$$\begin{Bmatrix}\tau_{zr}(r,\varphi)\\ \tau_{z\varphi}(r,\varphi)\end{Bmatrix}=\frac{K_{III}}{\sqrt{2\pi r}}\begin{Bmatrix}\sin\frac{1}{2}\varphi\\ \cos\frac{1}{2}\varphi\end{Bmatrix} \tag{1.7.39}$$

1.7.3 Mode III loading solutions for U and blunt V-shaped notches

The linear elastic solutions for the determination of the stress field ahead of a notch under torsion have been extended to U and blunt V-shaped notches by Zappalorto et al. (2010). In particular, this extension has been provided because the analytical solution obtained for hyperbolic notches is able to guarantee the necessary notch free-edge condition only when the notch profile is actually hyperbolic or sharp V- shaped, but generates some residual non-zero shear stresses on the edge in the case of a blunt V- or U-notch.

With reference to figure 1.7.3, it can be seen that a U or blunt V- notch the notch profile is discountinuos, being represented by a rounded circular tip of radius ρ and two rectilinear flanks. The circular part of the notch profile ends in correspondence of a limit angle denoted here as φ^*. The notch profile has been described by Berto and Lazzarin (2007) as:

$$z=x+iy=R(\varphi)e^{i\varphi} \tag{1.7.40}$$

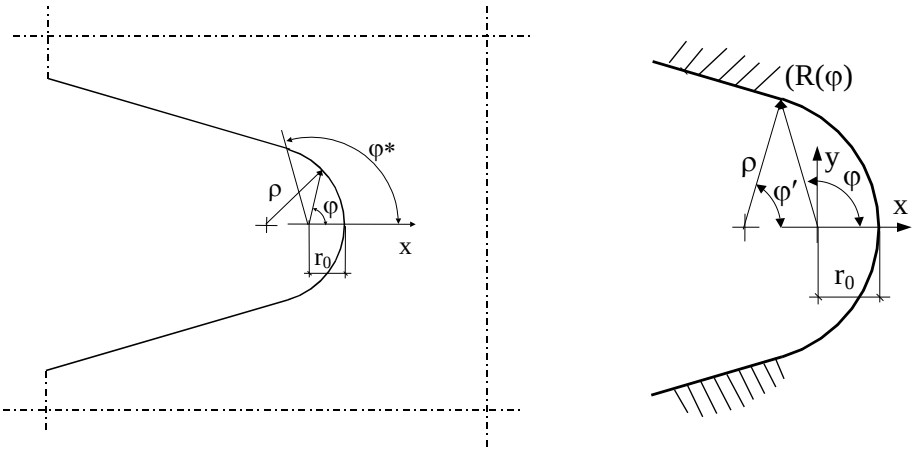

Figure 1.7.3. Schematic representation of the notch profile and significant geometrical parameters (figure from Berto and Lazzarin 2007)

where:

$$R(\varphi)=\begin{cases}\dfrac{\rho}{q}\left[\sqrt{\cos^2(\varphi)+q^2-1}-\cos(\varphi)\right] & \text{if } \varphi<\varphi^* \\ \dfrac{\rho\times f(\varphi^*)}{\sin(\varphi)+\tan(\alpha)\cdot\cos(\varphi)} & \text{if } \varphi>\varphi^*\end{cases} \tag{1.7.41}$$

And

$$f(\varphi^*)=\lambda_3\times\left[\sqrt{\cos^2(\varphi^*)+q^2-1}-\cos(\varphi^*)\right]\times\left[\sin(\varphi^*)+\tan(\alpha)\cdot\cos(\varphi^*)\right] \tag{1.7.42}$$

The limit angle φ* results:

$$\varphi^*=\tan^{-1}\left[\frac{q\cdot\cos(\alpha)}{q\cdot\sin(\alpha)-1}\right] \quad \text{if} \quad \left[\frac{q\cdot\cos(\alpha)}{q\cdot\sin(\alpha)-1}\right]\geq 0$$

$$\varphi^*=\pi-\tan^{-1}\left[-\frac{q\cdot\cos(\alpha)}{q\cdot\sin(\alpha)-1}\right] \quad \text{if} \quad \left[\frac{q\cdot\cos(\alpha)}{q\cdot\sin(\alpha)-1}\right]<0 \tag{1.7.43}$$

The angle φ′ between the *x*-direction and the direction *u* (see figure 1.7.2) is instead:

$$\varphi' = \begin{cases} \mathrm{Arcsin}\left(\boldsymbol{\lambda_3} \times \mathbf{sin}\varphi \times \left[\sqrt{\mathbf{cos^2(\varphi) + q^2 - 1}} - \mathbf{cos}(\varphi)\right]\right) & \text{if } \varphi < \varphi^{*} \\ \dfrac{\pi}{2} - \boldsymbol{\alpha} & \text{if } \varphi > \varphi^{*} \end{cases} \tag{1.7.44}$$

The following holomorphic function *H(z)* has been considered by the authors in order to address the problem of the determination of the stress distributions ahead of a U or rounded V-shaped notch:

$$H(z) = ia\, z^{\lambda} + ibz^{\mu} \tag{1.7.45}$$

where *a* and *b* are real coefficients. The first derivative is equal to:

$$H'(z) = ia\,\lambda\, z^{\lambda-1} + ib\,\mu\, z^{\mu-1} \tag{1.7.46}$$

Parameters λ and μ are real numbers such that $\mu < \lambda < 1$ by hypothesis.
Using Euler equation and according to Eq.(1.7.8) the stress components can be obtained as:

$$\begin{aligned} \tau_{zx} &= \mathrm{Re}\{H'(z)\} = -A\, r^{\lambda-1} \sin(1-\lambda)\varphi - B\, r^{\mu-1} \sin(1-\mu)\varphi \\ \tau_{zy} &= -\mathrm{Im}\{H'(z)\} = A\, r^{\lambda-1} \cos(1-\lambda)\varphi + B\, r^{\mu-1} \cos(1-\mu)\varphi \end{aligned} \tag{1.7.47}$$

Boundary conditions can be formulated in synthetic form as:

$$(\tau_{zu})_{u=u_0} = 0 \tag{1.7.48}$$

That, in Cartesian coordinates, can be rewritten as:

$$\tau_{zu} = \tau_{zx} \cos\varphi' + \tau_{zy} \sin\varphi' \tag{1.7.49}$$

Then, re-arranging:

$$AR^{\lambda-1}(\varphi)\sin[\varphi' - (1-\lambda)\varphi] + BR^{\mu-1}(\varphi)\sin[\varphi' - (1-\mu)\varphi] = 0 \tag{1.7.50}$$

This last equation has been imposed on the notch flank, far from the notch tip, resulting in:

$$AR^{\lambda-1}(\varphi)\sin\left[\frac{\pi}{2}-\alpha-(1-\lambda)(\pi-\alpha)\right]=0 \tag{1.7.51}$$

Eq. (1.7.51) has to satisfy:

$$\sin\left[\frac{\pi}{2}-\alpha-(1-\lambda)(\pi-\alpha)\right]=0 \tag{1.7.52}$$

Obtaining again:

$$\lambda=\lambda_3=\frac{\pi}{2\gamma}=\frac{1}{q} \tag{1.7.53}$$

The mathematical steps used in order to obtain parameter B have been omitted for sake of brevity. However the final form is reported in the following (see Zappalorto et al. (2010) for the whole determination procedure):

$$B=A\times R(\mu_3\cdot\varphi^*)^{\lambda_3-\mu_3} \tag{1.7.54}$$

In this manner, the stress components can be written as:

$$\begin{aligned}\tau_{zx}&=-A\,r^{\lambda_3-1}\left(\sin(1-\lambda_3)\varphi+R^{\lambda_3-\mu_3}(\mu_3\cdot\varphi^*)\,r^{\mu_3-\lambda_3}\left(\sin(1-\mu_3)\varphi\right)\right)\\ \tau_{zy}&=Ar^{\lambda_3-1}\left(\cos(1-\lambda_3)\varphi+R^{\lambda_3-\mu_3}(\mu_3\cdot\varphi^*)\,r^{\mu_3-\lambda_3}\left(\cos(1-\mu_3)\varphi\right)\right)\end{aligned} \tag{1.7.55}$$

Parameter A has been determined as a function of the maximum shear stress at the notch tip:

$$A=\frac{\tau_{max}}{r_0^{\lambda_3-1}\left(1+R^{\lambda_3-\mu_3}(\mu_3\cdot\varphi^*)\;r_o^{\mu_3-\lambda_3}\right)} \tag{1.7.56}$$

Finally, shear stress distributions turn out to be:

$$\tau_{zx} = -\frac{\tau_{max}}{\omega_3}\left(\frac{r}{r_0}\right)^{\lambda_3-1}\left(\sin(1-\lambda_3)\varphi + \left(\frac{r}{r_3}\right)^{\mu_3-\lambda_3}\left(\sin(1-\mu_3)\varphi\right)\right)$$
$$\tau_{zy} = \frac{\tau_{max}}{\omega_3}\left(\frac{r}{r_0}\right)^{\lambda_3-1}\left(\cos(1-\lambda_3)\varphi + \left(\frac{r}{r_3}\right)^{\mu_3-\lambda_3}\left(\cos(1-\mu_3)\varphi\right)\right) \quad (1.7.57)$$

where the parameters ω_3 and r_3 are equal to:

$$r_3 = R(\mu_3 \cdot \varphi^*) = \frac{\rho}{q}\left[\sqrt{\cos^2(\mu_3 \cdot \varphi^*) + q^2 - 1} - \cos(\mu_3 \cdot \varphi^*)\right] = \chi_3 \times \rho \quad (1.7.58)$$

$$\omega_3 = 1 + \left(\frac{R(\mu_3 \cdot \varphi^*)}{r_o}\right)^{\lambda_3-\mu_3} = 1 + \left(\frac{\lambda_3}{1-\lambda_3}\left[\sqrt{\cos^2(\mu_3 \cdot \varphi^*) + q^2 - 1} - \cos(\mu_3 \cdot \varphi^*)\right]\right)^{\lambda_3-\mu_3} \quad (1.7.59)$$

1.8 Three dimensional stress field solutions for notches

Engineering solutions related to three-dimensional problems are usually obtained by the use of two approximate assumptions, that is: plane stress and plane strain. In the literature, especially in relation to crack problems, the dominant state of stress is often estimated from the plate thickness by using a simple empirical rule. If the plate is thin enough the stress state is normally considered to be plane stress and thus to be plane strain for thicker plates. However, the most difficult problem is the identification of what thicknesses correspond to plane-stress or to plane-strain conditions. For these reasons, in the last years many three-dimensional based approaches have been developed in order to obtain the stress field solutions ahead of a notch. In the following the most important three-dimensional solutions will be recalled.

1.8.1 Kane and Mindlin's assumption

Let's consider a three-dimensional plate bounded by planes z=±h, Kane and Mindlin (1956) demonstrated that the three components of displacement are given with a good level of accuracy by the following relationships:

$$u_x = u(x,y) \qquad u_y = v(x,y) \qquad u_z = \frac{z}{h} w(x,y) \tag{1.8.1}$$

The equilibrium equations in terms of stress resultants can be written as follows, taking advantage by Eqs.(1.8.1):

$$\begin{cases} \dfrac{\partial N_{xx}}{\partial x} + \dfrac{\partial N_{xy}}{\partial y} = 0 \\ \dfrac{\partial N_{xy}}{\partial x} + \dfrac{\partial N_{yy}}{\partial y} = 0 \\ \dfrac{\partial R_{xz}}{\partial x} + \dfrac{\partial R_{yz}}{\partial y} - N_{zz} = 0 \end{cases} \tag{1.8.2}$$

where:

$$\begin{aligned} \left(N_{xx}, N_{xy}, N_{yy}, N_{zz}\right) &= \int_{-h}^{h} \left(\sigma_{xx}, \tau_{xy}, \sigma_{yy}, \sigma_{zz}\right) dz \\ \left(R_{xz}, R_{yz}\right) &= \int_{-h}^{h} \left(\tau_{xz}, \tau_{yz}\right) z \, dz \end{aligned} \tag{1.8.3}$$

Using displacement definitions, stress-strain relationships can be written as:

$$\begin{aligned} \sigma_{xx} &= (\lambda + 2G)\varepsilon_{xx} + \lambda\left(\varepsilon_{yy} + k\varepsilon_{zz}\right) \\ \sigma_{yy} &= (\lambda + 2G)\varepsilon_{yy} + \lambda\left(\varepsilon_{xx} + k\varepsilon_{zz}\right) \\ \sigma_{zz} &= (\lambda + 2G)k^2\varepsilon_{zz} + \lambda k\left(\varepsilon_{xx} + \varepsilon_{yy}\right) \\ \left(\tau_{xy}, \tau_{yz}, \tau_{zx}\right) &= G\left(\gamma_{xy}, \gamma_{yz}, \gamma_{zx}\right) \end{aligned} \tag{1.8.4}$$

Substituting of Eq.(1.8.4) into Eq. (1.8.3) one can obtain:

$$N_{xx} = 2h\left[(\lambda + 2G)\frac{\partial u}{\partial x} + \lambda\frac{\partial v}{\partial y} + k\lambda\frac{w}{h}\right] \qquad N_{xy} = 2hG\left(\frac{\partial u}{\partial y} + \frac{\partial v}{\partial x}\right)$$

$$N_{yy} = 2h\left[(\lambda + 2G)\frac{\partial v}{\partial y} + \lambda\frac{\partial u}{\partial x} + k\lambda\frac{w}{h}\right] \qquad R_{xz} = \frac{2h^2G}{3}\frac{\partial w}{\partial x} \qquad (1.8.5)$$

$$N_{zz} = 2h\left[k^2(\lambda + 2G)\frac{w}{h} + k\lambda\left(\frac{\partial u}{\partial x} + \frac{\partial v}{\partial y}\right)\right] \qquad R_{yz} = \frac{2h^2G}{3}\frac{\partial w}{\partial y}$$

Where k is the shear factor while λ is Lame's constant:

$$k = \frac{\pi}{2\sqrt{3}} = 0.907 \qquad \lambda = \frac{E\nu}{(1+\nu)(1-2\nu)} \qquad (1.8.6)$$

1.8.2 Derivations of Kane and Mindlin's assumption

Yang and Freund (1985) used Kane and Mindlin's assumption to analyse the state of stress in a thin elastic plate containing through-cracks.

They reconsidered Eq. (1.8.5) by rewriting N_{zz} in terms of the mean in-plane stress resultant $N = (N_{xx} + N_{yy})/2$ and w:

$$N_{zz} = \frac{k}{\lambda + G}\left[\lambda N + 2kG(3\lambda + 2G)w\right] \qquad (1.8.7)$$

Substituting then Eq. (1.8.7) and R_{xz} and R_{yz}, from Eqs. (1.8.5), into Eq. (1.8.2-c), the following differential equation was derived:

$$\frac{h^2}{3k^2}\frac{\lambda + G}{3\lambda + 2G}\nabla^2 w - w = \frac{1}{2kG}\frac{\lambda}{3\lambda + 2G}N \qquad (1.8.8)$$

The system of equations was then completed by enforcing the strain compatibility to obtain the following equation:

$$\nabla^2\left(\frac{\lambda + 2G}{2k\lambda G}N - w\right) = 0 \qquad (1.8.9)$$

Eqs. (1.8.8, 1.8.9) have then been solved by Yang and Freund using the Wiener-Hopf technique and, examining the solution for points very near to the crack tip, they demonstrated the existence of a *generalised plane strain field*, with the stress resultants $N_{\alpha\beta}$ having the following forms:

$$\begin{pmatrix} N_{xx} \\ N_{yy} \\ N_{xy} \end{pmatrix} = \frac{h\,K}{\sqrt{2\pi r}} \begin{pmatrix} \cos\frac{\theta}{2}\left(1-\sin\frac{\theta}{2}\sin\frac{3\theta}{2}\right) \\ \cos\frac{\theta}{2}\left(1+\sin\frac{\theta}{2}\sin\frac{3\theta}{2}\right) \\ \sin\frac{\theta}{2}\cos\frac{\theta}{2}\cos\frac{3\theta}{2} \end{pmatrix} \tag{1.8.10}$$

where K is the Mode I stress intensity factor.

1.8.3 Three-dimensional stress fields on sharp V-notches, Kotousov and Lew's approach

Kotousov and Lew (2006) analysed the asymptotic stress fields ahead of a three-dimensional V-notch. Kane and Mindlin's assumption on the displacement field was assumed as the basic theory, as given by Eq. (1.8.1). Kotousov and Lew imposed k=1 in Eqs.(1.8.8) and (1.8.9) and introduced the function Φ to automatically satisfy Eqs. (1.8.2-a, b):

$$N_{xx} = \frac{\partial^2\Phi}{\partial y^2} \quad N_{yy} = \frac{\partial^2\Phi}{\partial x^2} \quad N_{xy} = -\frac{\partial^2\Phi}{\partial x\partial y} \qquad N = \frac{1}{2}\nabla^2\Phi \tag{1.8.11}$$

In this manner, Eqs. (1.8.8) and (1.8.9) can be re-written as:

$$\nabla^2 w - \frac{6(1+\nu)}{h^2} w = \frac{3\nu(1+\nu)}{h^2 E}\nabla^2\Phi \qquad \nabla^4\Phi = \frac{2\nu E}{1-\nu^2}\nabla^2 w \tag{1.8.12}$$

or, equivalently:

$$\nabla^6\Phi-\kappa^2\nabla^4\Phi=0 \qquad\qquad \nabla^4 w-\kappa^2\nabla^2 w=0 \tag{1.8.13}$$

where $\kappa^2=\dfrac{1}{h^2}\dfrac{6}{1-\nu}$.

Writing the Eqs. (1.8.11) in polar coordinates one can obtain:

$$N_{\theta\theta}=\frac{\partial^2\Phi}{\partial r^2}\quad N_{rr}=\frac{1}{r^2}\frac{\partial^2\Phi}{\partial\theta^2}+\frac{1}{r}\frac{\partial\Phi}{\partial r}\quad N_{r\theta}=-\frac{\partial}{\partial r}\left(\frac{1}{r}\frac{\partial\ \Phi}{\partial\theta}\right) \tag{1.8.14}$$

Subsequently, Kotousov and Lew suggested the following forms for Φ and w:

$$\Phi(r,\theta)=\sum_{k=0}^{+\infty}\Phi_{\eta+2k}(r,\theta) \qquad w(r,\theta)=\sum_{k=0}^{+\infty}w_{\eta+2k}(r,\theta) \tag{1.8.15}$$

where:

$$\begin{aligned}
w_\eta(r,\theta)=&A_k\left[\tilde{\alpha}\,r^{\eta-2}-I_{\eta-2}(\kappa r)\right]\cos(\eta-2)\theta+B_k I_\eta(\kappa r)\cos\eta\theta\\
&+\overline{A}_k\left[\tilde{\alpha}\,r^{\eta-2}-I_{\eta-2}(\kappa r)\right]\sin(\eta-2)\theta+\overline{B}_k I_\eta(\kappa r)\sin\eta\theta
\end{aligned}$$

$$\begin{aligned}
\Phi_\eta(r,\theta)=&A_k\frac{2\nu E}{(1-\nu^2)\kappa^2}\left[\tilde{\alpha}\,r^{\eta-2}-I_{\eta-2}(\kappa r)\right]\cos(\eta-2)\theta-A_k\frac{\tilde{\alpha}E}{2\nu(\eta-1)}r^\eta\cos(\eta-2)\theta\\
&+\overline{A}_k\frac{2\nu E}{(1-\nu^2)\kappa^2}\left[\tilde{\alpha}\,r^{\eta-2}-I_{\eta-2}(\kappa r)\right]\sin(\eta-2)\theta-\overline{A}_k\frac{\tilde{\alpha}E}{2\nu(\eta-1)}r^\eta\cos(\eta-2)\theta\\
&B_k\frac{2\nu E}{(1-\nu^2)\kappa^2}I_\eta(\kappa r)\cos\eta\theta+\overline{B}_k\frac{2\nu E}{(1-\nu^2)\kappa^2}I_\eta(\kappa r)\sin\eta\theta+C_k r^\eta\cos\eta\theta+\overline{C}_k r^\eta\sin\eta\theta
\end{aligned}$$

(1.8.16)

Where $A_k, B_k, C_k, \overline{A}_k, \overline{B}_k$ and $\overline{C}_k$ are constants to be determined from the boundary conditions, $\tilde{\alpha} = \frac{(\kappa/2)^{\eta-2}}{\Gamma(\eta-1)}$, Γ is the Gamma function and I_η is the modified Bessel function of the first kind. It has to be noted that Eqs (1.8.16) automatically satisfy Eqs. (1.8.13).

By applying appropriate boundary conditions on the notch edge, Kotousov and Lew obtained the following eigen-equations for the "free-free edge" case:

$$\begin{aligned} &\left\{\sin[2(\eta-1)\gamma]+(\eta-1)\sin(2\gamma)\right\}\sin\eta\gamma = 0 \quad \text{(symmetric terms)} \\ &\left\{\sin[2(\eta-1)\gamma]-(\eta-1)\sin(2\gamma)\right\}\cos\eta\gamma = 0 \quad \text{(antisymmetric terms)} \end{aligned} \tag{1.8.17}$$

It is worth noting that the terms within curly brackets are exactly Williams' eigen-equations for the plane problem, while the term "cosηγ" represents an additional singular behaviour, related to the out-of-plane displacement.

The presence and the intensity of the out-of-plane mode was discussed by Berto et al. (2012) also in the case of notches characterised by a notch tip radius small but different from zero, confirming the presence of an out-of-plane mode at the tip of the notch.

After having determined the unknown coefficients resulting from boundary conditions and assuming k=0, Kotousov and Lew wrote the following expressions for Φ and w in the case of symmetric loading:

$$\begin{aligned} \Phi_\eta(r,\theta) &= B_0 \frac{2\nu E}{(1-\nu^2)\kappa^2}\left[I_\eta(\kappa r) - \frac{\kappa^\eta}{2^\eta}\frac{r^\eta}{\Gamma(\eta+1)}\right]\cos\eta\theta \\ w_\eta(r,\theta) &= B_0 I_\eta(\kappa r)\cos\eta\theta \end{aligned} \tag{1.8.18}$$

While in the case of skew-symmetric loading conditions:

$$\Phi_\eta(r,\theta) = B_0 \frac{2\nu E}{(1-\nu^2)\kappa^2}\left[I_\eta(\kappa r) - \frac{\kappa^\eta}{2^\eta}\frac{r^\eta}{\Gamma(\eta+1)}\right]\sin\eta\theta \tag{1.8.19}$$

$$w_\eta(r,\theta) = B_0 I_\eta(\kappa r)\sin\eta\theta$$

By using the series expansion for the Bessel function and imposing k=0, $I_\eta(\kappa r)$ becomes:

$$I_\eta(\kappa r) = \sum_{k=0}^{+\infty} \frac{\left(\frac{\kappa r}{2}\right)^{2k+\eta}}{k!\,\Gamma(k+\eta+1)} \cong \frac{\kappa^\eta}{2^\eta}\frac{r^\eta}{\Gamma(\eta+1)} \tag{1.8.20}$$

1.8.4 Three-dimensional stress fields on sharp V-notches, Lazzarin and Zappalorto's proposal

With the aim to theoretically clarify the key-concept of inherently coupled stress components, as already seen by Pook (2000a-2003), and by making use of the basic equations of elasticity a new approach to the three-dimensional problem has been developed by Lazzarin and Zappalorto (2012), which assumes as starting point the Kane and Mindlin hypothesis for displacement components:

$$u_x = u(x,y) \qquad u_y = v(x,y) \qquad u_z = f(z)\,w(x,y) \tag{1.8.21}$$

Where f(z)=bz.

Strain components can be written as:

$$\begin{aligned} \varepsilon_{xx} &= \frac{\partial u}{\partial x} & \gamma_{xy} &= \frac{\partial u}{\partial y} + \frac{\partial v}{\partial x} \\ \varepsilon_{yy} &= \frac{\partial v}{\partial y} & \gamma_{yz} &= f(z)\times\frac{\partial w}{\partial y} = bz\frac{\partial w}{\partial y} \\ \varepsilon_{zz} &= f'(z)\times w = bw & \gamma_{xz} &= f(z)\times\frac{\partial w}{\partial x} = bz\frac{\partial w}{\partial x} \end{aligned} \tag{1.8.22}$$

In this manner, the normal strains ε_{ii}, and γ_{xy} are independent of z. As a consequence also the stress components σ_{xx}, σ_{yy}, τ_{xy} and σ_{zz} are independent of z:

$$\sigma_{zz} = \frac{E}{(1-2\nu)(1+\nu)}\left[(1-\nu)\varepsilon_{zz} + \nu\left(\varepsilon_{xx} + \varepsilon_{yy}\right)\right] = \frac{E}{(1-2\nu)(1+\nu)}\left[(1-\nu)f'(z)\times w + \nu\left(\frac{\partial u}{\partial x} + \frac{\partial v}{\partial y}\right)\right]$$

$$\begin{aligned}\tau_{yz} &= G\gamma_{yz} = G\times f(z)\frac{\partial w}{\partial y} = \tau_{zy}\\ \tau_{xz} &= G\gamma_{xz} = G\times f(z)\frac{\partial w}{\partial x} = \tau_{zx}\end{aligned} \qquad (1.8.23)$$

The equilibrium equation in the z direction gives:

$$\nabla^2 w + \frac{2(1-\nu)}{(1-2\nu)}\frac{f''(z)}{f(z)}\times w = 0 \qquad (1.8.24)$$

That, when f(z)=bz, immediately leads to:

$$\nabla^2 w = 0 \qquad (1.8.25)$$

Consider now equilibrium equations in the x and in the y directions:

$$\begin{aligned}\frac{\partial\sigma_{xx}}{\partial x} + \frac{\partial\tau_{xy}}{\partial y} + Gb\frac{\partial w}{\partial x} &= 0\\ \frac{\partial\tau_{xy}}{\partial x} + \frac{\partial\sigma_{yy}}{\partial y} + Gb\frac{\partial w}{\partial y} &= 0\end{aligned} \qquad (1.8.26)$$

Differentiating the first one by x and the second one by y and making the sum and by further using the Schwarz theorem the result is:

$$\frac{\partial^2\sigma_{xx}}{\partial x^2} + \frac{\partial^2\sigma_{yy}}{\partial y^2} + 2\frac{\partial^2\tau_{xy}}{\partial y\partial x} = 0 \qquad (1.8.27)$$

Components σ_{xx}, σ_{yy} and τ_{xy} do not depend on z, and thus the classic Airy stress function $\phi(x,y)$ can be introduced:

$$\sigma_{xx} = \frac{\partial^2 \phi}{\partial y^2} \quad \sigma_{yy} = \frac{\partial^2 \phi}{\partial x^2} \quad \tau_{xy} = -\frac{\partial^2 \phi}{\partial x \partial y} \tag{1.8.28}$$

In this manner, Eq. (1.8.27) is automatically satisfied.
According to the Hooke's law for stresses and strains it is possible to write the in-plane compatibility equation as follows:

$$\frac{\partial^2}{\partial y^2}\left(\frac{\partial^2 \phi}{\partial y^2} - \nu \frac{\partial^2 \phi}{\partial x^2} - \nu \sigma_{zz}\right) + \frac{\partial^2}{\partial x^2}\left(\frac{\partial^2 \phi}{\partial x^2} - \nu \frac{\partial^2 \phi}{\partial y^2} - \nu \sigma_{zz}\right) = -2(1+\nu)\frac{\partial^4 \phi}{\partial x^2 \partial y^2} \tag{1.8.29}$$

Summarising:

$$\nabla^4 \phi = \nu \nabla^2 \sigma_{zz} \tag{1.8.30}$$

As already remarked, normal stress components do not depend on z, and thus the third of Beltrami-Mitchell's equations:

$$(1+\nu)\nabla^2 \sigma_{zz} + \frac{\partial^2}{\partial z^2}(\sigma_{xx} + \sigma_{yy} + \sigma_{zz}) = 0 \tag{1.8.31}$$

guarantees that $\nabla^2 \sigma_{zz} = 0$, so that:

$$\nabla^4 \phi = 0 \tag{1.8.32}$$

This mean that any three dimensional notch problem obeying to the Kane and Mindlin's displacement assumptions can be converted into a bi-harmonic problem (plane stress or plane strain conditions) and a harmonic problem (out-of-plane shear case) according to the following system:

$$\begin{cases} \nabla^4 \phi = 0 \\ \nabla^2 w = 0 \end{cases} \tag{1.8.33}$$

Both the two equations have to be simultaneously satisfied in order to solve the

three-dimensional problem. The second equation has been widely used by Lazzarin and Zappalorto (2012) to solve the problem of notched shafts under torsion loading, as already reported in the previous session.
Taking into account the V-notch problem Eqs. (1.8.33) has been written by the authors as follows:

$$\phi = r^{\lambda_1+1}\left[A_s \cos(\lambda_1+1)\theta + B_s \cos(1-\lambda_1)\theta\right] + r^{\lambda_2+1}\left[A_a \sin(\lambda_2+1)\theta + B_a \sin(1-\lambda_2)\theta\right]$$

$$w = D_s r^{\lambda_{3,s}} \cos(\lambda_{3,s})\theta + D_a r^{\lambda_{3,a}} \sin(\lambda_{3,a})\theta \qquad (1.8.34)$$

Since:

$$\sigma_{\theta\theta} = \frac{\partial^2\phi}{\partial r^2} \qquad \tau_{r\theta} = \frac{\partial}{\partial r}\left(-\frac{1}{r}\frac{\partial\phi}{\partial\theta}\right) \qquad \tau_{\theta z} = G\frac{1}{r}\frac{\partial u_z}{\partial\theta} = Gbz\frac{1}{r}\frac{\partial w}{\partial\theta} \qquad (1.8.35)$$

In the case of symmetric terms the free-of-stress conditions on the V-notch flank require:

$$\begin{bmatrix} \cos(\lambda_1+1)\gamma & \cos(1-\lambda_1)\gamma & 0 \\ (\lambda_1+1)\sin(\lambda_1+1) & (1-\lambda_1)\sin(1-\lambda_1)\gamma & 0 \\ 0 & 0 & \sin(\lambda_{3,s})\gamma \end{bmatrix} \begin{Bmatrix} A_s \\ B_s \\ D_s \end{Bmatrix} = 0 \qquad (1.8.36)$$

While for the antisymmetric terms:

$$\begin{bmatrix} \sin(\lambda_2+1) & \sin(1-\lambda_2)\gamma & 0 \\ (\lambda_2+1)\cos(\lambda_2+1)\gamma & (1-\lambda_2)\cos(1-\lambda_2)\gamma & 0 \\ 0 & 0 & \cos(\lambda_{3,a})\gamma \end{bmatrix} \begin{Bmatrix} A_a \\ B_a \\ D_a \end{Bmatrix} = 0 \qquad (1.8.37)$$

Equating to zero the determinants results:

$$\begin{aligned} &(\sin 2\lambda_1\,\gamma + \lambda_1 \sin 2\gamma)\sin\lambda_{3,s}\gamma = 0 && \text{symmetric terms} \\ &(\sin 2\lambda_2\,\gamma - \lambda_2 \sin 2\gamma)\cos\lambda_{3,a}\gamma = 0 && \text{antisymmetric terms} \end{aligned} \qquad (1.8.38)$$

Eqs. (1.8.38) match Kotousov and Lew's formulations, moreover, since $\lambda_{3,s} = 2\lambda_{3,a} = \pi/\gamma$, only the antisymmetric part of the out-of-plane shear stress results in a singular behaviour, whereas the symmetric part results in a non-singular behaviour.

2

The averaged SED over a control volume as a damage parameter

2.1 Introduction

This chapter focuses on the recall of the main concepts concerning the local energy based criterion of SED. This criterion was presented for the first time by Lazzarin and Zambardi (2001) dealing with the evaluation of sharp V-notches and then extended to blunt notches by Lazzarin and Berto (2005). The averaged SED criterion will be used in the next chapters in order to investigate the strength of notched components subjected to different remote loadings.

2.2 Averaged SED criterion to predict the static and fatigue behaviour of components weakened by sharp V- notches

By assuming linear elastic conditions, the strain energy density for an isotropic material can be written as follows:

$$W(r,\theta)=\frac{1}{2E}\left\{\sigma_{11}{}^2+\sigma_{22}{}^2+\sigma_{33}{}^2-2\nu(\sigma_{11}\sigma_{22}+\sigma_{11}\sigma_{33}+\sigma_{22}\sigma_{33})+2(1+\nu)\sigma_{12}{}^2\right\} \tag{2.2.1}$$

In the presence of a sharp V-notch, the stress distribution in the case of application of Mode I or Mode II loading can be obtained using Eqs.(1.5.36) and (1.5.37) respectively.

The stress distributions acting in the vicinity of the notch tip can be written as follows only by make use of the superposition of effects principle:

$$\sigma_{ij}(r,\theta) = r^{\lambda_1 - 1} \cdot K_1^N \cdot \begin{vmatrix} \tilde{\sigma}_{\theta\theta}^{(1)} & \tilde{\sigma}_{r\theta}^{(1)} & 0 \\ \tilde{\sigma}_{r\theta}^{(1)} & \tilde{\sigma}_{rr}^{(1)} & 0 \\ 0 & 0 & \tilde{\sigma}_{zz}^{(1)} \end{vmatrix} + r^{\lambda_2 - 1} \cdot K_2^N \cdot \begin{vmatrix} \tilde{\sigma}_{\theta\theta}^{(2)} & \tilde{\sigma}_{r\theta}^{(2)} & 0 \\ \tilde{\sigma}_{r\theta}^{(2)} & \tilde{\sigma}_{rr}^{(2)} & 0 \\ 0 & 0 & \tilde{\sigma}_{zz}^{(2)} \end{vmatrix} \qquad (2.2.2)$$

Parameters $\tilde{\sigma}_{\theta\theta}$, $\tilde{\sigma}_{rr}$ and $\tilde{\sigma}_{r\theta}$ are angular functions that can be determined from Eqs. (1.5.36) and (1.5.37). If each expression of stress component is substituted into Eq. (2.1.1) one can obtain the expression representing the strain energy density in terms of summation of different energy density components:

$$W(r,\theta) = W_1(r,\theta) + W_2(r,\theta) + W_{12}(r,\theta) \qquad (2.2.3)$$

Where the three energy density components are:

$$W_1(r,\theta) = \frac{1}{2E} r^{2(\lambda_1 - 1)} \cdot \left(K_1^N\right)^2 \left[\tilde{\sigma}_{\theta\theta}^{(1)2} + \tilde{\sigma}_{rr}^{(1)2} + \tilde{\sigma}_{zz}^{(1)2} - 2\nu\left(\tilde{\sigma}_{\theta\theta}^{(1)}\tilde{\sigma}_{rr}^{(1)} + \tilde{\sigma}_{\theta\theta}^{(1)}\tilde{\sigma}_{zz}^{(1)} + \tilde{\sigma}_{rr}^{(1)}\tilde{\sigma}_{zz}^{(1)}\right) + 2(1+\nu)\tilde{\sigma}_{r\theta}^{(1)2} \right]$$

$$W_2(r,\theta) = \frac{1}{2E} r^{2(\lambda_2 - 1)} \cdot \left(K_2^N\right)^2 \left[\tilde{\sigma}_{\theta\theta}^{(2)2} + \tilde{\sigma}_{rr}^{(2)2} + \tilde{\sigma}_{zz}^{(2)2} - 2\nu\left(\tilde{\sigma}_{\theta\theta}^{(2)}\tilde{\sigma}_{rr}^{(2)} + \tilde{\sigma}_{\theta\theta}^{(2)}\tilde{\sigma}_{zz}^{(2)} + \tilde{\sigma}_{rr}^{(2)}\tilde{\sigma}_{zz}^{(2)}\right) + 2(1+\nu)\tilde{\sigma}_{r\theta}^{(2)2} \right]$$

$$W_{12}(r,\theta) = \frac{1}{E} r^{\lambda_1 + \lambda_2 - 2} \cdot K_1^N \cdot K_2^N \left[\tilde{\sigma}_{\theta\theta}^{(1)}\tilde{\sigma}_{\theta\theta}^{(2)} + \tilde{\sigma}_{rr}^{(1)}\tilde{\sigma}_{rr}^{(2)} + \tilde{\sigma}_{zz}^{(1)}\tilde{\sigma}_{zz}^{(2)} - \nu\left(\tilde{\sigma}_{\theta\theta}^{(1)}\tilde{\sigma}_{rr}^{(2)} + \tilde{\sigma}_{\theta\theta}^{(1)}\tilde{\sigma}_{zz}^{(2)} + \tilde{\sigma}_{rr}^{(1)}\tilde{\sigma}_{\theta\theta}^{(2)} + \right.\right.$$
$$\left.\left. + \tilde{\sigma}_{rr}^{(1)}\tilde{\sigma}_{zz}^{(2)} + \tilde{\sigma}_{zz}^{(1)}\tilde{\sigma}_{\theta\theta}^{(2)} + \tilde{\sigma}_{zz}^{(1)}\tilde{\sigma}_{rr}^{(2)}\right) + 2(1+\nu)\tilde{\sigma}_{r\theta}^{(1)}\tilde{\sigma}_{r\theta}^{(2)} \right] \qquad (2.2.4)$$

With reference to figure 2.2.1, the elastic energy within the area of radius R is equal to:

$$E(R) = \int_A W \cdot dA = \int_0^R \int_{-\gamma}^{+\gamma} \left[W_1(r,\theta) + W_2(r,\theta) + W_{12}(r,\theta)\right] \cdot r dr d\theta \qquad (2.2.5)$$

By taking advantage of the symmetry of the integration field, the contribution of W_{12} is equal to zero, thus:

$$E(R) = E_1(R) + E_2(R) = \frac{1}{E}\frac{I_1(\gamma)}{4\lambda_1} \cdot \left(K_1^N\right)^2 \cdot R^{2\lambda_1} + \frac{1}{E}\frac{I_2(\gamma)}{4\lambda_2} \cdot \left(K_2^N\right)^2 \cdot R^{2\lambda_2} \qquad (2.2.6)$$

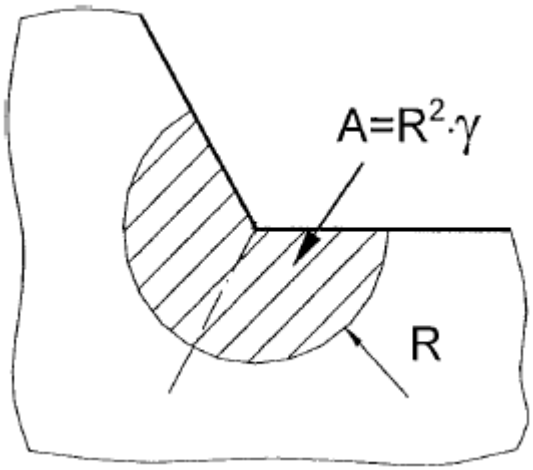

Figure 2.1.1. Critical volume surrounding the notch tip (figure from Lazzarin and Zambardi 2001)

Parameters I_1 and I_2 are integrals equal to:

$$I_1(\gamma)=\int_{-\gamma}^{+\gamma}\left(\tilde{\sigma}_{\theta\theta}^{(1)2}+\tilde{\sigma}_{rr}^{(1)2}+\tilde{\sigma}_{zz}^{(1)2}-2\nu\left(\tilde{\sigma}_{\theta\theta}^{(1)}\tilde{\sigma}_{rr}^{(1)}+\tilde{\sigma}_{\theta\theta}^{(1)}\tilde{\sigma}_{zz}^{(1)}+\tilde{\sigma}_{rr}^{(1)}\tilde{\sigma}_{zz}^{(1)}\right)+2(1+\nu)\tilde{\sigma}_{r\theta}^{(1)2}\right)d\theta$$

$$I_2(\gamma)=\int_{-\gamma}^{+\gamma}\left(\tilde{\sigma}_{\theta\theta}^{(2)2}+\tilde{\sigma}_{rr}^{(2)2}+\tilde{\sigma}_{zz}^{(2)2}-2\nu\left(\tilde{\sigma}_{\theta\theta}^{(2)}\tilde{\sigma}_{rr}^{(2)}+\tilde{\sigma}_{\theta\theta}^{(2)}\tilde{\sigma}_{zz}^{(2)}+\tilde{\sigma}_{rr}^{(2)}\tilde{\sigma}_{zz}^{(2)}\right)+2(1+\nu)\tilde{\sigma}_{r\theta}^{(2)2}\right)d\theta \tag{2.2.7}$$

The value of the integrating area is:

$$A(R)=\int_0^{R}\int_{-\gamma}^{+\gamma} r\,dr\,d\theta=R^2\gamma \tag{2.2.8}$$

Now it is possible to obtain the elastic strain energy averaged over the area A:

$$\overline{W}=\frac{E(R)}{A(R)}=\frac{1}{E}\cdot e_1\cdot\left(K_1^N\right)^2\cdot R^{2(\lambda_1-1)}+\frac{1}{E}\cdot e_2\cdot\left(K_2^N\right)^2\cdot R^{2(\lambda_2-1)} \tag{2.2.9}$$

Where:

$$e_1(2\alpha) = \frac{I_1(\gamma)}{4\lambda_1\gamma} \quad \text{and} \quad e_2(2\alpha) = \frac{I_2(\gamma)}{4\lambda_2\gamma} \tag{2.2.10}$$

Values of e_1 and e_2 are tabulated as a function of the notch opening angle 2α.

It is worth noting that, in the presence of a torsion loading, adding also the contribution tied to Mode III the expression for the strain energy density can be updated as follows:

$$\overline{W} = \frac{e_1}{E}\left[\frac{K_1}{R_0^{1-\lambda_1}}\right]^2 + \frac{e_2}{E}\left[\frac{K_2}{R_0^{1-\lambda_2}}\right]^2 + \frac{e_3}{E}\left[\frac{K_3}{R_0^{1-\lambda_3}}\right]^2 \tag{2.2.11}$$

The Mode III N-SIF is according to Eq.(1.7.34).

The most important peculiarity of an energy based criterion is that the critical configuration of different notch opening angle can be evaluated and compared each other with the same physical dimensions, in this case N·mm/mm^3. This cannot be stated in the case of a N-SIF based approach.

2.2.1 Failure criterion based on averaged SED

Lazzarin and Zambardi (2001), in the case of static loads, supposed that the material failure occurs when the averaged strain energy density over a control volume reaches a critical value:

$$\overline{W} = W_C \tag{2.2.12}$$

This particular and characteristic parameter can be evaluated by means of the mechanical properties of the material taken into account. The expression of the critical value of the strain energy density can be, thus, written as follows:

$$W_C = \sigma_R^2 / 2E \tag{2.2.13}$$

Where σ_R is the ultimate tensile stress of the material and E is the Young's modulus.

The critical radius has been thought to be a material property. It can be determined by imposing the strain energy component related to Mode II loading equal to zero. In this manner, the Mode I N-SIF can be linked to the related component of the averaged strain energy density:

$$K_1^N = \sqrt{\frac{4E\lambda_1\gamma}{I_1(\gamma)} \cdot \overline{W}} \cdot R^{(1-\lambda_1)} \tag{2.2.14}$$

Supposing critical configuration, the averaged strain energy density has to be equal to Wc. And so:

$$K_{1C}^N = \sqrt{\frac{2\lambda_1\gamma}{I_1(\gamma)}} \cdot \sigma_R \cdot R^{(1-\lambda_1)} = f_1(2\alpha) \cdot \sigma_R \cdot R^{(1-\lambda_1)} \tag{2.2.15}$$

By degenerating a V-shaped notch on a crack shaped notch, the value of K_{1C}^N coincides with the fracture toughness:

$$K_{1C}^N(0°) = K_{I\,C} = f_1(0°) \cdot \sigma_R \cdot R^{0.5} \tag{2.2.16}$$

The critical radius can be expressed in the following form:

$$R = \left(\frac{K_{IC}}{f_1(0°) \cdot \sigma_R} \right)^2 \tag{2.2.17}$$

The expression used to calculate the critical radius in the case of an opening angle of the notch different from zero is reported in the following:

$$R = \left[\frac{I_1 \times {K_{1C}}^2}{4\lambda_1\,(\pi-\alpha)\,E\,W_c} \right]^{1/2(1-\lambda_1)} = \left[\frac{I_1}{2\lambda_1\,(\pi-\alpha)} \left(\frac{K_{1C}}{\sigma_t} \right)^2 \right]^{1/2(1-\lambda_1)} \tag{2.2.18}$$

It is appropriate to remember that a useful expression for the radius R surrounding the control volume has been provided by Yoshibash et al. (2004) for the crack case under plane strain and plane stress conditions respectively:

$$R = \frac{(1+\nu)(5-8\nu)}{4\pi}\left(\frac{K_{IC}}{\sigma_t}\right)^2 \qquad \text{plane strain} \qquad (2.2.19)$$

$$R = \frac{(5-3\nu)}{4\pi}\left(\frac{K_C}{\sigma_t}\right)^2 \qquad \text{plane stress} \qquad (2.2.20)$$

Finally, the following expression permits to evaluate the critical N-SIF for different notch opening angle by considering known material properties and characteristic eigenvalues:

$$K_{1C}^{N} = f_1(2\alpha)\cdot\sigma_R\cdot\left(\frac{K_{IC}}{f_1(0°)\cdot\sigma_R}\right)^{2(1-\lambda_1)} \qquad (2.2.21)$$

In the case of notched components or welded joints subjected to fatigue loadings, the critical strain energy density turns to be:

$$W_C \cong \frac{\Delta\sigma_A^2}{2E} \qquad (2.2.22)$$

Where $\Delta\sigma_A$ represents the fatigue limit of an un-notched welded material taken into account at $N=2x10^6$ cycles with a PS equal to 97.7%.
In addition, if the contribution tied to Mode II loading can be neglected, it is possible to determine the variation of the strain energy density can be obtained as:

$$\Delta\overline{W} \cong \frac{I_1}{4E\lambda_1\gamma}\cdot\frac{\Delta K_1^2}{R^{2(1-\lambda_1)}} \qquad (2.2.23)$$

Equations (2.2.22) and (2.2.23) permit to determinate the critical radius as:

$$R = \left(\sqrt{\frac{I_1}{2\lambda_1 \gamma}} \frac{\Delta K_{1A}}{\Delta \sigma_A} \right)^{\frac{1}{1-\lambda_1}} \tag{2.2.24}$$

The critical value of the control radius has been determined by Lazzarin and Zambardi (2001) in the case of structural steel. The critical radius turned out to be equal to 0.28 mm.

Taking advantage of the above reported considerations, it is evident that the use of the local energy based criterion of SED can lead to overcome the complex problem tied to the different NSIF units of measure in the case of different notch opening angles (i.e crack initiation at the toe (2α=135°) or root (2α=0°) in a welded joint)

2.3 Averaged SED criterion extended to the evaluation of blunt V-notched components

Recalling section 1.6 of the previous chapter, the formulations describing the stress fields ahead of a rounded notch in a plane problem can be written in a compact form as follows (Filippi et al. 2002):

$$\sigma_{ij} = a_1 \, r^{\lambda_1 - 1} \left[f_{ij}(\theta, \alpha) + \left(\frac{r}{r_0} \right)^{\mu_1 - \lambda_1} g_{ij}(\theta, \alpha) \right] \tag{2.3.1}$$

In the following, problems related to the application of a Mode I loading, mixed mode loading (I+II) and Mode III loading will be analysed.

2.3.1 SED criterion applied to blunt notches under Mode I loading

Parameter a1 in Eq.(2.3.1) can be expressed by means the maximum principal stress value at the notch tip:

$$a_1 = \frac{\sigma_{tip}}{r_0^{\lambda_1-1}\left\{1+\dfrac{(1+\mu_1)\chi_{d_1}+\chi_{c_1}}{1+\lambda_1+\chi_{b_1}(1-\lambda_1)}\left(\dfrac{q}{4(q-1)}\right)\right\}} = \frac{\sigma_{tip}\, r_0^{1-\lambda_1}}{1+\tilde{\omega}_1} \tag{2.3.2}$$

where $\tilde{\omega}_1$ is a particular parameter reported in Lazzarin and Berto (2005). By using the elastic maximum notch stress, Eq.(2.3.1) becomes:

$$\begin{aligned}
\sigma_{\theta\theta}(r,\theta) &= \frac{\sigma_{tip}}{1+\tilde{\omega}_1}\left(\frac{r_0}{r}\right)^{1-\lambda_1}\left[f_{\theta\theta}+\left(\frac{r}{r_0}\right)^{\mu_1-\lambda_1} g_{\theta\theta}\right] \\
\sigma_{rr}(r,\theta) &= \frac{\sigma_{tip}}{1+\tilde{\omega}_1}\left(\frac{r_0}{r}\right)^{1-\lambda_1}\left[f_{rr}+\left(\frac{r}{r_0}\right)^{\mu_1-\lambda_1} g_{rr}\right] \\
\sigma_{r\theta}(r,\theta) &= \frac{\sigma_{tip}}{1+\tilde{\omega}_1}\left(\frac{r_0}{r}\right)^{1-\lambda_1}\left[f_{r\theta}+\left(\frac{r}{r_0}\right)^{\mu_1-\lambda_1} g_{r\theta}\right]
\end{aligned} \tag{2.3.3}$$

(36)

The elastic strain energy density can be expressed as follows:

$$W_1^{(e)}(r,\theta) = \frac{1}{2E}\left(\frac{\sigma_{tip}}{1+\tilde{\omega}}\right)^2\left\{\left(\frac{r}{r_0}\right)^{2(\lambda_1-1)}\tilde{F}_\lambda+\left(\frac{r}{r_0}\right)^{2(\mu_1-1)}\tilde{G}_\mu+2\left(\frac{r}{r_0}\right)^{\lambda_1+\mu_1-2}\tilde{M}_{\lambda\mu}\right\} \tag{2.3.4}$$

Where parameters F, G and M can be written as follows according to Beltrami's formulation:

$$\begin{aligned}
\tilde{F}_\lambda &= f_{\theta\theta}^2 + f_{rr}^2 + f_{zz}^2 - 2\nu\left(f_{\theta\theta}f_{rr}+f_{\theta\theta}f_{zz}+f_{rr}f_{zz}\right)+2(1+\nu)f_{r\theta}^2 \\
\tilde{G}_\mu &= g_{\theta\theta}^2 + g_{rr}^2 + g_{zz}^2 - 2\nu\left(g_{\theta\theta}g_{rr}+g_{\theta\theta}g_{zz}+g_{rr}g_{zz}\right)+2(1+\nu)g_{r\theta}^2 \\
\tilde{M}_{\lambda\mu} &= f_{\theta\theta}g_{\theta\theta}+f_{rr}g_{rr}+f_{zz}g_{zz}-\nu\left(f_{\theta\theta}g_{rr}+g_{\theta\theta}f_{rr}+f_{\theta\theta}g_{zz}+g_{\theta\theta}f_{zz}+f_{rr}g_{zz}+g_{rr}f_{zz}\right)+2(1+\nu)f_{r\theta}g_{r\theta}
\end{aligned} \tag{2.3.5}$$

Considering the area Ω shown in Figure (2.3.1), the strain energy can be obtained as:

$$E_1 = \int_{\Omega} W_1 \, d\Omega = \int_{-\bar{\theta}}^{+\bar{\theta}} d\theta \int_{R_1(\theta)}^{R_2} W_1 \, (r,\theta) \, r \, dr \tag{2.3.6}$$

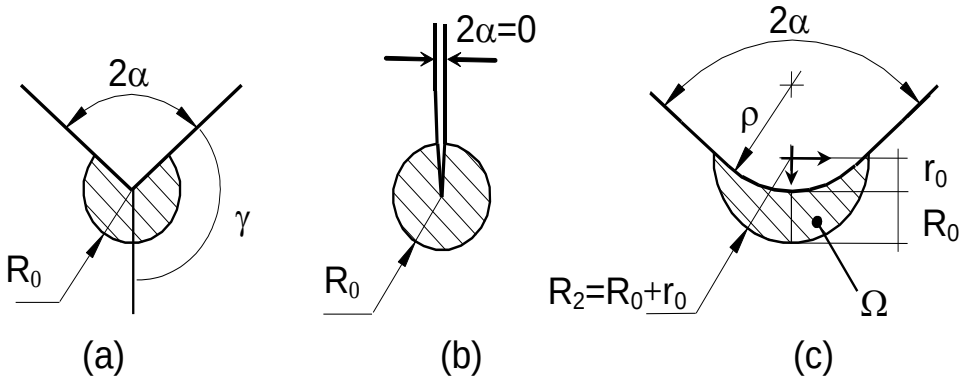

Figure 2.3.1. Critical volume (area) for sharp V-notch (a), crack (b) and blunt V-notch (c) under Mode I loading.

And in detail:

$$E_1 = \frac{1}{2E}\left[\frac{\sqrt{2\pi}\,\sigma_{tip}}{1+\tilde{\omega}_1}\right]^2 r_0^{2(1-\lambda_1)}\left(I_\lambda + I_\mu + I_{\lambda\mu}\right) \tag{2.3.7}$$

Where:

$$I_\lambda = \int_{-\bar{\theta}}^{+\bar{\theta}} \frac{\left(R_2{}^{2\lambda_1} - R_1(\theta)^{2\lambda_1}\right)}{2\lambda_1} \tilde{F}_\lambda \; d\theta$$

$$I_\mu = (r_0)^{2(\lambda_1-\mu_1)} \int_{-\bar{\theta}}^{+\bar{\theta}} \frac{\left(R_2{}^{2\mu_1} - R_1(\theta)^{2\mu_1}\right)}{2\mu_1} \tilde{G}_\mu \; d\theta \tag{2.3.8}$$

$$I_{\lambda\mu} = 2(r_0)^{\lambda_1-\mu_1} \int_{-\bar{\theta}}^{+\bar{\theta}} \frac{\left(R_2{}^{\lambda_1+\mu_1} - R_1(\theta)^{\lambda_1+\mu_1}\right)}{\lambda_1+\mu_1} \tilde{M}_{\lambda\mu} \; d\theta$$

The last of Eqs (2.3.8) is applicable only when the notch angle 2α is different from zero. In the presence of a U-shaped notch ($2\alpha=0$), a different equation should be used:

$$I_{\lambda\mu} = 2(r_0) \cdot \int_{-\bar{\theta}}^{+\bar{\theta}} \ln\left[\frac{R_2}{R_1(\theta)}\right] \tilde{M}_{\lambda\mu}\, d\theta \tag{2.3.9}$$

This integral is uniquely equal to zero for $2\alpha = 0$ and in general, it is possible to write:

$$I_1 = \frac{1}{2\pi}\left(I_\lambda + I_\mu + I_{\lambda\mu}\right) \tag{2.3.10}$$

where the introduction of 2π makes I_1 consistent with the expression already used for the sharp notch case.
In synthesis, the energy over a structural volume can be expressed as:

$$E_1^{(e)} = \frac{1}{2E}\left[\frac{\sigma_{tip}\sqrt{2\pi}}{r_0^{\lambda_1-1}(1+\tilde{\omega}_1)}\right]^2 \cdot I_1 \tag{2.3.11}$$

where I_1 depends on 2α, ρ and R_0. In the case of a U-shaped notch ($2\alpha=0$), Eq.(2.3.11) can be written as:

$$E_1 = \frac{1}{2E}\left(\frac{\sigma_{tip}\sqrt{\pi\rho}}{2}\right)^2 \cdot I_1 \tag{2.3.12}$$

The averaged strain energy density is then obtainable and equal to:

$$\overline{W}_1 = \frac{1}{E}\left(\frac{I_1}{2\Omega}\right) \sigma^2{}_{tip}\; r_0^{2(1-\lambda_1)}\left[\frac{\sqrt{2\pi}}{1+\tilde{\omega}_1}\right]^2 \tag{2.3.13}$$

The area Ω is defined by means of an integration and it is equal to:

$$\Omega = \int_{R_1(\theta)}^{R_2} \int_{-\bar{\theta}}^{+\bar{\theta}} r\, dr\, d\theta \tag{2.3.14}$$

In general, the integral I_1 and the area Ω depend on 2α, ρ, and R_0. However, I_1 is proportional to $\rho^{2\lambda}$ according to Eq.(2.3.10), whereas Ω is proportional to ρ^2. Then a suitable expression for $I_1/2\Omega$ is:

$$\frac{I_1}{2\Omega}(2\alpha,\rho,R_0)=\frac{1}{\rho^{2(1-\lambda)}}H(2\alpha,\frac{R_0}{\rho}) \tag{2.3.15}$$

When the area embraces the semicircular edge of the notch but not its rectilinear flanks, the averaged SED value can be expressed as:

$$\overline{W}_1 = F(2\alpha)\times H(2\alpha,\frac{R_0}{\rho})\times\frac{\sigma_{tip}^2}{E} \tag{2.3.16}$$

where $F(2\alpha)$ is defined as follows:

$$F(2\alpha)=\left(\frac{q-1}{q}\right)^{2(1-\lambda_1)}\left[\frac{\sqrt{2\pi}}{1+\tilde{\omega}_1}\right]^2 \tag{2.3.17}$$

While H is a function of the opening angle of the notch and the Poisson's ratio. By simply using the definition of the Mode I NSIF for blunt V-notches (Lazzarin and Filippi 2005) a simple relationship between σ_{tip} and $K_{1\rho}$ can be obtained:

$$K_{1\rho}=\sqrt{2\pi}\,\frac{\sigma_{tip}}{1+\tilde{\omega}_1}\left(\frac{q-1}{q}\rho\right)^{1-\lambda_1}=\sqrt{F(2\alpha)}\,\sigma_{tip}\rho^{1-\lambda_1} \tag{2.3.18}$$

Then it is possible to rewrite Eq. (2.3.16) in a more compact form:

$$\overline{W}_1 = H(2\alpha,\frac{R_0}{\rho})\times\frac{K_{1\rho}{}^2}{E}\times\frac{1}{R_0^{2(1-\lambda_1)}} \tag{2.3.19}$$

Equation (2.3.19) holds true also in the case of blunt notches subjected to fatigue loading.

2.3.2 SED criterion applied to blunt notches under mixed mode loading

In the case of blunt notches under mixed mode loading (I+II), the elastic stress reaches its maximum value out of the notch bisector line and its position varies along the notch edge as a function of the ratio between Mode I and Mode II stress distributions. The problem of a blunt notch subjected to a shear or mixed mode loading is in a certain manner more difficult with respect to the Mode I loading.

In order to address and overcome this particular problem, the concept of equivalent local Mode I, suggested among the others by Berto et al. (2007) and Gomez et al. (2007-2008), can be seen as an accurate engineering approximation. In particular the SED was generalised from Mode I to mixed mode (I+II), under the hypothesis of an equivalent local Mode I along the normal line to the notch edge, at the point where the principal stress reaches its maximum value.

Under mixed mode loading the critical volume is, thus, no longer centred on the notch tip, but rather on the point where the principal stress reaches its maximum value along the edge of the notch (Fig. 2.3.1b). It was assumed that the crescent shape volume rotates rigidly under mixed mode, with no change in shape and size. This is the governing idea of the '*equivalent local Mode I*' approach, as proposed and applied to U-notches.

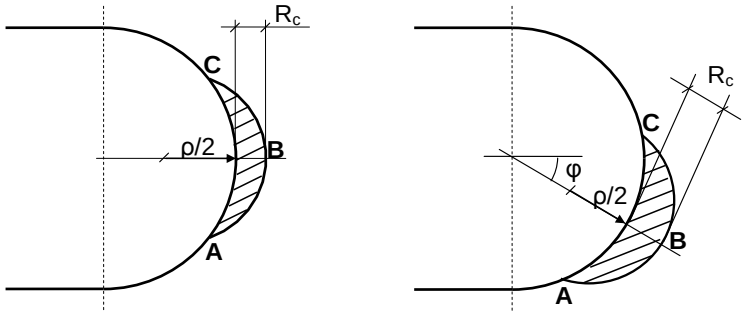

Figure 2.3.1. Critical volume (area) for U-notches subjected to Mode I (a) and mixed mode loading (b).

Summarising, under mixed mode loading the line normal to the notch edge and starting from the point of maximum principal stress becomes a virtual bisector

line under pure Mode I, confirming the applicability of the equivalent local Mode I concept.

The expression for U-notches under mixed mode is thus analogous to that valid for notches in Mode I:

$$\overline{W}^{(e)} = H^{*}\left(2\alpha, \frac{R_0}{\rho}\right) \times \frac{\pi\sigma_{max}^2}{4E} \tag{2.3.20}$$

where σ_{max} is the maximum value of the principal stress along the notch edge and H^* depends again on the normalized radius ρ/R_0, the Poisson's ratio ν and the loading conditions. For different configurations of mode mixity, the function H, analytically obtained under Mode I loading, was shown to be very close to H*.

2.3.3 SED criterion applied to blunt notches under torsion loading

Some closed-form expressions for the mean value of the strain energy density in the presence of theoretical parabolic and hyperbolic notches under Mode III loading were obtained by Zappalorto et al. and are going to be published on international journals.

3

3D effects in finite thickness plates weakened by rounded notches under in-plane shear

3.1 Introduction

The problem of characterizing analytically the stress field in three-dimensional components weakened by cracks and notches, both sharp and blunted, is far from easy. Closed form solutions are available only for simple geometries and in practice the simplify assumptions of plane stress or plane strain are widely employed to overcome the complexity of a complete three-dimensional analysis, that is time expensive and requires strong computational efforts. For components characterized by a reduced thickness, plane stress assumption is usually adopted. On the contrary, for larger values of the plate thickness, plane strain hypothesis is generally employed. Both plane stress and plane strain hypotheses are a simplification of the real three-dimensional problem and neglect *a priori* the complex state of stresses and strains through the plate thickness, due to the real constraint effects or to the induced modes, interacting from the mid plane to the free surface of the component. The assumption of a linear displacement through the plate thickness has been successfully adopted by some researchers as an approximation of real three-dimensional conditions (Kane and Mindlin 1956). This hypothesis, named generalized plane strain, has been found to be suitable to describe the stress field in notched components subjected to Mode I loading, at least in the central zone of the plate, where the hypothesis of a linear displacement in z direction is well verified (Yang and Freund 1985, Kotousov and Wang 2002, Berto et al. 2004). More recent papers have applied the generalized plane strain theory to sharp V-notches under in-plane shear loading deriving the equation for the out-of-plane eigenvalues (Huang 2004, Kotousov and Lew 2006, Kotousov 2007) not tackled in Williams solution (Williams 1952).

Dealing with in-plane solutions, the asymptotic nature of the linear elastic stress state at sharp corners was first discussed by Williams (1952) who explicitly referred to Coker and Filon's treatise on photoelasticity (Coker and Filon 1931, Fadle 1941). The degree of singularity of the stresses were explicitly provided in Williams (1952). Only the leading terms of the asymptotic stress distributions are discussed in that contribution. The degree of the stress singularity for the symmetric (Mode I) and antisymmetric (Mode II) loading have been shown to depend on the notch opening angle, 2α, only. In addition to the degree of the singularity the intensity of the singular terms in the asymptotic expansion play an important role in the integrity and failure assessment. These coefficients are usually quantified by the generalized (or notch) stress intensity factors (NSIFs).

The first paper where the NSIFs were analytically defined and numerically evaluated considering different geometries and boundary conditions was due to Gross and Mendelson (1972). However, the intensity of stress fields for a V-notch opening angle equal to 90°, was first investigated in a more dated paper (Brahtz 1933), where the stress distributions due to Mode I and Mode II are reported.

Dealing with out-of-plane solutions, the first pioneering contributions highlighting the existence of induced out-of-plane mode when a cracked plate is subjected to Mode II are due to Nakamura and Parks (1988-1989), while the first authors who extended the Williams' two dimensional solution to three-dimensional cases (at least for the crack case) were Hartranft and Sih (1968-1970). Some fundamental contributions in the field are due to Pook (1992-1994-2000a-2000b-2003) who confirmed the existence of coupled modes and widely discussed the corner point singularity of a notch flank intersecting the free surface of the plate, confirming some previous remarkable studies by other authors (Benthem 1977, Bazant and Estenssoro 1979). Due to the increase of computational power it is possible to investigate in detail three-dimensional effects by means of numerical models. Some recent works have been focused to investigate the intensity of coupled modes and in particular of Mode O, induced by an external in-plane shear loading (Harding et al. 2010, Berto et al. 2011a-2011b-2012a-2013a).

Other works have been aimed to investigate anti-symmetric in plane singular mode induced by an externally applied anti-plane loading (Berto et al. 2013b,

Kotousov et al. 2012). By adopting the generalized plane strain hypothesis, some approximate stress field equations have been recently derived and applied not only to sharp V-notches but also to rounded V-notches for small values of the notch tip radius (Lazzarin and Zappalorto 2012, Zappalorto and Lazzarin 2013).

The importance of three-dimensional effects, not only from a theoretical point of view but also for the influence of these effects on crack propagation, has been underlined in two recent reviews (Kotousov et al. 2010, Pook 2013). In particular, Pook (2013) presents a very wide and deep survey of three dimensional effects ahead of cracks and pointed V-notches discussing the effects and consequences on crack paths. The paper provides an overview of the main features of this topic providing to the reader a complete state of the art as well as a practical tool to face 3D effects. Although the aim of the present work does not deal with the crack propagation it is worth mentioning that in Pook (2013) crack paths are widely discussed paying attention to the interactions between different modes of loading and underlining that at the present state of the art the factors controlling the path taken by a propagating crack are not completely understood.

Three-dimensional effects can lead to an increase of stress concentration with respect to corresponding plane models (Jiang et al. 2011) and can substantially influence the out-of-plane constraint conditions through the plate thickness (Yang et al. 2013, Matvienko et al. 2013), being the fractography a powerful tool able to explain the complexity of events occurring during the cracking process (James 2013). Advanced imaging techniques are nowadays available with this aim (James et al. 2013a). They include confocal laser scanning microscopy (CLSM), and field emission scanning electron microscope (FESEM).

As stated in Khan et al. (2013), the use of two-dimensional plane stress or plane strain assumptions may deliver results that are reasonable in first approximation but a three-dimensional analysis is the only mean to fully understand the fracture process and in particular the crack initiation angle as a function of the plate thickness. The necessity to adopt a 3D perspective for characterization of the crack paths has been recently pointed out in Esnault et al. (2013), Doquet et al. (2013).

The importance of three dimensional finite element analyses and in particular the effects of thickness and notch radius on the fracture toughness of polycarbonate plates have been recently highlighted in Kattekola et al. (2013) explaining the brittle to ductile transition that usually occurs in polycarbonate decreasing the plate thickness and increasing the notch radius. A critical value of the ratio of the thickness to the notch root radius equal to 25.5 has been found to separate the brittle zone from the ductile one in a failure map, at least for polycarbonate.

As it seems evident considering the past and recent interest on 3D problems, the effect of finite thickness may play an important role in crack propagation process, may influence the constraint out-of-plane state and in some cases may influence also the fracture assessment in terms of the critical load that a structure can bear. In particular, the out-of-plane mode induced by an externally applied in-shear loading has some influences on the complex three-dimensional stress field close to the notch tip (Figure 3.1.1). While a systematic numerical study dealing with this induced mode has been carried out dealing with cracks and pointed V-notches (Harding et al. 2010, Berto et al. 2011a-2011b) only a limited number of papers have investigated the effect of a finite notch radius (Berto et al. 2012a-2013a), which is the aim of the present contribution. Recalling some observations reported in Berto et al. (2012a), a systematic parametric numerical study on the coupled Mode O in plates weakened by blunt V-notches and circular and elliptic holes is carried out herein. The main geometrical parameters (plate thickness, notch tip radius etc.) have been varied to investigate their influence on the coupled, induced out-of-plane mode.

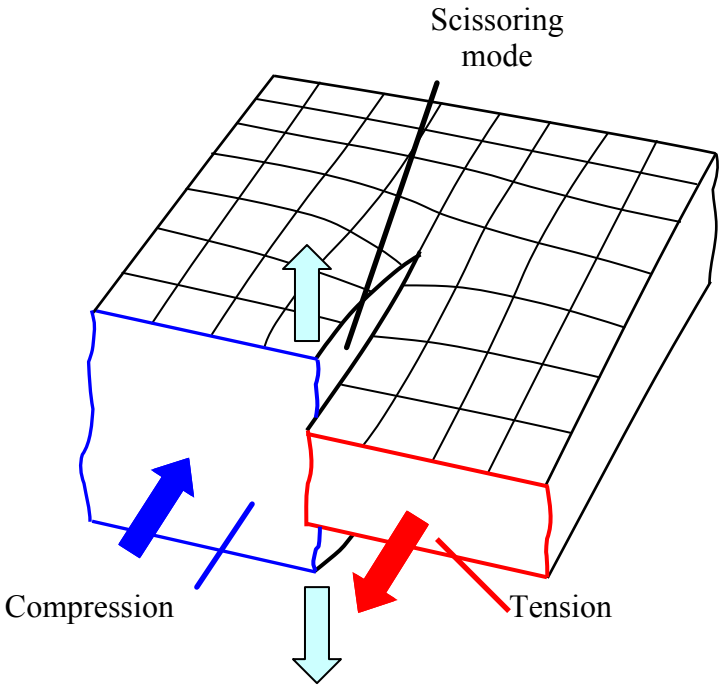

Figure 3.1.1. Scheme of the coupled out-of-plane mode induced by in-plane shear loading.

The extensive three-dimensional numerical study is performed focusing on the through the thickness effects as well as investigating the stress fields along the notch bisector line at different planes. The effect of the Poisson's ratio on the induced out-of-plane model has been also investigated ranging from the extreme cases $\nu=0$ to $\nu=0.5$. The two limit cases have been considered and studied for sake of completeness. In fact they allow to understand qualitatively the out-of-plane effect and to show the disappearance of the effect for $\nu=0$.

3.2 Out-of-plane mode in blunt V-notches

The first part of the chapter deals with plates of thickness 2t weakened by V-notches and subjected to an externally applied in-plane shear loading (Figure 3.2.1 a). The coordinate system is shown in Figure 3.2.1b.

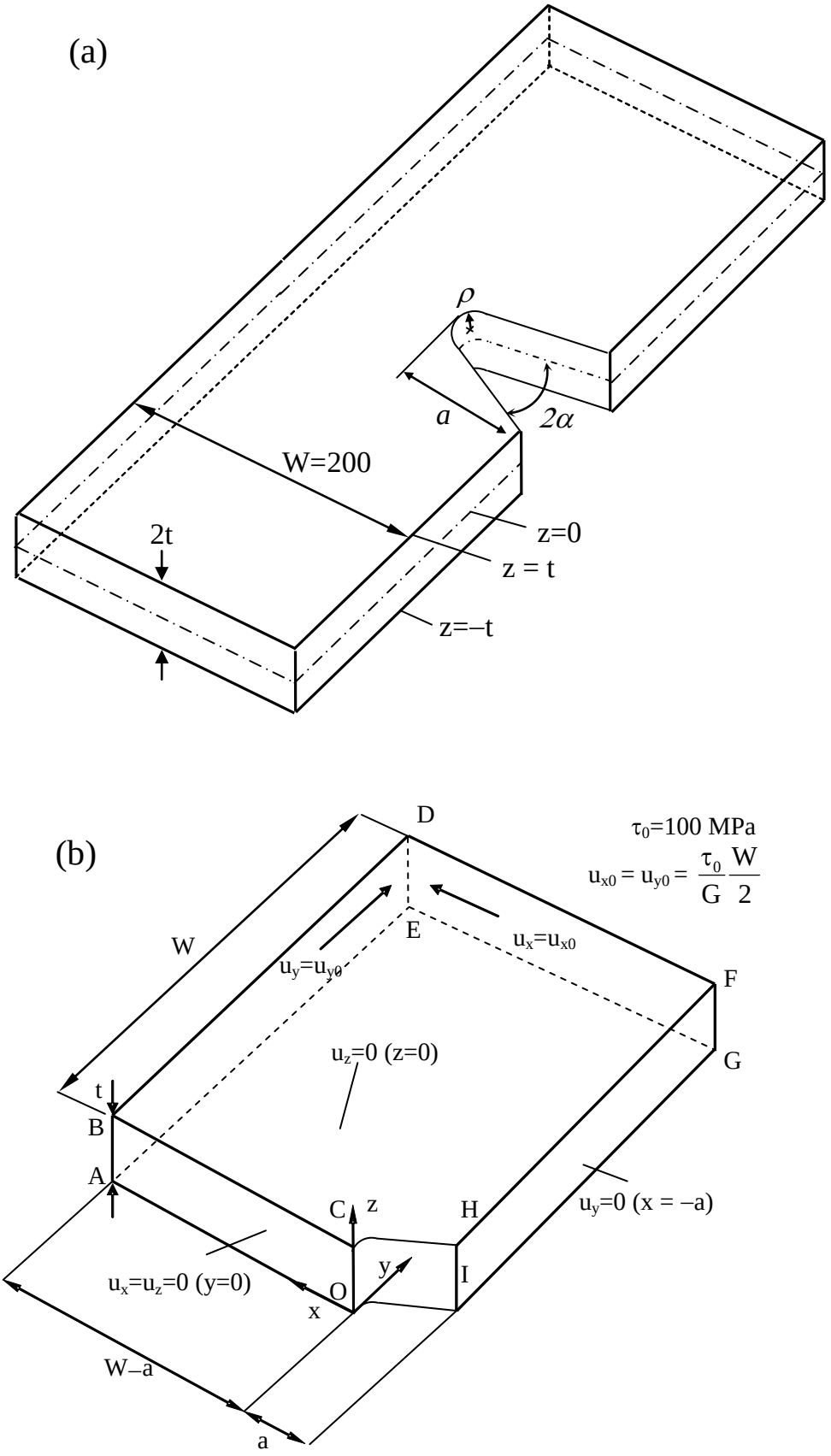

Figure 3.2.1. Geometry of the plate (a) and coordinate system having the origin on the notch tip, in the mid-plane of the plate (b).

The remote in-plane shear loading has been applied by means of displacements imposed on the far surfaces of the plates. By taking advantage of the symmetry of the plate only one quarter of the plate has been modelled.

With the aim to impose a nominal Mode II shear stress τ_0=100 MPa, the corresponding displacements have been imposed on the lateral surfaces named ABDE and DEGF (see Figure 3.2.1b). The intensity of the applied displacement is as follows:

$$u_{x0} = u_{y0} = \frac{\tau_0}{G} \times \frac{W}{2} \tag{3.2.1}$$

In Eq. (3.2.1) W is the plate width, G=E/2(1+ν) is the shear modulus and τ_0 the nominal applied stress which is equal to 100 MPa in all the models carried out in the present investigation. The Young's modulus, E, has been set equal to 206000 MPa in all analyses.

With the aim to capture the three-dimensional effects close to the notch tip and the free surface of the specimen a very fine mesh pattern has been created in those zones. The size of the element edge has been kept near the free surface and close to notch tip approximately equal to 1/30 of the notch root radius. The analyses were conducted by means of ANSYS code, version 13.0. A 20-node brick element, called Solid 95, has been used for the numerical analyses. This element allows high accuracy in three-dimensional analyses in comparison with hexahedral and tetragonal elements. It is well suited to model curved boundaries and it can also become tetrahedral or hexahedral managing automatically the transition. The shape function is characterized by a complete polynomial up to the fourth order.

A typical mesh pattern near the notch tip has been shown in Figure 3.2.2(a) as well as Figure 3.2.2(b) shows the stress component τ_{yz} through the plate thickness. This stress component is the so called out-of-plane shear stress tied to the coupled Mode O induced by the applied shear loading. It will be discussed in detail in the next session.

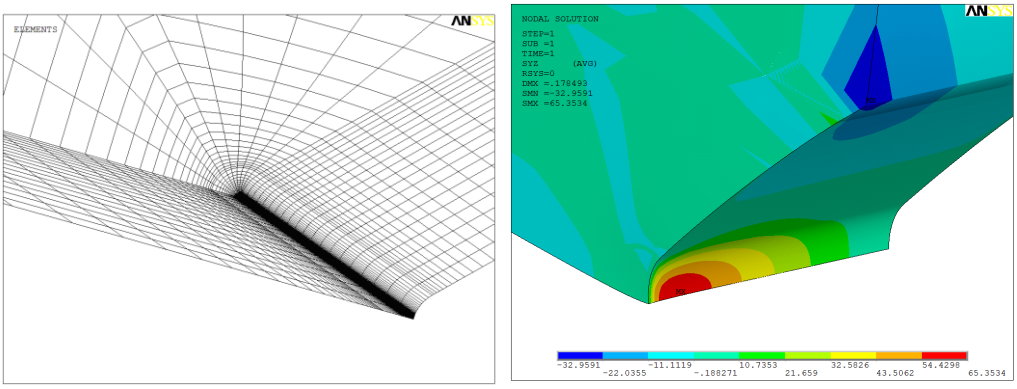

(a) (b)

Figure 3.2.2. Typical mesh pattern used for blunt V-notches (a); coupled stress component τ_{yz} through the thickness (b).

Four values of the notch radius (ρ=0.5, 1, 2 and 4 mm) have been considered in the analysis. The plate thickness, 2t, has been kept constant and equal to 40 mm. The notch depth, *a*, has been set equal to 20 mm and the plate width, W, equal to 200 mm. Two values of the notch opening angle (2α=90° and 135°) have been considered. All the analyses have been repeated for four different values of the Poisson's ratio (ν=0, 0.1, 0.3 and 0.5).

3.2.1 **Results from numerical analyses**

Figure 3.2.3a and 3.2.3b show the trend of the in-plane shear τ_{xy} and of the out-of-plane shear stress component, τ_{yz}, for the cases 2α=90° and ρ=0.5 and 1 mm, respectively. The plots are referred to the notch bisector line and different planes in z-direction. The out-of-plane stress is plotted in the plane where the induced mode presents its maximum intensity (z=19.48 mm). The in-plane shear has been plotted in the same plane (z=19.48 mm) but also in the mid-plane (z=0) and in the free surface (z=20 mm). From Figure 3.2.3a it is evident that a variation of the in-plane shear stress occurs at different planes. The trend is increasing from the mid-plane to the free surface of the plate with an increment equal to about 47%. In all the planes τ_{xy} drops to zero at the notch tip. In parallel τ_{yz} at z=19.48 mm shows a maximum at the notch tip which is higher than the nominal external applied stress (τ_0=100 MPa). The stress component, τ_{yz}, smoothly decreases along the notch

bisector line. A similar behaviour has been observed for ρ=1 mm (Figure 3.2.3b) even if in this last case the variation of the in-plane stress through different planes is more limited (25%) as well as the intensity of the out-of-plane shear stress is lower, but again higher with respect to the externally applied nominal stress.

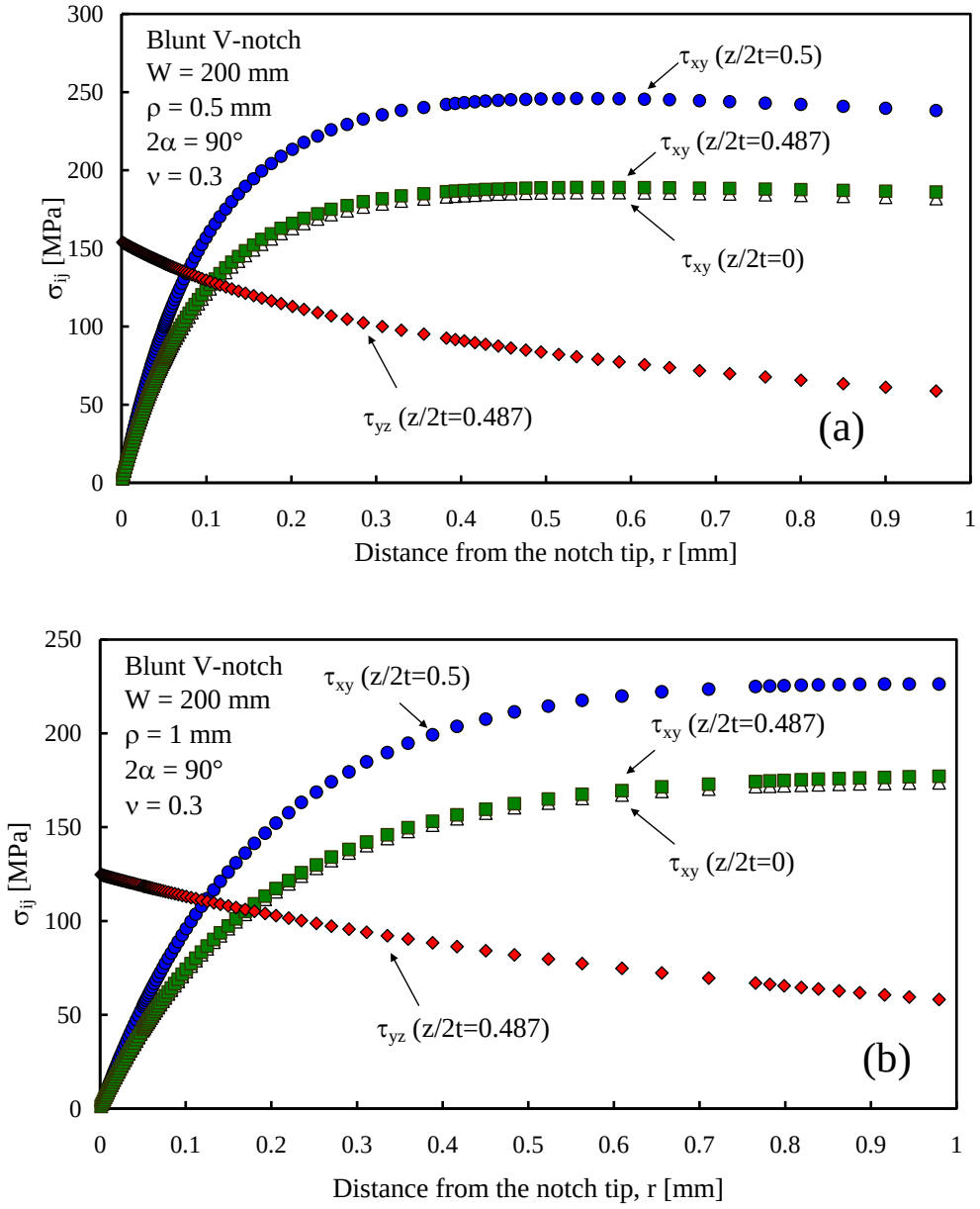

Figure 3.2.3. The trend of the in-plane shear τ_{xy} and of the out-of-plane shear stress component, τ_{yz}, for the cases 2α=90° and ρ=0.5 (a) and 1 mm (b), respectively.

By increasing the notch root radius and considering ρ=2 and 5 mm the out-of-plane mode is still present (see Figure 3.2.4a and 3.2.4b) but its maximum value at the notch tip, in the plane of higher intensity, is lower than the nominal applied stress and the case ρ=2 mm is found to be the transitional value. In that case, in fact, at the notch tip the out-of-plane stress is approximately equal to 100 MPa which coincides with the applied nominal stress. Also in these last cases, where the intensity of the Mode O seems to be limited, a stress redistribution of the in-plane shear stress, τ_{xy}, is evident due to non-negligible three-dimensional effects occurring through the plate thickness.

By analysing the first results provided in the present study, the existence of a distinctive out-of-plane shear stress component, not predicted by two-dimensional elasticity theory, has been proofed.

In Figures 3.2.5 (a-b) the stress component τ_{yz} has been plotted at the notch tip through the plate thickness varying the notch radius for 2α=90° and 135°, respectively. The variation of the out-of-plane shear stress is evident from the above mentioned figures. In particular, τ_{yz} is equal to zero at the mid-plane of the plate. Due to the symmetry conditions it changes its sign at z=0. The induced stress presents a maximum close to the free surface of the plate and it drops to zero at z=t. It is worth mentioning that by decreasing the ratio between the notch radius and the plate thickness, ρ/2t, the intensity of the coupled stress increases.

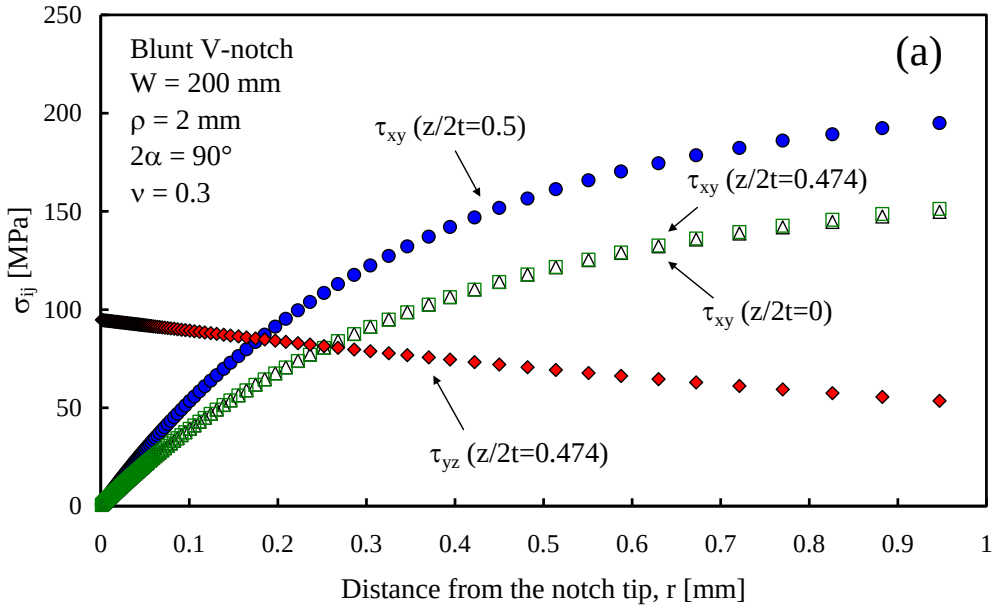

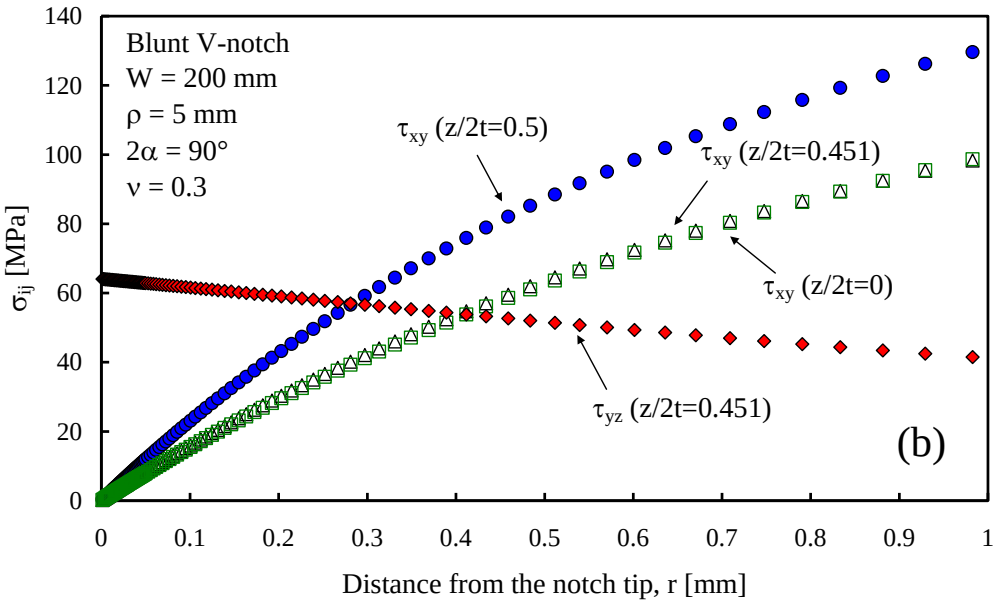

Figure 3.2.4. Trend of the in-plane shear τ_{xy} and of the out-of-plane shear stress component, τ_{yz}, for the cases $2\alpha=90°$ and $\rho=2$ (a) and 5 mm (b), respectively.

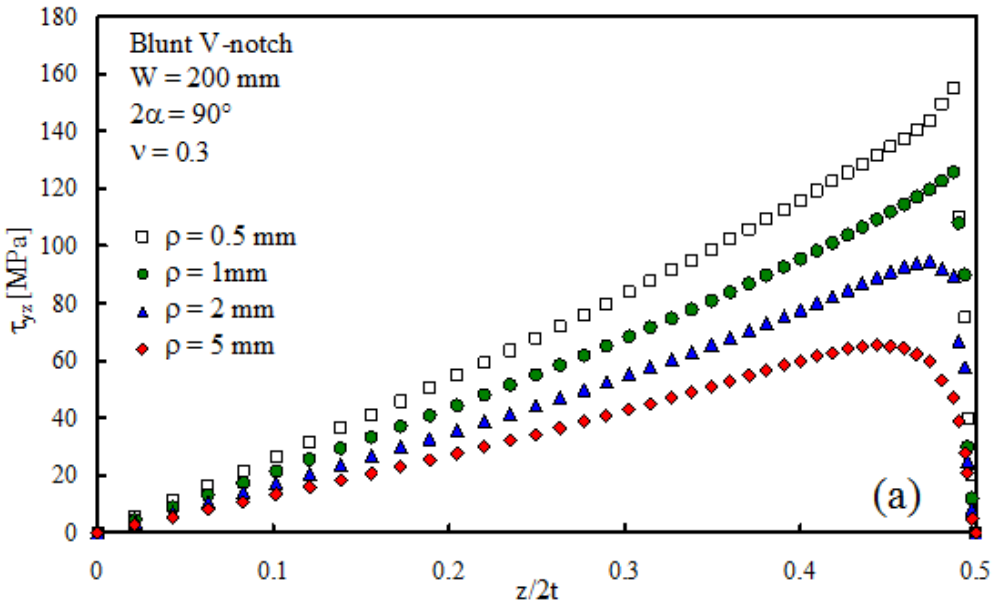

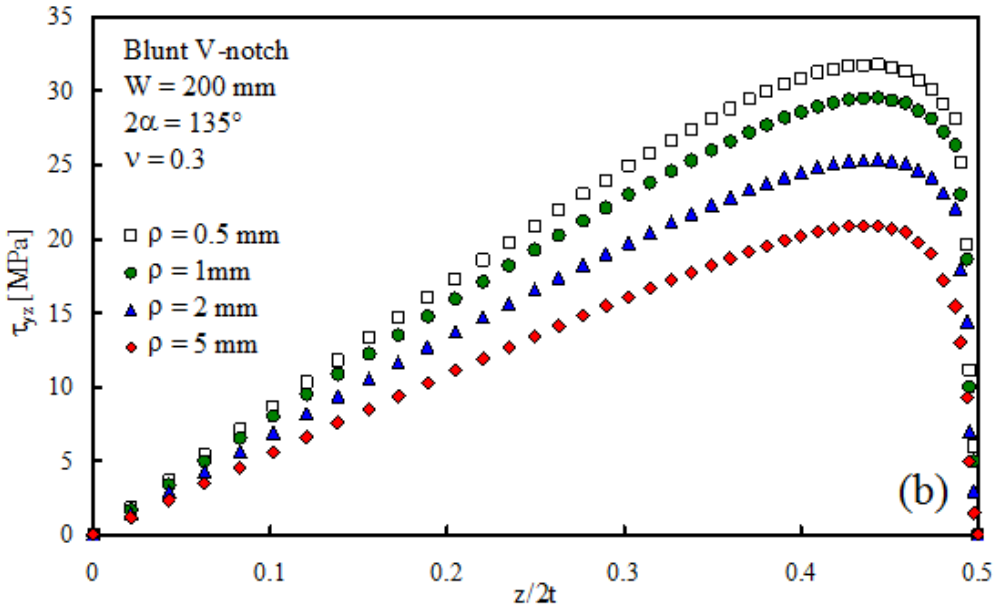

Figure 3.2.5. Out-of-plane stress through the plate thickness as a function of the notch radius for different values of the opening angle. 2α=90° (a), 2α=135° (b).

Figures 3.2.6 (a-b) show the effect of the Poisson's ratio for the case 2α=90° and 2α=135° with ρ=0.5 mm. From the figures it is clear that the induced out-of-plane stress is identically equal to zero through the plate thickness when the Poisson's ratio ν is equal to 0. The intensity of the Mode O increases as the Poisson's ratio ν increases. The same trend has been verified also for other values of the notch tip radius. Lateral contraction due to Poisson's ratio is then the cause of the coupled induced mode.

As discussed in Berto et al. (2011a) the intensity of Mode O is higher when the notch is sharp (ρ=0 mm). For sake of completeness an example is reported here.

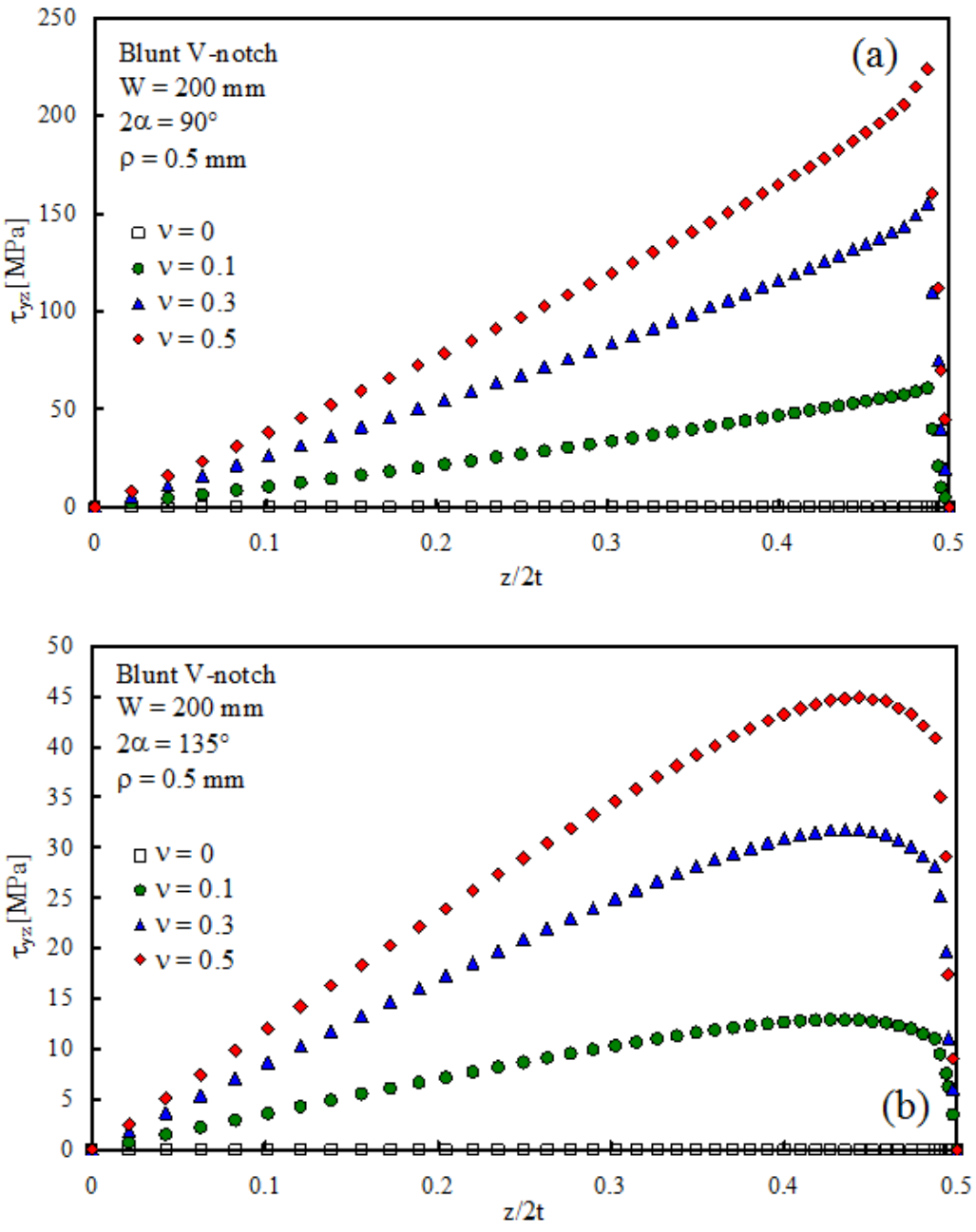

Figure 3.2.6. Out-of-plane stress through the plate thickness as a function of the Poisson's ratio for different values of the opening angle. 2α=90° (a), 2α=135° (b).

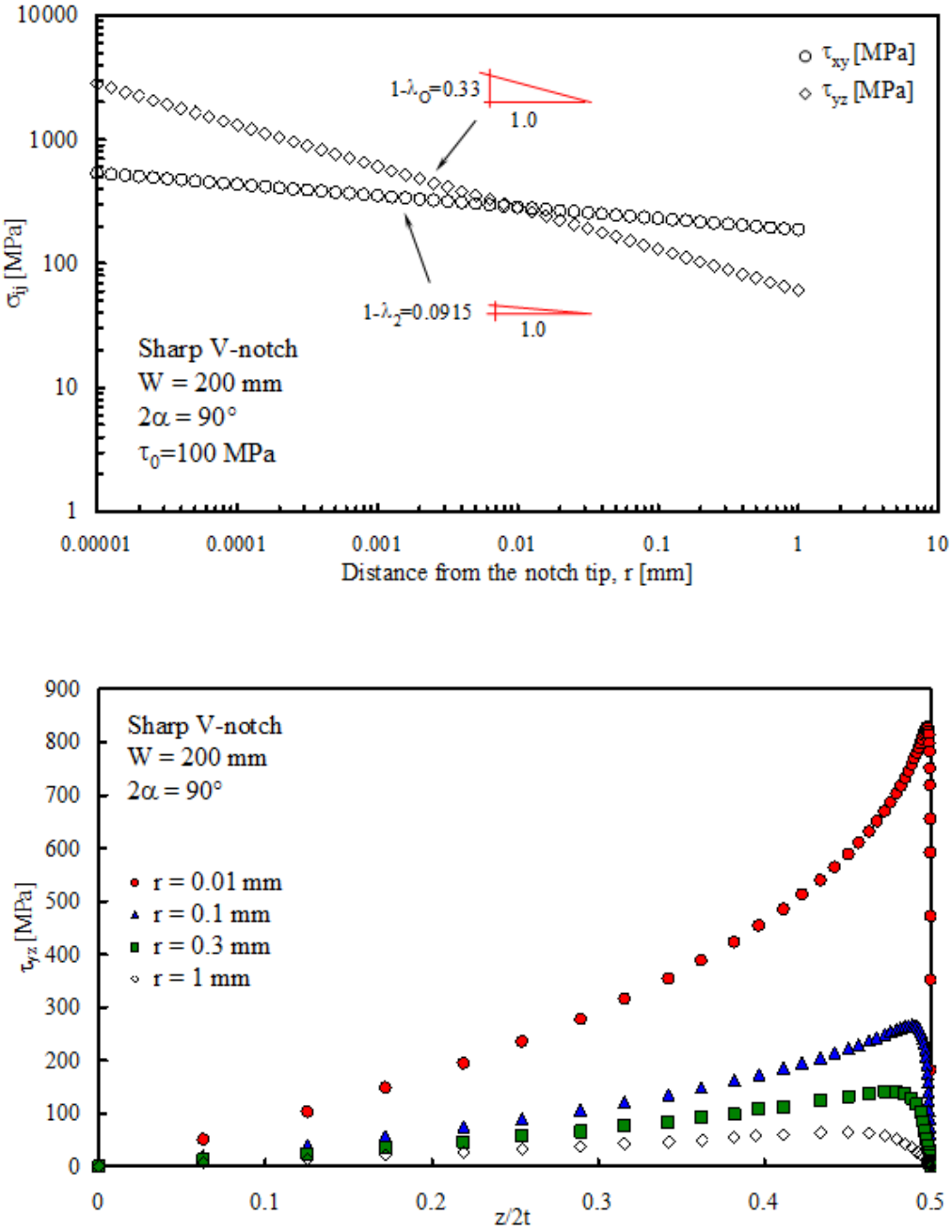

Figure 3.2.7. Stress distribution in a plate weakened by sharp notch under in plane shear. Trend along the notch bisector line (a); induced shear stress along the thickness (b).

Figures 3.2.7 (a-b) summarize results from a plate with $2\alpha=90°$ and $\rho=0$ mm. As in previous cases, the plate thickness, 2t, has been kept constant and equal to 40 mm. The notch depth, *a*, has been set equal to 20 mm and the plate width, W, equal to 200 mm. Figure 3.2.7a shows the trend of the in-plane shear stress at the mid-plane as a function of the distance from the notch tip and reports also the out-

of-plane stress detected at the plane corresponding to z=19.9 mm where the maximum intensity of the coupled mode is reached. Figure 3.2.7b shows the trend through the thickness of the out-of-plane stress for different distances from the notch tip (r=0.01, 0.1, 0.3 and 1.0 mm).

3.3 Finite thickness plates weakened by circular and elliptic holes

Dealing with circular and elliptic holes the geometry of the considered models is shown in Figure 3.3.1a while Figure 3.3.1b reports the externally applied displacements on the quarter of plate modelled in Ansys. Four different radii of the circular hole have been considered and set equal to 1, 5, 10 and 20 mm. The plate thickness, 2t, has been set equal to 40 mm while the width of the plate, W, has been kept constant and equal to 200 mm. As made for blunt V-notches the Poisson's ratio has been varied from 0 to 0.5 to investigate the effect of this parameter on the induced out-of-plane mode.

Dealing with plates weakened by elliptic holes the ratio between the semi-axis of the ellipse (a/b) has been set equal to 5, 10, 20, keeping constant the minor semi-axis b=1 mm. These ratios between the semi-axis correspond to a minimum radius of curvature equal to 0.2, 0.1 and 0.05 mm, respectively.

The plate thickness has been set equal to 40 mm and the plate width equal to 200 mm. The Poisson's ratio has been varied also in this case from 0 to 0.5.

The same boundary conditions used for blunt V-notches have been applied here. In particular, in the transverse sectional area, named OABC, u_x and u_z are imposed to be equal to zero. On the mid-plane z = 0 the displacement u_z has been set equal to 0. The lateral surface called GFHI has been constrained by imposing $u_y = 0$. The remotely applied displacements u_{x0} and u_{y0} have been applied accordingly to Eq. (3.2.1) to the lateral surfaces ABDE and DEGF assuring a nominal shear load τ_0 equal to 100 MPa. The same 20-nodes finite element (Solid 95) has been employed in the analyses. To capture the through the thickness effects a fine mesh is created near the notch tip and close to the lateral surface. Figures 3.3.2a and 3.3.2b show the specific mesh pattern adopted for circular and elliptic holes, respectively. As explained above, due to the fact that three-dimensional effects are

expected to occur near the close neighbourhood of the free surfaces a very fine mesh has been employed in that zone. This part of the chapter extends some previous preliminary results provided in the appendix of Berto et al. (2012a) where the attention was mainly paid to U-notches.

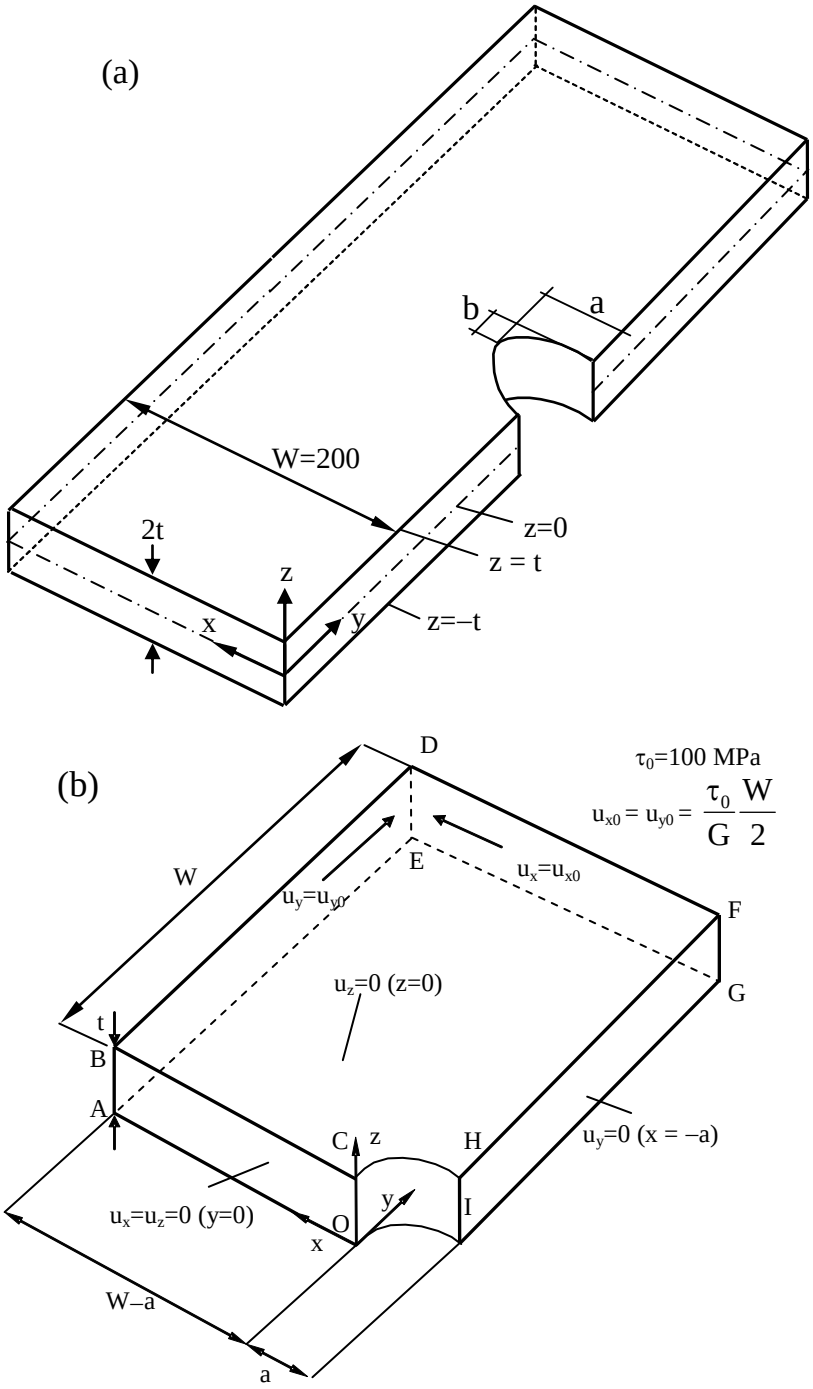

Figure 3.3.1. Geometry of the plate weakened by circular and elliptic holes (a) and coordinate system having the origin on the notch tip, at the mid-plane (b).

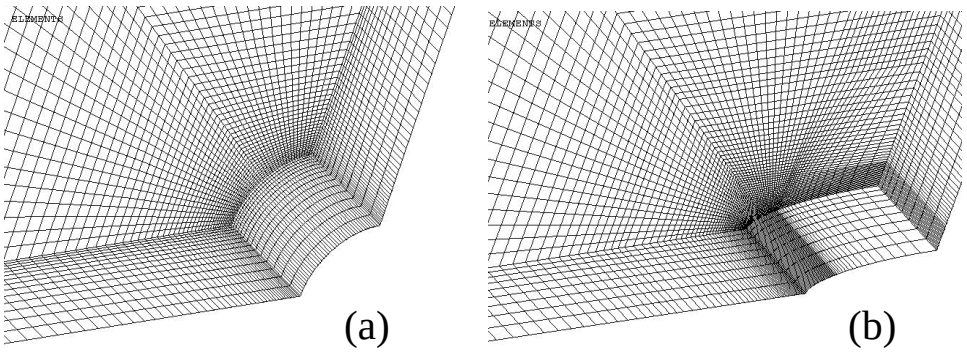

Figure 3.3.2. Mesh pattern used for the circular (a) and elliptic hole (b).

3.3.1 **Results from numerical models**

An example of the contour plots of the induced out-of-plane shear stress is depicted in Figures 3.3.3a and 3.3.3b for circular and elliptic holes, respectively. Figure 3.3.3 a refers to the case R=a=b=5 mm while Figure 3.3.3b reports the results from the case a/b=5.

The contour lines shown in Figure 3.3.3 allows to understand the behaviour of Mode O stress component through the plate thickness. It reaches a maximum close to the free surface of the specimen and drops to zero both on the mid-plane and on the lateral surface. The maximum value of the out-of-plane shear stress occurs on the notch tip and along the notch bisector line. Again it is worth mentioning that this effect is not contemplated in 2D models that a priori consider equal to zero the stress components tied to Mode O.

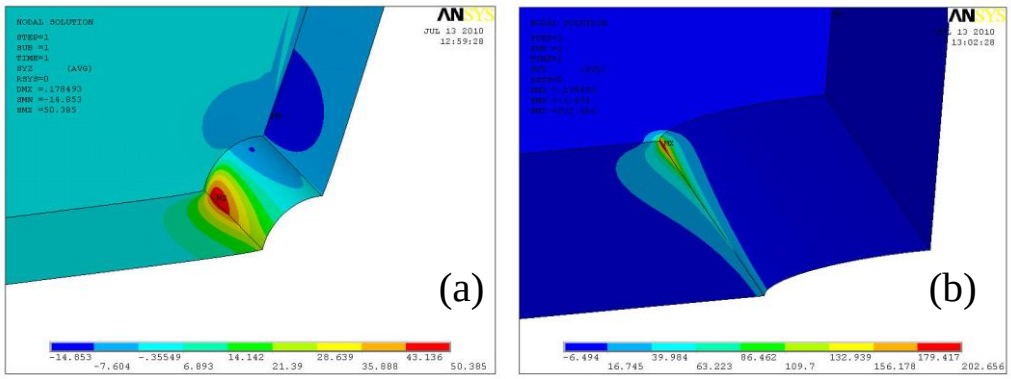

Figure 3.3.3. Contour lines of the stress component τ_{yz}, in plates weakened by circular holes (R=5 mm) (a) and elliptic holes (a/b)=5 (b).

Figure 3.3.4 reports the stress component τ_{yz} for the circular hole having a radius R= 1 mm. The plot is carried out along the notch bisector on the plane of maximum intensity of the Mode O (z=19.5 mm). The induced shear stress reaches significant values but remains lower than the external nominal stress. Figure 3.3.5a, 3.3.5b and 3.3.5c report the out-of-plane shear stress along the notch bisector (and on the plane of maximum intensity of the Mode O) for the elliptic holes characterized by a ratio between the semi-axis a/b equal to 5, 10 and 20, respectively. Contrary to the circular hole case reported in Figure 3.3.4, in these cases the intensity of the Mode O stress component is always much higher than the nominal external applied stress.

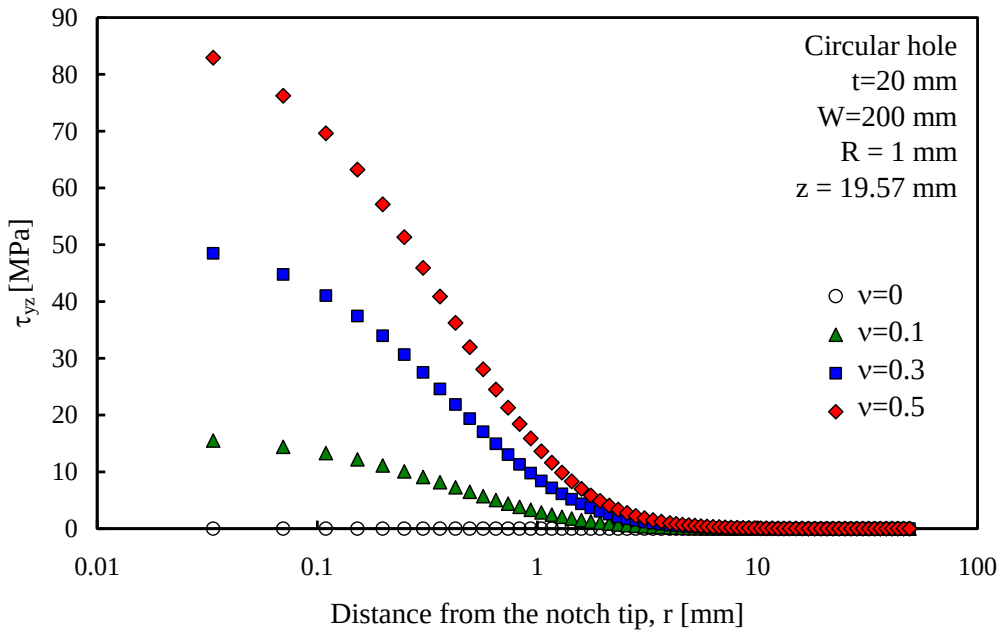

Figure 3.3.4. Coupled stress plot along the notch bisector line in the plane of maximum intensity as a function of the Poisson's ratio: case of a circular radius R=1 mm.

Figures 3.3.6a and 3.3.6b show the trend through the plate thickness of the shear stress component τ_{yz}, normalized with respect to the principal stress, σ_1. Due to the fact that the external applied load is a pure Mode II loading, the principal

stress reaches its maximum value outside the notch bisector line (see Figure 3.3.7). On the other hand the induced stress component τ_{yz}, reaches its maximum value along the notch bisector line as discussed describing Figure 3.3.3.

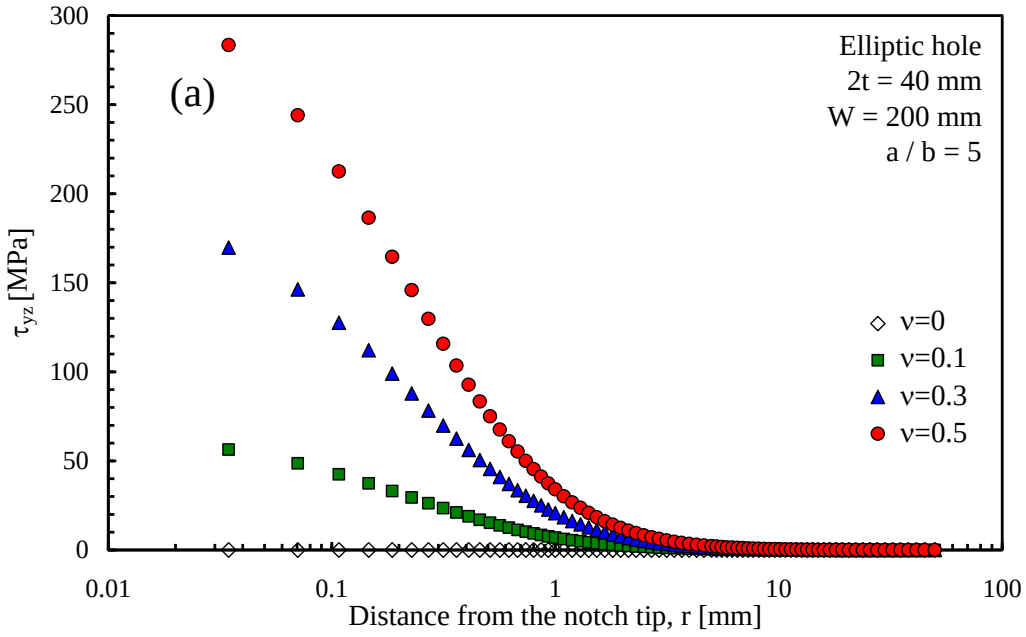

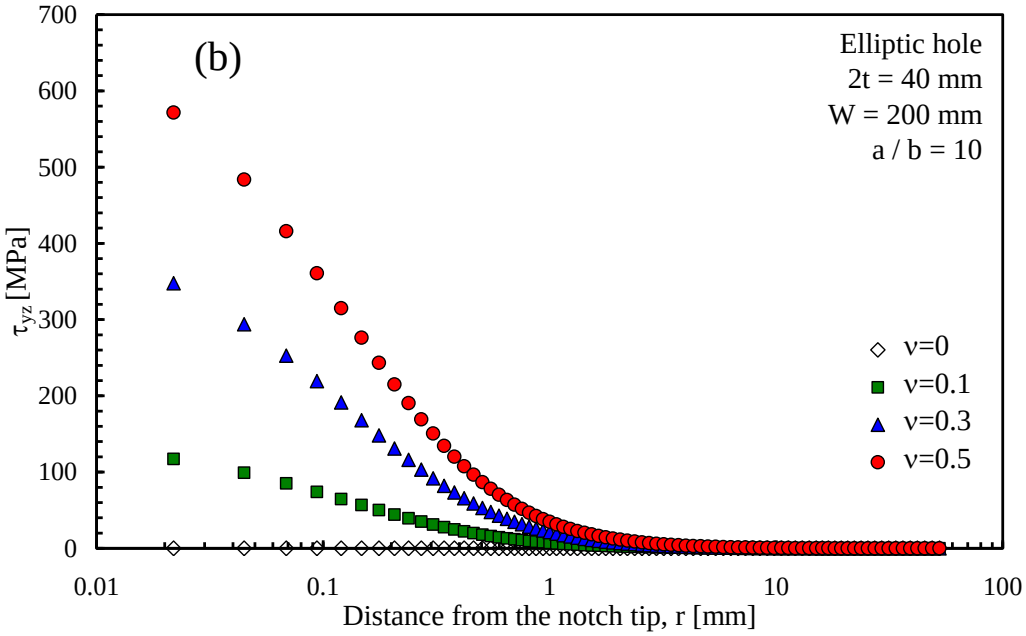

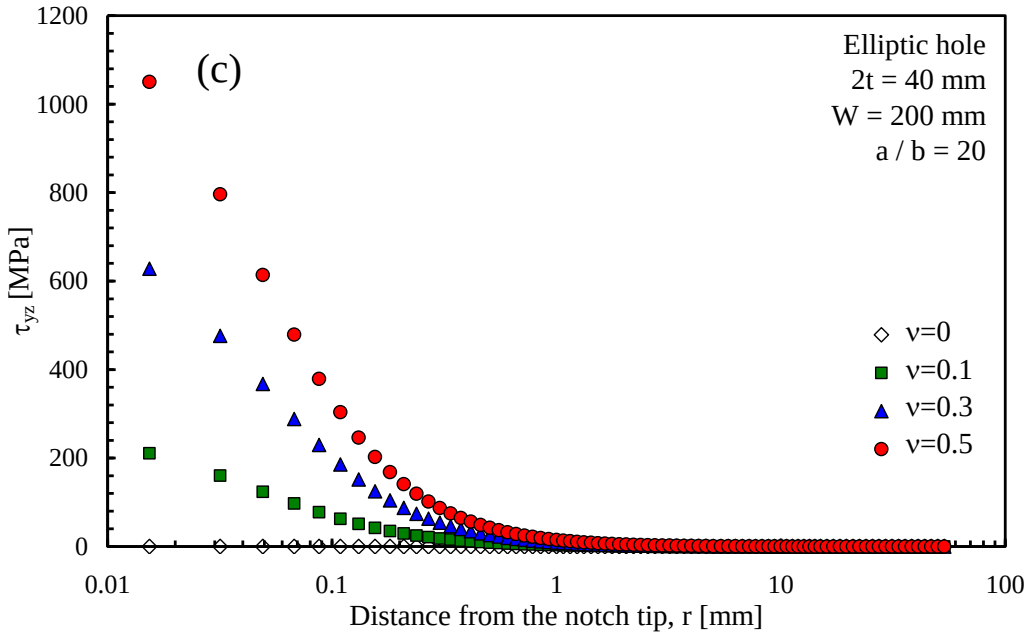

Figure 3.3.5. Coupled stress plot along the notch bisector line in the plane of maximum intensity as a function of the Poisson's ratio: case of a elliptic hole a/b=5 (a), a/b=10 (b) a/b=20 (c).

Both stresses reach their maximum through the plate thickness near the free surface of the plate. Fig. 3.3.6 refers to a value of the Poisson's ratio equal to 0.3.

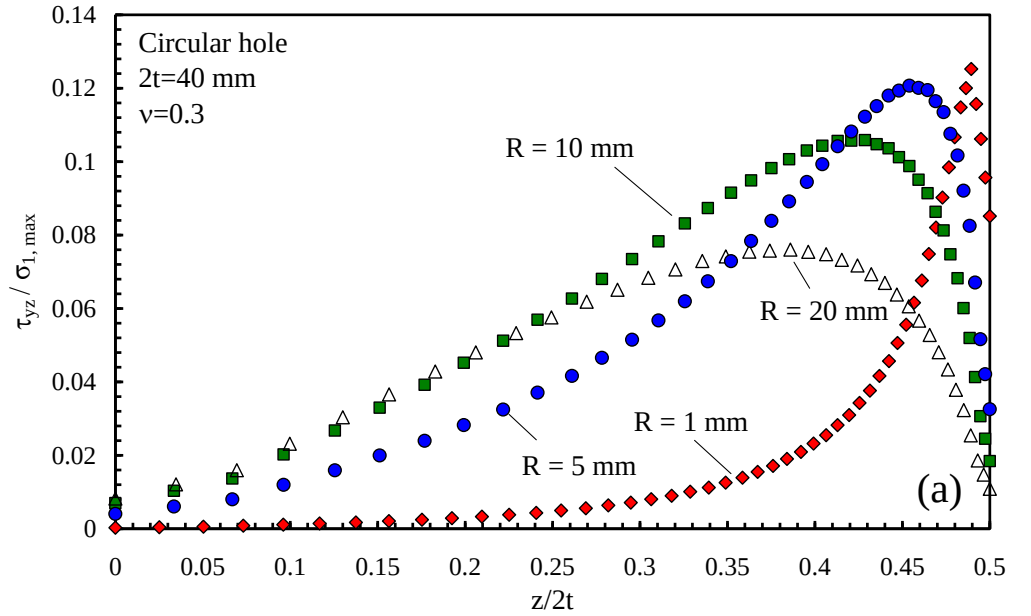

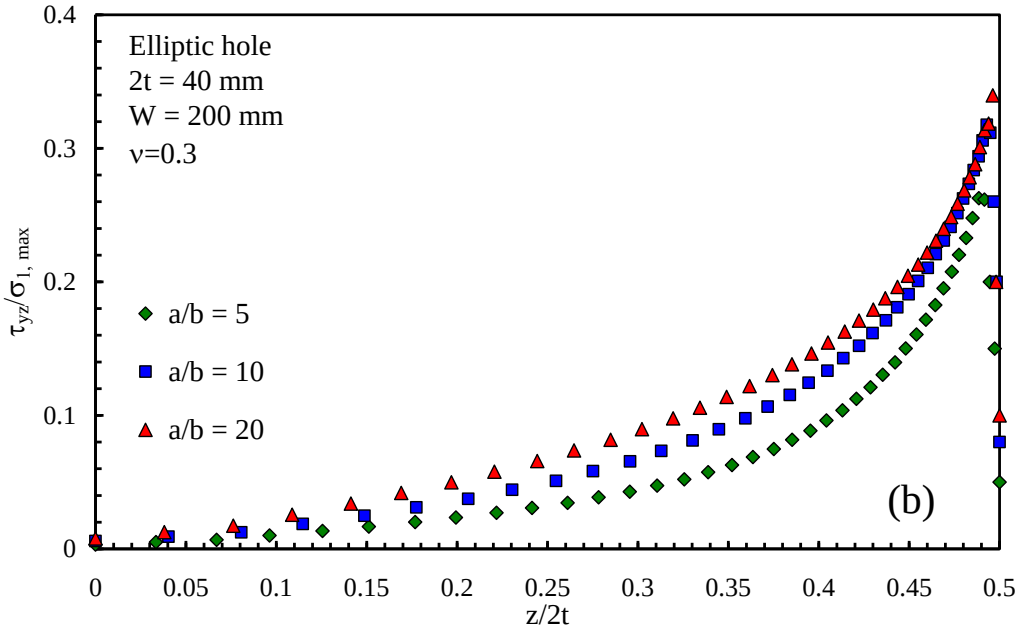

Figure 3.3.6. Through-the-thickness out-of-plane stress normalized to the maximum value of the principal stress; circular holes (a) and elliptic holes (b).

In Figure 3.3.6a, it is worth noting that when the radius of the hole decreases, the intensity of the induced out-of-plane stress tends to increase and the position of the maximum through the thickness tends to move towards the free surface of the specimen. In the case of elliptic holes the intensity of the induced out-of-plane stress is strongly influenced by the hole size and in particular by the semi-axis ratio but, due to the acuity of the notch, the effect remains limited within the close neighborhood of the lateral surface (z /(2t)> 0.48).

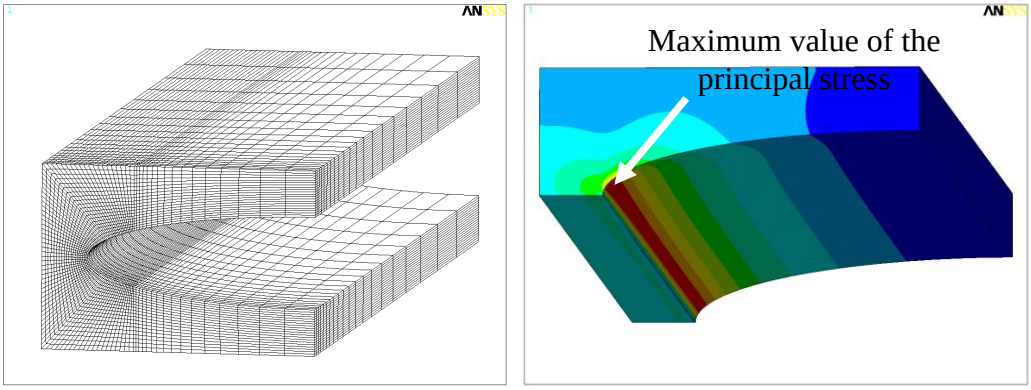

Figure 3.3.7. Contour lines of the principal stress through the plate thickness. The maximum is out of the notch bisector and close to the free surface (a), typical mesh used to capture this effect (b).

Figure 3.3.8(a,b) shows the trend of the principal stress, σ_1, and the out-of-plane shear stress τ_{yz} normalised to the maximum value of σ_1. The plot is carried out through the plate thickness and out of the bisector line. The path line coincides with that corresponding to the maximum value of σ_1. By observing Figure3.3.8 (b) it appears evident that dealing with elliptic holes the principal stress, σ_1, reaches is maximum value not on the free surface but inside the thickness and not far from the lateral surfaces.

Dealing with circular holes, Figure 3.3.8(a) shows that the maximum principal stress varies its position through the thickness as a function of the ratio between the radius R and the plate semi-thickness t, in agreement with Figure 3.3.6 (a). As discussed above for the case corresponding to R=1 mm and 2t=40 mm, the maximum value is placed very close to the free surface of the plate. On the other hand, it approaches the mid-plane for the case corresponding to R=20 mm and 2h=40 mm. By comparing the induced out- of-plane shear stress detected outside the notch bisector line its intensity decreases. For circular holes the ratio $\tau_{yz}/\sigma_{1,max}$ is always lower than 5%. The higher value corresponds to R=1 mm. On the other hand, considering elliptic holes, the Mode O shear stress component (τ_{yz}) is always not negligible both along the notch bisector and outside from it. For the ratio a/b=20, which is the most critical in terms of out-of-plane stress, the ratio $\tau_{yz}/\sigma_{1,max}$ results to be equal to 0.35 on the notch bisector and about 0.2 by considering the same ratio outside the notch bisector line. This means that the out-of-plane mode is far from being negligible in this last case and may influence not only the position of the fracture initiation along the edge of the notch and through the thickness of the plate but also the critical load that the component can bear before failure.

The out-of-plane stress component, τ_{yz}, plotted through the plate thickness is shown in Figure 3.3.9(a) and 3.3.9(b) as a function of the Poisson's ratio. Figure 3.3.9(a) is referred to the case of a circular hole having a radius R=5 while 3.3.9 (b) summarized the results from the elliptic case characterized by a ratio a/b=5 between the ellipse semi-axis. Both Figures evidence that the highest intensity of the Mode O is reached for elevate values of the Poisson's ratio and that the effect

has it maximum intensity under the free surfaces of the plate at a certain distance from them.

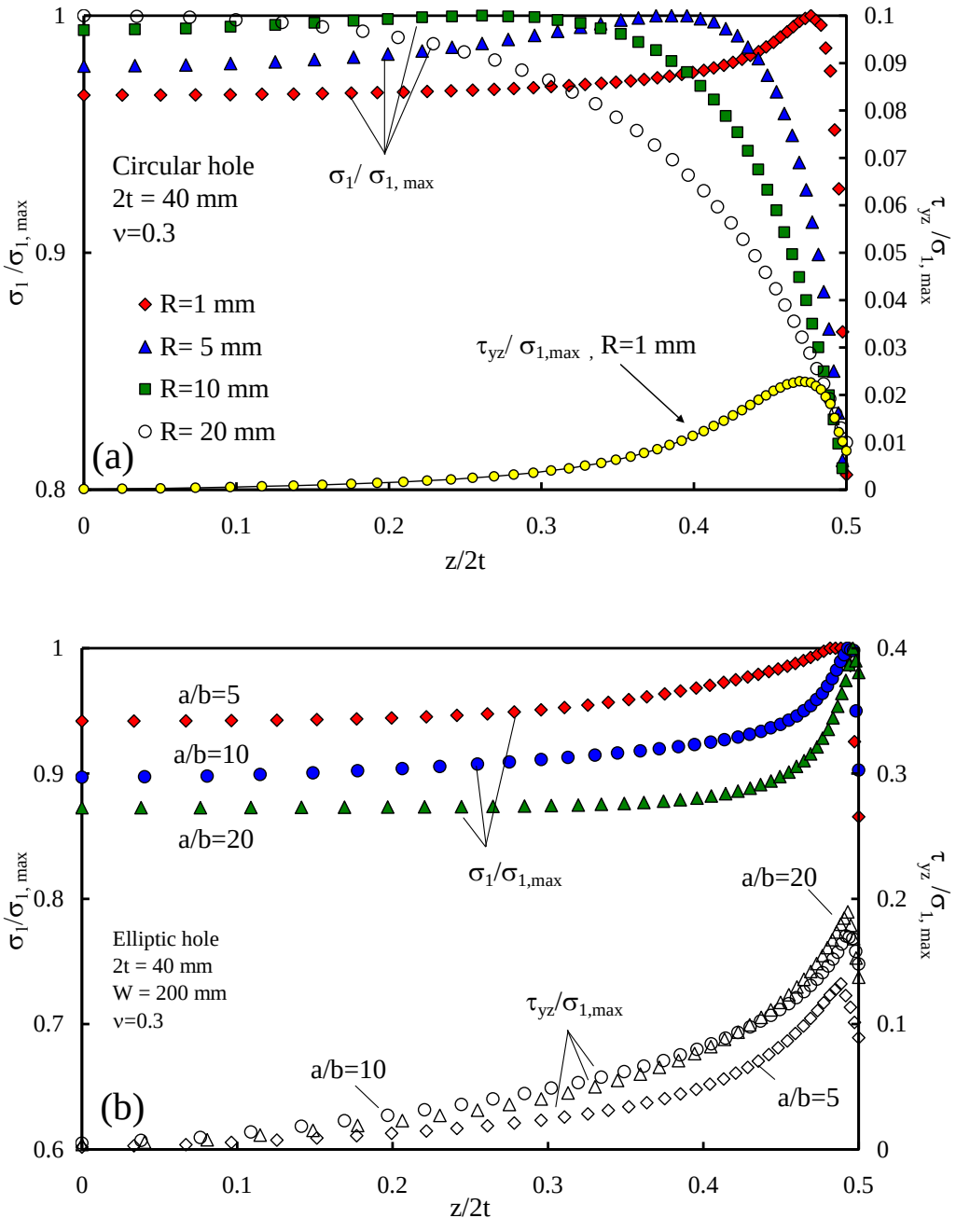

Figure 3.3.8. Principal stress σ_1 and the Mode O shear stress τ_{yz} normalised to the maximum value of the principal stress. Both stress components are plotted through the plate thickness but outside the bisector line, along the line where σ_1 reaches its maximum value; circular holes (a), elliptic holes (b).

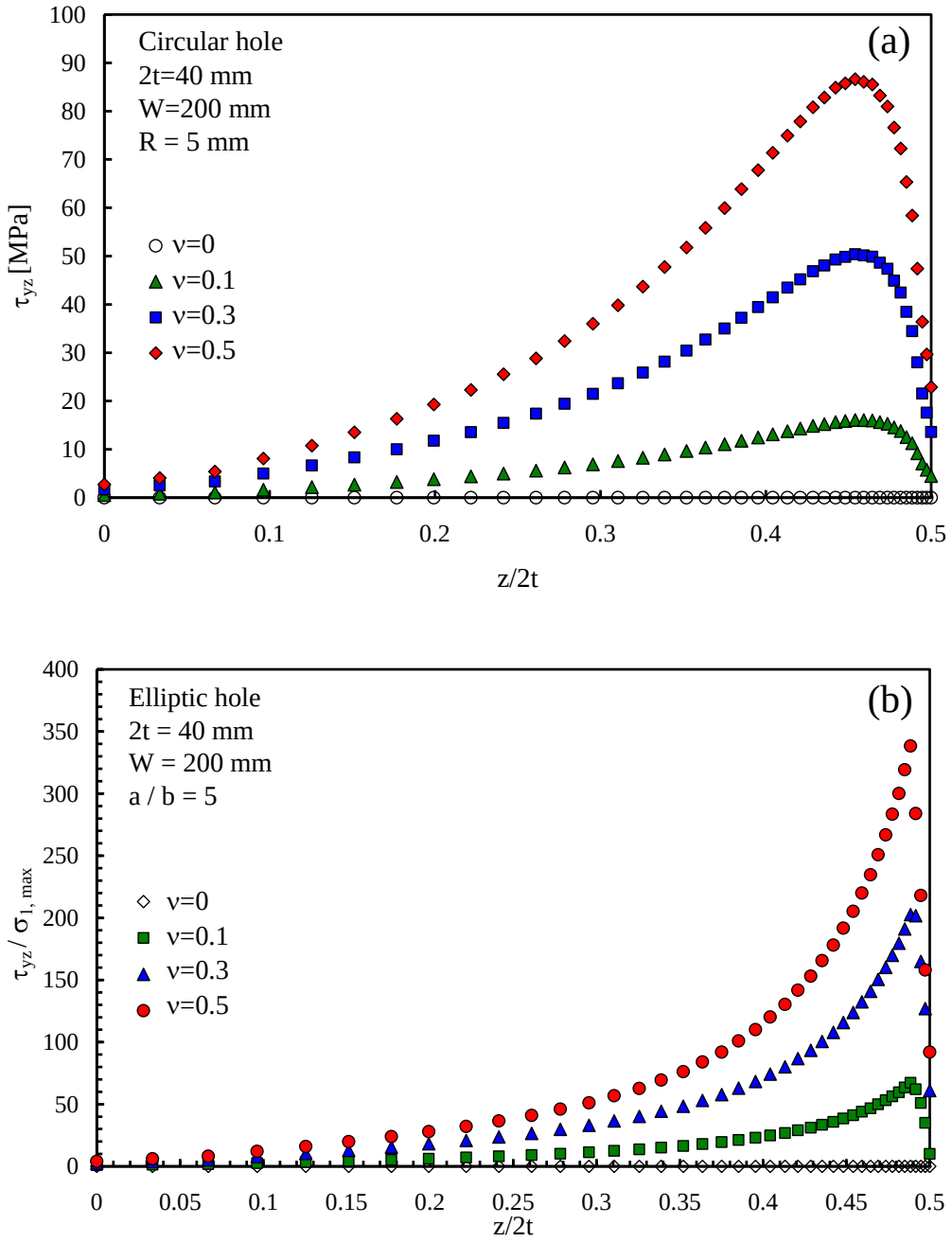

Figure 3.3.9. Trend of the out-of-plane stress τ_{yz} (Mode O) through the thickness as a function of the Poisson's ratio. Circular holes (a) and elliptic holes (b).

Finally Table 3.3.1 lists the values of the theoretical stress concentration factors (K_t) comparing the results from 2D analyses with those obtained from 3D models.

Table 3.3.1. Theoretical stress concentration factors for blunt V-notches (2a=90°) and circular and elliptic holes.

Blunt V-Notch 2α=90°							
	Kt 2D	Kt 3D			Δ [%]		
ρ [mm]		ν=0.1	ν=0.3	ν=0.5	ν=0.1	ν=0.3	ν=0.5
0.5	4.492	4.684	5.312	6.674	4.27	18.25	48.57
1	4.245	4.277	4.834	6.314	0.75	13.87	48.74
2	4.021	4.021	4.351	5.551	0.00	8.21	38.05
5	3.726	3.726	3.974	4.872	0.00	6.66	30.76
Circular Hole							
	Kt 2D	Kt 3D			Δ [%]		
R [mm]		ν=0.1	ν=0.3	ν=0.5	ν=0.1	ν=0.3	ν=0.5
1	4.001	4.013	4.159	4.407	0.3	3.95	10.15
5	4.005	4.024	4.175	4.424	0.5	4.24	10.46
10	4.002	4.025	4.179	4.425	0.57	4.42	10.57
20	3.998	4.015	4.215	4.509	0.42	5.43	12.78
Elliptic Hole							
	Kt 2D	Kt 3D			Δ [%]		
a/b		ν=0.1	ν=0.3	ν=0.5	ν=0.1	ν=0.3	ν=0.5
5	7.221	7.249	7.715	8.653	3.88	6.85	19.83
10	12.063	12.312	13.406	15.507	2.06	11.13	28.55
20	21.689	22.586	25.403	35.219	4.14	17.12	62.82

The theoretical stress concentration factor, K_t has been defined as the ratio between the maximum value of the principal stress over the nominal in-plane shear stress, applied to to the model (τ_0=100 MPa). The appropriate expression for K_t is as follows:

$$K_t = \frac{\sigma_{1,max}}{\tau_0} \tag{3.3.1}$$

It is interesting to observe that the theoretical stress concentration factor from 3D models is influenced by the Poisson's ratio and tends to increase for increasing values of ν. For the circular holes the relative deviation between K_t from a 2D and a 3D analyses is limited, being the maximum percentage deviation, $\Delta = 100\times(K_{t,3D}-K_{t,2D})/K_{t,2D}$, equal to 13% for the case R=20 mm and ν=0.5. On the other hand considering the elliptic holes, and in particular the case a/b=20 and

ν=0.5, Δ is equal to 62%. This last value confirms the necessity to carefully take into account three-dimensional effects and, at least, before going straightforward to a plane model, to verify if a 2D model is appropriate to the considered case. Dealing with blunt V-notches and in particular referring to the case 2α=90° the same effect has been found as visible from Table 3.3.1.

In some recent papers (She and Guo 2007, Yu et al. 2008) the influence of Poisson's ratio on the thickness-dependent stress concentration at elliptic holes in elastic plates under tension has been investigated showing that it cannot be ignored. A relative deviation equal to 25% has been detected in the investigated cases.

When the applied mode and the induced modes due to three-dimensional effects are automatically present in a component, the arising problem is how to take these effects contemporary into accounts. In Esnault et al. (2013) the energy release rate has been adopted to combine together the effects of coupled modes. The advantage of an energy based approach is that it permits to easily link, with a single parameter, the effects occurring in a plane together with the complex state of strains and stresses that usually characterized a three-dimensional problem. Some recent contributions of Lazzarin and Berto have shown as the local energy averaged over a control volume (SED) is a powerful tool to determine a critical parameter for the material (Berto and Lazzarin 2009, Berto et al. 2011c, Lazzarin et al. 2013a), able to capture also the effects due to finite plate thicknesses. Some recent applications have shown the applicability of the SED also to non homogeneous materials like functionally graded materials (Barati and Alizadeh 2011, Mehram et al. 2012) and at low scale levels dealing with crystals and atoms dimensions (Wang et al. 2011, Liu et al. 2011).

As discussed by Pook (2013) Mode II and Mode III are always combined together. One mode causes the automatic arise of a coupled mode which, in some cases, can be damaging as the generating mode itself. In other words a three-dimensional problem is always at least dual scale and a parameter able to capture the simultaneous presence of different modes is required.

Another important aspect, to be carefully considered, is the influence of the higher order non-singular terms on the stress field near cracks or notches. In some cases

these terms can play an important and non-negligible role (Ayatollahi and Nejati 2011, Sousa et al. 2013, Cheng et al. 2013) also can influence the fracture assessment as well as the crack initiation and propagation angle during failure phenomena. As described in Berto et al. (2011b) the non-singular terms can also generate coupled mode that in some cases can be more dangerous than the generating modes themselves. Again a based on energy parameter is sensitive to all these complex effects occurring in-plane but also out-of-plane, through the plate thickness.

3.4 Conclusions

The main aim of the present chapter is to discuss the existence of the Mode O in components weakened by blunt notches of different shape under an externally applied pure in-plane shear loading. Blunt V-notches as well as circular and elliptic holes have been considered to address this objective. The following conclusions can be drawn by the present analysis:

– It has been shown that the so called Mode O is always coupled with the generating Mode II loading and this is true independent of the notch shape.

– The intensity of the Mode O is strongly linked to the Poisson's ratio and the coupled mode disappears when the limit case $\nu=0$ is reached.

– The main geometrical parameters of the notch and the component, in particular the notch root radius and the plate thickness, play a fundamental role and strongly influence the intensity of the out-of-plane effects.

Finally one can conclude saying that it is not easy to give a simple rule of thumb to say a priori if three-dimensional effects are negligible or not in a given geometry. On the other hand it seems clear that before simplifying the problem by means of a 2D model this possibility has to be verified and checked carefully also depending on the degree of accuracy required by the analysis. In some cases, in fact, not negligible differences may exist between 2D and 3D models. This does not mean to completely abandon 2D analyses. In many cases they provide acceptable and reasonable engineering results. The main message that the present chapter would like to transmit is that the simplification of a 3D problem into a 2D

one is not so trivial and requires some careful considerations otherwise some important effects could be neglected a priori.

Another important key-point to be underlined is that always a real problem is at least dual-scale because generating and induced modes are combined together giving origin to a complex state of stresses and strains through the plate thickness.

4

SED criterion on three-dimensional plates weakened by free clamped V-notches

4.1 Introduction

Dealing with fracture assessment of cracked and notched components a clear distinction should be done between large and small bodies (Tang and Sih 2005, Sih and Tang 2005a). The design rules applied to large bodies are based on the idea that local inhomogeneities, where material damage starts, can be averaged being large the volume to surface ratio. The concept of "elementary" volume and "structural support length" was introduced many years ago by Neuber (1958). It states that not the theoretical maximum notch stress is the static or fatigue strength-effective parameter in the case of pointed or sharp notches, but rather the notch stress averaged over a short distance normal to the notch edge.

In small bodies the low ratio between volume and surface makes strong any local discontinuities present in the material and the adoption of a multiscaling and segmentation scheme is the only way to capture what happens at pico, nano and micro levels (Sih 2007- 2009a- 2009b- 2010). In this scheme the crack tip has no dimension or mass to speak; it is the sink and source that absorbs and dissipates energy while the stress singularity representation at every level is the most powerful tool to quantify the energy packed by an equivalent crack reflecting both material effect and boundary conditions. This new representation implies also a new definition of mass (Sih 2010). The distinction between large and small bodies should ever be considered by avoiding to transfer directly the design rules valid for large components to small ones under the hypothesis that all material inhomogeneities can be averaged (Tang and Sih 2005, Sih and Tang 2005a).

Other approaches considered the multiscale problems by the investigation of the non linear effects occurring at different scale levels (Panin V. et al. 2007- 2008, Panin S. et al. 2010).

Since Beltrami to nowadays, the strain energy density (SED) has been found being a powerful tool to assess the static and fatigue behavior of unnotched and notched components in structural engineering. The strain energy density factor *S* was defined by Sih as the product of the strain energy density by a critical distance from the point of singularity (Sih 1974). Failure was thought of as controlled by a critical value S_c, whereas the direction of crack propagation was determined by imposing a minimum condition on *S*. The theory was extended to employ the total strain energy density near the notch tip (Sih and Ho 1991), and the point of reference was chosen to be the location on the surface of the notch where the maximum tangential stress occurs. The material element was always kept at a finite distance from the crack or the notch tip, outside the "core region" where the inhomogeneity of the material due to micro-cracks, dislocations and grain boundaries precludes an accurate analytical solution. The criterion based on the factor *S* gave a sound theoretical basis to Gillemot's experimental findings (Gillemot 1965, Gillemot et al. 1985) based on the absorbed specific energy.

A volume-based Strain Energy Density approach has been applied to static and fatigue strength assessments of notched and welded structures (Lazzarin and Zambardi 2001, Lazzarin and Berto 2005a-2008, Berto and Lazzarin 2009, Lazzarin et al. 2009a-2009b, Radaj et al. 2009a, Gomez et al. 2009a). The control volume radius, which depends on material and loading conditions, was found to vary between about 10^{-2} mm (brittle material under static loading conditions) to about 0.3 mm (steel welded joints under high cycle fatigue) or more.

Recently, as stated above, the volume energy function has been scaled from macro to micro to take into account the micro-cracks with a stronger stress singularity (Tang and Sih 2005, Sih and Tang 2005a). Positive definiteness of energy density can be a guide for precluding physical contradictions that are hidden at different scales of the material (Sih and Tang 2005a). As widely described in (Sih 2007) a mixed condition would be more realistic to represent a micro crack behaviour due to the fact that the micro-crack surfaces are partly closed and partly open. The

macro-crack has a stress singularity of the order $r^{-1/2}$ while near the micro-crack a stress singularity of the order $r^{-3/4}$ is not unrealistic because the crack surfaces may be irregular and jag-shaped. The apex of the micro-crack can be represented by a V-notch under free-clamped boundary conditions (Tang and Sih 2005, Sih and Tang 2005a, Neuber 1958, Sih 2007).

Dealing with elastic stress singularities and corresponding generalized stress intensity factors for corners under various boundary conditions, Seweryn and Molski (1996) summarizes the analytical description of the stress and displacement fields around a sharp angular corner subjected to various loading and displacement boundary conditions in plane problems of elasticity. The clamped-free conditions have been shown to correspond to a rigid punch with a strong friction applied to one face of an elastic corner or to a rigid inclusion connected with one side to elastic medium subjected to any load, while the second face of the medium remains free from traction.

An interesting three-dimensional effect was described in the case of a cracked plate subjected to shear loading by Nakamura and Parks (1989) who first found a new singular behaviour for the transverse shear stress components in thin plates subjected to in-plane loading. This effect has also been studied for through-the-thickness cracks in finite thickness plates utilising analytical and numerical methods (Jin and Batra 1997, Pook 2000a, Huang 2004, Kotousov 2007). In particular, Kotousov (2007) formalised this three-dimensional singular effect for sharp notches with arbitrary notch opening angles based on the first order plate theory. This singular mode, which was called '*the out-of-plane mode'*, or *'Mode O*', was found to be coupled with the classical antisymmetric stress distribution (Mode II). Kotousov also demonstrated that the out-of-plane mode is provoked by the three-dimensional effects which increase as the Poisson's ratio of the material increases. Important features of this recently identified singular mode, the out-of-plane singular mode, conduct a comprehensive three-dimensional numerical study of V-notched plates and welded lap joint-like geometries (Berto et al. 2011a, Kotousov et al. 2010, Harding et al. 2010). In Berto et al. (2011a) the intensity of the Mode O stress distributions has been discussed as a function of the opening angle and plate size, paying particular attention to the scale effect due to this

singular mode, which is characterised by a degree of singularity matching that due to Mode III. It is clear from those analyses that the intensity of Mode O increases as the model size increases. This means that there exists the geometrical proportional factor at which the contribution into the failure initiation of the out-of-plane shear stresses will be always greater than the contribution from the generating in-plane shear stresses.

The influence on Mode O of non-singular terms in cracked plates is investigated in (Berto et al. 2011b-2011d).

Dealing with a three-dimensional plate weakened by a sharp notch under free-clamped boundary conditions the mixed mode is automatically generated by the edge constraints as explained in Tang and Sih (2005), Seweryn and Molski (1996). The presence of mode II should generate a singular Mode O which has been neglected in all previous papers.

The aim of the chapter is to investigate the contribution and the intensity of this mode into the overall three dimensional stress states in the close vicinity of the notch tip. Since the out-of-plane mode is not a point-wise effect but rather a volume-based effect, it is shown how the strain density over a control volume is sensitive to all the three-dimensional effects occurring through the plate thickness and a parameter suitable for identifying the most critical zone. The results summarised in the chapter are general and can be directly shifted to the mesomechanical approach proposed in Tang and Sih (2005), Sih and Tang (2005a) which models the micro-crack tip as a fixed-free sharp V-notch as well as to the cases discussed in Seweryn and Molski (1996) dealing with in-plane solution and extended to the three-dimensional models.

4.2 Analytical background

The Fadle eigen-function expansion method was first used in the1930s to find the eigen-values for a pointed notch with different boundary conditions along the notch edges (Fadle 1941). However the modern literature usually refers mostly to Williams (1952), Coker and Fillon (1931) in two dimensions and to Hartranft and Sih (1969-1973) in three dimensions. The results in Fadle (1941) are for the plane stress case whereas the plane strain case has been solved in Tang and Sih (2005).

The biharmonic stress function $\chi(r,\theta)$ and the harmonic function $\psi_1(r,\theta)$ can be expressed in the following form:

$$\chi[r,\theta] = r^{\lambda+1}F[\theta]$$

$$\psi_1[r,\theta] = r^{\lambda-1}G[\theta] \tag{4.2.1}$$

where $F(\theta)$ and $G(\theta)$ are as follows:

$$G[\theta] = \left(\frac{4}{\lambda-1}B\sin[(\lambda-1)\theta] - \frac{4}{\lambda-1}D\cos[(\lambda-1)\theta]\right)$$

$$F[\theta] = (A\cos[(\lambda+1)\theta] + B\cos[(\lambda-1)\theta] + C\sin[(\lambda+1)\theta] + D\sin[(\lambda-1)\theta]) \tag{4.2.2}$$

The displacement in radial and circumferential direction, u_r and u_θ, respectively, may be written in terms of $\chi(r,\theta)$ and $\psi_1(r,\theta)$ under plane stress (Fadle 1941, Williams 1952) or plane strain conditions (Tang and Sih 2005):

$$2\mu u_r = -\partial_r\chi + (1-\sigma)r\partial_\theta\psi_1$$

$$2\mu u_\theta = -\frac{1}{r}\partial_\theta\chi + (1-\sigma)r^2\partial_r\psi_1 \tag{4.2.3}$$

where μ is the shear modulus $\mu=E/(2(1+\nu))$ and $\sigma=\nu/(1+\nu)$ under plane stress conditions and ν (Poisson's ratio) under plane strain. The displacement field can be expressed also by the following equations:

$$u_r = \frac{r^\lambda}{2\mu}(-(\lambda+1)F[\theta] + (1-\nu)\partial_\theta G[\theta])$$

$$u_\theta = \frac{r^\lambda}{2\mu}(-\partial_\theta F[\theta] + (1-\nu)(\lambda-1)G[\theta]) \tag{4.2.4}$$

The stresses are given as:

$$\sigma_r = \frac{1}{r^2}\partial_\theta^2\chi + \frac{1}{r}\partial_r\chi$$
$$\sigma_\theta = \partial_r^2\chi \qquad (4.2.5)$$
$$\sigma_{r\theta} = -\frac{1}{r}\partial_\theta\partial_r\chi + \frac{1}{r^2}\partial_\theta\chi$$

or, alternatively, as:

$$\sigma_r[r,\theta] = r^{\lambda-1}(\partial_\theta(\partial_\theta F[\theta]) + (\lambda+1)F[\theta])$$
$$\sigma_\theta[r,\theta] = r^{\lambda-1}(\lambda+1)\lambda F[\theta] \qquad (4.2.6)$$
$$\sigma_{r\theta}[r,\theta] = r^{\lambda-1}(-\lambda\partial_\theta F[\theta])$$

The stress components can be explicitly expressed in terms of the unknown parameters:

$$\sigma_r = r^{\lambda-1}\lambda(-B(-3+\lambda)\cos[(\lambda-1)\theta] - (1+\lambda)(A\cos[(1+\lambda)\theta] + C\sin[(1+\lambda)\theta]) + D(-3+\lambda)\sin[(1-\lambda)\theta]$$
$$\sigma_\theta = r^{\lambda-1}\lambda(1+\lambda)(B\cos[(-1+\lambda)\theta] + A\cos[(1+\lambda)\theta] + D\sin[(-1+\lambda)\theta] + C\sin[(1+\lambda)\theta]$$
$$\sigma_{r\theta} = r^{\lambda-1}\lambda(C(1+\lambda)\cos[(1+\lambda)\theta] - A(1+\lambda)\sin[(1+\lambda)\theta] + (\lambda-1)(D\cos[(-1+\lambda)\theta] + B\sin[(1-\lambda)]\theta))$$

(4.2.7)

The same can be done for the radial and circumferential displacements under plane strain conditions:

$$u_r = \frac{1}{2\mu}r^\lambda(-A(1+\lambda)\cos[\theta(1+\lambda)] - (-3+\lambda+4\nu)(B\cos[\theta(-1+\lambda)] + D\sin[\theta(-1+\lambda)]) - C(1+\lambda)\sin[\theta(1-\lambda)])$$

(4.2.8)

$$u_\theta = -\frac{1}{2\mu}r^\lambda(D(3+\lambda-4\nu)\cos[\theta(-1+\lambda)] + C(1+\lambda)\cos[\theta(1+\lambda)] + 4B\nu\sin[\theta(-1+\lambda)]) - A(1+\lambda)\sin[\theta(1+\lambda)] + B(3+\lambda)\sin[\theta(1-\lambda)]$$

The free-fixed condition where the top edge is traction-free while the bottom edge is fixed from displacing can be expressed in the form:

$$\sigma_\theta = \sigma_{r\theta} = 0, \text{ for } \theta = \beta^* \qquad u_r = u_\theta = 0, \text{ for } \theta = -\beta^* \tag{4.2.9}$$

Dealing with the free-fixed case and by calling κ the eigenvalue of this particular case, as made in Ref [1], the eigen-equation becomes:

$$\begin{bmatrix} \cos[(\kappa+1)\beta^*] & \cos[(\kappa-1)\beta^*] & \sin[(\kappa+1)\beta^*] & \sin[(\kappa-1)\beta^*] \\ (\kappa+1)\sin[(\kappa+1)\beta^*] & (\kappa-1)\sin[(\kappa-1)\beta^*] & -(\kappa+1)\cos[(\kappa+1)\beta^*] & -(\kappa-1)\cos[(\kappa-1)\beta^* \\ -(\kappa+1)\cos[(\kappa+1)\beta^*] & -(-3+\kappa+4\nu)\cos[(\kappa-1)\beta^* & (\kappa+1)\sin[(\kappa+1)\beta^*] & -(-3+\kappa+4\nu)\sin[(-\kappa+1)\beta^* \\ (\kappa+1)\sin[(\kappa+1)\beta^*] & (3+\kappa-4\nu)\sin[(\kappa-1)\beta^* & (\kappa+1)\cos[(\kappa+1)\beta^*] & (3+\kappa-4\nu)\cos[(\kappa-1)\beta^* \end{bmatrix} \begin{pmatrix} A \\ B \\ C \\ D \end{pmatrix} \tag{4.2.10}$$

The non-trivial solution of Eq.(4.2.10) requires that the determinant of coefficients must vanish. This leads to the equation:

$$2(1+\kappa)[-5+\kappa^2+4(3-2\nu)\nu-\kappa^2\cos(4\beta^*)+(4\nu-3)\cos(4\beta^*\kappa)]=0 \tag{4.2.11}$$

By neglecting the solution κ= −1 which would generate infinite displacements at the notch tip, the eigen-equation can be written as a function of the Poisson's ratio:

$$-5+\kappa^2+4(3-2\nu)\nu-\kappa^2\cos(4\beta^*)+(4\nu-3)\cos(4\beta^*\lambda)=0 \tag{4.2.12}$$

One should note that Eq. (4.2.12) gives the same eigenvalues of the equation

$$4(1-\nu)^2-\kappa^2\sin^2(2\beta^*)-(3-4\nu)\sin^2(2\kappa\beta^*)=0 \tag{4.2.13}$$

already reported in Tang and Sih (2005).

The link between the unknown parameters can be expressed by taking advantage of three auxiliary parameters e_1, e_2 and e_3, where:

$$e_1(\beta^*,\nu) = \\ = \frac{B}{A} = \frac{(1+\kappa)((-3+\kappa+4\nu)\sin[\beta^*(-1+\kappa)]-\kappa\sin[\beta^*(3+\kappa)]+\sin[\beta^*(1+3\kappa)])}{(-1+\kappa^2)\sin[\beta^*(1+\kappa)]+(-3+\kappa+4\nu)(-\kappa\sin[\beta^*(-3+\kappa)]+\sin[\beta^*(1-3\kappa)])}$$

$$e_2(\beta^*,\nu) = \\ = \frac{C}{A} = \frac{(-1+\kappa^2)\cos[\beta^*(1+\kappa)]+(-3+\kappa+4\nu)(-\kappa\cos[\beta^*(-3+\kappa)]+\cos[\beta^*(1-3\kappa)])}{(-1+\kappa^2)\sin[\beta^*(1+\kappa)]+(-3+\kappa+4\nu)(-\lambda\sin[\beta^*(-3+\kappa)]+\sin[\beta^*(1-3\kappa)])}$$

$$e_3(\beta^*,\nu) = \\ = \frac{D}{A} = \frac{(1+\kappa)(-(-3+\kappa+4\nu)\cos[\beta^*(-1+\kappa)]+\kappa\cos[\beta^*(3+\kappa)]+\cos[\beta^*(1+3\kappa)])}{(-1+\kappa^2)\sin[\beta^*(1+\kappa)]+(-3+\kappa+4\nu)(-\kappa\sin[\beta^*(-3+\kappa)]+\sin[\beta^*(1-3\kappa)])} \tag{4.2.14}$$

The factor $K_{I/II}$ can be defined in terms of A as:

$$K_{I/II} = \sqrt{2\pi}A$$

The corresponding displacements are:

$$2\mu u_r = \frac{K_{I/II}}{\sqrt{2\pi}} r^{\kappa}[-(\kappa+1)\cos(\kappa+1)\theta - e_1(\beta^*,\nu)((\kappa+1)-4(1-\nu))\cos(\kappa-1)\theta \\ -(\kappa+1)e_2(\beta^*,\nu)\sin(\kappa+1)\theta - e_3(\beta^*,\nu)[(\kappa+1)-4(1-\nu)]\sin(\kappa-1)\theta]$$

$$2\mu u_\theta = \frac{K_{I/II}}{\sqrt{2\pi}} r^{\kappa}[(\kappa+1)\sin(\kappa+1)\theta + e_1(\beta^*,\nu)[(\kappa-1)+4(1-\nu)\sin(\kappa-1)\theta \\ -(\kappa+1)e_2(\beta^*,\nu)\cos(\kappa+1)\theta - e_3(\beta^*,\nu)[(\kappa-1)+4(1-\nu)]\cos(\kappa-1)\theta] \tag{4.2.15}$$

In parallel, the stresses are:

$$\sigma_r = \frac{K_{I/II}}{r^{1-\kappa}\sqrt{2\pi}} \kappa[-(\kappa+1)\cos(\kappa+1)\theta + (3-\kappa)e_1(\beta^*,\nu)\cos(\kappa-1)\theta \\ -(k^*+1)e_2(\beta^*,\nu)\sin(k^*+1)\theta + (3-k^*)e_3(\beta^*,\nu)\sin(k^*-1)\theta]$$

$$\sigma_\theta = \frac{K_{I/II}}{r^{1-\kappa}\sqrt{2\pi}}\kappa(\kappa+1)[\cos(\kappa+1)\theta + e_1(\beta^*,\nu)\cos(\kappa-1)\theta + e_2(\beta^*,\nu)\sin(\kappa+1)\theta + e_3(\beta^*,\nu)\sin(\kappa-1)\theta)]$$

$$\sigma_{r\theta} = \frac{K_{I/II}}{r^{1-\kappa}\sqrt{2\pi}}\kappa[(\kappa+1)\sin(\kappa+1)\theta + (\kappa-1)e_1(\beta^*,\nu)\sin(\kappa-1)\theta - (\kappa+1)e_2(\beta^*,\nu)\cos(\kappa+1)\theta - (\kappa-1)e_3(\beta^*,\nu)\cos(\kappa-1)\theta] \quad (4.2.16)$$

Under plane strain conditions, the strain energy density (SED) evaluated over a control volume of radius R_0 is as follows:

$$\overline{W} = \frac{\kappa K_{I/II}^2 R_0^{2(\kappa-1)}}{2\pi E\beta^*(\kappa-1)}\{(1-\nu-2\nu^2)(e_1^2-e_3^2)\mathrm{Sin}[2\beta^*(\kappa-1)] + (\kappa-1)(1+\nu)[(\kappa^2-1)e_1\mathrm{Sin}[2\beta^*] + \beta^*(3-(\kappa-2)\kappa-4\nu)e_1^2 + \beta^*(1+\kappa)^2(1+e_2^2) + (\kappa^2-1)e_2e_3\mathrm{Sin}[2\beta^*] + \beta^*(3+(\kappa-2)\kappa-4\nu)e_3^2]\} \quad (4.2.17)$$

The analytical frame described above allows us to consider the stress field at different scale levels as linear elastic. The singularity depends on the considered scale level, from macro to micro.

Alternative to the linear elastic multiscale models, other models consider the non linear effects occurring at different scale levels abandoning the field of the linear elasticity. A multilevel approach based on the physical mesomechanics of the material has been systematically used in Panin V. et al. (2007) dealing with thin films (Panin V. et al. 2007). Nonlinear effects in surface layers under severe plastic deformation have been investigated experimentally in Panin V. et al. (2008). This issue is crucial for a number of applications (nanomaterials and nanotechnology, multilayer materials for electronics, deposition of nanostructured protective and hardening coatings, catalysis and functional role of interfaces in biological objects). Experimental techniques mainly based on acoustic emission

have been used to monitor the multiscale of localized plastic strain evolution stages in notched aluminum AA 2024 alloy tension specimens (Panin S. et al. 2010). Digital Image Correlation (DIC) method for strain estimation and acoustic emission (AE) have been also used for investigating strain and fracture patterns at various scale levels.

4.3Geometry and boundary conditions

The study considers an arbitrary semi-infinite plate of finite thickness 2*h* containing a V-notch subjected to a remote loading. In the finite element models, a denser nodal arrangement is created in the proximity of the crack notch tip where the mesh is very fine. All analyses are carried out using the ANSYS 11 code.

The mesh consists of an initial arrangement of 15-node trapezoidal elements at the notch tip, surrounded by a radial array of 20-node brick elements, where each element spans an angular sweep of 11.25°. The considered geometry is shown in Figure 4.3.1.

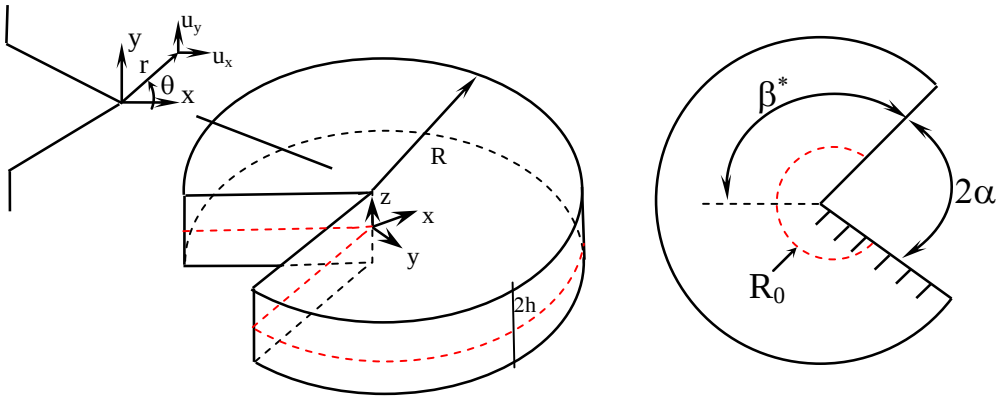

Figure 4.3.1. Geometry and coordinate system having the origin on the notch tip in the mid- plane of the plate.

In two-dimensional models the eight nodes iso-parametric element plane 82 is used under the plane strain hypothesis.

To simulate the remotely applied constraint conditions corresponding to the free-clamped boundary conditions, the displacements are applied to the nodes

belonging to the outer cylindrical surfaces of the finite element models. The displacements exactly correspond to those of a far-field two-dimensional plane strain distribution given by the solution in Tang and Sih (2005) (Eqs. (4.2.15)).

In the beginning, in order to validate the developed finite element models and compare the results with previous findings, four opening angles are considered in two-dimensional models, 2α= 45°, 60°, 90° and 135°, all referred to a constant value of the radius (R=100 mm) and to plane strain hypothesis.

In all these cases the notch stress intensity factor $K_{I/II}$ has been set equal to 1000 MPa·mm$^{1-\kappa^*}$, whereas the eigenvalue κ^* and the functions e_1, e_2 and e_3 have been updated as a function of the notch opening angle according to Eqs (4.2.11-4.2.13) and Eq. (4.2.14), respectively (see Table 4.3.1). The Poisson's ratio has been kept constant and equal to 0.49.

In the three-dimensional models the same notch opening angles and the same radius R have been considered. The thickness is 2h=50 mm.

Table 4.3.1. Eigenvalues κ and functions e_1 e_2 and e_3 in terms of notch opening

2α (°)	κ	$1-\kappa$	e_1	e_2	e_3	κ_O
45	0.253	0.747	1.5566	-1	-1.5566	0.2857
60	0.257	0.743	1.4854	-1	-1.4854	0.3000
90	0.2744	0.7256	1.3252	-1	-1.3252	0.3333
135	0.3384	0.6616	1.1059	-1	-1.1059	0.4000

4.4Results and discussions

4.4.1 Results from 2D numerical analyses

Two-dimensional models were carried out by imposing the displacements which exactly correspond to those of a far-field two-dimensional plane strain distribution given in Tang and Sih (2005). For sake of brevity only the results from models with 2α=45° and 135° are summarised below without loosing any significant information.

These preliminary analyses have been carried out to set up the model and to verify how the boundary conditions affect the two-dimensional stress field.

Figure 4.4.1 shows the stress distributions along the bisector line in a two-dimensional plate weakened by a V-notch with an opening angle $2\alpha = 45°$. Eqs (4.2.15) have been used for calculating the displacements to be applied to the contour nodes of the model.

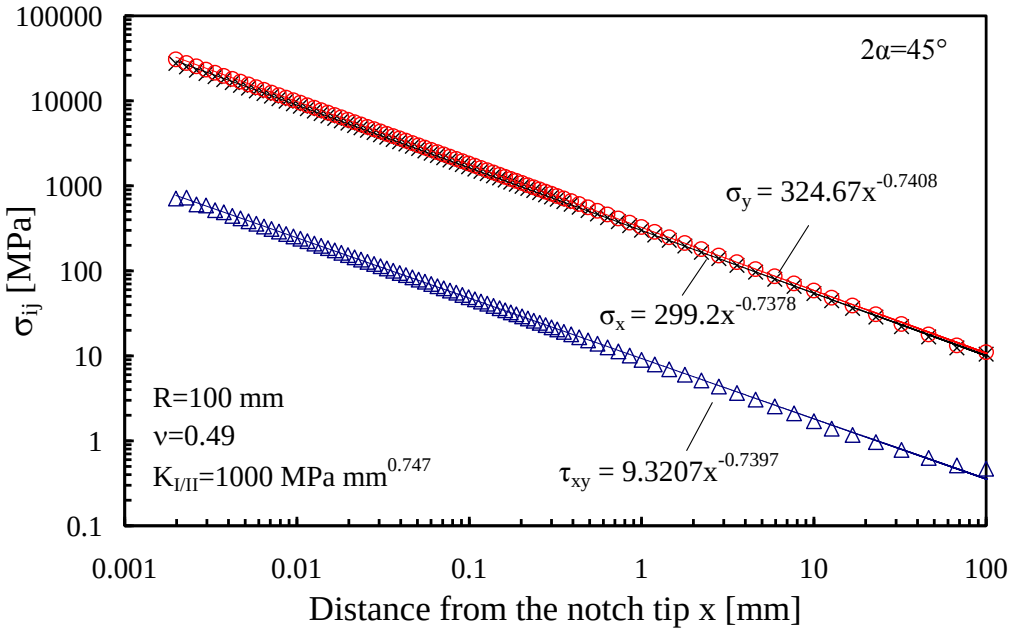

Figure 4.4.1. Stress distributions in the two-dimensional plate with an opening angle $2\alpha = 45°$. The applied stress intensity factor is equal to 1000 MPa $mm^{0.747}$; plane strain conditions are considered in the model

As shown in the figure, the applied boundary conditions corresponding to the free-clamped configuration generate not only Mode I but also Mode II in the plate. The stress field is typical of a mixed mode configuration. The degree of singularity of the stress components is $1-\kappa = 0.747$ and exactly matches the value predicted by the solution given in Tang and Sih (2005) for the free-fixed configuration. In the case of $2\alpha = 45°$ the intensity of the generated Mode II remains much lower than that due to Mode I. Along the notch bisector line it has been also possible to determine the factor $K_{I/II}$ by inverting Eq. 4.2.16b. Doing so we have:

$$K_{I/II} = \frac{r^{1-\kappa}\sqrt{2\pi}\sigma_\theta}{\kappa(\kappa+1)[1+e_1(\beta^*,\nu)]} \qquad (4.3.1)$$

where for the specific case κ=0.253 and e_1=1.5566 (see Table 4.3.1).

Figure 4.4.2 confirms that applying Eq. (4.3.1) along the notch bisector line $K_{I/II}$ results to be equal to 1000 MPa $mm^{0.747}$, which matches the value applied when imposing the boundary conditions. The correctness of the applied displacements is then verified.

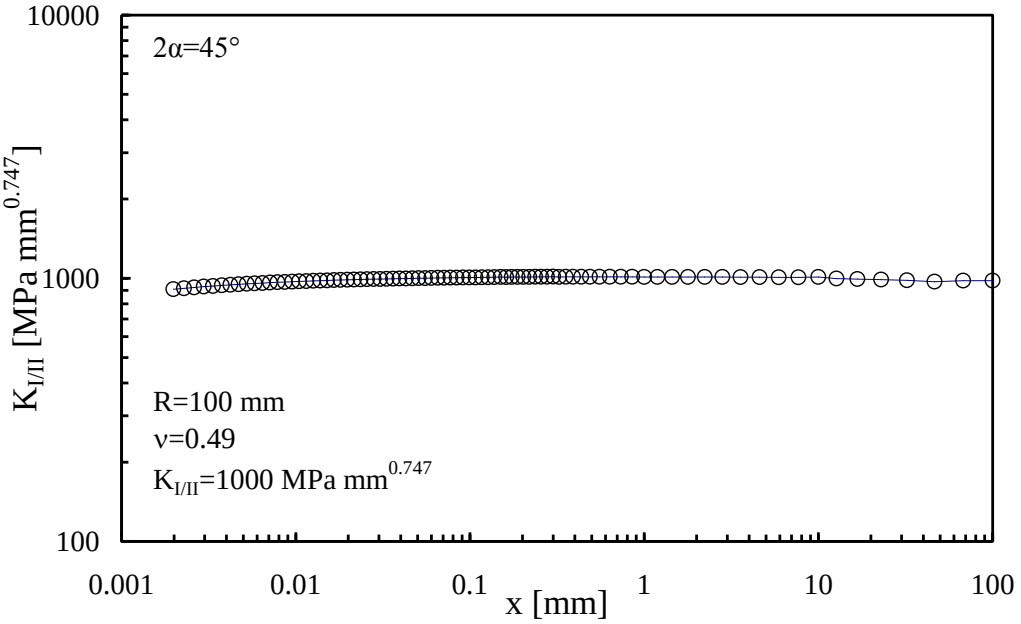

Figure 4.4.2. Plot of $K_{I/II}$ along the crack bisector line, from the notch tip to the outer radius R. Displacements u_x and u_y applied only to the nodes of the lateral surface (R=100 mm).

Figure 4.4.3 shows the stress field corresponding to the opening angle 2α= 135°. Also in this case the degree of singularity matches the theoretical value 1−κ = 0.66 (Tang and Sih 2005). The intensity of the shear stress τ_{xy} corresponding to an applied stress intensity factor $K_{I/II}$=1000 MPa $mm^{0.662}$ is higher than that found in the previous case, 2α=45°. Comparing Figures 4.4.1 and 4.4.3 the main conclusion is that the Mode II stress intensity increases with respect to the Mode I intensity as the notch opening angle increases.

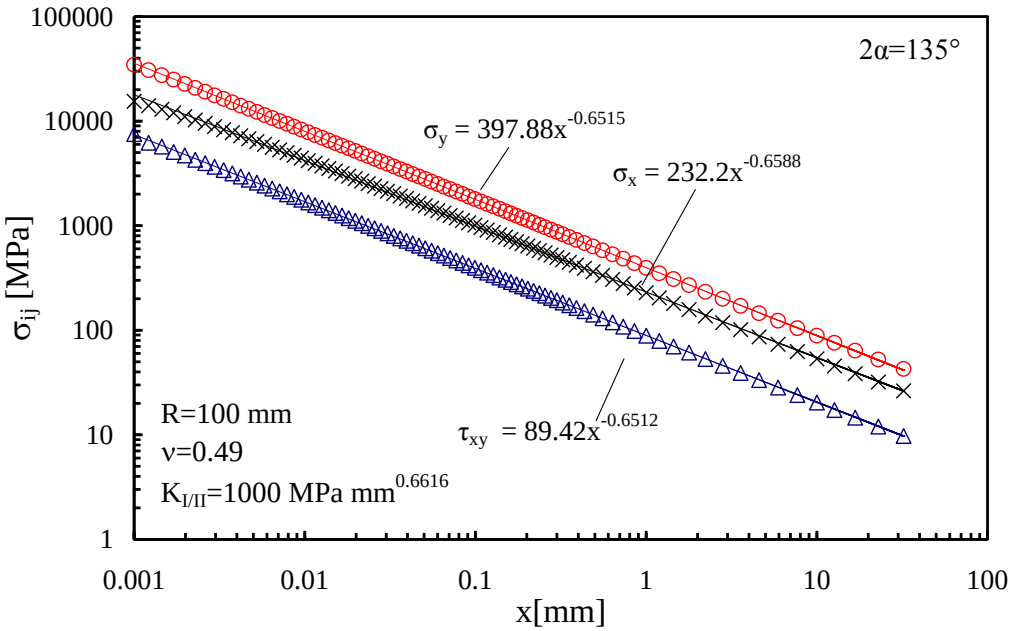

Figure 4.4.3. Stress distributions in the two-dimensional plate with an opening angle $2\alpha = 135°$. The applied stress intensity factor is equal to 1000 MPa $mm^{0.6616}$; plane strain conditions are considered in the model .

Finally, Figure 4.4.4 confirms that also in this case the applied boundary conditions would generate along the notch bisector line the value of $K_{I/II}$ introduced in Eqs (4.2.15).

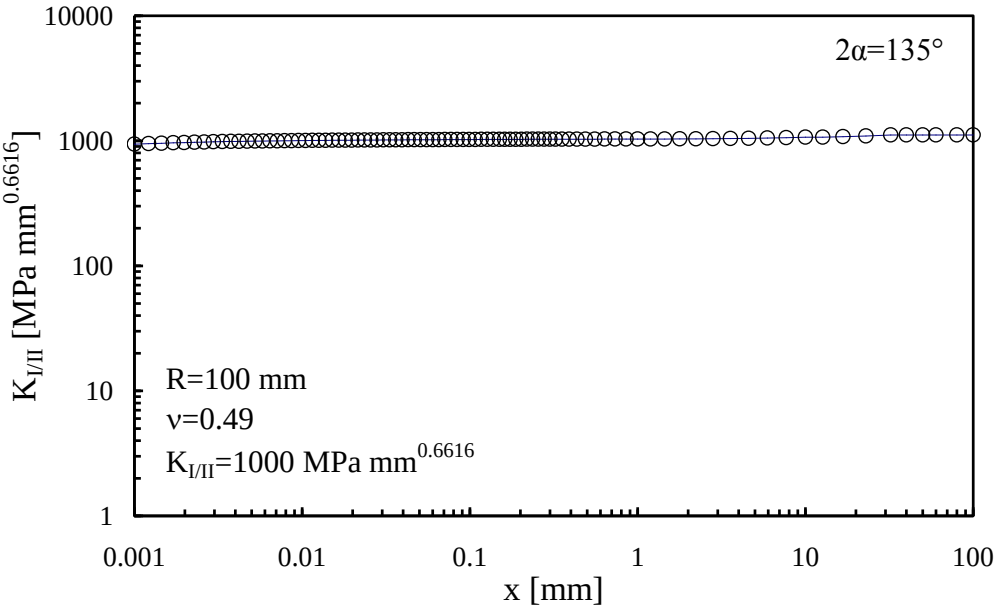

Figure 4.4.4. Plot of $K_{I/II}$ along the crack bisector line, from the notch tip to the outer radius R. Displacements u_x and u_y applied only to the nodes of the lateral surface (R=100 mm).

4.4.2 Results from 3D numerical analyses and proof of Mode O existence

The problem considered here is the three-dimensional finite size plate containing a sharp V-notch, subjected to remote displacements. The V-notch is characterised by a notch opening angle, 2α, and a depth a=R. The plate thickness is again equal to 2h. To observe the variability of the intensity of the singular modes as a function of the notch angle, different finite element models are created, characterised by a varying notch opening angle, $2\alpha = 45^{o}$, 60°, 90^{o} and 135°.

The origin of the Cartesian coordinate system (x,y,z) is located in the middle plane of the plate as shown in Fig. 4.3.1. For a three dimensional sharp notch subjected to in-plane loads it was shown in Nakamura and Parks (1989), Jin and Batra (1997), Pook (2000a), Huang (2004), Kotousov (2007) that a singular mode, which was called '*the out-of-plane mode'*, or *'Mode O*', is coupled with the antisymmetric loading (Mode II).

Similar to the in-plane singular modes, the power of singularity for Mode O does depend on the V-notch opening angle according to the Eq. (4.3.2), valid for the free-fixed configuration (Sih and Tang 2005b):

$$\cos(2\kappa_{O}\beta^{*}) = 0 \tag{4.3.2}$$

The lowest real eigenvalue of Eq. (4.3.2) is:

$$\kappa_{O} = \frac{\pi}{4\beta^{*}} \qquad \vdots \quad \frac{1}{4} \le \beta^{*} \le \frac{1}{2} \tag{4.3.3}$$

(see the last column of Table 4.3.1). The expression $\cos(2\kappa_{O}\beta^{*}) = 0$ corresponds to the out-of-plane singular mode, which results in the same eigenvalues of the Mode III. Therefore, this mode remains singular for notch opening angles ranging from 0^{o} to 180^{o}. However, there are some differences between the out-of-plane mode and the Mode III. The out-of-plane singular mode is not an independent mode but it is coupled with antisymmetric in-plane loading (Mode II). The displacement field associated with this mode is symmetric with respect to the mid-

plane z=0. Moreover its intensity strongly depends on the Poisson's ratio ν, vanishing when ν=0. Conversely, the Mode III is independent of the Poisson's ratio, with an anti-symmetric distribution about the mid-plane.

As it was shown by Pook (2000a) at a corner point the Mode II and the out-of-plane mode cannot exist in isolation. If one of these modes is applied then the other is always induced. In order to describe the shape of cracks' displacements and to explain the link between Mode II and the out-of-plane mode, "*Volterra distorsioni*" in a ring element were used (Pook 2000a). Dealing with the induced mode, Pook underlined that some controversies are still open: it is not clear over how best to characterize stress and displacement fields in the corner point region. He also wrote that '*the crack tip surface displacement behaviour is not yet well understood. As a corner point is approached, there are conflicting theories which have to be resolved on the value of the out-of-plane stress intensity factor. Either it tends to infinity or drops to zero*' (Pook 2000a).

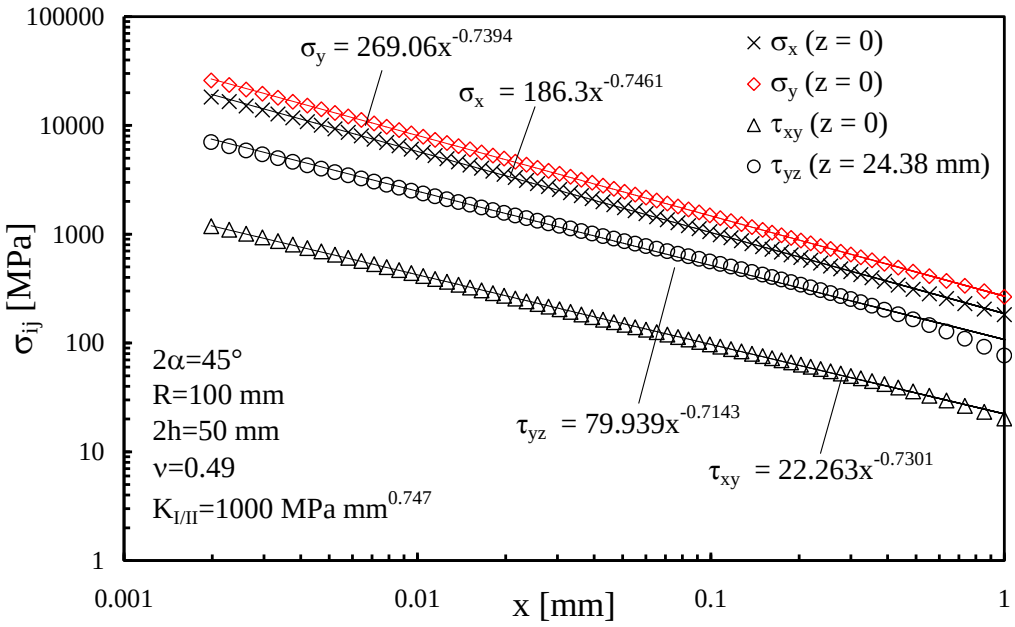

Figure 4.4.5. Three-dimensional stress distributions in a plate with an opening angle 2α= 45°. The applied stress intensity factor is equal to 1000 MPa mm$^{0.747}$

It is clear that the boundary conditions corresponding to the free-clamped constraints along the notch edge provoke a mixed mode state in the plate (I+II+O). The stress component τ_{xy} is plotted in Figure 4.4.5 along the notch

bisector line as a function of the coordinate x from the V-notch tip. The notch opening angle is $2\alpha = 45°$.

This figure shows that also in a three-dimensional model the degree of singularity of the stress components σ_x, $\sigma_{y,}$ τ_{xy} exactly matches the values predicted on the basis of Eqs (4.2.12, 4.2.13) and already verified in the two-dimensional model with the same opening angle. Obviously, the previous two-dimensional studies could not recover the presence of the out-of-plane mode (Mode O). Only the three-dimensional model, as shown in Figure 4.4.5, permits to capture the presence of τ_{yz} along the notch bisector line. This stress component is plotted in the plane at z=24.38 mm where the Mode O reaches its maximum intensity through the plate thickness. The out-of-plane stress component τ_{yz} shows a degree of singularity $1 - \lambda_O = 0.71$, in fully agreement with Eq. (4.3.2). It is also worth noting that the intensity of the generating Mode II is lower than that of the coupled Mode O. Once again, the notch stress intensity factor $K_{I/II}$ has been plotted in the middle plane of the plate to verify that the boundary conditions would correctly been applied to the model (Fig. 4.4.6).

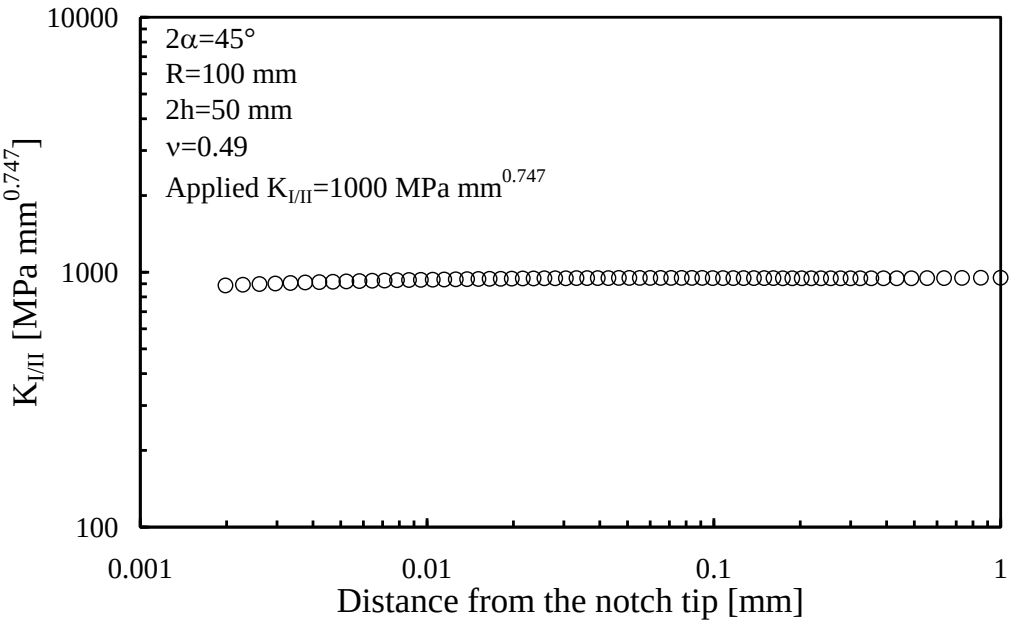

Figure 4.4.6. Plot of $K_{I/II}$ along the crack bisector line in the middle plane of the plate, from the notch tip to the outer radius R. Displacements u_x and u_y applied only to the nodes of the lateral surface (R=100 mm).

The plot of the notch stress intensity factor, K_O is shown in Fig. 4.4.7. This factor is determined on the notch bisector line according to the expression

$$K_O = \sqrt{2\pi} \lim_{x \to 0} \tau_{yz}(x)^{1-\kappa_0} \tag{4.3.4}$$

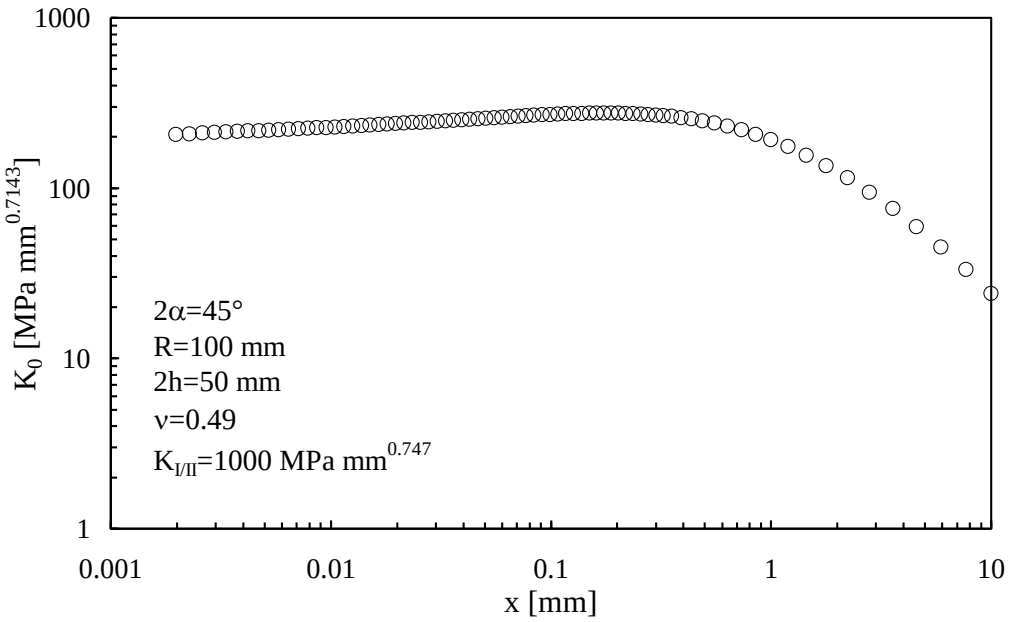

Figure 4.4.7. Mode O stress intensity factor at a distance z = 24.38 mm as a function of the distance x from the notch tip.

K_O represents the natural extension to V-notches of the stress intensity factor for the crack case.

The stress component σ_z, which has been omitted from the figures, respects the plane strain conditions, applied by means of contour nodal displacements, at least near the mid plane of the model. On the other hand it is negligible near the free surfaces where the Mode O reaches its maximum intensity.

Figure 4.4.7 shows the variability of K_O as a function of the distance from notch tip in the plane corresponding to the maximum intensity of the Mode O. K_O presents a significant value until a distance approximately equal to 1 mm.

Figure 4.4.8 shows the trend of K_O through the plate thickness at a constant distance, x=0.3 mm, from the notch tip. The intensity of K_O varies through the thickness of the plate. It has zero value at the mid-plane of the plate where it

changes sign (due to symmetry conditions) and has a maximum in an interior point prior to reaching the outer free surface of the plate where, theoretically, it should drop to zero. Surface stresses, obtained from the finite element analysis, are simple extrapolations since the 3D mesh used is not refined enough to provide shear stresses equal to zero on the free surfaces.

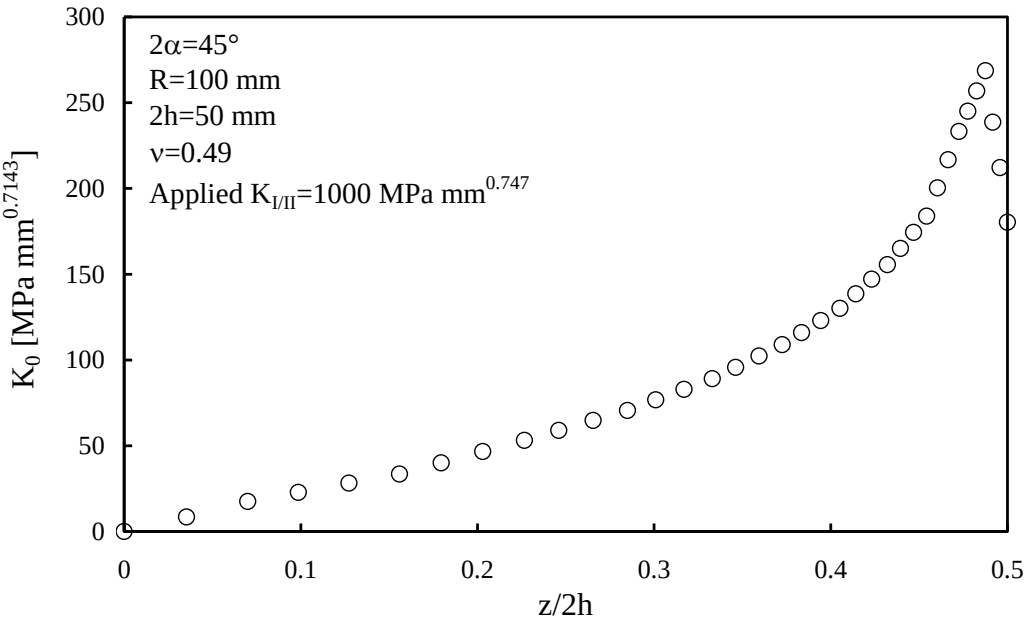

Figure 4.4.8. Mode O SIF through the plate thickness at x=0.3 mm

The stress intensity factor $K_{I/II}$ is plotted in Fig. 4.4.9 along the notch bisector line as a function of the transverse coordinate z for two radial distances from the V-notch tip (r = x = 0.3 mm, and 1,0 mm). This figure shows that there is a large central zone within the plate where $K_{I/II}$ does depend only on the radial distance from the notch tip, r, and not on the vertical position, z-axis. A strong dependence on z-coordinate occurs in the vicinity of the free surface where the decrease of the τ_{xy} stress component is particularly strong. In that limited zone, which has a size in the z direction of about 5% of the total plate thickness, the out-of-plane stress component τ_{yz} reaches its minimum or maximum values.

By increasing the notch opening angle from 45° to 60° the theoretical eigenvalue κ changes from 0.253 to 0.257 whereas the Mode O eigenvalue κ_O for the free fixed configuration changes from 0.2857 to 0.3000. As expected from the theory, an increase of the opening angle 2α, leads to the decrease of the power of the

singular behaviour. Both the in-plane stresses and the out-of-plane stresses remain singular and are characterized by a singularity stronger than that induced by a free-free notch configuration. It is worth noting that also the in-plane shear stress remains singular when opening the notch angle over the value $2\alpha=102°$, contrary to the free-free case.

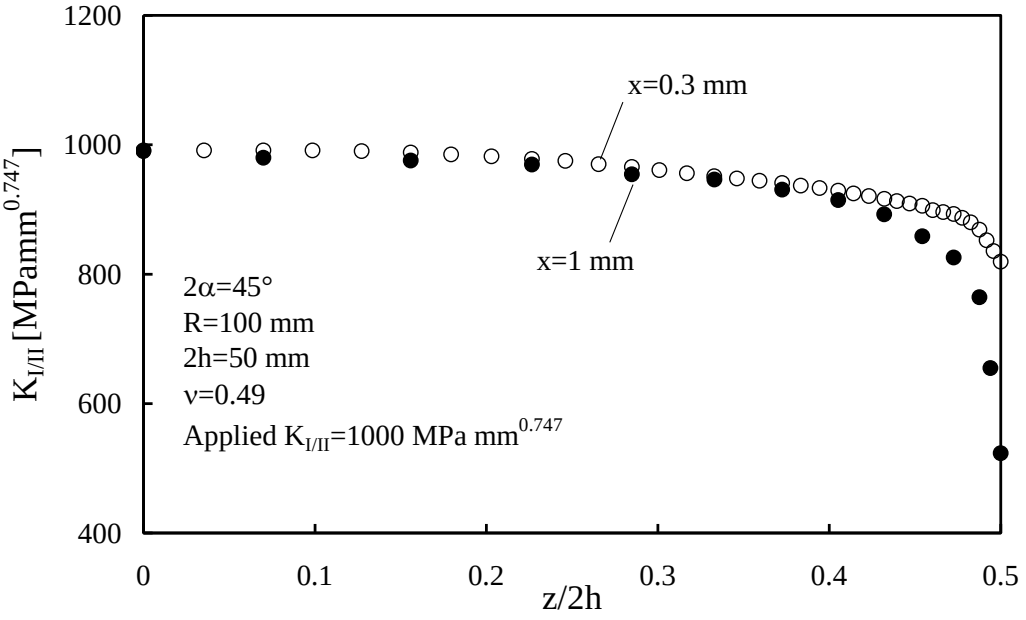

Figure 4.4.9. $K_{I/II}$ through the plate thickness at different distances from the tip

Figure 4.4.10 summarizes the stress field obtained along the notch bisector line for the case of $2\alpha=60°$. The figure is almost coincident to that obtained for $2\alpha=45°$. The plane where the intensity of Mode O reaches its maximum value is at the coordinate z = 24.38 mm, very close to the free-surfaces of the plate. Figure 4.4.11 shows the trend of K_O, evaluated according Eq. (4.3.4), through the plate thickness at a distance x=0.3 mm from the notch tip. Also in this case the intensity of K_O is found to vary through the thickness of the plate. The stress intensity factor $K_{I/II}$ remains constant in a large central zone of the plate whereas a strong dependence on z-coordinate occurs in the vicinity of the free surface where the decrease of the intensity of τ_{xy} stress component is very strong. The figure is omitted for sake of brevity being the behaviour analogous to that just described for the case $2\alpha=45°$. Also for the case $2\alpha=60°$ the notch stress intensity factor $K_{I/II}$

has been plotted in the middle plane of the plate to verify that the applied boundary conditions would correctly apply to the model.

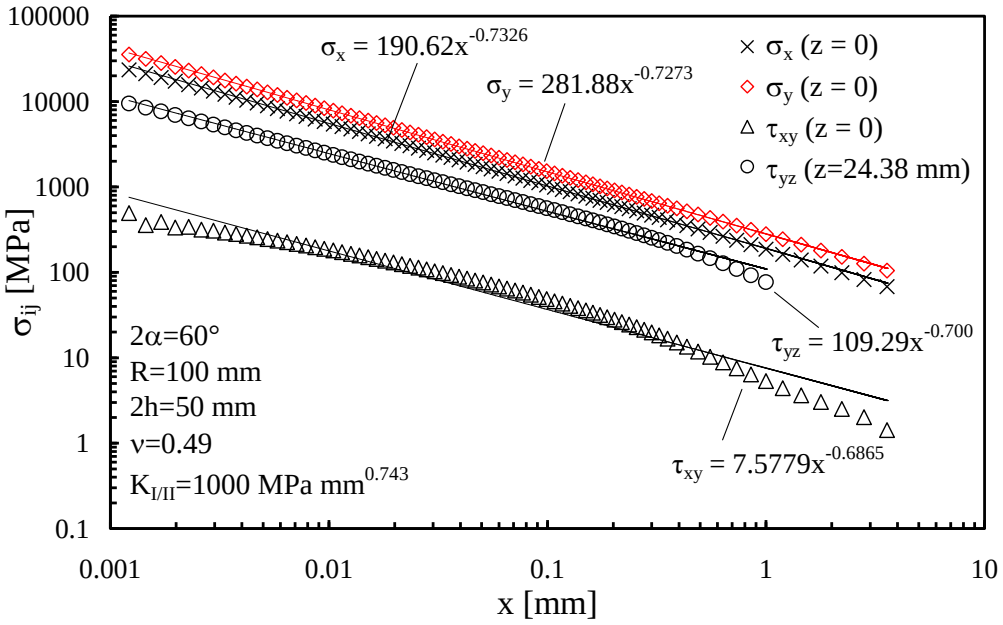

Figure 4.4.10. Three-dimensional stress distributions in a plate with an opening angle 2α= 60°. The applied stress intensity factor is equal to 1000 MPa $mm^{0.743}$

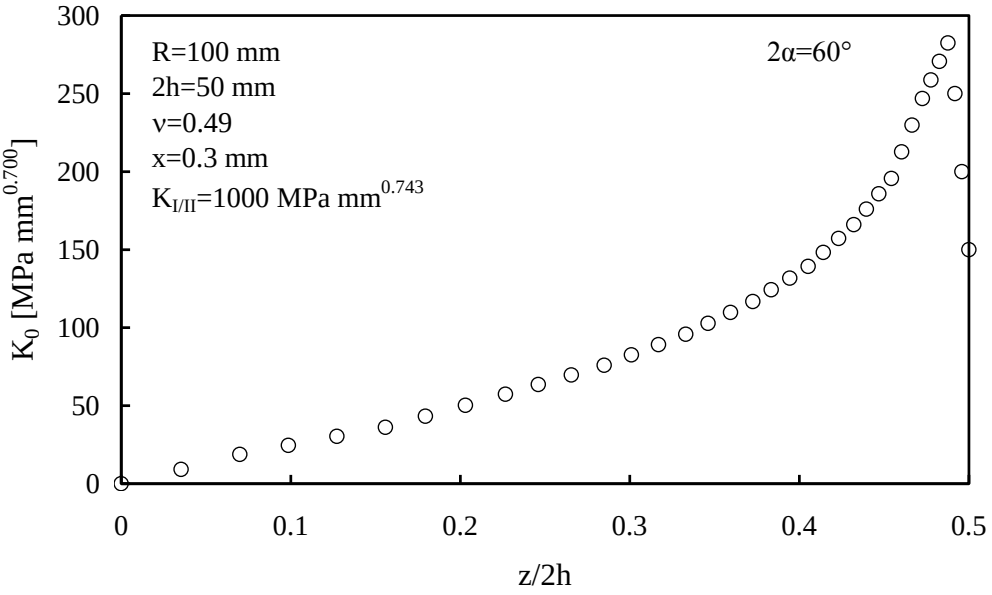

Figure 4.4.11. Mode O SIF through the plate thickness at x=0.3 mm

While the case 2α=90° does not present any novelty with respect to the previous two angles, the case corresponding to a notch opening angle equal to 135°

presents some peculiarities. Figure 4.4.12 plots the in plane stress field along the bisector line and in the middle plane of the plate together with the shear stress component τ_{yz} in the plane of maximum intensity (z=24.38 mm). The intensity of τ_{yz} is in this case comparable to that of the in-plane stress component σ_x and then is stronger with respect to the previous cases.

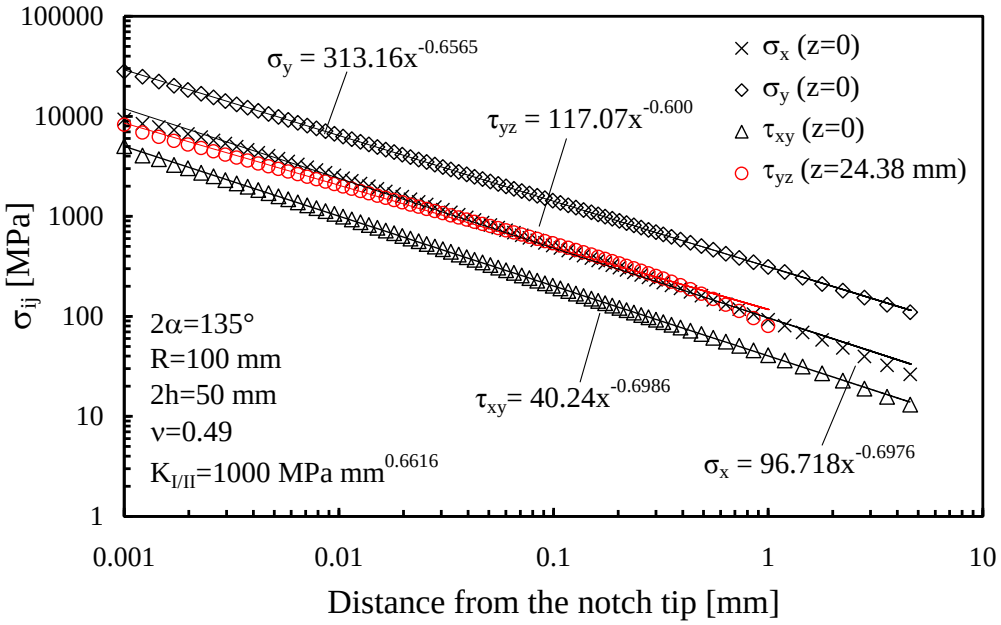

Figure 4.4.12 Three-dimensional stress distributions in a plate with an opening angle $2\alpha = 135°$. The applied stress intensity factor is equal to 1000 MPa $mm^{0.6616}$

In parallel the behaviour of the Mode O through the plate thickness confirms the previous trends, shown in Figure 4.4.13. The main novelty is the variability of the stress intensity factor $K_{I/II}$ which increases its intensity approaching the free surfaces of the plate, contrary to the previously investigated cases (see Figure 4.4.14).

Finally Figure 4.4.15 plots the shear stress component τ_{yz} through the thickness for the different notch angles considered in the present investigation. The stress component τ_{yz} is plotted at a distance x=0.3 mm from the notch tip. It is evident that the notch opening angle does not influence the intensity of the out-of-plane stress contrary to the free-free notch configuration.

The main conclusion of this section is that the existence of the out-of-plane mode has been proofed for a V-notch under a free-fixed configuration.

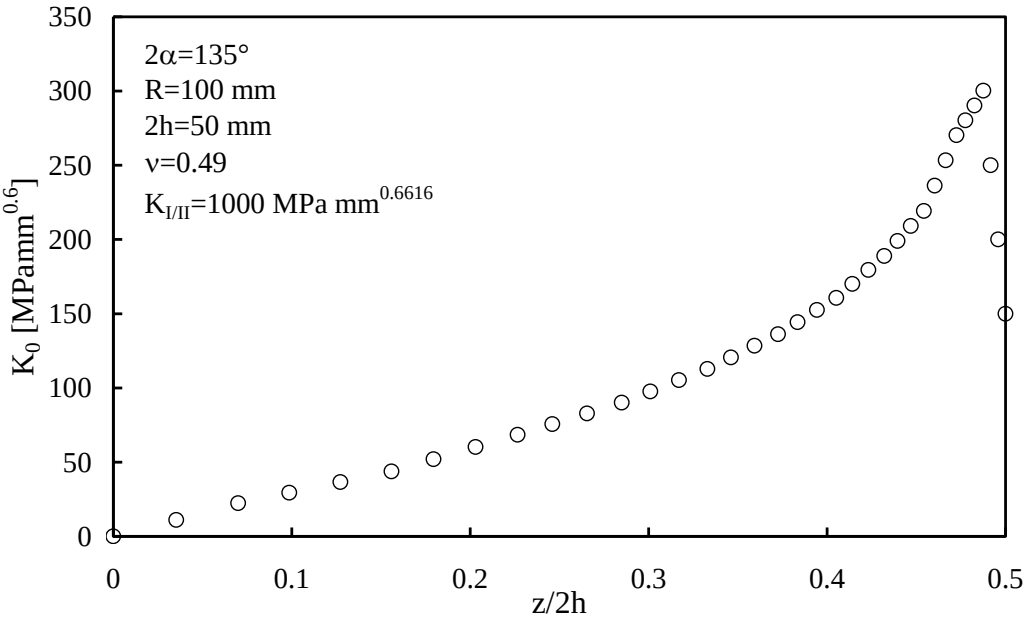

Figure 4.4.13. Mode O SIF through the plate thickness at x=0.3 mm

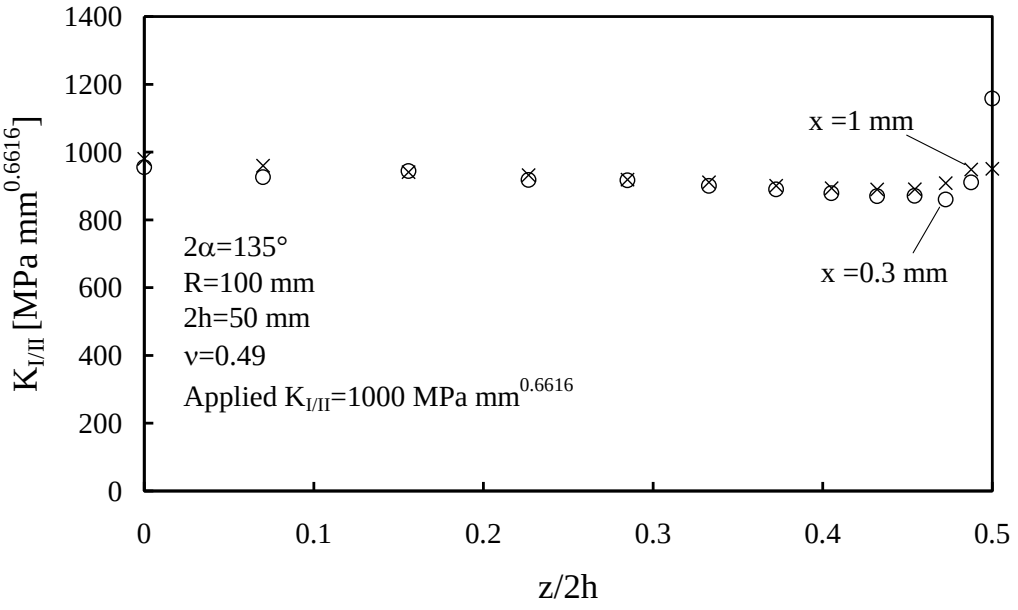

Figure 4.4.14. $K_{I/II}$ through the plate thickness at different distances from the notch tip

By investigating different notch opening angle has been shown that the singularity of the new investigated mode matches that obtained by using the theoretical solution of a free-fixed notch under antiplane loading (Sih and Tang 2005b).

While the stress intensity factor $K_{I/II}$ is equal to the applied value on the mid plane it varies along the plate thickness decreasing near the free surfaces for small opening angle (2α=45, 60 and 90°) and increasing for larger values (2α=135°). It has also shown that, contrary to the expectations, the intensity of the out-of-plane shear stress through the plate thickness is not influenced by the notch opening angle for the same applied value of $K_{I/II}$.

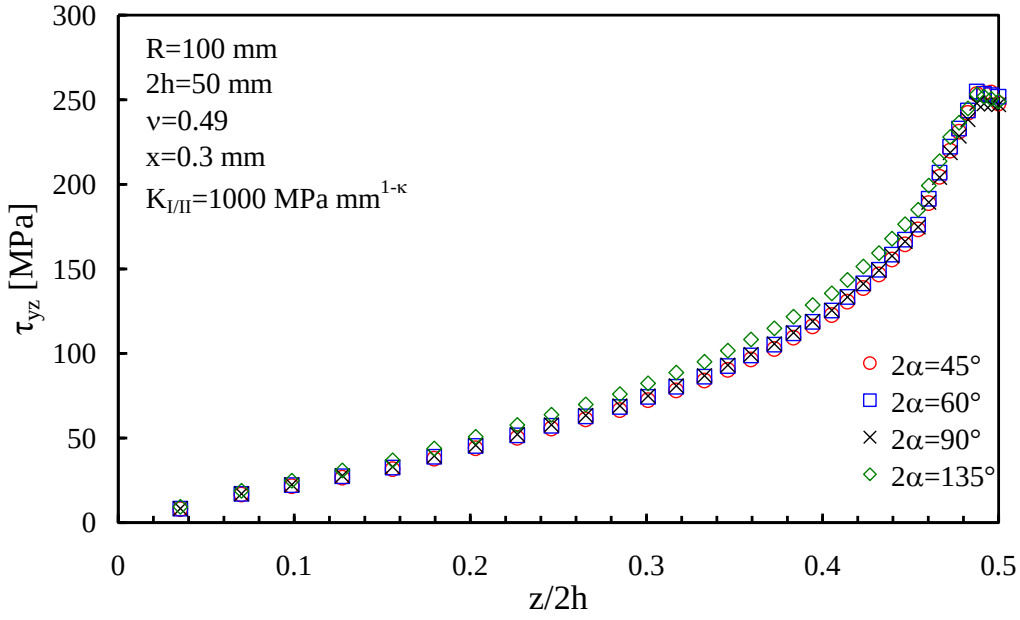

Figure 4.4.15. A comparison of the shear stress τ_{yz} through the thickness for different opening angles from 2α=45° to 135°.

4.5 Strain Energy Density in a control volume surrounding the notch tip

To compare the severity of the singular stress fields some assumptions are necessary to introduce, which should involve a material's characteristic length or the microstructural support length. Recent papers suggest to use as a characteristic of failure initiation the strain energy density averaged over a characteristic control volume (Lazzarin and Zambardi 2001, Lazzarin and Berto 2005a-2008, Berto and Lazzarin 2009-2011, Radaj et al. 2009a, Gomez et al. 2009a, Lazzarin et al. 2008a-2009a-2009b-2010, Berto et al. 2007-2011c, Gomez et al. 2007). This characteristic length varies from material to material and can range from 10^{-6} to 10^{-3} m. However some recent applications (Wang et al. 2011, Liu et al. 2011) have demonstrated that the elastic energy evaluated in a control volume of radius R_0 (as defined in Lazzarin and Zambardi 2001) remains a powerful tool also at lower scale levels. In Wang et al. (2011), taking R_0 as the diameter of Au atoms and *a* as the crack length, the elastic energy has been used to explain the different scenarios observed in propagation of two sub-cracks under similar loading conditions. A bi-crystal model showed that the elastic energy (measured over a volume of radius 0.3 nm) decreased with increasing the notch angle, which implies that cracks with small angles could propagate along the grain boundaries more easily (Liu et al. 2011).

A possible synthesis of the magnitude of the stress state through the plate thickness is carried out here by using the mean value of the strain energy density (SED) over a control volume embracing the notch tip. The control volume can be though of as a cylinder having a radius and a height equal to R_0 (see Figure 4.3.1). Recently the approach based on the SED has been used to summarize a large bulk of experimental data from fatigue failures of seam and spot welded joints and from static tests under Mode I and Mode II loading (Berto and Lazzarin 2009, Berto et al. 2007, Gomez et al. 2007). As discussed in Lazzarin and Berto (2008), Lazzarin et al. (2008a-2008b) the SED can be evaluated directly with a coarse mesh also in complex cases where an analytical formulation is far from easy. One of the most important advantages of the SED approach is that to provide a mean

value which is substantially mesh independent. In fact, contrary to some stress parameters integrated in the local criteria (e.g. maximum principal stress, hydrostatic stress, deviatoric stress), which are mesh-dependent, the SED averaged over a control volume is insensitive to the mesh refinement. As widely documented in Lazzarin and Berto (2008), Lazzarin et al. (2008a-2008b) dealing with sharp V-notches, refined meshes are not necessary, because the mean value of the SED on the control volume can be directly determined *via* the nodal displacements, without involving their derivatives. As soon as the average SED is known, the notch stress intensity factors (NSIFs) quantifying the asymptotic stress distributions can be calculated *a posteriori* on the basis of very simple expressions linking the local SED and the relevant NSIFs. This holds true also for the stress concentration factors (SCFs), at least when the local stress distributions ahead of the blunt notch are available for the plane problem. The extension of the SED method to three-dimensional cases is also possible as well as its extension to notched geometries exhibiting small scale yielding (Lazzarin and Berto 2008).

Figure 4.5.1 plots the local SED and makes it evident that the maximum value is close to the lateral surface where the maximum intensity of the Mode O takes place. This behavior can be explained by analyzing the complex stress state through the plate thickness. The SED is able to naturally capture and unite the features of the combined effects. The results summarised in the chapter are general and can be directly translated to the mesomechanic approach proposed by Sih which models the micro-crack tip as a fixed-free sharp V-notch as well as to the cases discussed in Tang and Sih (2005) dealing with in-plane solution and straight extended to the three-dimensional models.

Moreover it is strongly confirmed the fact that the notch opening angle has a negligible influence in the vicinity of the free surface and that the variability is slight also in the mid-plane. For the V-notched plates the importance of the out-of-plane mode has been investigated in Berto et al. (2011a) by increasing the plate size. Also for this geometry and boundary conditions the importance of Mode O has been strongly expected to be dependent on the main plate thickness.

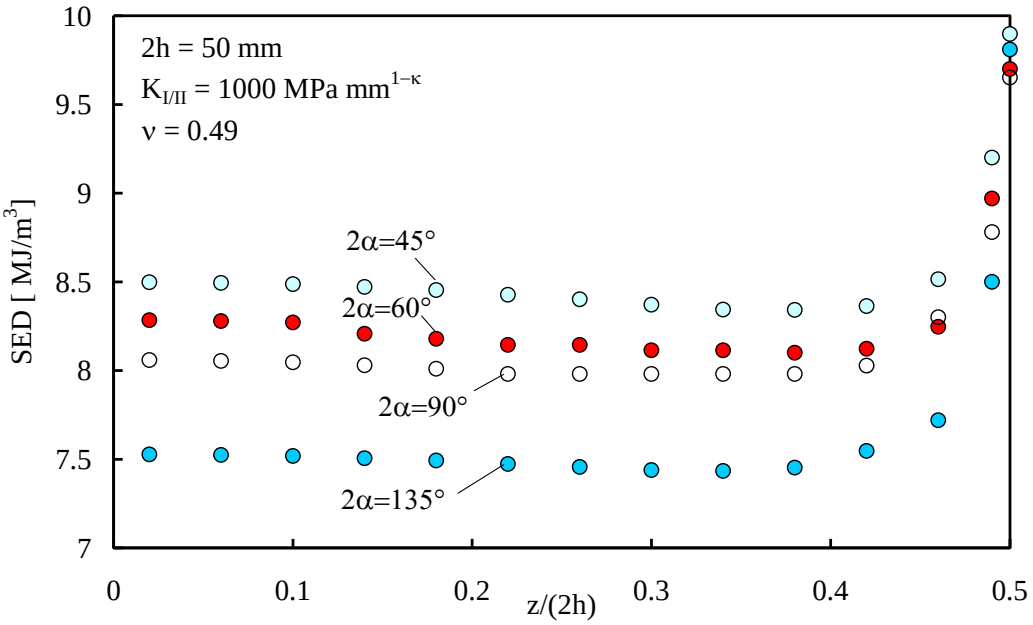

Figure 4.5.1. Local strain energy density (SED) averaged over a cylindrical volume having radius R_0 and height H, with H about equal to R_0.

4.6Conclusions

Irregularities of the material microstructure tend to torture the crack tip being the clamped-free boundary conditions the more realistic and general representation of what occurs on the micro V-notch. As a result, mixed mode conditions are always present along the V-notch bisector line. Physically, the different orders of the stress singularities are related to the different constraints associated with the defect thought as a micro V-notch at the tip of the main crack.

Dealing with a three-dimensional plate weakened by a sharp notch under free-clamped boundary conditions the mixed mode is automatically generated by the edge constraints. The presence of Mode II has been proofed to generate a singular Mode O which has been neglected in all previous papers. Different values of the notch opening angle have been considered to show the variability of the intensity and singularity of the new detected mode. It has been found that the singularity of Mode O matches that obtained by using the theoretical solution of a free-fixed notch under anti-plane loading.

Dealing with three-dimensional model it has been highlighted that the influence of the notch opening angle on the intensity of the Mode O is very low even for large values of 2α.

Finally the local energy has been used to capture the features of the combined effects through the plate thickness. Despite the complexity of the stress state, a simple scalar parameter, i.e. the strain energy density over a given control volume, makes easy the identification of the critical zones of the notched plate. It has been found that the most critical zone of the plate is close to the free surface and that the notch opening angle does not affect significantly the value of the SED when the notch is modelled by using a free-clamped configuration.

The SED can be applied at different scale levels keeping into account the boundary conditions that should be updated at every level. In fact the constraint conditions are sensitive to the environments and cannot be captured or simulated by using a model with the same conditions at nano, micro or macro levels. The change of boundary conditions at different scale level permits to overcome a complex elasto-plastic formulation and bypass the problem by maintaining a multi-scale model in the field of elasticity. This is enormously advantageous and powerful.

5

SED criterion on U-notched graphite plates under mixed mode loading

5.1 Introduction

Several criteria have been proposed for the failure assessment of brittle or quasi-brittle materials under monotonic loading subjected to Mode I and weakened by sharp and blunt notches.

A "Line criterion" was applied by Knésl (1991) who dealt with components weakened by sharp V-shaped notches. Some important aspects of the stress field in the proximity of the notch tip were highlighted by Nui et al. (1994) who demonstrated that, for distances from the notch tip less than 0.2 times the notch radius, stress distributions along the notch bisector depend only on the notch root and not on the opening angle. Seweryn provided a set of experimental data from sharp V-notches specimens made of PMMA and applied a criterion where the asymptotic stresses governed by the notch stress intensity factor (NSIF) were integrated over a material-dependent distance from the point of singularity (Seweryn 1994). Strandberg (2002) successfully applied the NSIF criterion to V-notched samples made of annealed tool steel, AISI O1, tested at –50˚C. Dealing with different ceramic materials, Gogotsi (2003) investigated the sensitivity of the Mode I fracture toughness as a function of the notch tip radius.

Considering failures from sharp and blunt notched specimens the Cohesive Zone Model (CZM) criterion has been successfully used and continuously improved considering the influence of different softening curve for the material (Gomez et al. 2000, Gomez and Elices 2003). Two essential parameters are associated with the softening curve: the ultimate tensile strength σ_t and the specific fracture energy G_f. Just considering linear elastic behaviour and ideally sharp notches, Gómez and Elices (2003) were able to demonstrate that a single non-dimensional

curve fits the experimental data from V-notched specimens made of steel, aluminium, polymethyl-metacrylate (PMMA) and PVC.

In a recent contribution (Ghasemnejad and Aboutorabi 2011), by using the Ansys code, the cohesive zone model, which is known as a variation in the cohesive stresses with the interfacial opening displacement along the localized fracture process zone, has been applied by Ghasemnejad and Aboutorabi (2011) to assess the Mode I and Mode II delamination failure in laminated composite structures.

In parallel a criterion based on the strain energy density (SED) averaged over a control volume was developed in (Lazzarin and Zambardi 2001, Lazzarin et al. 2003) for static and fatigue strength assessments of notched components and welded joints. By using the SED approach, Yosibash et al. (2004) showed a very good correlation to a large amount of experimental data from Alumina-7% Zirconia and PMMA specimens. A criterion based on the J-integral has been proposed by Matvienko and Morozov (2004) for a body with a U-notch considering an elastic and elastic-plastic behaviour of the material. The J-integral has been recently applied to homogeneous plates and functionally graded aluminum–silicone carbide composite with U-notches under bending loading (Barati et al. 2010a-2010b). A modified maximum tangential stress criterion has been proposed for fracture assessment of plates weakened by blunt V-notches (Ayatollahi and Torabi 2010a). An accurate review of the main criteria applicable under prevalent Mode I loading is carried out in Gomez et al. (2006).

Under mixed mode loading, particularly for notches with a non-negligible radius, providing a suitable fracture criterion is more complex than under Mode I loading because the maximum elastic stress is out of the notch bisector line and its position varies as a function of Mode I to Mode II stress distributions, along the notch edge. For this reason, the problem of brittle or quasi-brittle fracture of blunt notched components loaded under mixed mode (I+II) requires further investigations. Another important reason is the scarcity of experimental results available in the literature, in particular dealing with blunt notches under prevalent Mode II loading and, then, the possibility to set up an approach for the fracture assessment under the above mentioned conditions.

The proposal of Mode I dominance for crack plates was suggested first by Erdogan and Sih (1963) when dealing with cracked plates under plane loading and transverse shear, where the crack grows in the direction almost perpendicular to the maximum tangential stress in radial direction from its tip. Dealing with the strain energy density concept, it is worthwhile contemplating some fundamental contributions provided by Sih (1974). The strain energy density factor S was defined as the product of the strain energy density by a critical distance from the point of singularity. Failure was thought of as controlled by a critical value S_c, whereas the direction of crack propagation was determined by imposing a minimum condition on S. Several criteria have been applied mainly to sharp V-notched samples but also to U-notches (Papadopoulos and Paniridis 1988, Seweryn and Lucaszewicz 2002, Yosibash et al. 2006, Priel et al. 2008, Chen and Ozaki 2008, Ayatollahi and Torabi 2010b-2010c) showing a different degree of accuracy with respect to the experimental results. Seweryn and Lucaszewicz (2002) reviewed the main criteria available under mixed mode loading. A failure criterion at re-entrant corners in brittle elastic materials, validated in (Yosibash et al. 2004) for Mode I loading, was extended to mixed mode loading and validated by experimental observations (Yosibash et al. 2006, Priel et al. 2008). Chen and Ozaki (2008) provided some interesting results under mixed mode loading. However, the prevalent mode during the test was Mode I. A modified maximum tangential stress criterion has been developed to predict the fracture toughness and fracture initiation angle in U-shaped notches under mixed mode loading or prevalent Mode II loading (Ayatollahi and Torabi 2010b-2010c).

In the latest years a criterion based on the strain energy density (SED) over a control volume has been developed Lazzarin and Zambardi (2001), Lazzarin et al. (2003), Lazzarin and Berto (2005a) and applied to assess failure from cracked, U-notched and sharp V-notched components and also from structural components (Berto et al. 2008, Berto and Barati 2011). Over a small but finite volume of material close to the notch, the energy always has a finite value. Lazzarin and Zambardi (2001) predicted the static and fatigue behaviour of components weakened by sharp V-notches with variable notch angles using the mean value of the local strain energy. The control radius R_c of the volume, over which the energy

was averaged, depended on the fracture toughness and the ultimate tensile stress in the case of static loads and brittle materials. Different from Sih's criterion, which is a point-wise criterion, the averaged strain energy density criterion (SED) states that brittle failure occurs when the mean value of the strain energy density over a control volume (which becomes an area in two dimensional cases) is equal to a critical energy W_c.

The SED criterion has been recently extended to mixed mode loading (see Gomez et al. 2007-2008-2009a-2009b, Berto et al. 2007, Berto and Ayatollahi 2011).

The equivalent local Mode I concept on U-notched specimens has been applied by moving the control volume along the notch edge in such a way that it is centred in relation to the maximum elastic stress (Gomez et al. 2007-2008, Berto et al. 2007) and a simply but accurate expression has been found to evaluate the SED once the maximum value of the principal stress along the notch edge is known (Berto et al. 2007, Berto and Ayatllahi 2011). The SED criterion has been widely compared with the CZM in Berto et al. (2007).

This criterion is used in the present contribution to assess the brittle fracture on graphite U-notched specimens. Isostatic graphite is manufactured by using cold isostatic pressing technique and is often known for its homogeneous structure and excellent isotropic electrical, thermal properties. Moreover this kind of graphite is known for its high mechanical performances and for this reason is used in mechanical applications. It is sometimes purified in special-designed graphitization furnace to remove non-carbonaceous inclusions and impurities. Isostatic graphite is extensively used in various industrial applications such as: molds in continuous casting systems for making shaped steel, cast iron and copper; crucibles for melting precious metals or alloys; molds for making shaped glass; heating elements, heat shields, crucibles, etc.

There are various practical conditions where the notches in graphite components are subjected to a combination of tensile and shear deformation (or mixed Mode I/II loading). Cracks on graphite components are generated by manufacturing faults and other defects are also due to the coalescence of the micro-structural pores that are inherently embedded in graphite. While cracks are viewed as unpleasant entities in most engineering materials, notches of U or V-shape are

sometimes desirable in design and manufacturing of products made from graphite. Moulds, heating elements and chucks are only some examples of industrial graphite components that contain U or V-shape notches.

Extensive studies on Mode I and mixed mode fracture in cracked graphite specimens are present in literature but very few papers have dealt with brittle fracture in V-shaped and U-shaped notched graphite components. Ayatollahi and Torabi (2010d) conducted a series of fracture tests on three different V-notched test specimens made of a polycrystalline graphite material. Instead Ayatollahi et al. (2011) recently performed some tests on brazilian disk specimens to investigate failures on polycrystalline graphite weakened by blunt V-notches. Some tests have been recently carried out also considering graphite bars weakened by V-notches subjected to torsion loading (Berto et al. 2012b).

The present research deals with mixed mode (I+ II) brittle fracture of U-notched specimens made of isostatic graphite.

The purpose of the present chapter is twofold:

a. - To provide a large body of experimental data from static fracture of notched graphite specimens subjected to mixed mode loading with varying notch root radii and different mode mixities. Such data should be helpful to engineers engaged in static strength analysis of graphite components. Sixty new experimental results are summarised in the chapter with reference to various notch configurations.

b. - To provide a fracture model in order to estimate the critical loads to failure in notched isostatic graphite components subjected to in plane mixed mode loading. The strain energy density averaged on a control volume is used for brittle failure assessments of notched graphite samples in mixed Mode I/II loading conditions.

The chapter is structured in the following way: in the first section the experimental work is described including specimen geometries, testing procedures and experimental results. The second section is focused on the SED criterion applied to U-notches and to the numerical models. Finally, the third section presents a synthesis of all data in terms of averaged SED using a control volume

based on the basic material properties under mixed mode loading and a final discussion of the present results.

5.2 Fracture experiments

5.2.1 Materials and geometry

The material used is a commercial isostatic graphite particularly used in mechanical applications for its high performances. The mean grain size was measured by using the SEM technique and the density was determined from the buoyancy method.

Table 5.2.1. Mechanical properties

Material Property	Value
Elastic Modulus E [MPa]	8050
Shear Modulus G [MPa]	3354
Poisson's Ratio ν	0.2
Ultimate Torsion Strength [MPa]	30
Ultimate Compression Strength [MPa]	110
Ultimate Tensile Strength [MPa]	46
Fracture toughness [MPa $m^{0.5}$]	1.06
Density [Kg/dm^3]	1.85
Porosity [%]	7
Resistivity [μohm·m]	11
Thermal Conductivity [W/(m·K)]	110

Table 5.2.1 presents the most important material properties: mean grain size is 2 μm, porosity 7%, bulk density of 1850 kg/m^3, tensile strength of 46 MPa, Young's modulus of 8.05 GPa and shear modulus 3.35 GPa. The flexural strength is 49 MPa, whereas the compressive strength is equal to 110 MPa. In a previous investigation (Ayatollahi et al. 2011), the detected mean grain size was 320 μm whereas the tensile strength was equal to 27.5 MPa, resulting in a mechanical behaviour very different from that of the isostatic graphite considered in the present work.

All tests were performed under load control on a servocontrolled MTS axial testing device (±100 kN/± 110 Nm, ± 75mm/± 55°). The load was measured by a MTS cell with ± 0.5 % error at full scale.

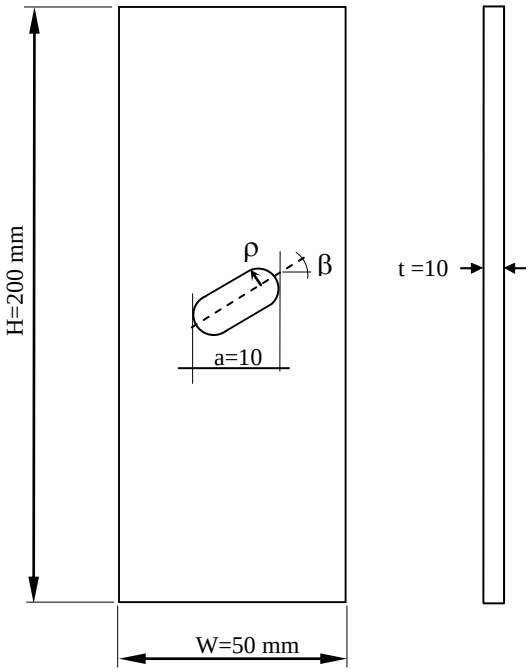

Figure 5.2.1. Geometry and main dimensions of the tested specimens

The samples used in this investigation are plates with a central blunt U-notch, as shown in Figure 5.2.1. Different radii at the notch tip, ρ, and tilt angles of the notch, β, are used in order to investigate their influence on the failure. All the specimens are subjected to tensile load. By varying the tilt angle β different mode-mixity can be produced. If the tilt angle is equal to zero the notches are subjected to pure Mode I, while varying β the loading condition changes from pure Mode I towards mixed Mode I+II. For all the tested graphite specimens, the width, the distance between the tip of the notches and the thickness were 50 mm, 10 mm and 10 mm, respectively.

Five values of notch radius ρ=0.25, 0.5, 1, 2, 4 mm were considered for manufacturing the test specimens so that the effects of the notch tip radius on mixed mode fracture of the graphite specimens are studied. With the aim to obtain different mode mixities four values of the angle β were considered (β=0°, β=30°,

β=45° and β=60°). Figures 5.2.2 and 5.2.3 show some photos of the tested specimens and some details of the notches.

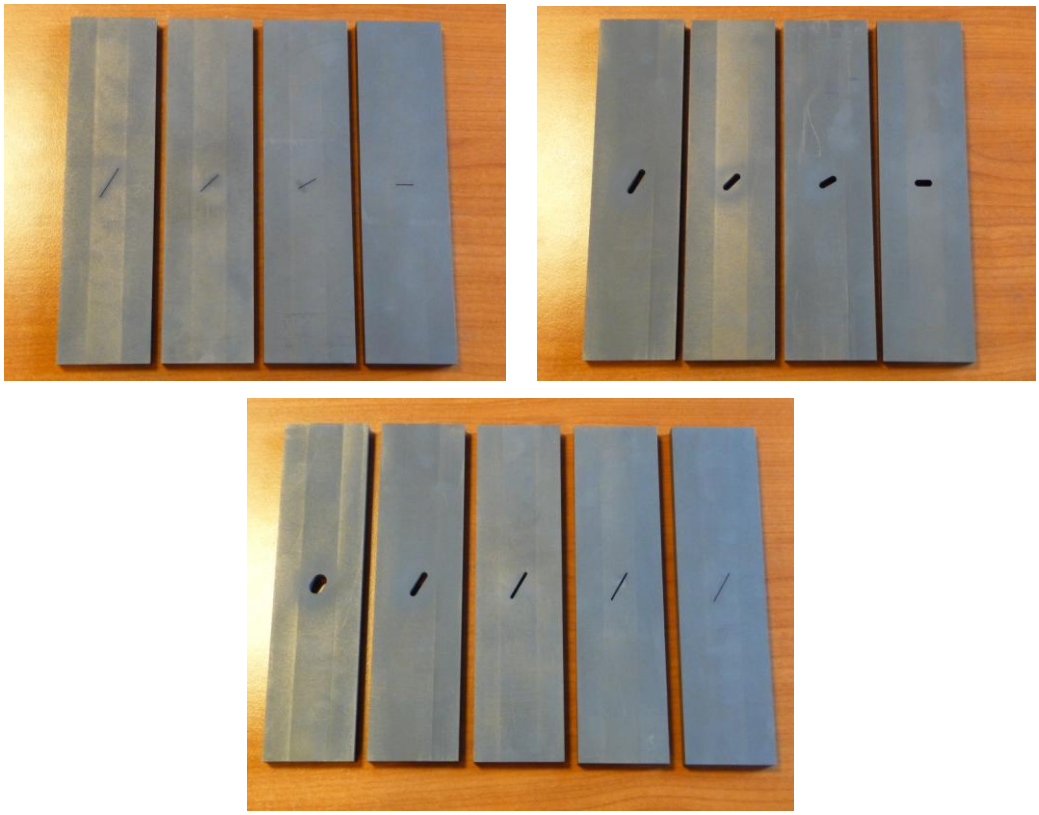

Figure 5.2.2: Different U-notched specimens (a) ρ=0.25 (b) ρ= 2 mm (c) β=60°

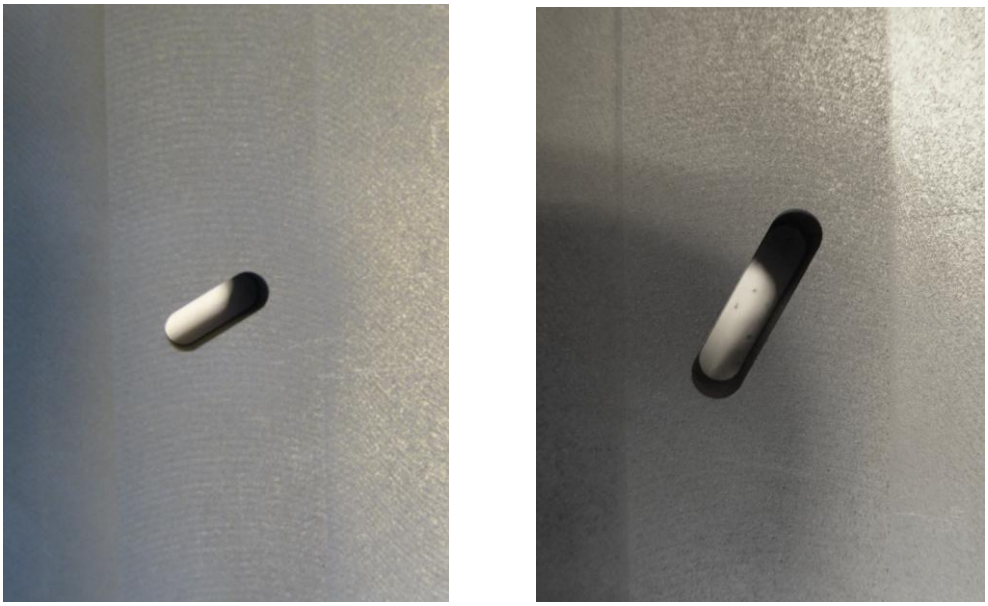

Figure 5.2.3. Two inclined U-notches: (a) ρ=2mm, β=30° (b) ρ=2mm, β=60°.

5.2.2 **Experimental procedure**

In order to prepare the graphite test specimens (see Figures 5.2.2 and 5.2.3), first several plates of 10 mm thick were cut from a graphite block. Then, the specimens were precisely fabricated by using a 2-D CNC water-jet cutting machine. In order to assure plane strain conditions at the notch tip, in the absence of specific standards for graphite subjected to stress concentration effects, the thickness of the specimens was chosen following the guidelines drawn in (Lomakin et al. 1975, Yamauchi et al. 2001)

Before conducting the experiments, the cut surfaces of the graphite specimens were polished by using a fine abrasive paper to remove any possible local stress concentrations due to surface roughness. A total number of 60 mixed Mode I/II fracture tests were performed for various notch geometry parameters. For each geometry shape and loading angle, three separate fracture tests were performed by using a universal tension-compression test machine under displacement-control conditions with a loading rate of 0.05 mm/min. The load-displacement curves recorded during the fracture tests were all linear and the specimens fractured suddenly. Therefore, the use of a brittle fracture criterion based on the linear elastic fracture mechanics (LEFM) is permissible. The values of the fracture loads for each experimental test and the mean values (<F>) recorded by the test machine are presented in Table 5.2.2.

A re-analysis of Table 5.2.2 shows that the fracture load increases when the radius ρ increases from 0.25 mm to 4 mm.

Dealing with crack initiation angles they have been measured experimentally by using an optical microscope and a dedicate software called Las (Leica Application Suite), see Figure 5.2.4 as example. All the values of the initial crack angles are reported in Table 5.2.2 also with the mean value of the three performed tests (<φ>).

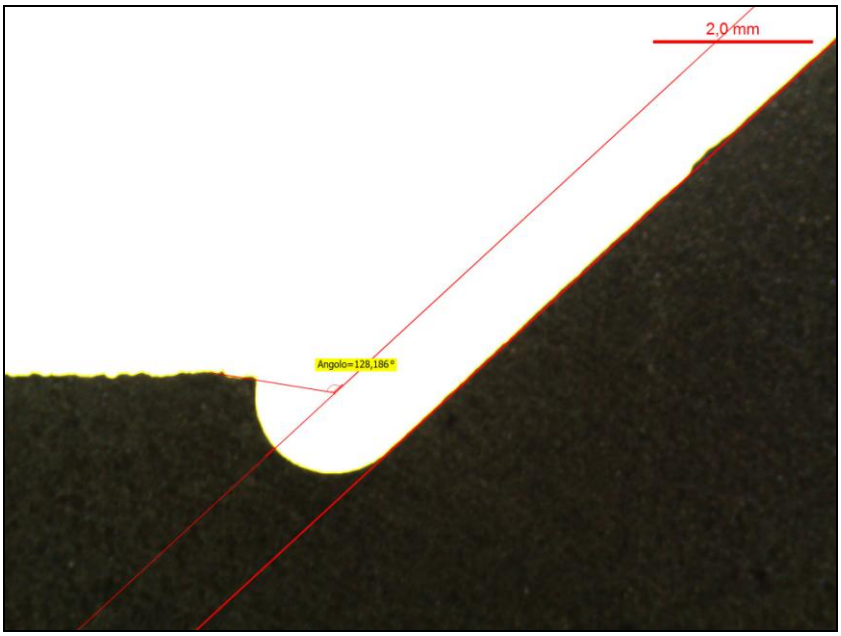

Figure 5.2.4: Experimental measure of the initial crack angle with the dedicated software LAS

Table 5.2.2. Experimental critical loads and initial crack angles

β [degrees]	ρ [mm]	F_1 [N]	F_2 [N]	F_3 [N]	<F> [N]	φ_1 [degrees]	φ_2	φ_3	<φ> [degrees]
		Exp.				Exp.			
0	0.25	4115	4708	4455	4426	0	0	0	0
	0.5	4592	4495	4429	4505	0	0	0	0
	1	4461	5152	4830	4814	0	0	0	0
	2	5182	5824	5541	5516	0	0	0	0
	4	7083	6406	6879	6789	0	0	0	0
30	0.25	3979	4009	4114	4034	35.82	28.78	27.87	30.82
	0.5	4254	4422	4370	4349	28.60	43.10	34.79	35.50
	1	4756	4829	4888	4824	32.95	29.26	28.13	30.11
	2	5906	5965	5876	5916	26.05	29.53	29.31	28.30
	4	6685	7098	6875	6886	27.68	33.06	30.74	30.49
45	0.25	3848	3954	3979	3927	53.99	33.26	40.10	42.45
	0.5	4302	4164	4318	4261	46.55	48.00	44.62	46.39
	1	4756	4846	4729	4777	44.81	52.52	50.54	49.29
	2	5448	5666	5696	5603	47.94	42.61	41.91	44.15
	4	7041	6799	6747	6862	43.67	49.79	50.06	47.84
60	0.25	4034	3847	3944	3942	65.01	51.54	58.15	58.23
	0.5	4536	4491	4626	4551	64.97	48.84	53.70	55.84
	1	4697	4829	4810	4779	64.21	58.06	59.95	60.74
	2	5511	5363	5491	5455	59.79	54.21	55.72	56.57
	4	6941	6602	6704	6749	59.49	55.94	58.94	58.12

5.2.3 **Mode mixity**

In order to quantify the mode mixity of the tested specimens, some FE analyses were carried out. In agreement with Lazzarin and Filippi (2006) the definition of generalized notch stress intensity factors (N-SIF) for Mode I and Mode II is as follows:

$$K_{I\rho} = \sqrt{2\pi r}\,\frac{(\sigma_\theta)_{\theta=0}}{1+\frac{\rho}{2r}}$$

$$K_{II\rho} = \sqrt{2\pi r}\,\frac{(\tau_{r\theta})_{\theta=0}}{1-\frac{\rho}{2r}} \qquad (5.2.1)$$

where σ_θ and $\tau_{r\theta}$ are the stresses along the notch bisector line at a distance r from the local frame origin placed at a distance $\rho/2$ from the notch tip.

Eq. (5.2.1) is not expected to give a constant value for N-SIFs but slight variations are possible. The slightly oscillating trend ahead of the notch tip is widely investigated in Lazzarin and Filippi (2006) and Lazzarin et al. (2011). In order to eliminate the weak dependence on the notch tip distance, the following expressions have been defined to calculate the mean values of the generalized NSIFs (Lazzarin and Filippi 2006):

$$\overline{K}_{I\rho} = \frac{1}{\eta\rho}\int_{\rho/2}^{\rho/2+\eta\rho}\left(K_{I\rho}\right)dr$$

$$\overline{K}^{V}_{\rho,II} = \frac{1}{\eta\rho}\int_{\rho/2}^{\rho/2+\eta\rho}\left(K_{II\rho}\right)dr \qquad (5.2.2)$$

where η is set equal to 0.2 in the present work.

The mode mixity has been defined according to the following definition:

$$\chi = \frac{2}{\pi}\arctan\left[\frac{\overline{K}_{II\rho}}{\overline{K}_{I\rho}}\right] \tag{5.2.3}$$

The values of χ are listed in Table 5.2.3 and varies from 0 (pure Mode I) to 0.9 (prevalent Mode II).

Dealing with Mode II notch stress intensity factors some recent developments can be found in Lazzarin et al. (2011). In particular by taking advantage of some analytical formulations which are able to describe stress distributions ahead of parabolic, hyperbolic and V-shaped notches with end holes, the paper discusses the form and the significance of the NSIFs with reference to in-plane shear loading, considering explicitly the role played by the notch opening angle and the notch tip radius.

Table 5.2.3. Mode mixity of the investigated geometries

β [degrees]	ρ [mm]	$\overline{K}_{I\rho}$ / σ_{nom} $mm^{0.5}$	$\overline{K}_{II\rho}$ / σ_{nom} $mm^{0.5}$	$\overline{K}_{II\rho}$ / $\overline{K}_{I\rho}$	χ
0	0.25	4.63	0.00	0.00	0.00
0	0.5	4.78	0.00	0.00	0.00
0	1	4.99	0.00	0.00	0.00
0	2	5.31	0.00	0.00	0.00
0	4	5.81	0.00	0.00	0.00
30	0.25	3.71	3.81	1.03	0.51
30	0.5	3.78	4.10	1.08	0.53
30	1	3.89	4.58	1.18	0.55
30	2	4.05	5.41	1.33	0.59
30	4	4.30	6.85	1.60	0.64
45	0.25	2.71	4.89	1.80	0.68
45	0.5	2.72	5.22	1.92	0.69
45	1	2.73	5.76	2.12	0.72
45	2	2.73	6.71	2.46	0.75
45	4	2.71	8.35	3.08	0.80
60	0.25	1.60	5.18	3.23	0.81
60	0.5	1.54	5.47	3.56	0.83
60	1	1.44	5.94	4.13	0.85
60	2	1.27	6.77	5.31	0.88
60	4	0.97	8.17	8.44	0.92

5.3 SED criterion applied to U-notches and numerical models

The averaged strain energy density criterion (SED) as presented in Lazzarin and Zambardi (2001) states that brittle failure occurs when the mean value of the strain energy density over a given control volume is equal to a critical value W_c. This critical value varies from material to material but does not depend on the notch geometry and sharpness. The control volume is thought of as dependent on the ultimate tensile strength and the fracture toughness K_{Ic} in the case of brittle or quasi-brittle materials subjected to static loads. For a blunt U-notch under Mode I loading, the volume assumes the crescent shape shown in Fig. 5.3.1a, where R_c is the depth measured along the notch bisector line. The outer radius of the crescent shape is equal to $R_c+\rho/2$, being $\rho/2$ the distance between the notch tip and the origin of the local coordinate system.

Under mixed mode loading the critical volume is no longer centred on the notch tip, but rather on the point where the principal stress reaches its maximum value along the edge of the notch (Fig. 5.3.1b). It was assumed that the crescent shape volume rotates rigidly under mixed mode, with no change in shape and size. This is the governing idea of the '*equivalent local Mode I*' approach, as proposed and applied to U-notches (Gomez et al. 2007, Berto et al. 2007).

Some closed-form expressions correlating SED and maximum elastic stress are reported in the literature (Berto et al. 2007). In this paper, however, to avoid any simplified assumption, the SED values will be those directly determined from FE models.

Under plane strain conditions the critical length, R_c, can be evaluated according to the following expression (Yosibash et al. 2004, Lazzarin and Berto 2005a):

$$R_C = \frac{(1+\nu)(5-8\nu)}{4\pi}\left(\frac{K_{Ic}}{\sigma_t}\right)^2 \qquad (5.3.1)$$

where K_{Ic} is the fracture toughness, ν the Poisson's ratio and σ_t the ultimate tensile stress of a plain specimen that obeys a linear elastic behaviour.

This critical value can be determined from the ultimate tensile stress σ_t according to Beltrami's expression:

$$W_c = \frac{\sigma_t^2}{2E} \tag{5.3.2}$$

Unnotched specimens often exhibit a non-linear behaviour whereas the behaviour of notched specimens remains linear. Under these circumstances the stress σ_t should be substituted by the maximum normal stress existing at the edge at the moment preceding the cracking, as underlined in (Seweryn 1994) where it is also recommended to use tensile specimens with large semicircular notches to avoid any notch sensitivity effect.

In parallel, the control volume definition *via* the control radius R_c needs the knowledge of the fracture toughness K_{Ic} and the Poisson's ratio ν, see Eq. (5.3.1). The critical load that is sustainable by a notched component can be estimated by imposing $\overline{W}$ equal to the critical value W_c. This value is considered here constant under Mode I, Mode II and in plane mixed-mode conditions. This assumption has been extensively verified for a number of different brittle and quasi-brittle materials (Gomez et al. 2007, Berto et al. 2007). Dealing with blunt notches under mixed mode loading, the problem becomes more complex than under Mode I loading, mainly because the maximum elastic stress is out of the notch bisector line and its position varies as a function of Mode I and Mode II.

As discussed above, the idea of the '*equivalent local Mode I*' approach, as proposed and applied to plates made of PMMA and weakened by U-notches is used here. The critical volume is no longer centred on the notch tip, but rather on the point where the principal stress reaches its maximum value along the edge of the notch and it is assumed that the crescent shape volume rotates rigidly under mixed mode, with no change in shape and size with respect to Mode I.

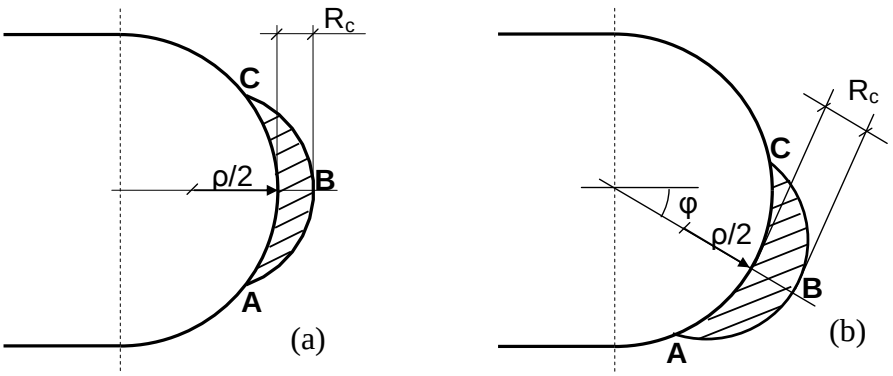

Figure 5.3.1. Control volume under Mode I (a) and mixed mode loading (b) for U-notched specimens

The maximum stress occurring along the edges of V-notches has been calculated numerically by using the FE code ANSYS 12.0®. For each geometry, two models were created. The first model was mainly oriented to the determination of the point where the maximum principal stress and the maximum SED were located; the second model was more refined, with an accurate definition of the control volume where the strain energy density should be averaged. All the analyses have been carried out by using eight-node elements under the hypothesis of plane strain conditions (see Figure 5.3.2). The procedure for building the two models necessary to determine the SED in the rotated volume can be easily automated by simply writing an APDL (ANSYS Parametric Design Language) subroutine which permits the direct evaluation of the SED in the control volume.

Figure 5.3.3 shows the shape of the control volume in the case of $\beta=45°$, with $\rho=0.25$ mm (a, b) and $\rho=2$ mm (c, d). The contour lines of the maximum principal stress (a, c) as well as the SED isolines (b, d) are shown in the figure. As discussed in Lazzarin and Berto (2005a), the volume adapts itself varying the notch tip radius ρ.

Figure 5.3.3 shows that a relatively refined mesh was used to model the notch profiles. However, one of the most important advantages of the SED approach is that to provide a mean value which is substantially mesh independent. In fact, contrary to some stress parameters integrated in the local criteria (e.g. maximum principal stress, hydrostatic stress, deviatoric stress), which are mesh-dependent,

the SED averaged over a control volume is insensitive to the mesh refinement. As widely documented in Lazzarin et al. (2008a-2010) dealing with sharp V-notches, refined meshes are not necessary, because the mean value of the SED on the control volume can be directly determined *via* the nodal displacements, without involving their derivatives. As soon as the average SED is known, the notch stress intensity factors (NSIFs) quantifying the asymptotic stress distributions can be calculated *a posteriori* on the basis of very simple expressions linking the local SED and the relevant NSIFs. This holds true also for the stress concentration factors (SCFs), at least when the local stress distributions ahead of the blunt notch are available for the plane problem. The extension of the SED method to three-dimensional cases is also possible as well as its extension to notched geometries exhibiting small scale yielding (Lazzarin and Berto 2008).

Dealing with the SED approach, the main properties of the material are the ultimate tensile strength σ_t= 46 MPa and the fracture toughness K_{Ic} = 1.06 $\mathrm{MPa}\sqrt{\mathrm{m}}$. Using Eq. (5.3.2), the critical value of SED for the tested material is found to be W_c=0.13 MJ/m^3, whereas the radius of the control volume is $R_c \cong 0.17$ mm, considering realistic plane strain conditions.

In the absence of specific data from cracked components, the parameter K_{Ic} can be estimated considering the results from the three specimens with the minimum available radius, $\rho = 0.25$ mm, and β=0°. In parallel, the tensile strength has been evaluated using the experimental data from the samples with ρ=4 mm and β=0°, according to some indications drawn by Seweryn (1994).

Table 5.3.1 summarizes the values of SED as directly evaluated by means of the numerical models. The table also gives the maximum value of the principal stress (σ_{max}) and the SED value as obtained from the FE models of the graphite specimens by applying to the model the mean value of the critical loads. It is interesting to observe that the maximum principal stress along the notch edge is much greater (about two times) than the ultimate tensile stress of the material justifying the SED approach based on a control volume.

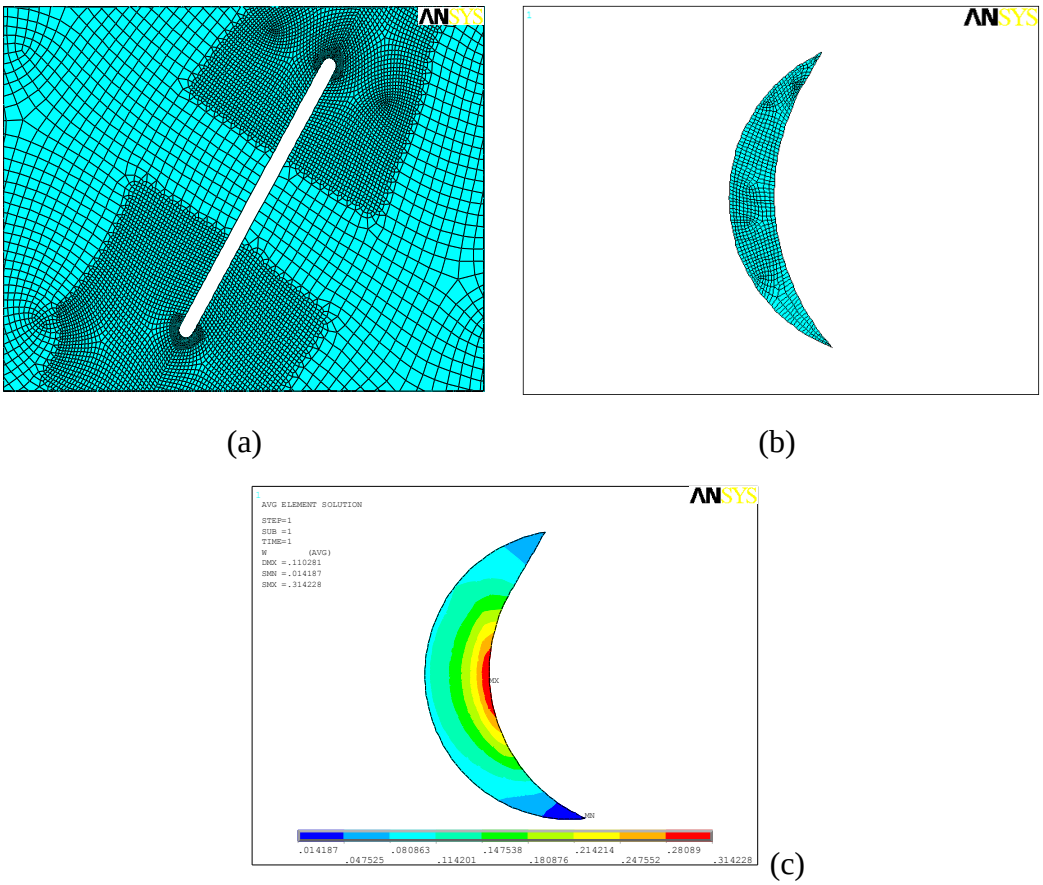

Figure 5.3.2 Typical mesh used to evaluate the SED (a), control volume (b) and SED contour lines (c)

The stress component $\sigma_{\theta\theta}$ is plotted in Figure 5.3.4 versus the normalised distance ξ/ρ. The inclined path is perpendicular to the notch edge and starts from the point on the notch profile where the stress component $\sigma_{\theta\theta}$ is maximum. The finite element results are compared with the Mode I theoretical solution given by Creager and Paris (1967) for the 'blunt crack' case. The agreement is satisfactory also under prevalent Mode II, independent of the notch radius. In parallel, the shear stress component has been verified to be close to zero, as it happens along the notch bisector under pure Mode I loading conditions. This observation leads to the conclusion that under mixed mode loading the line normal to the notch edge and starting from the point of maximum principal stress behaves as a virtual bisector line under pure Mode I, confirming the applicability of the equivalent local Mode I concept.

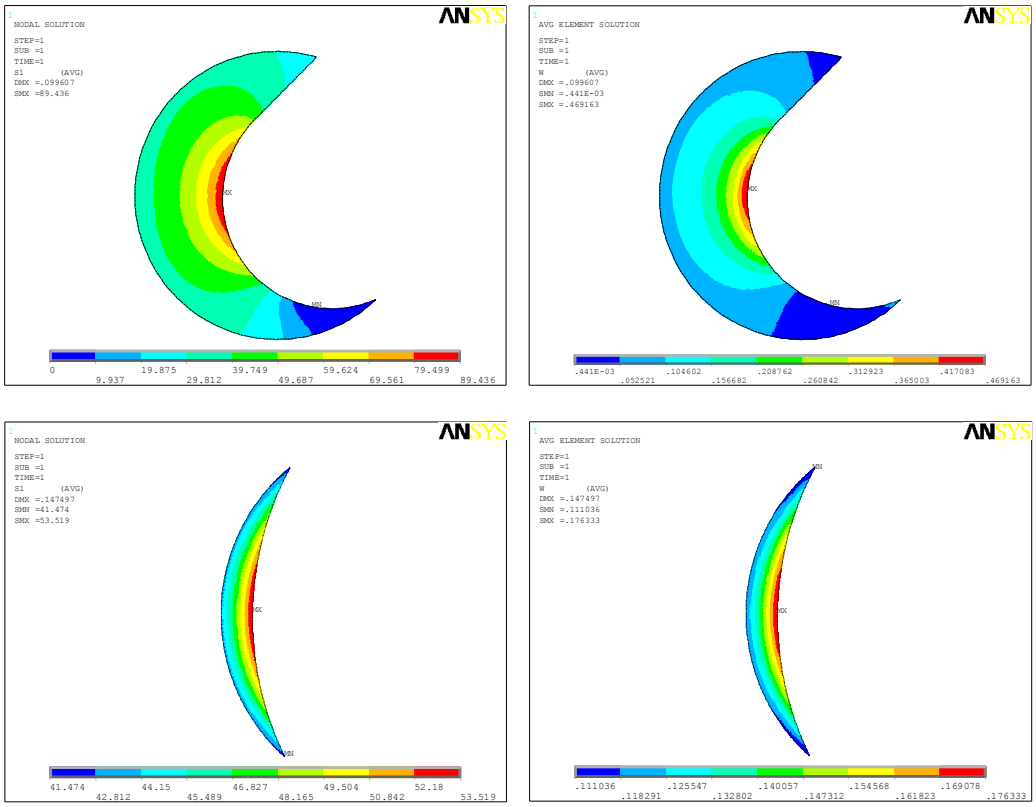

Figure 5.3.3. Contour lines of the maximum principal stress and of the SED in the case β= 45° with ρ=0.25 mm (a, b) and ρ=2 mm (c, d).

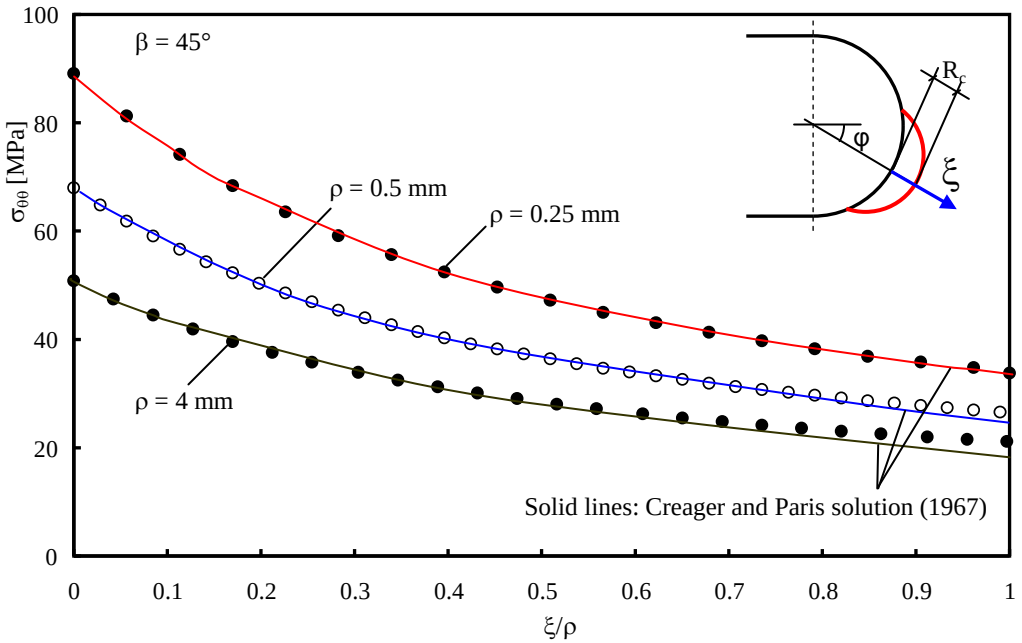

Figure 5.3.4. Stress distribution along the line of maximum tangential stress out of the notch bisector line; β=45° and applied load equal to average value of the experimental loads, <F>.

Table 5.3.1. Numerical values of principal stresses and strain energy density

β [degrees]	ρ [mm]	φ [degrees]		σ_{max} [MPa]			$\overline{W}$ [MJ/m^3]		$<\overline{W}>$ [MJ/m^3]
		FEM		FEM			FEM		FEM
0	0.25	0	86.94	99.47	94.14	0.1306	0.1709	0.1531	0.1515
	0.5	0	71.33	69.81	68.81	0.149	0.1428	0.1387	0.1435
	1	0	51.49	59.47	55.76	0.1081	0.1442	0.1267	0.1263
	2	0	45.26	50.87	48.40	0.1009	0.1275	0.1154	0.1146
	4	0	48.08	43.49	46.70	0.1264	0.1034	0.1192	0.1163
30	0.25	34.44	87.95	88.61	90.93	0.135	0.137	0.1443	0.1387
	0.5	32.22	68.37	71.09	70.25	0.1378	0.149	0.1455	0.1441
	1	31.11	56.51	57.37	58.08	0.1315	0.1355	0.1389	0.1353
	2	30.90	53.30	53.83	53.03	0.1408	0.1436	0.1394	0.1412
	4	30.00	47.63	50.58	48.98	0.1243	0.1402	0.1315	0.132
45	0.25	47.78	86.36	88.74	89.30	0.1291	0.1363	0.1381	0.1345
	0.5	46.67	70.59	68.32	70.84	0.1445	0.1353	0.1455	0.1418
	1	46.67	58.15	59.24	57.81	0.1388	0.1441	0.1372	0.1401
	2	46.11	51.19	53.23	53.52	0.1302	0.1408	0.1423	0.1377
	4	45.28	53.24	51.41	51.02	0.1557	0.1452	0.143	0.1479
60	0.25	56.67	87.32	83.28	85.38	0.13	0.1182	0.1243	0.1242
	0.5	57.78	73.28	72.55	74.74	0.1513	0.1484	0.1574	0.1524
	1	58.89	57.97	59.59	59.37	0.1343	0.1419	0.1409	0.139
	2	58.89	53.86	52.41	53.66	0.1428	0.1352	0.1417	0.1399
	4	59.45	56.61	53.85	54.68	0.1757	0.159	0.1639	0.1662

5.4 Results and discussions

As underlined in Gomez et al. (2007-2008-2009a-2009b) and Berto et al. (2007) dealing with mixed mode loading, particularly for notches with a non-negligible root radius, providing a suitable fracture criterion is more complex than under Mode I loading because the maximum elastic stress is out of the notch bisector line and its position strongly varies on the notch edge as a function of Mode I to Mode II stress distributions. The problem is solved here by applying the SED criterion to rounded-tip U-notched domains, with the aim to estimate the fracture load of notched graphite components.

As underlined before, the purpose of this research is twofold: to provide a new set of experimental data from brittle fractures under mixed mode of an isostatic ghaphite with a low mean grain size, and to document the applicability of the local SED method in the presence of U-notches, by rigidly rotating the crescent shape volume defined under Mode I loading.

The experimental results are summarised in Table 5.2.2 whereas a comparison between experimental data and theoretical results is documented in Table 5.4.1. The average value of the measured critical loads are compared with the values computed by assuming a constant critical strain energy density over the control volume (W_c = 0.13 MJ/m^3). A good agreement can be observed from the table.

Figures 5.4.1, 5.4.2, 5.4.3 and 5.4.4 plot the experimental results and the theoretical predictions based on the SED approach as a function of the notch root radius for each value of the tilt angle, β.

The relative deviation between experimental and predicted values ranges from –7% to +7%, with an exception (+12%) in the case ρ = 4 mm and β = 60°. However it is important to note that for all the cases taken into account the scatter between theoretical and experimental values is very narrow.

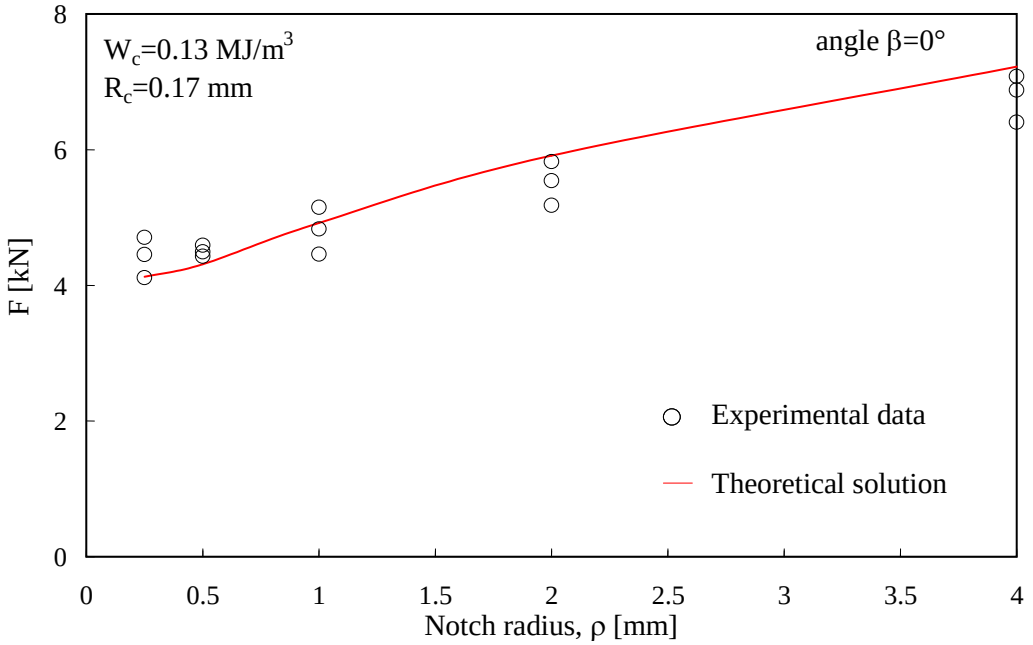

Figure 5.4.1. Comparison between experimental and predicted values of the critical load for different notch radii and tilt angle of the notch β=0°.

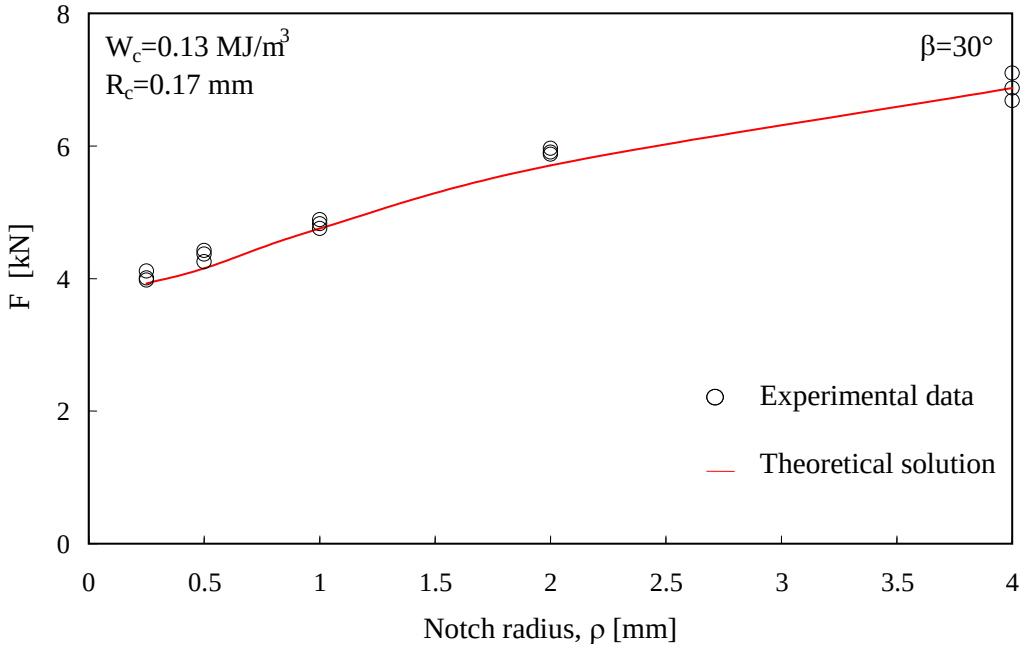

Figure 5.4.2. Comparison between experimental and predicted values of the critical load for different notch radii and tilt angle of the notch β=30°

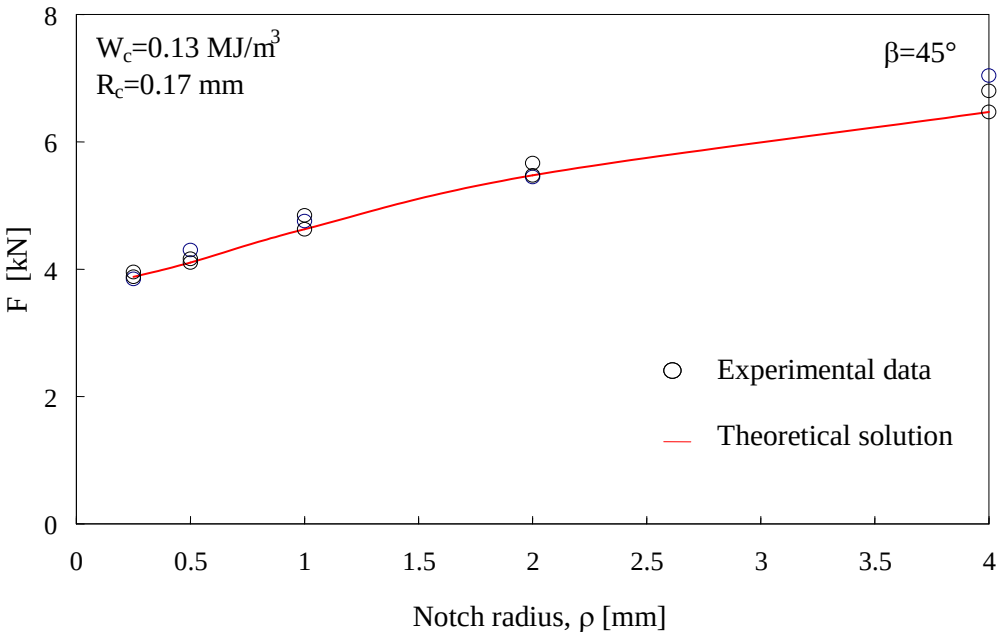

Figure 5.4.3. Comparison between experimental and predicted values of the critical load for different notch radii and tilt angle of the notch β=45°.

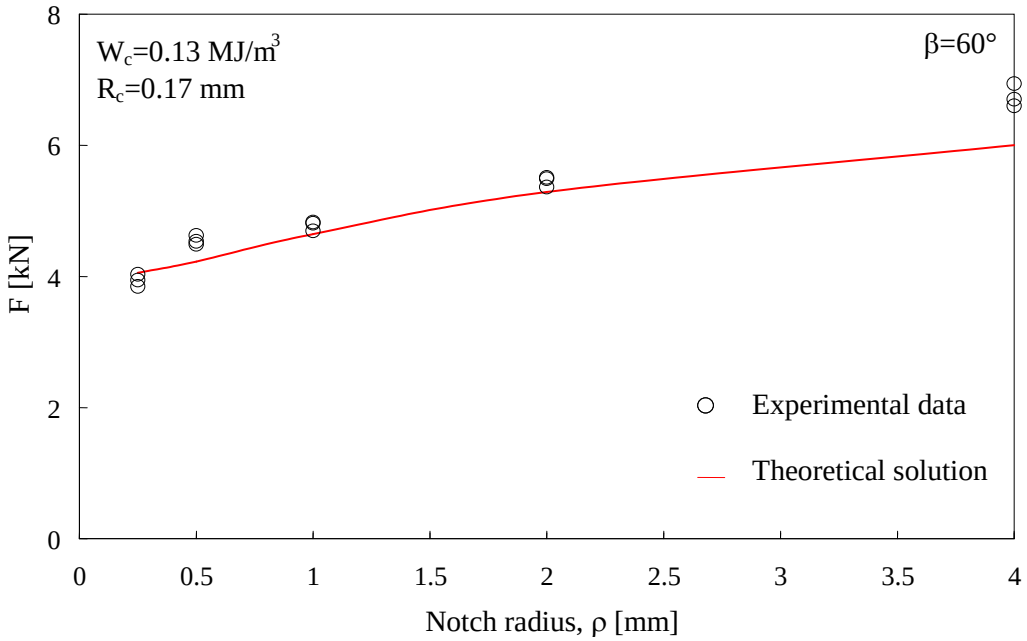

Figure 5.4.4. Comparison between experimental and predicted values of the critical load for different notch radii and tilt angle of the notch β=60°.

Table 5.4.2 summarizes the average values of the measured initiation crack angle φ compared with the values obtained from Finite Element analyses. In the numerical analyses the angles where the principal stress (and then the strain energy density) reaches its maximum value along the notch edge has been considered. It is worth nothing from the table that the relative deviation between experimental and predicted results is higher with respect to the case of critical loads as well as the intrinsic scatter of the experimental results (see Figures 5.4.5, 5.4.6 and 5.4.7).

Table 5.4.1. Comparison between experimental and theoretical critical loads.

β [degrees]	ρ [mm]	<F_{EXP}> [N]	<F_{th}> [N]	F_{EXP}/F_{th}
		Exp.	Theor.	
0	0.25	4426	4128	1.072
	0.5	4505	4313	1.045
	1	4815	4919	0.979
	2	5516	5914	0.933
	4	6789	7223	0.940
30	0.25	4034	3927	1.027
	0.5	4349	4154	1.047
	1	4824	4755	1.015
	2	5916	5707	1.037
	4	6886	6874	1.002
45	0.25	3927	3882	1.012
	0.5	4261	4103	1.038
	1	4777	4628	1.032
	2	5603	5474	1.024
	4	6862	6469	1.061
60	0.25	3942	4056	0.972
	0.5	4551	4227	1.077
	1	4779	4646	1.028
	2	5455	5288	1.032
	4	6749	6004	1.124

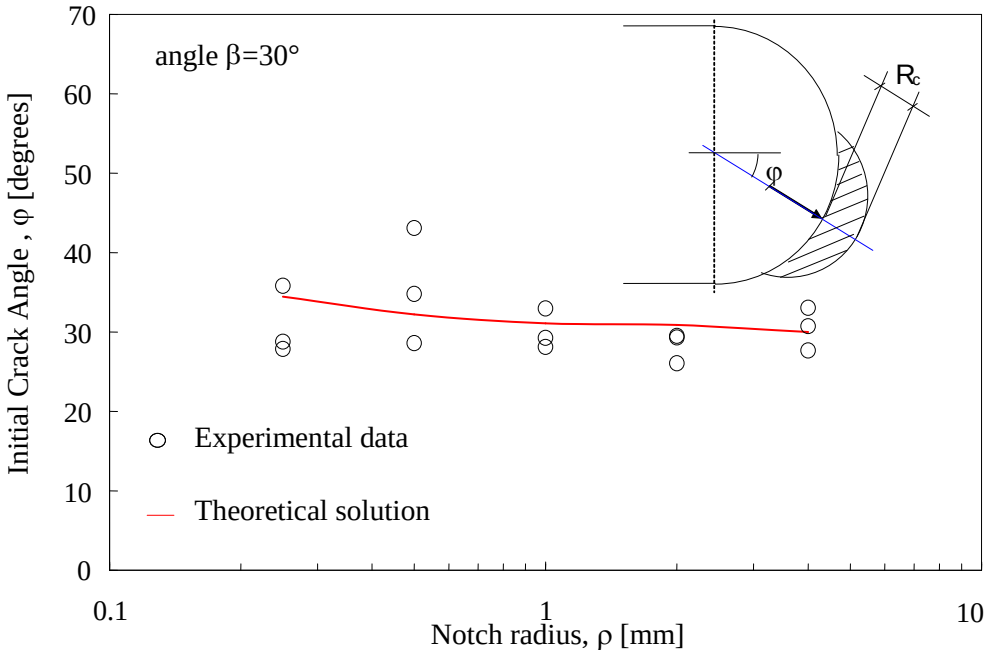

Figure 5.4.5. Comparison between experimental and numerical values of the initial crack angle for different notch radii and tilt angle of the notch β=30°.

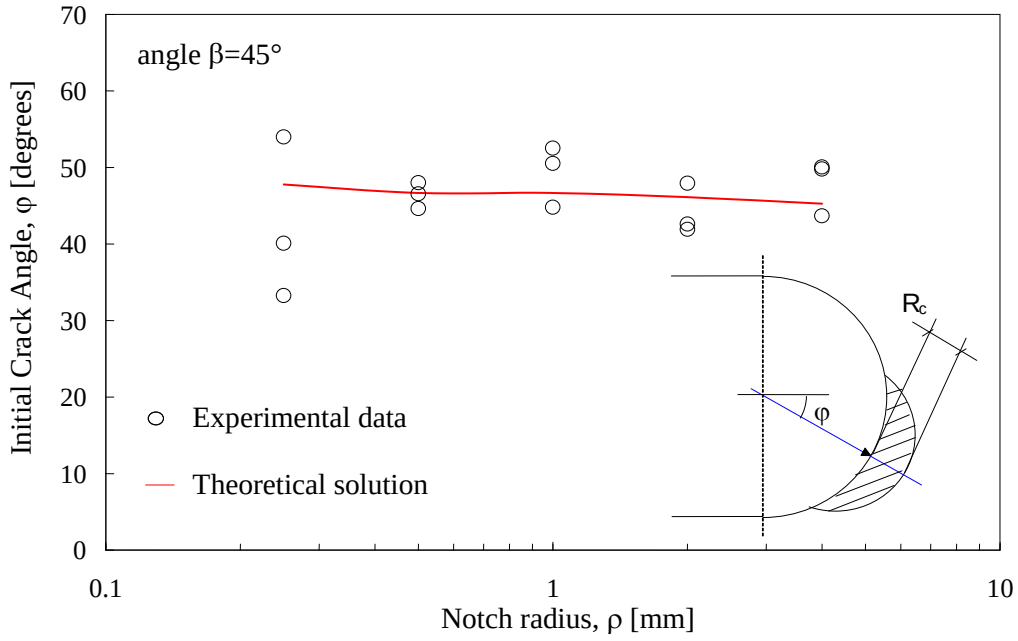

Figure 5.4.6. Comparison between experimental and numerical values of the initial crack angle for different notch radii and tilt angle of the notch β=45°.

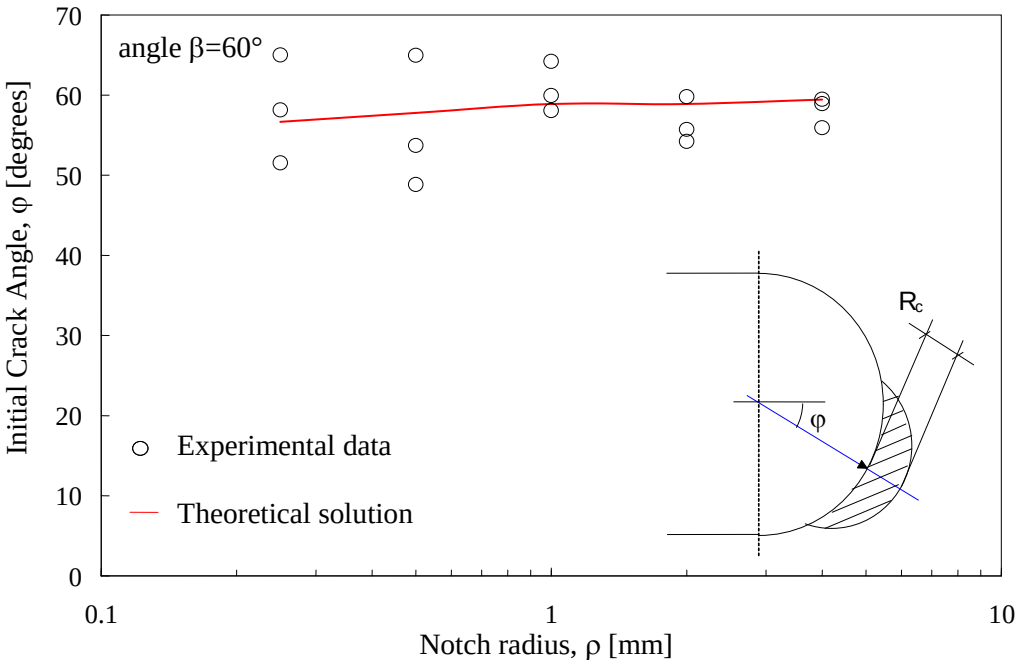

Figure 5.4.7. Comparison between experimental and numerical values of the initial crack angle for different notch radii and tilt angle of the notch β=60°.

Table 5.4.2. Comparison between experimental and numerical initial crack angles

β [degrees]	ρ [mm]	<φ> [degrees]	<φ EXP> [degrees]	Δφ [%]
		FEM	Exp.	
0	0.25	0	0	0
	0.5	0	0	0
	1	0	0	0
	2	0	0	0
	4	0	0	0
30	0.25	34.44	30.82	10.5
	0.5	32.22	35.50	-10.2
	1	31.11	30.11	3.2
	2	30.9	28.30	8.4
	4	30	30.49	-1.6
45	0.25	47.78	42.45	11.2
	0.5	46.67	46.39	0.6
	1	46.67	49.29	-5.6
	2	46.11	44.15	4.2
	4	45.28	47.84	-5.7
60	0.25	56.67	58.23	-2.8
	0.5	57.78	55.84	3.4
	1	58.89	60.74	-3.1
	2	58.89	56.57	3.9
	4	59.45	58.12	2.2

As discussed in Zheng et al. (2001) and Zacharopoulos (2004), the finite element technique can be used to calculate the strain energy density (SED) contours and the SED can be used not only to estimate the fracture initiation but also the crack propagation inside the material. The predicted trajectory of the crack during stable and unstable propagation can be assumed to coincide with the minimum of the strain energy density function according to the SED criterion (Sih 1974). This simple method has been found to offer a reliable prediction of the crack path stability for two as well as three-dimensional problems with complex geometry structures and arbitrary loadings. In Zacharopoulos (2004) both Three Point Bending (TPB) and Double Cantilever Beam (DCB) specimens have been analysed showing a good agreement with a large number of experimental results taken from the literature.

The scatter of the critical loads to failure presented here is in good agreement with that documented in Lazzarin et al. (2009b) and Berto and Lazzarin (2009) where a synthesis based on more than one thousand experimental data taken from the recent literature were summarised in terms of SED. Those data came from tests on U- and V-notched specimens made of very different materials and subjected to Mode I and Mode II loading.

The proposed scatter band was plotted by using, as a synthesis parameter, the square root value of the local energy averaged over the control volume, normalised with respect to the critical energy of the material. This parameter was plotted as a function of the notch radius to control radius ratio, ρ/R_c. The data were characterized by a high variability of the ratio ρ/R_c, which ranged from about 0 to 1000. The fracture toughness K_{IC} and the ultimate fracture stress ranged from 0.15 to 55 $\mathrm{MPa}\sqrt{\mathrm{m}}$ and from 2.5 to 1200 MPa, respectively. The non negligible influence of the Poisson's ratio was also underlined. The materials were characterized by a critical radius ranging from 0.4 to 500 μm. Data from graphite specimens were not included in that synthesis. The new analyses represent an extension of the previous database, with values of R_c close to the minimum and the maximum values of the previously considered range.

A synthesis in terms of the square root value of the local energy averaged over the control volume, normalised with respect to the critical energy of the material, as a function of the notch tip radius is shown in Figure 5.4.8 while the mean values detailed are listed in Table 5.4.3. Together with the new data, the normalised scatterband includes also previous results from V-shaped notches (Ayatollahi et al. 2011). The plotted parameter is proportional to the fracture load. Figure 5.4.8 makes it evident that the scatter of the data is quite limited, and independent both of the loading mode and the notch root radius. All the values fall well inside a band where the square root of the normalised SED ranges from 0.80 to 1.20. The synthesis confirms also that the choice of the crescent shape volume surrounding the highly stressed region is suitable to characterize the material behaviour under mixed mode loading.

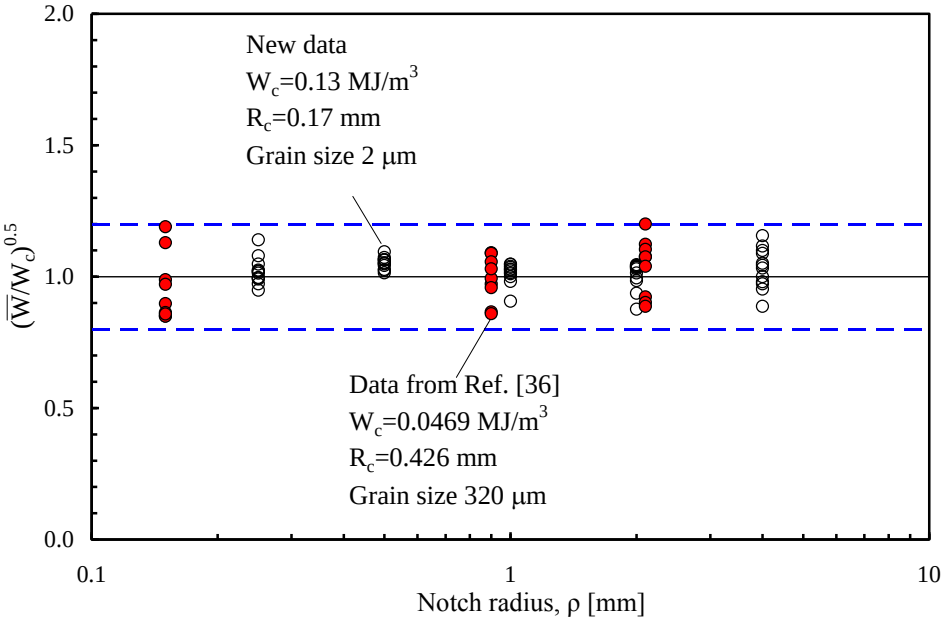

Figure 5.4.8. Scatterband summarising new data and old data taken from Ref. [36] based on an isostatic graphite with an average grain size equal to 320 μm and lower mechanical properties.

Table 5.4.3. Comparison between experimental and theoretical critical SED.

β [degrees]	ρ [mm]	$<\overline{W}>$ [MJ/m^3]	W_c [MJ/m^3]	$(\overline{W}/W_c)^{0.5}$
		FEM	Theor.	
0	0.25	0.1515	0.1314	1.074
	0.5	0.1435		1.045
	1	0.1263		0.98
	2	0.1146		0.934
	4	0.1163		0.941
30	0.25	0.1387	0.1314	1.027
	0.5	0.1441		1.047
	1	0.1353		1.015
	2	0.1412		1.037
	4	0.132		1.002
45	0.25	0.1345	0.1314	1.012
	0.5	0.1418		1.039
	1	0.1401		1.032
	2	0.1377		1.024
	4	0.1479		1.061
60	0.25	0.1242	0.1314	0.972
	0.5	0.1524		1.077
	1	0.139		1.029
	2	0.1399		1.032
	4	0.1662		1.124

5.5 Conclusions

Brittle fracture in U-notched isostatic graphite specimens is investigated both experimentally and theoretically under in plane mixed mode loading. Fracture tests are conducted on U-notched specimens subjected to different degrees of mode mixity, which ranges from pure Mode I to almost pure Mode II.

The *equivalent local Mode I* concept is used here in combination with an approach based on the mean value of the strain energy density (SED), which makes the fracture load assessment independent of the loading angle β. The isostatic graphite tested here is characterised by very low values of the grain size (2 μm) and the control volume (R_C=0.17 mm). This last value is very different from that detected in previous investigations (R_C=0.43 mm), where the mean grain size of the graphite was more than 300 μm. Different with respect to the previous studies is also the shape of the notches as well as the stronger variability of the notch tip radius, which ranges here from 0.25 mm to 4.0 mm.

The evaluation of the SED over a control volume rigidly rotated with respect to the Mode I case is justified by the analysis of the stress field along the inclined path perpendicular to the notch edge and starting from the point of the maximum elastic stress. The stress components along that line have been proven to be very close to the Mode I stress distributions along the notch bisector line.

It is shown that the method based on the local SED is suitable for the graphite stressed under mixed mode loading conditions, being the experimental loads to failure always in good agreement with the values estimated by assuming constant the mean value of the SED over the control volume. From the sound agreement between the theoretical and experimental results, it can be straightforward deduced that for the isostatic graphite the critical energy and the radius of the control volume are both material properties, which depend on the grain size. They do not depend on the in-plane mixed mode loading and the notch acuity and then they can be simply evaluated in pure Mode I loading. The synthesis confirms also the choice of a crescent shape volume which seems to be suitable to characterize the material behaviour under different mode mixities.

The experimental angles corresponding to the point of crack initiation are compared with the values obtained from the FE analyses on the basis of maximum

values of the principal stress and the strain energy density along the notch edge. The relative deviation is quite limited, but greater than that that exhibited from the critical loads to failure.

Future work should be planned to show whether, varying the materials, the constancy of the control radius under Mode I and Mode II loading remains a realistic assumption also in the presence of small scale yielding conditions. Another intriguing topic will be the extension of the SED approach to the cases of pure compression or combined compression and shear, which should require an update of the control radius R_c, due to the increase the critical strain energy density W_c with respect to the uniaxial tension case.

6

SED criterion on notched specimens under multiaxial cyclic loading

6.1Introduction

With reference to cracked and notched components a number of multi-axial predictive models were proposed in the last years (Lagoda et al. 1999, Carpinteri and Spagnoli 2001, Carpinteri et al. 2009, Ye et al. 2008, Nieslony and Sonsino 2008), often as variants of the critical plane approach formulated at the end of '80s by Fatemi, Socie and Kurath (Fatemi and Socie 1988, Fatemi and Kurath 1988). An overview on multiaxial fatigue is due to Fatemi and Shamsaei (2011) where some approximated models for fatigue life assessments are applied also in the presence of blunt notches. A comparison among different failure criteria, the volume-based strain energy density (SED) approach among the others, was carried out also by Sonsino and Nieslony (2008) considering a large bulk of experimental data from notched specimens.

Łagoda et al. (1999) suggested a criterion based on a damage parameter defined as the sum of the energies associated with the normal and shear strains on the critical plane. Calculations based on the critical plane approach for blunt notches with low stress concentrations were carried out also by Lazzarin and Susmel (2003). The critical plane approach was reviewed and modified by Carpinteri and Spagnoli (2001) and Carpinteri et al. (2009), who correlated the critical plane orientation with the weighted mean principal stress directions.

The extension of the critical plane criterion to sharp notches characterized by high stress concentrations is far from easy. In this ambit energy-based criteria find important applications. A thermodynamic analysis of cyclic plastic deformation was carried out by Ye et al. (2008) to establish an energy transition relation for describing the elastic–plastic stress and strain behavior of the notch-tip material

element in bodies subjected to uni-axial and multiaxial cyclic loads. According to the actual energy conversion occurring in the notch-tip material element during cyclic plastic deformation, a unified expression for estimating the elastic–plastic notch stress–strain responses in bodies subjected to multiaxial cyclic loads was developed. Neuber's rule (1961) and Glinka's ESED method (Molski and Glinka 1981, Moftakhar et al. 1995) represent two particular cases of Ye's formulation.

Recently seven different multiaxial fatigue criteria based on stress, strain and energy have been used to estimate the fatigue lives of double shear lap joint specimens of aluminum 2024-T3 with bolt clamped and interference fitted-bolt clamped fastener holes (Abazadeh et al. 2013). Another recent contribution (Cristofori et al. 2011) has proposed a frequency-domain formulation of a stress invariant based on a multiaxial fatigue criterion, called "Projection by Projection" (PbP) approach, suitable for estimating the fatigue life in presence of complex multiaxial loadings. The newly proposed spectral method has been validated with experimental data from the literature, concerning bending-torsion random loading, showing a general sound accuracy.

Dealing more specifically with energy-based approaches, worth mentionning is the pioneering work dated 1923 due to Jasper (1923), who used an energy-based parameter to analyze fatigue strength under tension–compression loadings. In the last years well known are the contributions by Ellyin (1989, 1997) who developed an energy based formulation where a combination of both the plastic and elastic strain work could be efficiently used as a damage parameter in multiaxial fatigue. In a review by Macha and Sonsino (1999) on energy based multiaxial fatigue life criteria, it is shown that energy based formulations are good candidates when dealing with loadings presenting complex temporal histories.

In a very recent contribution by Saintier et al. (2013), a fatigue life assessment method is proposed for proportional and non-proportional multiaxial variable amplitude loadings in the range 10^4–10^7 cycles. This method, which is based on the *non-local energy*, takes its origins from a previous contribution by Palin-Luc and Lasserre (1998), later extended to multiaxial loading under constant amplitude by Banvillet et al. (2003). The new proposal consists of a complete reformulation and extension of the previous energy-based fatigue strength

criterion. It includes two major extensions with respect to the past: the former is represented by a fatigue criterion for multiaxial variable amplitude loadings, the latter by an incremental fatigue life assessment method for proportional and non-proportional multiaxial variable amplitude loadings. The criterion is applicable to un-notched components as well as to components with notches with low stress concentration effects. The new method has been successfully applied to a variety of materials (Saintier et al. 2013).

Theoretical and experimental difficulties arising in multi-axial fatigue testing and in the interpretations of the results were discussed in the past by several researchers. Prediction of the branch crack threshold condition under mixed mode (I+III) was suggested by Pook and Sharples (1979) through the analysis of the main crack tip stress field. Pook (1985) pointed out that it is necessary to distinguish between the different thresholds for the initiation of crack growth, crack arrest and specimen failure. It was clearly shown by Tong et al. (1986) that a definition of a fatigue threshold ΔK_{th} under poly-modal loading is far from easy mainly because under torsion loading an extensive plastic zone is developed at the tip of a Mode III crack. The presence of yielding in conjunction with the dissipative phenomena due to the possible contact of the crack flanks results in a strong influence of the specimen geometry on the test data. The intrinsic and extrinsic mechanisms producing shielding effects during fatigue crack propagation were classified by Ritchie (1988) whereas near threshold fatigue crack propagation was examined by Yu et al. (1998) and by Tanaka et al. (1999). The crack propagation rate decreased with crack extension because of the shear contact of the crack faces causing an increase in friction, abrasion and interlocking. Recently the mechanisms of crack propagation were examined also by Pippan et al. (2011) dealing with ductile metallic materials. Particular attention is paid to the analysis of the various parameters, the environment, the short cracks, the small and large scale yielding conditions. It was underlined the essential role played by the crack propagation mechanisms: a methodology developed for a certain material and loading case can be applied to other materials under similar loading conditions only when the fatigue crack propagation mechanisms are the same.

A novel mathematical model of the stresses around the tip of a fatigue crack, which considers the effects of plasticity through an analysis of their shielding effects on the applied elastic field was developed by Christopher et al. (2007). The ability of the model to characterize plasticity-induced effects of cyclic loading on the elastic stress fields was demonstrated using the full field photoelasticity and displacement image correlation technique (Christopher et al. 2008, Colombo et al. 2010, James et al. 2013b). In parallel the complex initiation of crack growth under a combination of opening and anti-plane shearing mode loading was studied by Lin et al. (2010) showing that the cracks do not grow through a continuous evolution of the crack surface but rather by means of an abrupt fragmentation or segmentation of the crack front.

Worth mentioning are also two recent papers by Tanaka (2012). Circumferentially notched bars of austenitic stainless steel, SUS316L, and carbon steel, SGV410, with three different notch-tip radii were fatigued under cyclic torsion without and with static tension. The main result was that in pure cyclic torsion, the fatigue life of circumferentially notched bars of austenitic stainless steel SUS316L was found to be longer than that of smooth bars. This effect was found to be longer with increasing stress concentration under the same amplitude of the nominal shear stress on the net transverse area. The anomalous behavior of the notch-strengthening effect was ascribed to the larger retardation of fatigue crack propagation by crack surface contact for the sharper notches. The superposition of static tension on cyclic torsion of SUS316L reduced the retardation due to the smaller amount of crack surface contact, which gave rise to the well-known notch-weakening of the fatigue strength. A '*notch-strengthening*' effect was found also in SGV410 (Tanaka 2012) under cyclic torsion with and without static tension, as well as in a recent work dealing with sharply V-notched specimens made of 39NiCrMo3 steel (Berto et al. 2011c). Here all data from multiaxial loads were re-analysed in terms of strain energy density (SED) averaged over a control volume.

Dealing with multi-axial fatigue strength data from specimens with mild notches, the deviatoric SED at the notch tip has already been used by Park and Nelson (2000) to predict the fatigue behavior under multi-axial stresses. That point-wise

approach cannot be applied to sharply notched components due to the high stress gradients surrounding the notch tips. With the aim to overcome this problem, a volume-based SED approach originally proposed for plane problems in the presence of stress singularity due to sharp, zero radius, V-notches and cracks (Lazzarin and Zambardi 2001) has been extended to multiaxial fatigue conditions (Berto et al. 2011c, Lazzarin et al. 2004-2008b, Atzori et al. 2006, Berto et al. 2008, Berto and Lazzarin 2011) as well as to the case of quasi-brittle failure of a variety of brittle and quasi-brittle materials [ceramics (Lazzarin et al. 2009b), graphite (Berto et al. 2012c), PMMA (Berto et al. 2013c)] under static loads. In parallel, the link between averaged SED and the notch rounding concept was discussed in detail by Radaj et al. (2009a-2009b) with reference to welded joints under fatigue loading conditions.

The averaged SED was used in Atzori et al. (2006) to summarize about 300 fatigue data from sharply notched axis-symmetric specimens made of a medium carbon steel (C40) under combined tension and torsion loadings keeping unchanged the control volume. This simplifying assumption was not valid for the 39NiCrMo3 steel weakened by circumferential quasi-sharp V-notches (Berto et al. 2011c) due to strong dissipative phenomena provoked in this steel by torsion loads even in the high cycle regime. The length of non-propagating cracks detected in run-out specimens varied as a function of the loading conditions. Since under Mode III loading the control volume radius was strongly influenced by extrinsic shielding mechanisms, a single SED-based scatterband was possible only adapting the control volume to the loading mode. Moreover, the out-of-phase data were excluded from the synthesis, being such data located visibly below the lower limit of the scatterband for the 39NiCrMo3 steel. This phenomenon was not detected for C40 steel (Atzori et al. 2006).

The volume-based SED approach was used also in Berto and Lazzarin (2011) where fatigue strength properties of 13 series of plain and notched specimens made of AISI 416 (at hardened and tempered state) were determined under tension, torsion and combined tension and torsion, both in-phase and out-of-phase. Also for this steel, two distinct radii of the control volume were necessary under torsion and tension loading due to presence of strong non-linear effects. The

SED was called ‘apparent linear elastic SED’ to remember that the evaluation of the strain energy in two different volumes (for tension and torsion) allows us to overcome the problem tied to shielding mechanisms maintaining a linear elastic model. The fact that under torsion loading plasticity might play an important role also when tensile loading induces effects fully contained within the linear elastic field is deeply discussed in Lazzarin and Berto (2008). The different inverse slope of the fatigue curves under tension and torsion loadings has been motivated by means of some elasto-plastic finite element analyses aimed to show the difference effect of plasticity under the above mentioned loading conditions. An extensive review of the volume-based SED approach was presented in Berto and Lazzarin (2009).

6.2 Aims of the work

The present work deals with multiaxial fatigue strength of 40CrMoV13.9. The tested material is characterized by four different heat treatments able to assure a high strength at room and elevate temperatures. The most important applications are cold or hot rolling of magnesium and aluminium alloys. The service conditions are usually characterized by a complex stress state combined with aggressive in-service conditions. The 40CrMoV13.9 steel combines very good static and fatigue properties with an excellent wear resistance, also at high temperature and in corrosive environments. At the best of author’s knowledge, a complete set of data from notch specimens under torsion and combined tension and torsion loadings are not available in the literature for 40CrMoV13.9 whereas other Cr steels have been widely investigated (see, among the others, Nian et al. 1984, Bai-ping et al. 1987, Bai-ping and Nian 1989, Nian and Bai-ping 1995, Terres et al. 2012, Terres and Sidhom 2012). In particular, the effect on microstructure and fatigue threshold of pure tension fatigue at a stress level below the fatigue limit and high cycle regime has been studied in Nian et al. (1984), Bai-ping et al. (1987), Bai-ping and Nian (1989), Nian and Bai-ping (1995). Those works considered a 12Cr steel and a 40Cr steel under different heat treatments. The effects of nitriding and shot-peening treatments on the tensile fatigue behavior of 42CrMo4 steel have been investigated in Terres et al. (2012) and

Terres and Sidhom (2012) considering notches of different acuity. The phenomenon of fatigue is critical in many sectors, not only dealing with structural steels (Li et al. 2013). It is a common task for engineers engaged in fatigue problems to search suitable solutions for improving the life of the components both acting on the material (see, for example, Bagherifard et al. 2013) and on the geometry of the components.

The absence of data from 40CrMoV13.9 steel under multiaxial fatigue loading has motivated the present work. Circumferential V-notched and semicircular notched specimens have been tested under combined tension and torsion loading, both in-phase and out-of-phase. The results of one-year experimental programme consists of 10 new fatigue curves corresponding to more than 120 fatigue data.

The behaviour at medium and high cycle fatigue is found to be within the elastic regime without any particular non-linear elastic effect. The approach based on the strain energy density averaged on a control volume will be employed to summarise all the data in a single scatterband. A single value of the control volume, evaluated accordingly to the threshold stress intensity range reported in Nian et al. (1984), Bai-ping et al. (1987), Bai-ping and Nian (1989) for 40Cr steels characterized by similar heat treatments, will be used in the synthesis, independent of the loading mode.

The chapter is structured in the following way: in the first section, the experimental work is described including specimen geometries, testing procedures and experimental results. The second section is focused on the discussion of the new experimental results as well as it is aimed to present the synthesis of all data in terms of averaged SED.

6.3 Material properties and specimens geometry

Static tensile tests were carried out to evaluate the elastic and the strength properties of 40CrMoV13.9 steel, see Table 6.3.1. The chemical composition of the material is reported in Table 6.3.2. The heat treatment schedules that characterize the tested material are shown in Table 6.3.3. The material was first quenched at 920°C and subsequently tempered at about 580°C twice. A final

stress relieving treatment at 570°C was carried out. The final microstructure was characterized by a high strength bainitic martensitic structure.

The geometries of the specimens tested in the present investigation are shown in Figure 6.3.1. The axis-symmetric V-notched specimens were characterized by a depth d = 4 mm, and an opening angle equal to 90°. Constant was also the notch root radius, 1 mm. The semicircular specimens presented instead a notch root radius of 4 mm (Figure 6.3.1b).

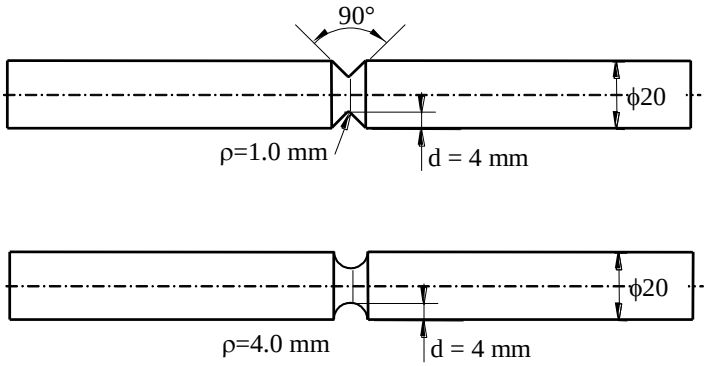

(a)

(b)

Figure 6.3.1. Geometry of V-notches and semicircular notches (a) and details of the notch tip (b)

All tests were performed under load control on a MTS 809 servo-hydraulic bi-axial testing device (±100 kN, ± 1100 Nm, ± 75mm/± 55°). The load was measured by a MTS cell with ± 0.5 % error at full scale. The specimens were tested under pure tension, pure torsion and multiaxial tension-torsion loading with different biaxiality ratios ($\lambda=\tau_a/\sigma_a$=0.6 and 1.0). In particular, 10 series of fatigue test were conducted, according to the following subdivision:

- Two series of tests on notched specimens (V and semicircular notches) under pure torsion fatigue loading (nominal load ratio R=-1);
- One series of tests on V-notched specimens under pure tension fatigue loading (R=-1).
- Two series of tests on V-notched specimens under combined tension-torsion fatigue loading, with biaxiality ratio λ=1, load ratio R=-1, load phase angle Φ=0° and Φ=90°;
- Two series of tests on V-notched specimens under combined tension-torsion fatigue loading, under constant biaxiality ratio λ=0.6, load ratio R=-1, load phase angle Φ=0° and Φ=90°;
- Two series of tests on semicircular specimens under combined tension-torsion fatigue loading, with biaxiality ratio λ=1, load ratio R=-1, load phase angle Φ=0° and Φ=90°;
- One series of tests on semicircular specimens under combined tension-torsion fatigue loading, with biaxiality ratio λ=0.6, load ratio R=-1, load phase angle Φ=0°.

Table 6.3.1. Mechanical properties of 40CrMoV13.9.

Ultimate tensile strength (MPa)	Yield stress (MPa)	Elongation to fracture (%)	Brinell Hardness
1355	1127	15.2	393-415

Table 6.3.2. Chemical composition wt.%, balance Fe.

C	Mn	Si	S	P	Cr	Ni	Mo	V	Al	W
0.38	0.5	0.27	0.006	0.003	3.05	0.24	1.04	0.24	0.013	0.005

Table 6.3.3. Heat treatment schedules

	Heat treatment	Heating ratio (°C/h)	Temperature (°C)	Holding (hours)	Cooling
1	Quenching	100	920° ± 10°	3	water
2	Tempering 1	100	580° ± 10°	5	air
3	Tempering 2	100	590° ± 10°	5	air
4	Stress relieving	100	570° ± 10°	3	air

6.4Results from fatigue tests

Before being tested, all specimens have been polished in order to both eliminate surface scratches or machining marks and to make the observation of the fatigue crack path easier. As stated above, fatigue tests have been carried out on a MTS 809 servo-hydraulic biaxial machine with a 100 kN axial load cell and a torsion load cell of 1100 Nm. All tests have been performed under load control, with a frequency ranging from 1 to 10 Hz, as a function of the geometry and load level. At the end of the fatigue tests, the notch root and the fracture surfaces were examined using optical and electronic microscopy.

The results of statistical analyses carried out by assuming a log-normal distribution are summarised in Table 6.4.1. In particular, it is summarised the mean value of the nominal stress amplitudes at different number of cycles, the inverse slope k of the Wöhler curves and the scatter index T, which gives the width of the scatterband related to 10 - 90% probabilities of survival. All failures from 10^4 to $5x10^6$ have been processed in the statistical analysis whereas run-outs were excluded.

Figure 6.4.1 depicts fatigue data from V-notched specimens tested under tension, torsion and combined tension and torsion with different load phases (0° and 90°). In this case the biaxiality ratio was equal to 1. It is evident from the figure that the out of phase loading causes a slight but visible detrimental effect on the fatigue life of the V-notched specimens, almost independent of the number of cycles.

Figure 6.4.2 summarizes fatigue data from V-notched specimens tested under multiaxial fatigue at a biaxiality ratio λ=0.6, both in-phase and out-of-phase. The two mean curves are compared with the curve from pure tension. It is possible to observe that multiaxial loading decreases the fatigue life with respect to the tensile loading. Also for λ=0.6 the out-of-phase loading is more damaging.

Table 6.4.1. Results from fatigue tests. P_s=50%. Stresses referred to the net area.

Series	Load	N		k	T_σ or T_τ	σ_a or τ_a		
						10^6	$2\ 10^6$	$5\ 10^6$
1	Torsion R= -1	16	τ	13.33	1.144	281.16	266.91	249.18
2	Multiaxial R=-1, Φ=0°, λ=1.0	14	σ	9.39	1.176	182.6	169.91	153.84
3	Multiaxial R=-1, Φ=90°, λ=1.0	13	σ	7.67	1.428	145.83	133.23	118.23
4	Tension R= -1	12	σ	8.42	1.335	253.69	233.64	209.55
5	Multiaxial R=-1, Φ=0°, λ=0.6	12	σ	9.9	1.202	214.61	200.10	182.41
			τ			128.77	120.06	109.45
6	Multiaxial R=-1, Φ=90°, λ=0.6	13	σ	7.63	1.485	187.45	171.17	151.8
			τ			112.47	102.7	91.08
7	Torsion R= -1 Semicircular	11	τ	14.27	1.160	367.17	349.76	328.01
8	Multiaxial R=-1, Φ=0°, λ=1.0 Semicircular	15	σ	7.68	1.268	239.57	218.9	194.28
9	Multiaxial R=-1, Φ=90°, λ=1.0 Semicircular	17	σ	10.79	1.260	263.82	247.4	227.26
10	Multiaxial R=-1, Φ=0°, λ=0.6 Semicircular	12	σ	11.45	1.307	332.64	313.10	289.02
			τ			199.58	187.86	173.41

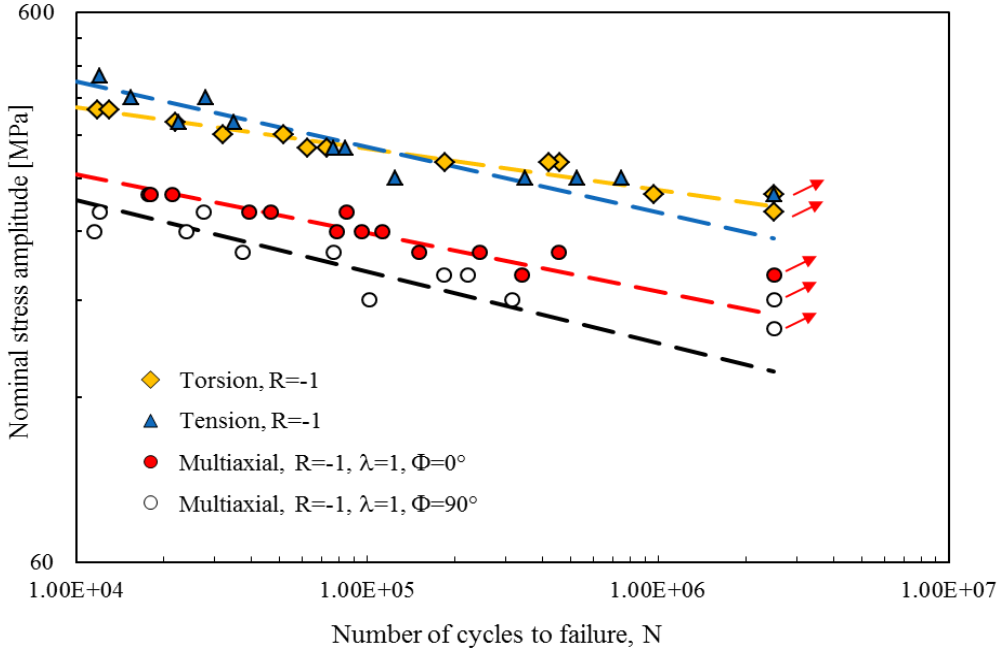

Figure 6.4.1. Data from V-notches under pure tension, torsion and multiaxial loading (λ=1)

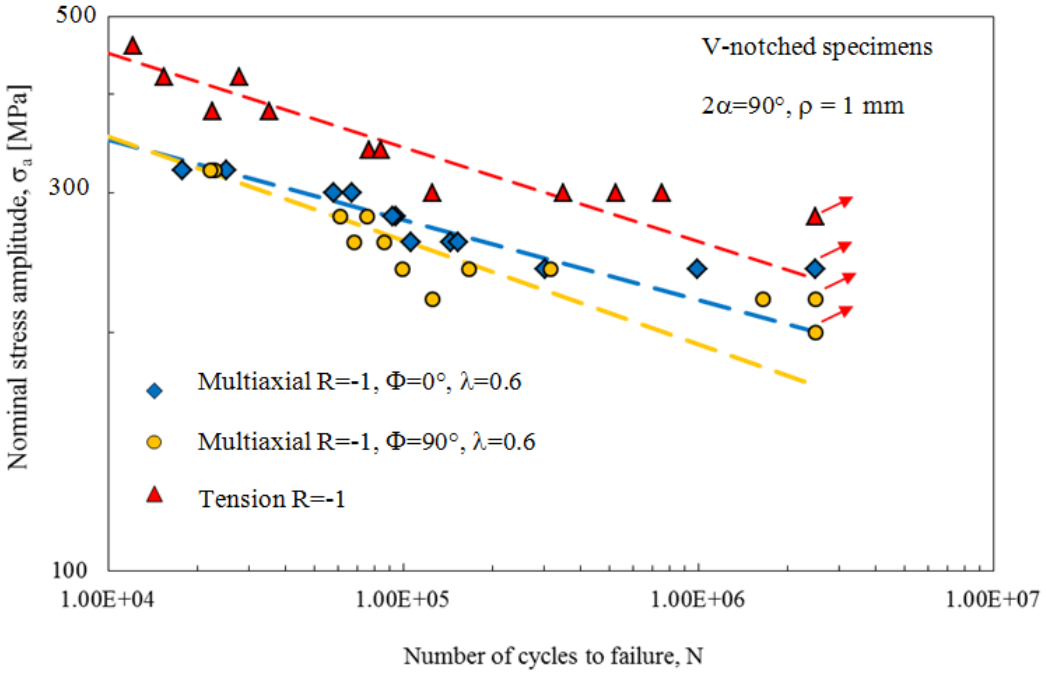

Figure 6.4.2. Data from V-notches under multiaxial loading (λ=0.6): comparison with pure tension

Figure 6.4.3 reports the fatigue curves related to semicircular notches. In particular it summarises the curves from pure torsion, multiaxial loading with λ=1 (in phase and out-of-phase) and multiaxial loading with λ=0.6 (only in phase). In this case it is interesting to observe that for this particular notch radius and specimen geometry the out-of-phase loading is slightly beneficial with respect to in-phase loading at high cycle regime while the fatigue strength is the same at low cycle regime. This means that the non-proportional loading effect may be different not only for different materials but also for the same material by moving from a sharply notched specimen to a specimen with a large notch root radius.

A distinction between sharp and blunt notches has been drawn in Atzori-Lazzarin's diagram (Atzori et al. 2003) mainly on the basis of the product of the squared stress concentration factor and a characteristic length of the material, eventually modified by a shape factor. Notch sensitivity and defect sensitivity were seen as two sides of the same medal. The local SED allows a natural transition between the fatigue strength of the parent material and that of the notched components (Lazzarin and Berto 2005b), independent on the notch acuity, keeping constant R_c.

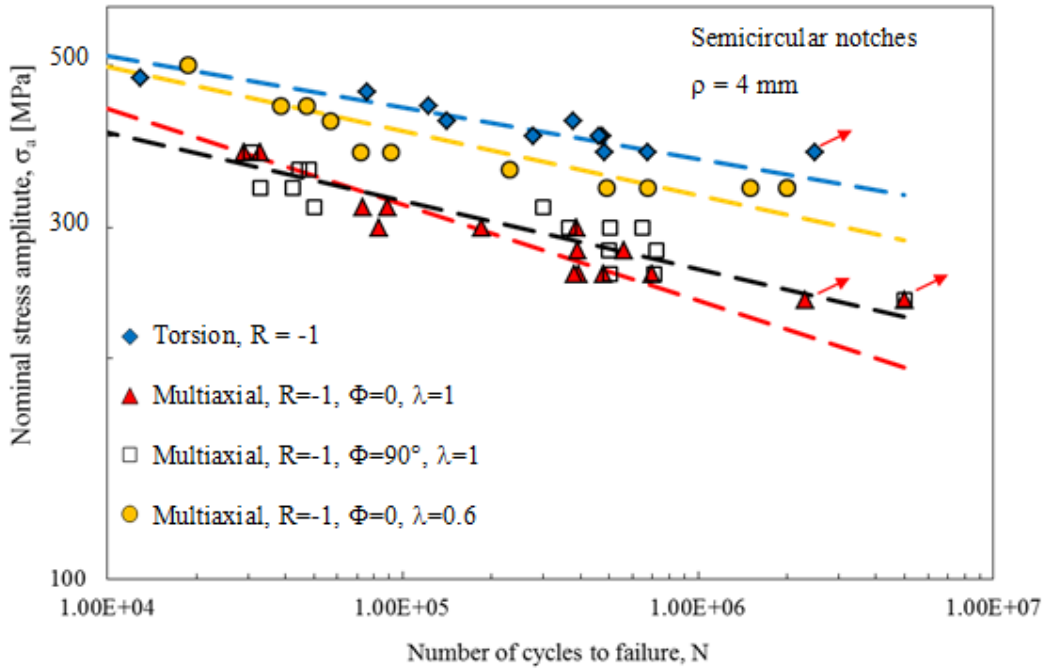

Figure 6.4.3. Data from semicircular notches under pure torsion and multiaxial loading (λ=0.6 and 1)

6.5 Fracture surfaces of V-notches

The failure surface of a V-notched specimen broken after 970000 cycles under torsion is shown in Figure 6.5.1a. The outer diameter of the fracture surface is largely flat, suggesting a Mode III fracture mechanism. The classical Mode I 'factory roof' morphology is also evident in large areas of the centre of the fracture surface together with evidence of abrasion mainly on the bottom hand side of the image.

Figure 6.5.1b shows the image of a specimen broken at 83000 cycles under tension loading. The surface is flat, some small signs of abrasion are present and it is well distinguishable the zone corresponding to the final static failure which generally tends to decrease in size at high cycle regime.

Generally for V-notches, in presence of torsion loading, the crack nucleated at 30% of the fatigue life and all the rest of the life was spent in crack propagation. Under pure tension approximately 80% of the fatigue life was spent in crack nucleation and only the final part of the life was spent in crack propagation. By avoiding to interrupt the tests, the presence of the crack was detected by means of

an optical microscope used to monitor the notch tip state during the fatigue life of the specimen. Generally a limited but distinguishable quantity of debris and powder was emanated from the notch tip when a visible crack was detected and started to propagate significantly.

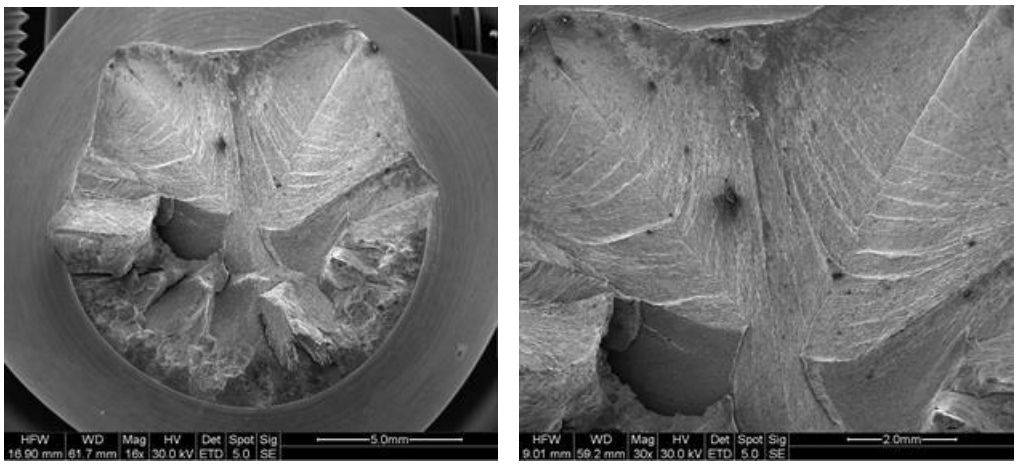

Pure torsion, N=970000, τ_a=280 MPa

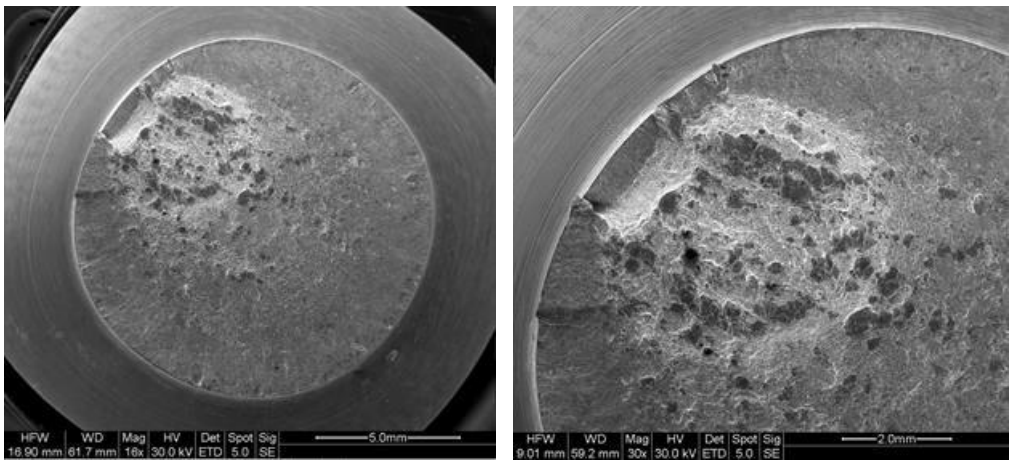

Pure tension, N=84000, σ_a=340 MPa

Figure 6.5.1. Fracture surfaces from V-notched specimens under pure torsion (a) and pure tension (b)

Fatigue damage is generally described as the nucleation and growth of cracks to final failure, although the differentiation of two stages is "qualitatively distinguishable but quantitatively ambiguous", as underlined by Jiang and Feng (2004). No demarcation line being drawn between fatigue crack initiation and early micro-crack propagation inside the control volume, both phases are thought of as strictly dependent on the averaged SED initially present on the uncracked

specimens.

Fracture surfaces of some specimens tested under multiaxial conditions are shown in Figure 6.5.2a and 6.5.2b. All the specimens were from tests at the same phase angle, Φ=0, and at the same bi-axiality ratios: λ=1. A general comment on the two figures is the presence of the 'factory roof' morphology extending from the initial notch root. This changes to a single, inclined fracture surface as one of the Mode I crack becomes dominant. The detail differences between the in-phase and out-phase loading cases are discussed below.

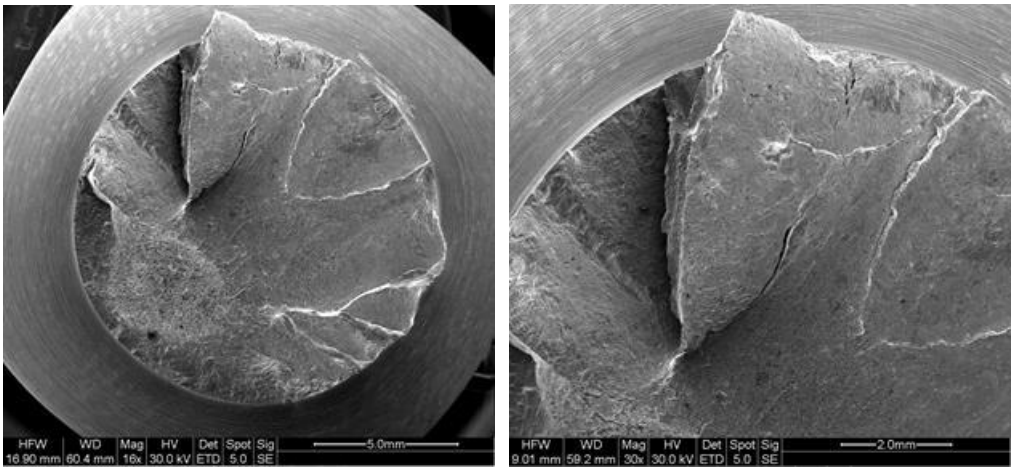

Multiaxial fatigue, N=456750, σ_a=220 MPa, λ=1, Φ=0°

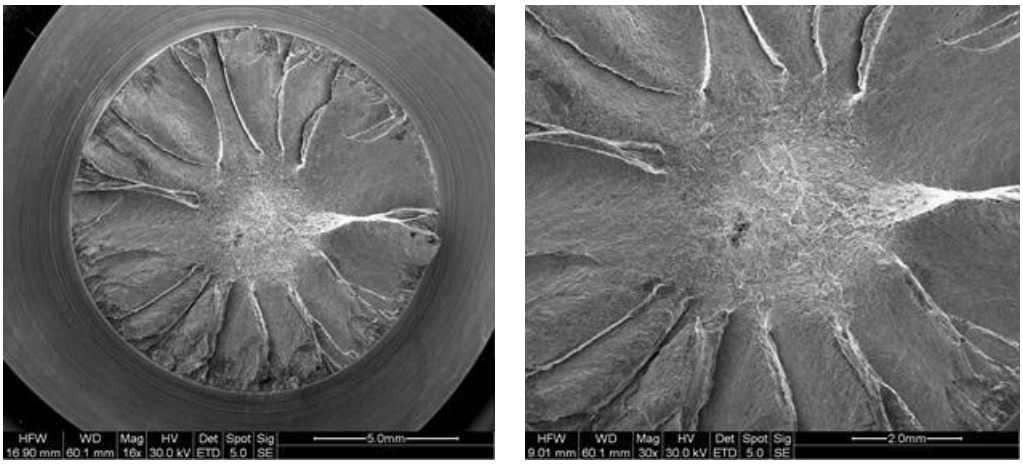

Multiaxial fatigue, N=151000, σ_a=220 MPa, λ=1, Φ=0°

Figure 6.5.2. Fracture surfaces from V-notched specimens under in-phase multiaxial loading

By considering in-phase loading cases shown in figure 6.5.2, some observations can be made:

- At medium-high cycle regime, few cracks nucleate, and the crack propagation phase takes a significant fraction of the fatigue life of the specimen. Under low-cycle fatigue, the number of initiated cracks generally increases, and the propagation phase is much reduced (see Figure 6.5.3);
- The inclination of the planes of crack propagation is less than the 45° that occurs under pure torsional loading. This is due to the change in the angle of the opening displacements from 45° to 0° as the level of axial load increases;
- The irregular surface corresponding to the final static failure is not perpendicular with the specimen axis, indicating a non-uniform crack propagation front from the outside toward the centre of the specimen;

The fracture surface morphology of specimens tested was strongly influenced by the phase angle. Signs of micro abrasions may be observed on all fracture surfaces and the extent to which the rubbing occurred appears to depend on phase angle. Most visible abrasion appears to occur at $\lambda=0.6$ or $\lambda=1$ and $\Phi=90°$ resulting in a smooth featureless fracture topography. Small spherical oxide debris, evidence of wear, can be observed in the scanning electron micrographs (see Figure 6.5.4a and 6.5.4b).

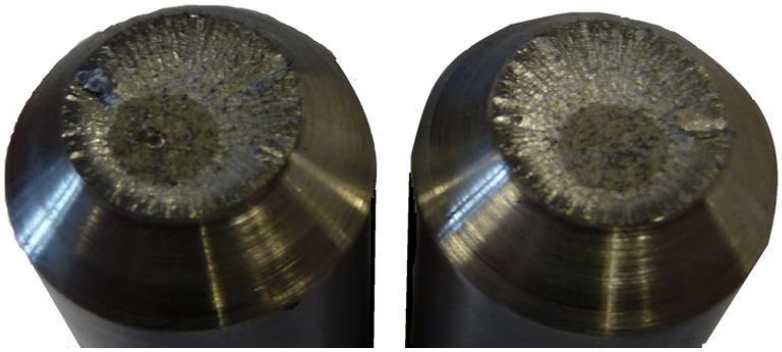

Figure 6.5.3. Fracture surfaces from V-notched specimens under multiaxial fatigue: $\lambda=0.6$ and $\Phi=0°$

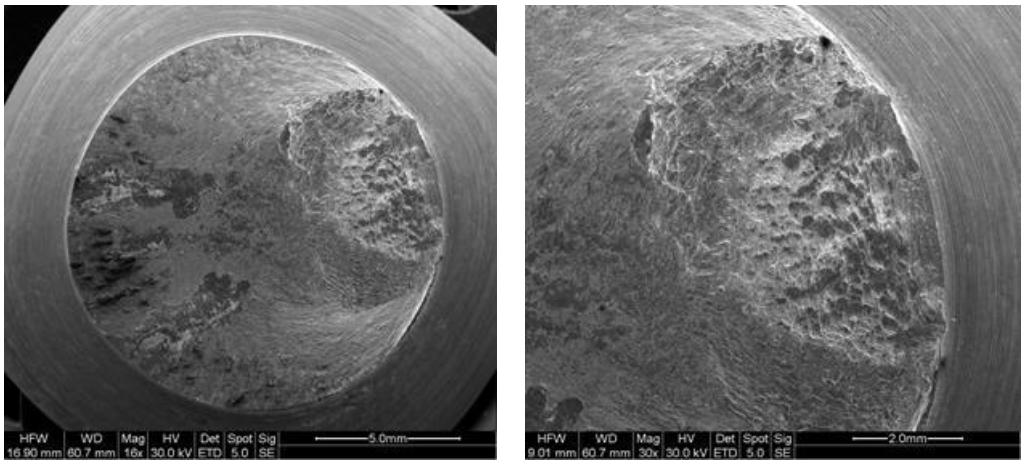

Multiaxial, N=94698 , σ_a=280 MPa, λ=0.6, Φ=90°

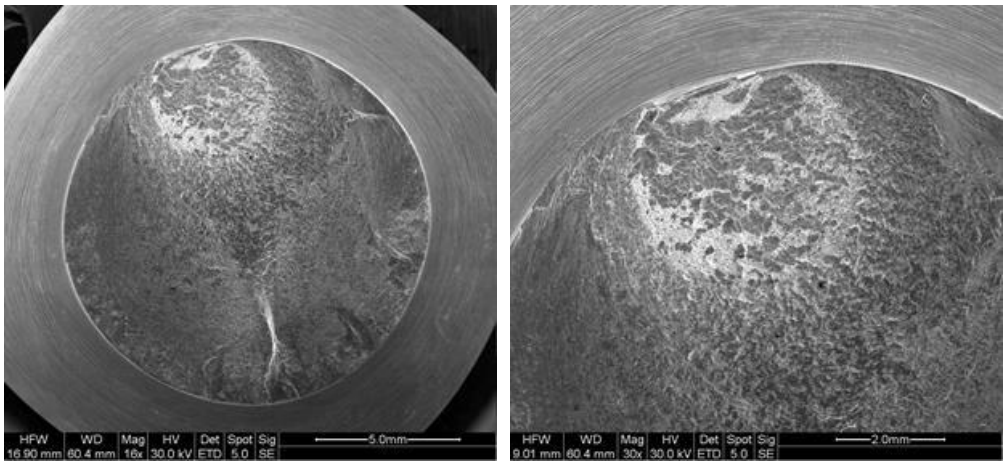

Multiaxial, N=27500 , σ_a=260 MPa, λ=1, Φ=90°

Figure 6.5.4. Fracture surfaces from V-notched specimens under multiaxial fatigue: λ=0.6 and Φ=90° (a), λ=1 and Φ=90° (b)

The main features were as follows:

- The fracture surfaces are generally flatter than those from in-phase tests. This may be due to the increased abrasion observed in these tests.
- In the zone of crack initiation micro abrasions due to the interference between the mating surfaces are well visible. During the tests, in fact, the two surfaces of the cracks slightly scrape each other.

6.6Fracture surfaces of semicircular notches

Semicircular notches were characterized by different fracture surfaces with respect to V-notches. For this kind of notches the main part of the fatigue life was spent in the crack initiation and only a small part, approximately equal to 10%, was spent in the crack propagation with visible debris emanated by the notch tip. Some differences were observed under in-phase and out-of-phase loading. Figure 6.6.1a-b show the final crack propagating at notch tip under in-phase and out-of-phase loading: under in-phase loading the crack branching is visible while it is absent under out-of-phase loading. This effect does not influence substantially the fracture surfaces which generally do not present clear planes of crack propagation (see Figure 6.6.2a-b). They appear only slightly more flat under out-of-phase loading (see Figure 6.6.2b).

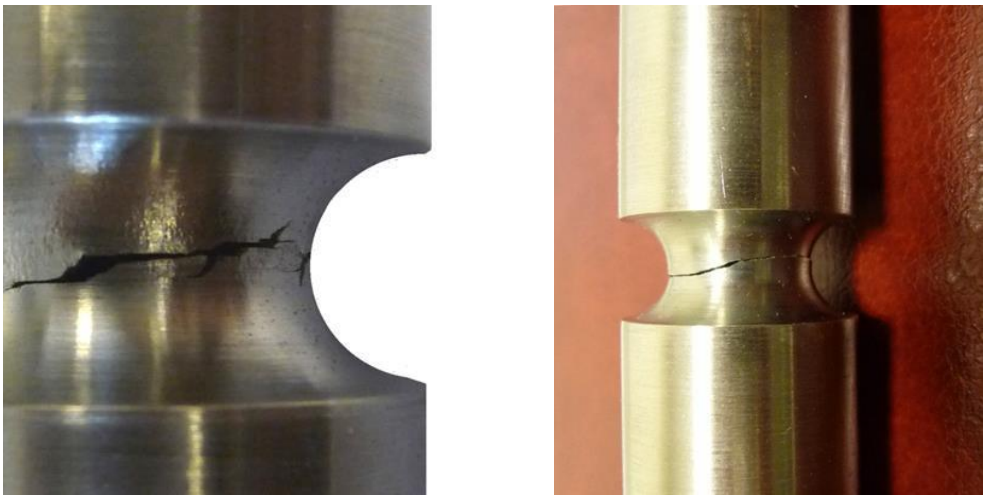

Figure 6.6.1. Typical crack propagating from a semicircular notch under multiaxial loading under in phase and out-of-phase loading

Figure 6.6.2. Typical fracture surface from a semicircular notch under multiaxial loading: in phase (a) and out-of-phase (b)

6.7 **A synthesis in terms of linear elastic SED averaged over a control volume**

The averaged strain energy density criterion (SED) states that brittle failure occurs when the mean value of the strain energy density over a given control volume is equal to a critical value W_c.

This critical value varies from material to material but does not depend on the notch geometry and sharpness and the criterion can be applied to sharp notches (also with $\rho = 0$) as well as to blunt notches. In Beltrami's original formulation W_c does not depend on the loading mode.

In the particular case of 40CrMoV13.9 steel the radius of the control volume R_c has been estimated here by using the fatigue properties of a quenched and tempered 40Cr steel reported in Nian et al. (1984), Bai-ping et al. (1987), Bai-ping and Nian (1989) which presented a chemical composition, a static strength analogous to those of the material considered herein. Also the heat treatments were almost coincident. In particular the threshold value of stress intensity factor range ($\Delta K_{th} = 6\ MPa\sqrt{m}$ at R=0) from pure tension fatigue and the fatigue limit range of plain material, $\Delta\sigma_A$ at R=0 (430 MPa), taken from Nian et al. (1984) have been used. Moreover in Nian et al. (1984) the trend of the threshold stress intensity factor and of the ultimate tensile strength is plotted as a function of the tempering treatment temperature. For tempering temperature higher than 500°C, ΔK_{th} reaches almost a plateau value equal to 6 MPa $m^{0.5}$.

A convenient expression for the critical radius is as follows (Berto et al. 2011c, Lazzarin et al. 2008b):

$$R_c = \left(\frac{\sqrt{2e_1}\ \Delta K_{th}}{\Delta\sigma_A} \right)^2 \tag{6.7.1}$$

where e_1 is equal 0.1345 (Park and Nelson 2000). By using Eq. (6.7.1) in combination with the material properties reported above, the estimated control radius is equal to 0.05 mm. A characteristic length equal to about 0.05 was found by Li Nian et al. (1984) for the 12CrNi3 steel, characterized by a tempering temperature equal to 600° and by a threshold stress intensity factor range equal to 6.4 $MPam^{0.5}$.

Dealing with V-shaped notches the control volume is as shown in Figure 6.7.1a; the volume assumes a crescent shape and it is centred at the distance r_0 from the notch tip. The distance r_0 depends on the notch radius, ρ, and the notch opening angle, 2α according to the simple Eqs (6.7.2, 6.7.3) (Lazzarin et al. 2008b) derived from Neuber's conformal mapping:

$$q = \frac{2\pi - 2\alpha}{\pi} \tag{6.7.2}$$

$$r_0 = \frac{q-1}{q}\rho \tag{6.7.3}$$

For semicircular notches under Mode I and III loadings, the volume assumes the crescent shape shown in Fig. 6.7.1b, where R_c is the depth measured along the notch bisector line. The outer radius of the crescent shape is equal to $R_c+\rho/2$, being $\rho/2$ the distance between the notch tip and the origin of the local coordinate system.

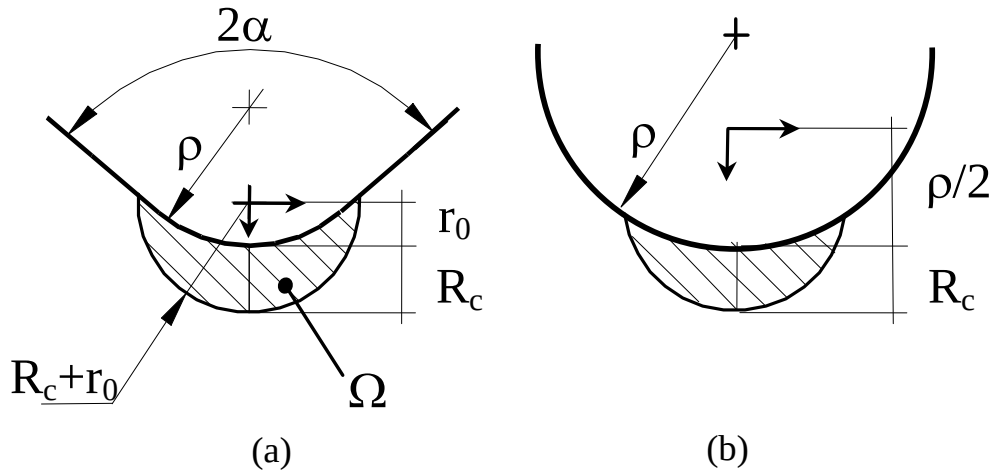

Figure 6.7.1. Critical volume for V-shaped notches(a) and semicircular notches(b)

The value of the SED averaged over the control volume has been calculated numerically by using the FE code ANSYS 12.0® both for V-notches and semicircular notches.

Being in this case the nominal load ratio constant and equal to R=-1 the synthesis based on the SED has been carried out directly with the values obtained by the numerical simulations. Without entering in the details, it is worth mentioning that the effect of different nominal load ratios can be quantified by introducing the parameter c_w, as made in previous works (Lazzarin et al. 2004, Atzori et al. 2006, Lazzarin et al. 2008b). As applied here the averaged SED approach is not sensitive to the variation of the phase angle. To fully take into account the effect of the out-of-phase loading, which varies from material to material, the radius of

the control volume should be updated by using a specific information from cracked or sharply V-notched specimens tested under out-of-plane loading conditions. Two parameters are not sufficient, a third parameter is necessary.

Figure 6.7.2 shows the final synthesis based on the averaged SED. Since all data come from specimens tested under the same nominal load ratio, R=-1, the coefficient c_w=0.5 is not introduced herein (Berto et al. 2011c, Lazzarin et al. 2004, Atzori et al. 2006, Lazzarin et al. 2008b). c_w should be taken into account when the comparison would involve different steels tested under different nominal load ratios.

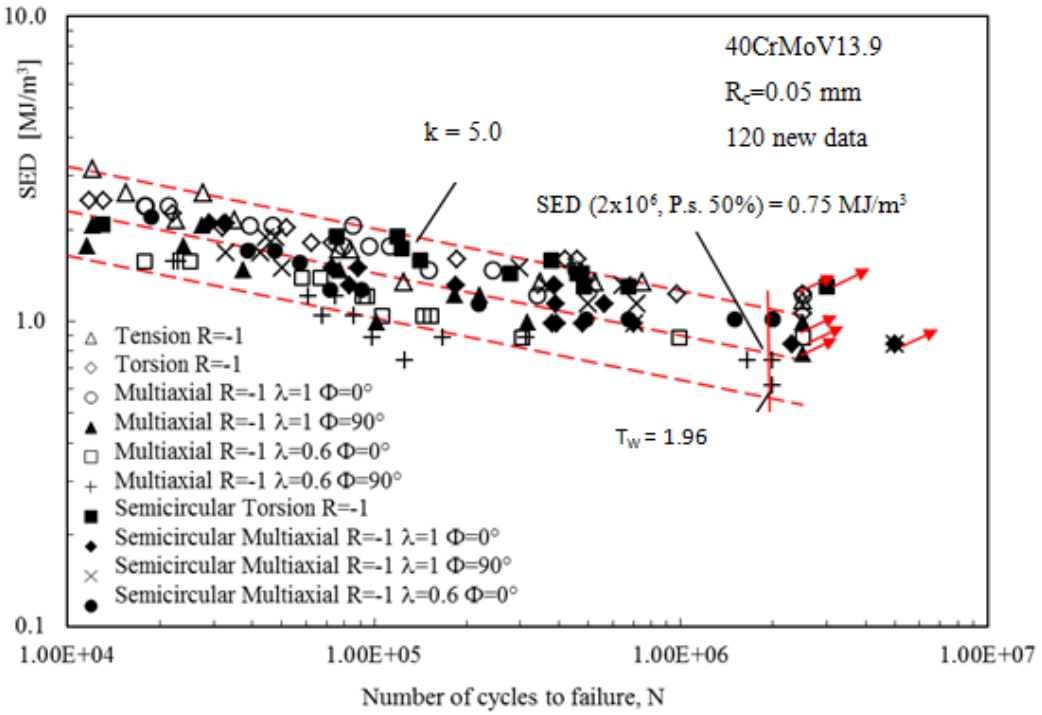

Figure 6.7.2. Synthesis by means of local SED of multiaxial series data

The scatter index T_W, related to the two curves with probabilities of survival P_S= 10% and 90%, is 1.96, to be compared with the variation of the strain energy density range, from about 2.5 to about 0.75 MJ/m^3. T_W=1.96 becomes equal to 1.40 when reconverted to an equivalent local stress range with probabilities of survival P_s=10% and 90%. The inverse slope of the scatterband is equal to 5.0.

At the light of the present results and application of the SED criterion it is clear that a single value of the control volume, independent of the loading modes, is sufficient to characterize the multiaxial fatigue behavior of 40CrMoV13.9 steel.

This result was not known *a priori* and usually depends on the tested material. In some previous works it has been shown that different phenomena can influence the size of the control volume under different loading modes (Berto et al. 2011c, Berto and Lazzarin 2011). These effects have been recently investigated also in Tanaka (2012) dealing with notched bars of austenitic stainless steel, SUS316L, and carbon steel, SGV410, with three different notch-tip radii. It has been shown that, under torsion loading, the fatigue life of circumferentially notched bars of austenitic stainless steel SUS316L is longer than that of smooth bars. This effect has been found to be longer with increasing stress concentration under the same amplitude of the nominal shear stress on the net transverse area. The anomalous behavior of the notch-strengthening effect was ascribed to the larger retardation of fatigue crack propagation by crack surface contact for the sharper notches. In fact, strong dissipative phenomena and extrinsic shielding mechanisms may be present in some steels under torsion loading also in the high cycle regime (Berto et al. 2011c). Moreover, it plays a fundamental role the fact that under torsion loading plasticity might be induced also when tensile loading induces effects fully contained within the linear elastic field (Lazzarin and Berto 2008). All these combined effects can influence the fatigue life under multiaxial loading and, in some cases, these dissipative phenomena are not easy to be clearly distinguished. In the present investigation, as also found in Atzori et al. (2006) dealing with C40 steel notched specimens, plasticity and shielding effects are very limited and play only a secondary role on the fatigue crack nucleation and propagation in the medium and high cycle fatigue regime. The absence of non linear effects combined with the high notch sensitivity of the present steel allows us to use a single control volume independent of the loading modes. Due to the high strength of the tested steel the size of the volume has been found to be very limited (0.05 mm). The synthesis by means of SED has confirmed the choice of the control volume being the obtained scatterband very narrow if compared with those obtained in previous works (Berto et al. 2011c, Berto and Lazzarin 2011, Lazzarin and Berto 2008). By comparing Figure 6.7.2 with Figures 6.4.1-6.4.3, based on nominal stresses at the net area, it is evident the unifying capacity of the SED

which is able to summarize all the data in a single scatterband independent of the loading mode and notch geometry.

6.8 Conclusions

A large bulk of results from multiaxial tests from V-notched and semicircular notched specimens made of 40CrMoV13.9 steel are discussed together with those obtained under pure tension and pure torsion loading from notched specimens with the same geometry. Altogether more than 120 new fatigue data (10 fatigue curves) are summarised in the present work.

All fatigue data are presented first in terms of nominal stress amplitudes and then re-analysed in terms of the mean value of the strain energy density evaluated over a finite size semicircular sector surrounding the tip of the notch. The synthesis permits to obtain a very narrow band characterised by a scatter index equal to 1.96. The synthesis has been carried out with a constant value of the control radius, R_C, independent of the loading conditions.

7

The influence of the phase angle on multiaxial fatigue of sharp V-notches

7.1 Introduction

Several criteria have been proposed in order to assess the behaviour of un-notched or largely blunted components subjected to multi-axial fatigue. It is well known that this type of loading condition induces the formation of surface cracks that usually nucleate on the plane characterized by the maximum shear.

After the pioneering works by Ewing and Humfrey (1903) and Forsyth (1961) many criteria have been developed with the aim of considering the components of stresses and strains acting on the plane experiencing the maximum shear. The so called "critical plane approaches" gave different damage parameters based on the components of stress/strain considered as critical on the maximum shear plane. Brown and Miller (1973) considered both the shear and the normal strain acting on the critical plane. Fatemi and Socie (1988) took in consideration the shear strain and the stress acting normal to the crack flanks. Smith et al. (1970) predicted that the critical plane is the plane where the maximum tensile stress acts. The critical plane approach has recently been reviewed and modified by Carpinteri and Spagnoli (2001), who have correlated the critical plane orientation with the weighted mean principal stress directions. Accordingly, the fatigue failure assessment is performed by considering a nonlinear combination of the maximum normal stress and the shear stress amplitude acting on the critical plane.

Some energy based criteria have been also developed to face the problem of multi-axial loadings. The common denominator of these approaches is to consider a critical parameter based on the strain energy density evaluated on the critical plane. Among the others it is worth mentioning the contributions by Liu (1993), Chu et al. (1995a), Glinka et al. (1995) and Jiang (2000).

Liu (1993) considered two different energy failure modes and the collapse of the component was expected on the plane where the maximum virtual strain energy was reached. Chu et al. (1995a) used a similar approach in order to relate the work of shear and normal components of stress/strain. Glinka et al. (1995) modified Chu's criterion in order to better consider the effect of the mean stress in the case of non proportional loading. Jiang (2000) developed another multi-axial fatigue approach based on the cyclic plasticity and the plastic strain energy concept. A wide review of the main multi-axial fatigue criteria is carried out in Socie and Marquis (2000) and Susmel (2009).

Dealing with multi-axial fatigue of un-notched specimens or largely blunted specimens, some papers are available in the recent literature confirming the actual interest of the scientific community on this topic. Among the others the reader can refer to (Hertel and Vormwald 2011, Doring et al. 2006, Reis et al. 2009) and references therein.

In particular Hertel and Vormwald (2011) and Doring et al. (2006) determined the fatigue lives of tubular and round shafts with blunt shoulder fillets (notch tip radius equal to 1.4 mm) under combined tension/compression and torsion. A short crack model originally proposed for multi-axial constant amplitude loading is extended and applied to multi-axial variable amplitude loading. The comparison between theoretical assessment and experimental results reveals that the proposed approach enables an accurate estimation.

In Reis et al. (2009) the effects of multi-axial loading paths on the cyclic deformation behaviour, crack initiation and crack path have been investigated considering three types of structural steels (Ck45, medium carbon steel, 42CrMo4, low alloy steel and the AISI 303 stainless steel) and plain specimens. Theoretical predictions of the damage plane were conducted using some critical plane approaches, based on stress analysis or strain analysis (Findley, Smith–Watson–Topper, Fatemi–Socie, Wang–Brown–Miller, etc). Comparisons of the predicted crack orientation based on the critical plane approaches with the experimental observations were shown and discussed. Results showed the applicability of the critical plane approaches to predict the fatigue life and crack initial orientation in structural steels.

While the application of critical plane approaches to plain specimens is quite diffuse, data from pointed V-notches and application of suitable criteria for fatigue assessment is very limited and nowadays debated among researchers in the field (Capetta et al. 2011, Berto et al. 2011c, Atzori et al. 2006, Li et al. 2011, Susmel and Taylor 2012, Berto and Lazzarin 2011). Some of the just mentioned criteria have been extended to welded joints under multi-axial loading (Susmel 2010, Lazzarin et al.2004). One of the more intriguing problems dealing with sharp notches is how to take into account the effect of the phase angle in the fracture assessment. The problem is very complex because the sensitivity of the material to the phase angle varies from case to case. As well discussed and shown in Reis et al. (2009) the effect of out-of-phase is generally negative on the fatigue life.

The degree of penalization due to the phase angle can be partially explained by considering linear elastic hypothesis and the stress field acting near the notch tip but it is also influenced by the microstructural properties of the material and by the shielding effects occurring during crack propagation which are different under proportional and non-proportional loading. Ritchie (1988) schematically classified shielding effects in two classes of mechanisms involved in the material threshold behaviour. The intrinsic mechanisms determine the inherent resistance of the material against fatigue crack propagation while a second class, the extrinsic mechanisms are the cause of local reduction in the crack driving force at the crack tip and for this reason they are called shielding mechanisms. Among the others the most important extrinsic mechanisms are geometrical shielding (crack deflection and crack branching), contact shielding (plasticity, corrosion, roughness, debris) and zone shielding (micro-cracks and mismatch of different phases).

Keeping account the shielding effects, Tanaka et al. (1999) derived an elliptic equation for the threshold condition under mixed modes I and III and also an equation to express the threshold condition for the initiation of crack growth from an initial circumferential crack.

More recently, a novel mathematical model of the stresses around the tip of a fatigue crack, which includes the T-stress and considers the effects of plasticity through an analysis of their shielding effects on the applied elastic field, was

developed by Christopher et al. (2007-2008). The ability of the CJP model to characterize plasticity-induced effects of cyclic loading and on the elastic stress fields was demonstrated using full field photoelasticity. The effects due to overloads have been also discussed in (Colombo et al. 2010, Colombo and Vergani 2010). The variability of the stress intensity factor ahead of the crack tip is shown in Colombo and Vergani (2010) on the basis of nonlinear FE models. The CJP model can be seen as a modified linear elastic approach, to be applied outside the zone where nonlinear effects are prevailing. Two logarithmic terms are added to the Williams' solution and three new stress intensity factors K_F, K_R and K_S are proposed to quantify shielding effects ahead of the crack tip and on its back.

Being conscious of the problems related to shielding effects, which are material dependent, the main aim of the present chapter is to provide a possible explanation of the fatigue life reduction in sharply V-notched components due to phase angle by simply considering a linear elastic model.

The proposed approach is based on the local maximum shear stress averaged over a single fatigue cycle evaluated at a certain distance from the notch tip. The model, which is based on Cardano's analytical formulation (Cardano 1545), is able to take into account not only the effect of the phase angle but also the effect of the nominal load ratio and the biaxiality ratio. The analogy of the present model with the critical plane approach is only the consideration of a shear stress as a critical parameter. On the other hand substantial differences exist between the present approach and those based on critical planes. The main difference with the critical plane approach is that in the present work, due to the fact that sharp notches are considered, the critical point is not known a priori and its determination is based on the maximization of the critical parameter.

By applying the proposed model to different loading configurations some interesting observations can be drawn.

7.2 Analytical frame

The aim of the present work is to analyze the effect of the phase angle on axis-symmetric sharp V-notched components subjected to multi-axial loading. A

schematic representation of a typical circumferentially V-notched specimen is shown in Figure 7.2.1a. Only the notch opening angle $2\alpha=90°$ is considered in order to focus the attention on the effect induced by the phase angle on the strength of the component varying the applied loads. However, the analytical frame presented in the next sessions is applicable to a generic notch opening angle and not only to that considered herein.

The polar coordinate system shown in Figure 7.2.1b is used to express the stress field near the notch tip. The origin is centered on the notch tip. The coordinate r denotes the radial coordinate while θ is the angle between a particular point and the notch bisector line.

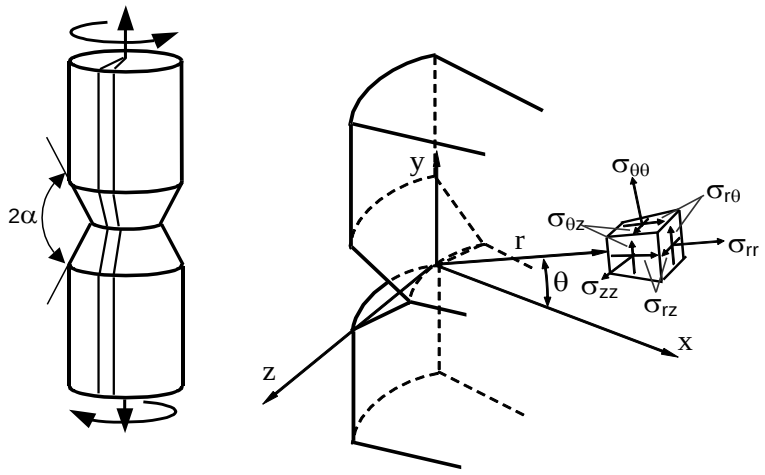

Figure 7.2.1. Component weakened by a sharp V-shaped notch subjected to multi-axial loading conditions (a). The centre of the polar coordinate system is located at the V-notch tip (b).

As it is well known the presence of a sharp V-notch and the application of a multi-axial loading induce a complex state of stress in the vicinity of the notch tip. The stress field can be described by using the following expressions dealing with Mode I and Mode II loadings (Williams 1952, Lazzarin and Tovo 1996):

$$\sigma_{rr} = \frac{K^{N_1} \cdot r^{\lambda_1 - 1}}{\sqrt{2\pi} \cdot (1+\lambda_1) + \chi_1 \cdot (1-\lambda_1)} \cdot \left[(3-\lambda_1)\cos((1-\lambda_1)\theta + \chi_1 \cdot (1-\lambda_1) \cdot (-\cos((1+\lambda_1)\theta)) \right] +$$

$$+ \frac{K^{N_2} \cdot r^{\lambda_2 - 1}}{\sqrt{2\pi} \cdot (1-\lambda_2) + \chi_2 \cdot (1+\lambda_2)} \cdot \left[-(3-\lambda_2)\sin((1-\lambda_2)\theta + \chi_2 \cdot (1+\lambda_2) \cdot (\sin((1+\lambda_2)\theta)) \right]$$

(7.2.1)

$$\sigma_{\theta\theta} = \frac{K^{N_1} \cdot r^{\lambda_1 - 1}}{\sqrt{2\pi} \cdot (1+\lambda_1) + \chi_1 \cdot (1-\lambda_1)} \cdot \left[(1+\lambda_1)\cos((1-\lambda_1)\theta + \chi_1 \cdot (1-\lambda_1) \cdot (\cos((1+\lambda_1)\theta)) \right] +$$

$$+ \frac{K^{N_2} \cdot r^{\lambda_2 - 1}}{\sqrt{2\pi} \cdot (1-\lambda_2) + \chi_2 \cdot (1+\lambda_2)} \cdot \left[-(1+\lambda_2)\sin((1-\lambda_2)\theta + \chi_2 \cdot (1+\lambda_2) \cdot (-\sin((1+\lambda_2)\theta)) \right]$$

(7.2.2)

$$\tau_{r\theta} = \frac{K^{N_1} \cdot r^{\lambda_1 - 1}}{\sqrt{2\pi} \cdot (1+\lambda_1) + \chi_1 \cdot (1-\lambda_1)} \cdot \left[(1-\lambda_1) \cdot \sin((1-\lambda_1)\theta + \chi_1 \cdot (1-\lambda_1) \cdot (\sin((1+\lambda_1)\theta)) \right] +$$

$$+ \frac{K^{N_2} \cdot r^{\lambda_2 - 1}}{\sqrt{2\pi} \cdot (1-\lambda_2) + \chi_2 \cdot (1+\lambda_2)} \cdot \left[(1-\lambda_2) \cdot \cos((1-\lambda_2)\theta + \chi_2 \cdot (1+\lambda_2) \cdot (\cos((1+\lambda_2)\theta)) \right]$$

(7.2.3)

The last out-of-plane component of the stress field can be written by assuming plane strain conditions. This approximation is generally well aligned with the real stress field near the notch tip in the case of axis-symmetric components.

$$\sigma_{zz} = \nu \cdot (\sigma_{rr} + \sigma_{\theta\theta}) \tag{7.2.4}$$

In the presence of a sharp V-notch, the remaining two tangential components of stress can be written in the following form as suggested in Dunn et al. (1997), Qian and Hasebe (1997), Seweryn and Molski (1996).

$$\tau_{rz} = \frac{K^{N_3} \cdot r^{1-\lambda_3}}{\sqrt{2\pi}} \cdot \sin(\lambda_3 \cdot \theta) \tag{7.2.5}$$

$$\tau_{\theta z} = \frac{K^{N}{}_{3} \cdot r^{1-\lambda_3}}{\sqrt{2\pi}} \cdot \cos(\lambda_3 \cdot \theta) \tag{7.2.6}$$

Parameters K_1^N, K_2^N and K_3^N are the Notch Stress Intensity Factors (N-SIFs) related to Mode I, Mode II and Mode III stress distributions respectively, λ_1 and λ_2 are Williams' eigenvalues (Williams 1952), λ_3 is the Mode III eigenvalue (Dunn et al. 1997, Qian and Hasebe 1997, Seweryn and Molski 1996) and, finally, χ_1 and χ_2 are parameters which depend on the opening angle.

In the case of an opening angle of the notch equal to 90° the eigenvalues are 0.5445, 0.9085 and 0.6667 for Mode I, Mode II and Mode III respectively, while χ_1 is equal to 1.841 and χ_2 to 0.219.

In order to better describe the behaviour of every singular component of stress during the cyclic loading, the notch stress intensity factors can be re-written as follows:

$$K_1{}^{N} = k_1 \cdot S_{NOM} \tag{7.2.7}$$

$$K_2{}^{N} = k_2 \cdot S_{NOM} \tag{7.2.8}$$

$$K_3{}^{N} = k_3 \cdot T_{NOM} \tag{7.2.9}$$

Where k_1, k_2 and k_3 are the unitary N-SIFs normalised by the applied stress and are obtained by means of a finite element analysis. Considering a multi-axial tension-torsion loading, k_2 can be set equal to zero. The values of k_1 and k_3 has been found equal to 5.4 and 5.88 respectively. S_{nom} and T_{nom} are the nominal tension and nominal torsion applied to the specimen. They can be written as follows:

$$S_{NOM} = S_a \cdot \sin(\beta) + S_a \cdot \frac{1+R}{1-R} \tag{7.2.10}$$

$$T_{NOM} = T_a \cdot \sin(\beta - \phi) + T_a \cdot \frac{1+R}{1-R} \tag{7.2.11}$$

S_a and T_a are the nominal stress amplitude tied to the applied loads, β is the machine angle that varies between 0° and 360° in order to complete one cyclic loading, R is the load ratio and ϕ is the phase angle.

As written above, dealing with multi-axial problems on notched and un-notched components, many contributions in the literature are focused on the determination of the critical plane of maximum shear. In this work the aim is not to search a particular plane, but a particular point where the maximum shear stress averaged over one cycle of fatigue loading acts.

To find out the critical point just mentioned, the Mohr's theory has to be used in order to obtain the values of the three principal stresses acting during the cyclic loading. Only when the principal stresses are known the critical maximum shear stress can be derived.

By substituting Eqs. (7.2.7-7.2.9) into Eqs. (7.2.1-7.2.6) the trend of each stress component in a fatigue cycle can be obtained. All the components vary with the distance from the notch tip (r), the machine angle (β), the polar coordinate (θ) and the phase angle (ϕ). Parameter r can be set equal to a material characteristic length. Lazzarin and Zambardi (2001) formalized a criterion on which the strain energy density was averaged over a circular control volume centered at the notch tip, later widely employed to assess the fracture and fatigue behaviour of notched components and welded joints (Berto and Lazzarin 2009-2013, Lazzarin et al. 2013b). The radius of the critical control volume in the case of welded steel has been found to be equal to 0.28 mm. The same value is used here for applying the proposed criterion. The phase angle is also set as a constant value and is updated in each analysis.

All the stress components acting on a particular point at a distance equal to r=0.28 mm from the notch tip and induced by two different loads characterized by a precise phase angle vary as a function of the machine angle β and the polar coordinate θ.

The stress tensor at a particular point "P" can be written as follows:

$$[T]_P = \begin{bmatrix} \sigma_{rr}(\beta,\theta) & \tau_{r\theta}(\beta,\theta) & \tau_{rz}(\beta,\theta) \\ \tau_{r\theta}(\beta,\theta) & \sigma_{\theta\theta}(\beta,\theta) & \tau_{\theta z}(\beta,\theta) \\ \tau_{rz}(\beta,\theta) & \tau_{\theta z}(\beta,\theta) & \sigma_{zz}(\beta,\theta) \end{bmatrix}_P \tag{7.2.12}$$

In order to avoid numerical problems related to the evaluation of the principal stresses and with the aim to write a dedicate software able to calculate all the required stress components, Cardano's formulation for the resolution of cubic equations has been implemented.
The well known cubic equation that has to be solved in order to obtain the principal stresses is:

$$\sigma^3 - I_1 \cdot \sigma^2 - I_2 \cdot \sigma - I_3 = 0 \tag{7.2.13}$$

The first step of the present formulation needs the knowledge of the three stress invariants that can be extensively written as follows:

$$I_1 = \sigma_{rr} + \sigma_{\theta\theta} + \sigma_{zz} \tag{7.2.14}$$

$$I_2 = -\sigma_{rr} \cdot \sigma_{\theta\theta} - \sigma_{rr} \cdot \sigma_{zz} - \sigma_{\theta\theta} \cdot \sigma_{zz} + \tau_{r\theta}^2 + \tau_{\theta z}^2 + \tau_{rz}^2 \tag{7.2.15}$$

$$I_3 = \sigma_{rr} \cdot \sigma_{\theta\theta} \cdot \sigma_{zz} - \sigma_{rr} \cdot \tau_{\theta z}^2 - \sigma_{\theta\theta} \cdot \tau_{rz}^2 - \sigma_{zz} \cdot \tau_{r\theta}^2 + 2 \cdot \tau_{r\theta} \cdot \tau_{\theta z} \cdot \tau_{rz} \tag{7.2.16}$$

Following Cardano's formulation the principal stresses assume the following form:

$$\sigma_1 = u + v + \frac{I_1}{3} \tag{7.2.17}$$

$$\sigma_2 = -\frac{u+v}{2} + i \cdot \frac{u-v}{2} \cdot \sqrt{3} + \frac{I_1}{3} \tag{7.2.18}$$

$$\sigma_3 = -\frac{u+v}{2} - i \cdot \frac{u-v}{2} \cdot \sqrt{3} + \frac{I_1}{3} \tag{7.2.19}$$

Parameters u and v are as follows:

$$u = \left(-\frac{q}{2} + \sqrt{\frac{q^2}{4} + \frac{p^3}{27}} \right)^{\frac{1}{3}} \tag{7.2.20}$$

$$v = \left(-\frac{q}{2} - \sqrt{\frac{q^2}{4} + \frac{p^3}{27}} \right)^{\frac{1}{3}} \tag{7.2.21}$$

Parameters p and q can be written in the following form:

$$p = -\frac{I_1^2}{3} - I_2 \tag{7.2.22}$$

$$q = -\frac{2 \cdot I_1^3}{27} - \frac{I_1 \cdot I_2}{3} - I_3 \tag{7.2.23}$$

It is visible from Eqs. (7.2.17) and (7.2.18) that σ_2 and σ_3 assume a complex form. In order to omit the imaginary part, the following assumption has to be done:

$$\frac{q^2}{4} + \frac{p^3}{27} \leq 0 \tag{7.2.24}$$

By using this particular assumption it is possible to obtain three different real roots of the cubic Eq. (7.2.13). By defining two new parameters η and ξ it is possible to obtain a more compact form of the principal stresses:

$$\eta = -\frac{q}{2} \tag{7.2.25}$$

$$\xi = \sqrt{-\frac{q^2}{4} - \frac{p^3}{27}} \tag{7.2.26}$$

Now it is possible to re-write the parameters u and v in the following simpler way:

$$u = (\eta + i\xi)^{1/3} = w^{1/3} \tag{7.2.27}$$

$$v = (\eta + i\xi)^{1/3} = \overline{w}^{1/3} \tag{7.2.28}$$

By using some well known properties of complex variables, u and v can be re-written:

$$u = |w|^{1/3} \cdot \left[\cos\left(\frac{1}{3} \cdot \mathrm{Arg}(w)\right) + i \cdot \sin\left(\frac{1}{3} \cdot \mathrm{Arg}(w)\right) \right] \tag{7.2.29}$$

$$v = |w|^{1/3} \cdot \left[\cos\left(\frac{1}{3} \cdot \mathrm{Arg}(w)\right) - i \cdot \sin\left(\frac{1}{3} \cdot \mathrm{Arg}(w)\right) \right] \tag{7.2.30}$$

where:

$$|w| = \sqrt{\eta + i\xi} \tag{7.2.31}$$

$$\mathrm{Arg}(w) = \begin{cases} \mathrm{Arctan}\left(\dfrac{\xi}{\eta}\right) & \text{if } \eta \geq 0 \\ \mathrm{Arctan}\left(\dfrac{\xi}{\eta}\right) + \pi & \text{if } \eta < 0 \end{cases} \tag{7.2.32}$$

The principal stresses can be finally obtained:

$$\sigma_1 = \frac{I_1}{3} + 2 \cdot |w|^{1/3} \cdot \cos\left[\frac{1}{3} \cdot \mathrm{Arg}(w)\right] \tag{7.2.33}$$

$$\sigma_2 = \frac{I_1}{3} - |w|^{1/3} \cdot \cos\left[\frac{1}{3} \cdot \mathrm{Arg}(w)\right] - \sqrt{3} \cdot |w|^{1/3} \cdot \sin\left[\frac{1}{3} \cdot \mathrm{Arg}(w)\right] \quad (7.2.34)$$

$$\sigma_3 = \frac{I_1}{3} - |w|^{1/3} \cdot \cos\left[\frac{1}{3} \cdot \mathrm{Arg}(w)\right] + \sqrt{3} \cdot |w|^{1/3} \cdot \sin\left[\frac{1}{3} \cdot \mathrm{Arg}(w)\right] \quad (7.2.35)$$

Once known the principal stresses it is straightforward to obtain the three related shear stresses:

$$\tau_{1max} = \frac{\sigma_1 - \sigma_3}{2} \quad (7.2.36)$$

$$\tau_{2max} = \frac{\sigma_1 - \sigma_2}{2} \quad (7.2.37)$$

$$\tau_{3max} = \frac{\sigma_2 - \sigma_3}{2} \quad (7.2.38)$$

All the three maximum shear stresses depend again on the polar coordinate θ and on the machine angle β. They are also function of the distance from the notch tip and the phase angle.

The criterion requires now to determine, along a circumferential path (varying the parameter θ, see Figure 7.2.2), at a distance r=0.28 mm from the notch tip, the point where the areas subtended by the three different shear stress functions reach their maximum values during one loading cycle. Once the values of the three different areas are known, the averaged values of the three shear stresses can be calculated on a full loading cycle. Finally, it has to be selected the maximum between the three shear stresses, that corresponds to the maximum shear stress averaged on a loading cycle. The three averaged values of the shear stresses are obtainable as follows:

$$\bar{\tau}_1 = \frac{\int_0^{2\cdot\pi} \tau_{1max}[\beta] \cdot d\beta}{2 \cdot \pi} \quad (7.2.39)$$

$$\bar{\tau}_2 = \frac{\int_0^{2\cdot\pi} \tau_{2max}[\beta]\cdot d\beta}{2\cdot\pi} \tag{7.2.40}$$

$$\bar{\tau}_3 = \frac{\int_0^{2\cdot\pi} \tau_{3max}[\beta]\cdot d\beta}{2\cdot\pi} \tag{7.2.41}$$

The maximum value between the three averaged shear stresses is finally called $\bar{\tau}$ ($\bar{\tau} = \max[(\bar{\tau}_1, \bar{\tau}_2, \bar{\tau}_3)]$).

The maximum value in each analysis has been compared considering different values of the phase angle and the biaxiality ratio ($\Lambda = \frac{T_{NOM}}{S_{NOM}}$). This analysis permits to understand if these two variables induce significant effects on the averaged shear stress and thus on the strength of a sharp V-notched component.

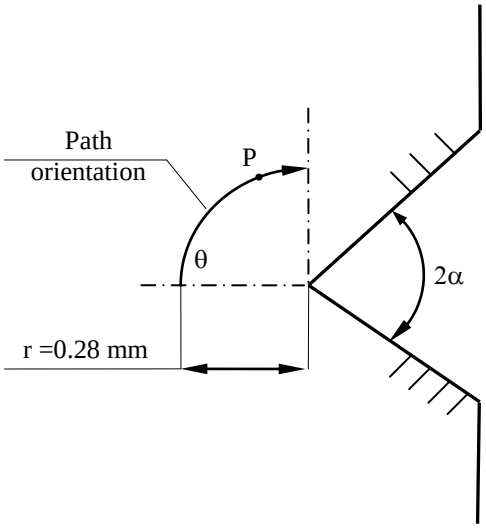

Figure 7.2.2. Definition of the circumferential path used to discover the critical point where the maximum averaged shear stress reaches its maximum value.

7.3 Results and discussions

In order to provide the value of the maximum shear stress averaged on a multi-axial fatigue cycle a dedicate software has been implemented on Wolfram Mathematica®. This software permits to compute $\bar{\tau}$ for different angle θ and to search the critical angle on which the maximum value of the averaged shear stress

is reached. The angle θ, has been varied between 0 and 90 degrees with incremental steps of 1°.

All in all, considering all the varied parameters, 4500 different analyses have been carried out in order to investigate the effect of the phase angle. Only the most significant results are reported below.

Two different load ratios have been considered, R=0 and R=-1, the biaxiality ratio has been set equal to $1/\sqrt{3}$, 0.6, 1, 1.6 and $\sqrt{3}$ and finally the phase angles taken into account were five: 0° (in phase loading), 45°, 90°, 135° and 180°.

The behaviour of the maximum averaged shear stress along the circumferential path matching the increment of θ is investigated in Figures 7.3.1-7.3.6. Not all the studied cases are shown in the figures because a similar trend has been detected in the cases $\Lambda=1/\sqrt{3}$, $\Lambda=0.6$ and $\Lambda=1.6$, $\Lambda=\sqrt{3}$.

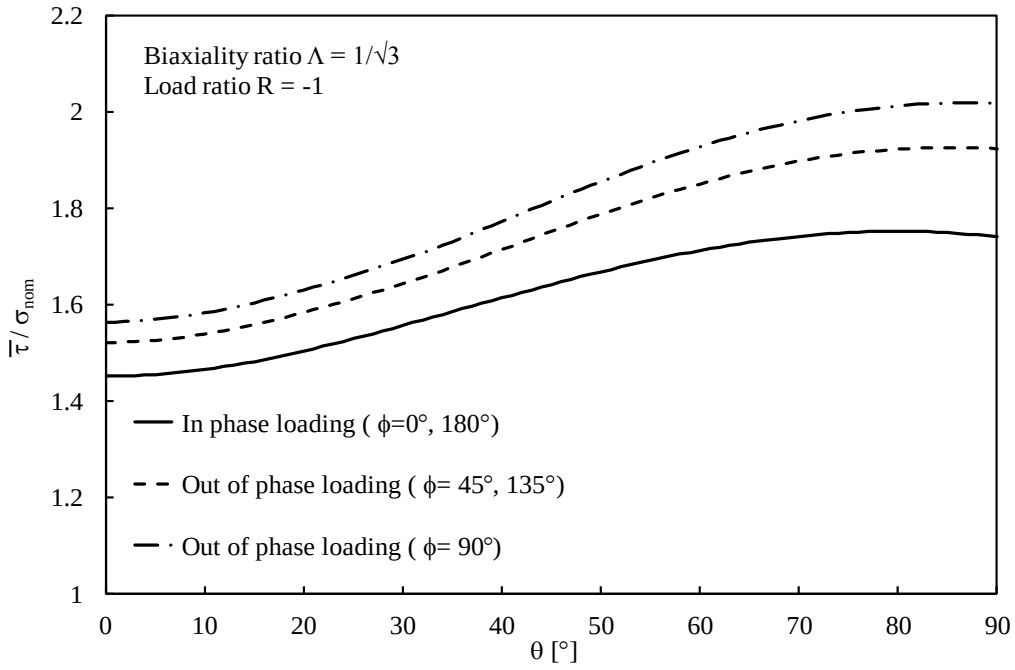

Figure 7.3.1. Behaviour of the averaged maximum tangential stress varying the polar coordinate θ and the phase displacement in the particular case of R=-1; $\Lambda=1/\sqrt{3}$.

Figure 7.3.1 shows the behaviour of $\bar{\tau}$ normalised by the nominal tensile stress in the case of a load ratio equal to -1 and Λ equal to $1/\sqrt{3}$ for all the different phase

angles. Obviously, for this particular load ratio, the results in the case of in phase loading and 180° out of phase loading give identical results. The same consideration remains valid for ϕ=45° and ϕ=135°. From the figure it can be seen that the averaged maximum shear stress assumes higher values moving from the in phase configuration to the out of phase configuration (90°) for the whole circumferential path. The three curves tend to reach an almost constant value on the right hand side of the diagram where the maximum value is reached in a range between 70° and 90° (see Table 7.3.1). This means that, according to the present criterion, the critical point for a V-notched specimen subjected to multi-axial loading is far from the notch bisector line. However it is worth mentioning that also on the notch bisector line the out of phase loading is more damaging. The same behaviour is noticed in the case of a biaxiality ratio equal to 0.6. Increasing Λ, the same trend has been observed becoming the scatter between the in phase loading and the out of phase loading (90°) slightly higher (see Figure 7.3.2 and 7.3.3).

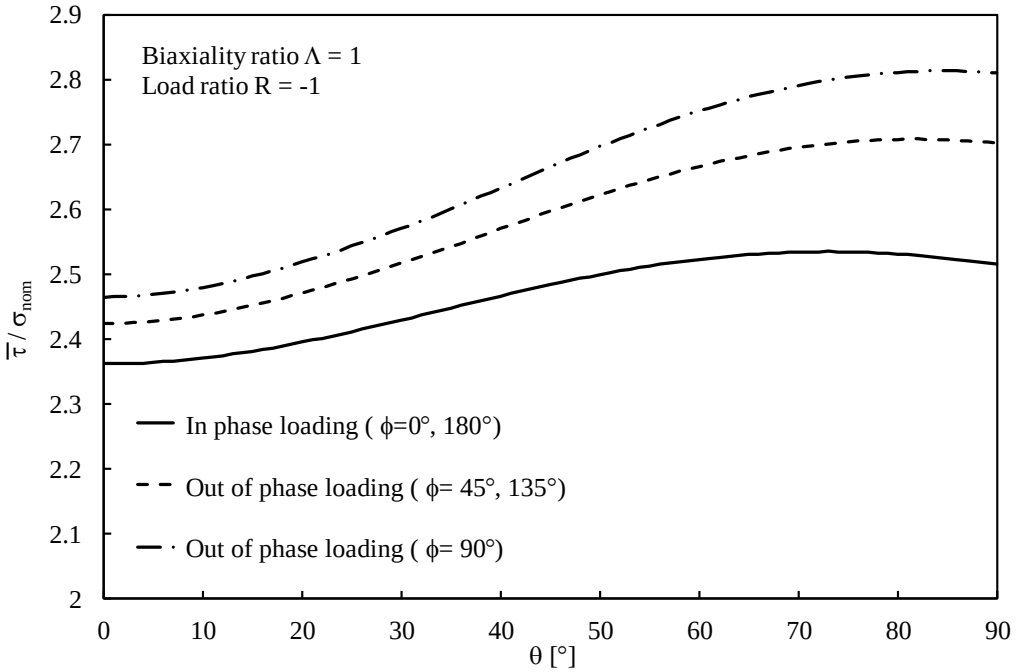

Figure 7.3.2. Behaviour of the averaged maximum tangential stress varying the polar coordinate θ and the phase displacement in the particular case of R=-1; Λ=1.

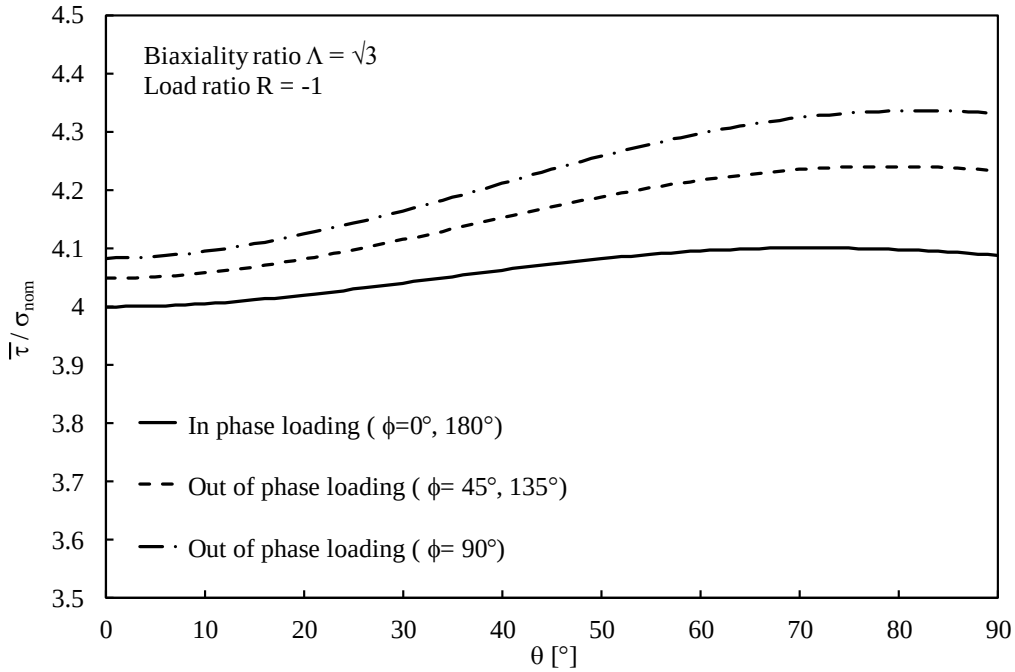

Figure 7.3.3. Behaviour of the averaged maximum tangential stress varying the polar coordinate θ and the phase displacement in the particular case of R=-1; Λ=√3.

Table 7.3.1. Critical θ where the averaged maximum tangential stress is reached.

Load ratio, R	Phase displacement [°]	Biaxiality ratio, Λ				
		1/√3	0.6	1	1.6	√3
-1	0	80°	79°	73°	71°	71°
	45	85°	85°	82°	79°	79°
	90	87°	87°	84°	83°	82°
	135	85°	85°	82°	79°	79°
	180	80°	79°	73°	71°	71°
0	0	80°	79°	73°	71°	71°
	45	84°	84°	80°	77°	77°
	90	87°	87°	85°	84°	83°
	135	88°	88°	87°	86°	86°
	180	88°	88°	88°	87°	87°

The same diagrams are provided also in the case of a load ratio R=0. From Figures 7.3.4, 7.3.5 and 7.3.6 it is evident that the results are close to those obtained in the case of R=-1. The only difference is that the normalised value of the averaged shear stress increases from the in phase to the out of phase condition corresponding to ϕ=180° for R=0. Also for this load ratio the maximum value is reached far from the notch bisector line at an inclination between 70 and 90 degrees.

In table 7.3.1 all the values of the critical angle, θ, where the averaged shear stress reaches its maximum value are shown. One can state that for a fully reversed fatigue test the angle increases reaching the maximum value for ϕ=90° and then it decreases. On the other hand, in the case of R=0, the higher becomes the phase angle, the higher becomes the value of the critical angle where the averaged stress is reached.

Moreover, from all the analyses carried out, it is visible that at a fixed phase angle, the critical angle decreases when the biaxiality ratio increases (see again Table 7.3.1).

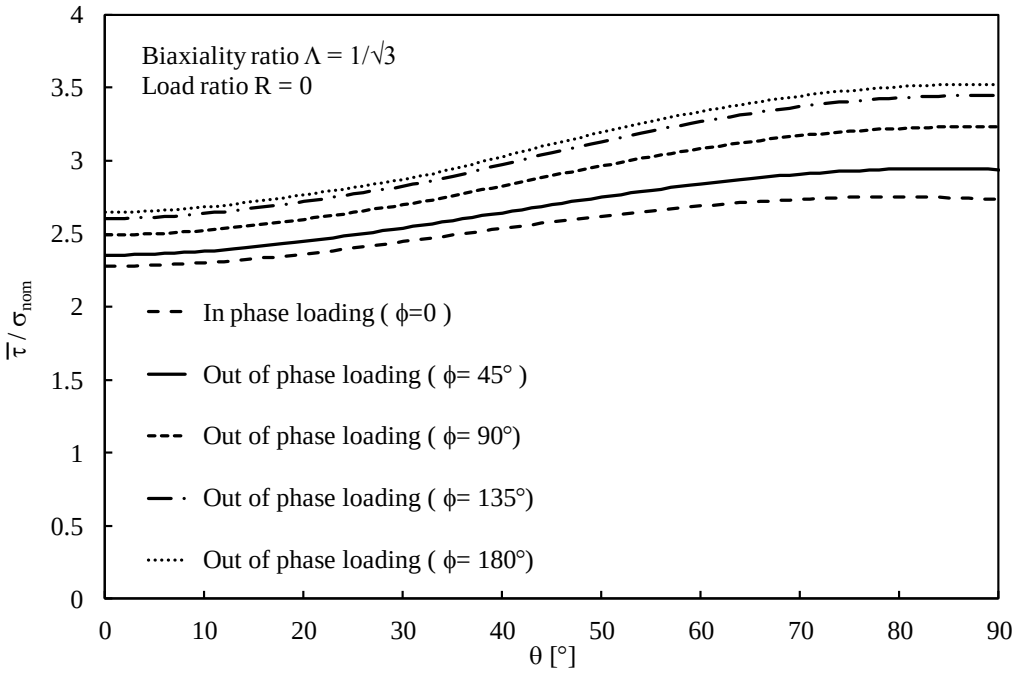

Figure 7.3.4. Behaviour of the averaged maximum tangential stress varying the polar coordinate θ and the phase displacement in the particular case of R=0; $\Lambda=1/\sqrt{3}$.

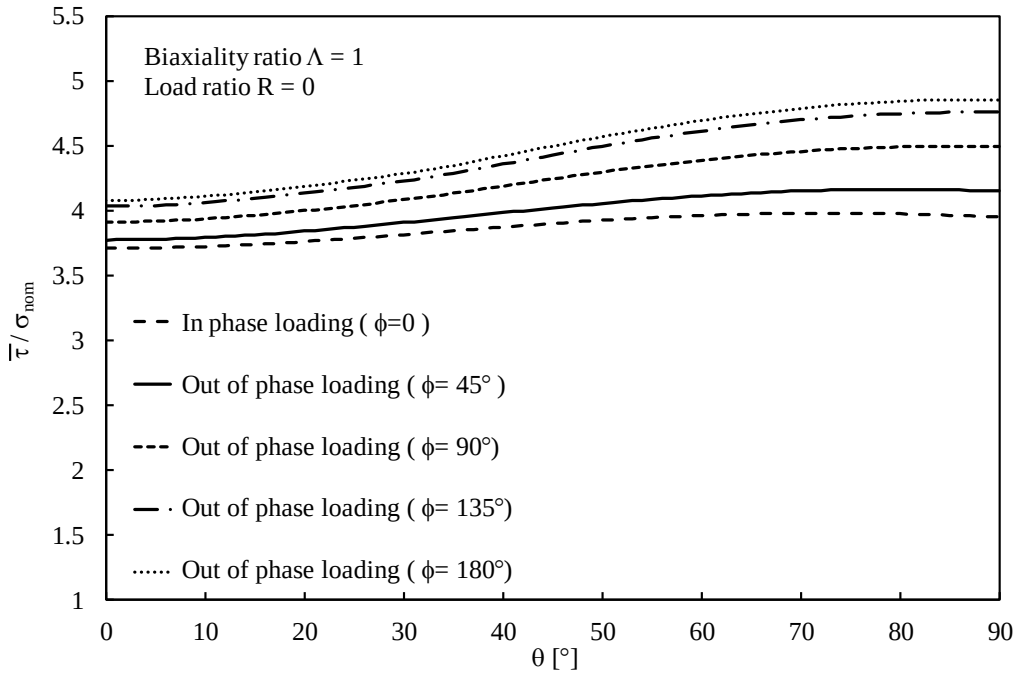

Figure 7.3.5. Behaviour of the averaged maximum tangential stress varying the polar coordinate θ and the phase displacement in the particular case of R=0; Λ=1.

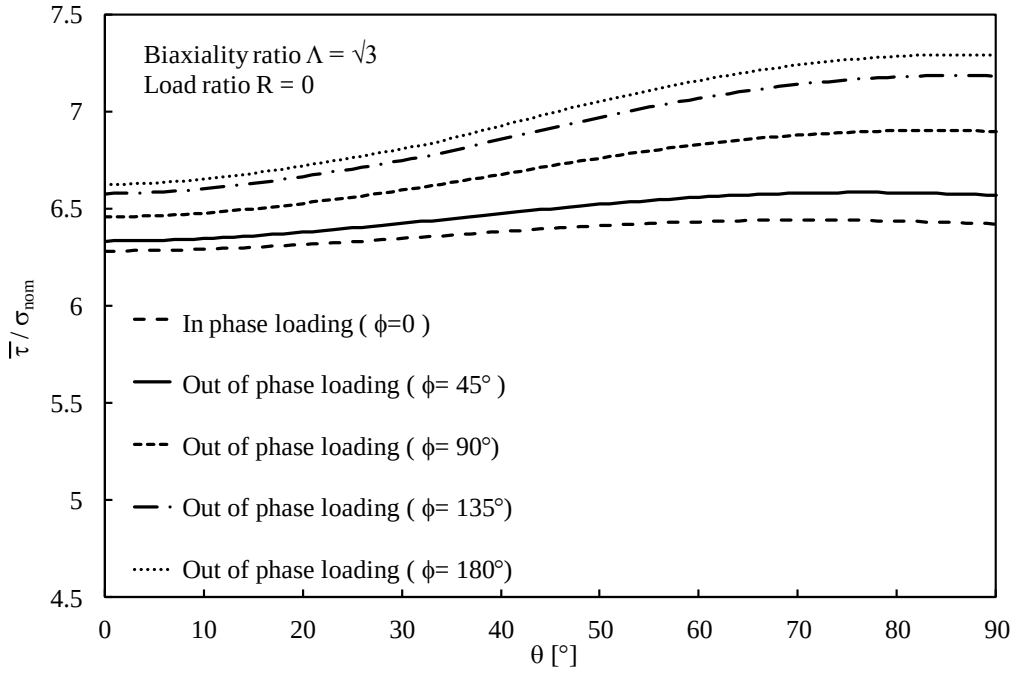

Figure 7.3.6. Behaviour of the averaged maximum tangential stress varying the polar coordinate θ and the phase displacement in the particular case of R=0; Λ=√3.

Figures 7.3.1-7.3.6 just commented above make it evident the trend of the averaged maximum tensile stress by varying the polar coordinate θ. Figures 7.3.7-7.3.12 can justify that trend (of $\bar{\tau}$) by investigating the changing of the maximum shear stress over a single multi-axial fatigue cycle. The normalised maximum shear stress, τ_{max}, which is the maximum of the three different principal shear stresses, has been computed at the critical angle on which $\bar{\tau}$ reaches its maximum value.

Figures 7.3.7, 7.3.8 and 7.3.9 plot τ_{max} in the case of R=-1 and biaxiality ratio equal to $1/\sqrt{3}$, 1 and $\sqrt{3}$ respectively. It can be noted that, in the first case, an in phase loading condition generates a maximum shear stress ranging between zero and an absolute maximum value. By increasing the phase angle from 0° to 90° it can be seen that the peak tends to decrease but, at the same time, the minimum assumes a value not much far from the maximum one. This consideration leads to the conclusion that the mean effect just described is more effective by moving the phase angle from 0° to 90°.

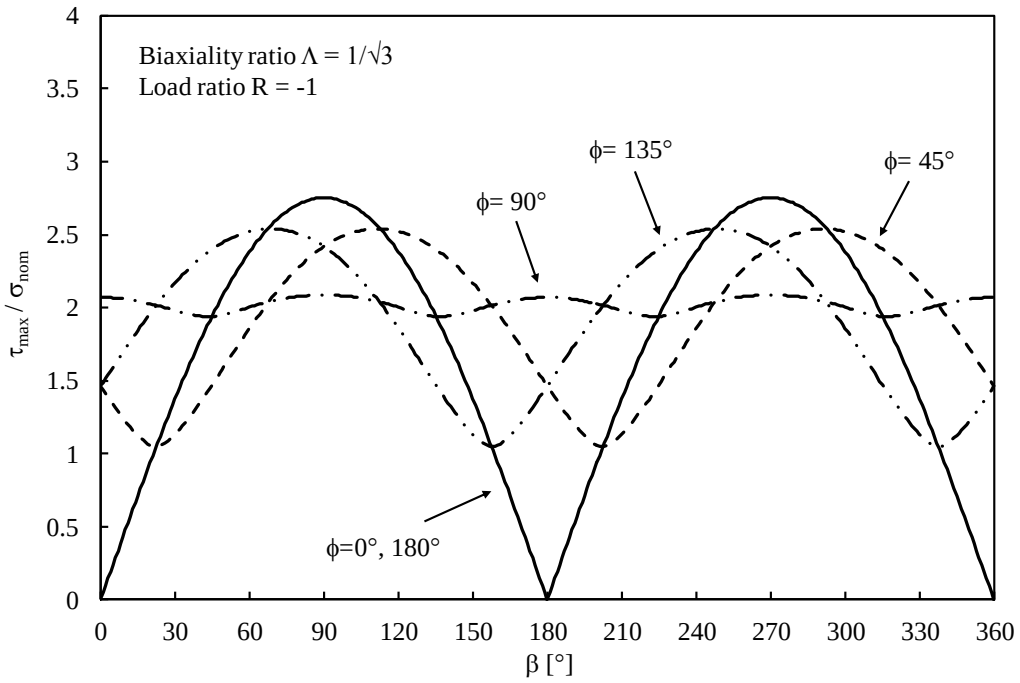

Figure 7.3.7. Variation of the maximum tangential stress on the critical coordinate θ during an entire loading cycle for different phase displacements. Case R=-1, $\Lambda=1/\sqrt{3}$.

The same trend has been observed for the five biaxiality ratios considered herein. Figures 7.3.8 and 7.3.9 show the same effects, just described for the case $\Lambda = 1/\sqrt{3}$, considering the cases $\Lambda = 1$ and $\sqrt{3}$. The only difference with the previous case is that the higher becomes the biaxiality ratio, Λ, the lower is the decreasing of the maximum value of the shear stress. In fact, it is well visible from Figures 7.3.8 and 7.3.9 that the maximum value of the shear stress is almost constant, with a slight decrease for larger values of phase angles.

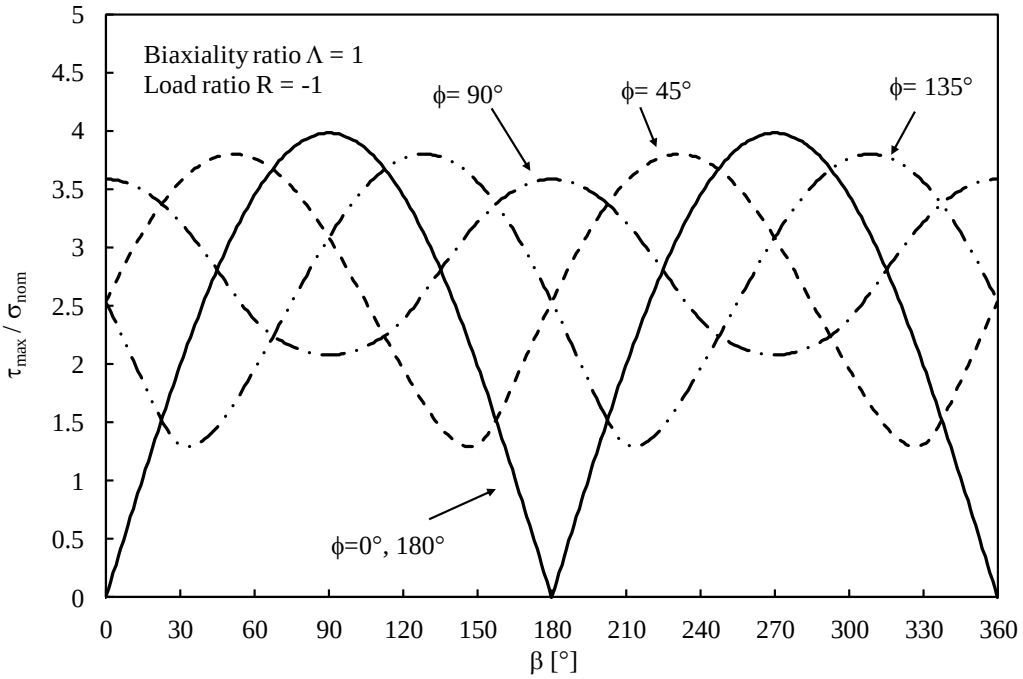

Figure 7.3.8. Variation of the maximum tangential stress on the critical coordinate θ during an entire loading cycle for different phase displacements. Case R=-1, Λ=1.

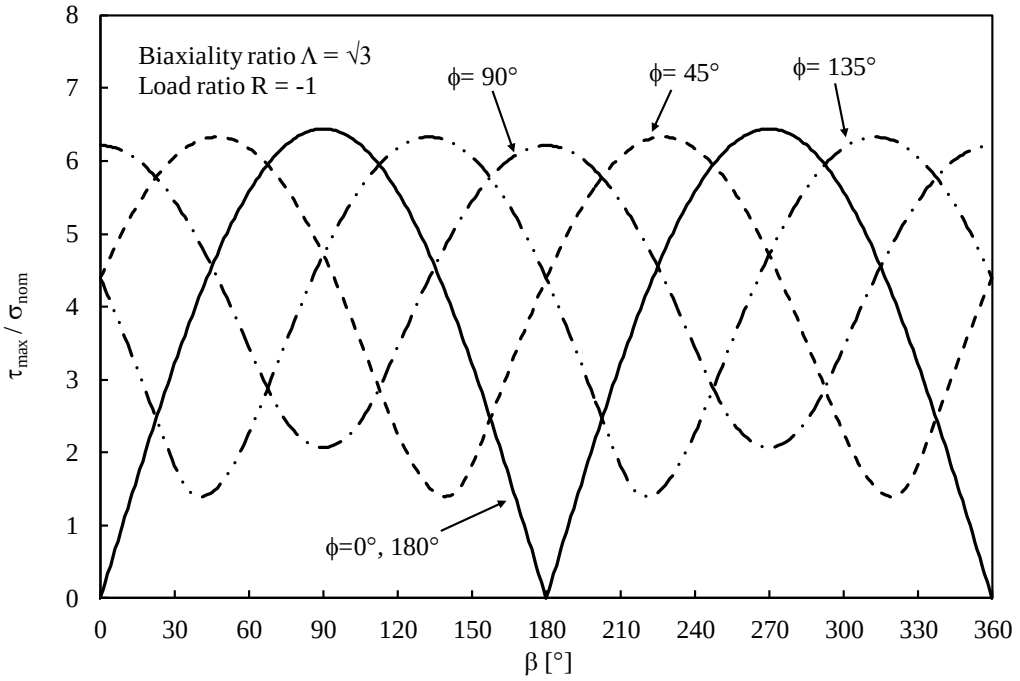

Figure 7.3.9. Variation of the maximum tangential stress on the critical coordinate θ during an entire loading cycle for different phase displacements. Case R=-1, Λ=√3.

In the case of a load ratio equal to 0, the maximum shear stress for ϕ=0°, ranges, once again, between 0 and an absolute maximum. By increasing the phase angle from 0° to 180°, the maximum value decreases and the minimum value increases. It is worth noting from Figure 7.3.10 that when τ_{max} reaches its minimum value for the case ϕ=0°, a second maximum occurs for the case ϕ=180°. Also for this load ratio, the phase angle generates a mean effect in terms of the averaged shear stress. This effect could be detrimental for the multi-axial fatigue strength of the component. Figures 7.3.11 and 7.3.12 show the trends hold in the case of higher biaxiality ratios (Λ=1, √3). All the considerations made for Figure 7.3.10 remain valid. The only difference is that when the maximum is reached for the case ϕ=0°, a relative maximum is reached for the case ϕ=180°. In parallel the minimum of the in phase case corresponds to the absolute maximum of the out of phase condition. Finally, it can be noted that at the highest value of the biaxiality ratio (Λ=√3) the maximum value of the shear stress is almost constant independent of the phase angle.

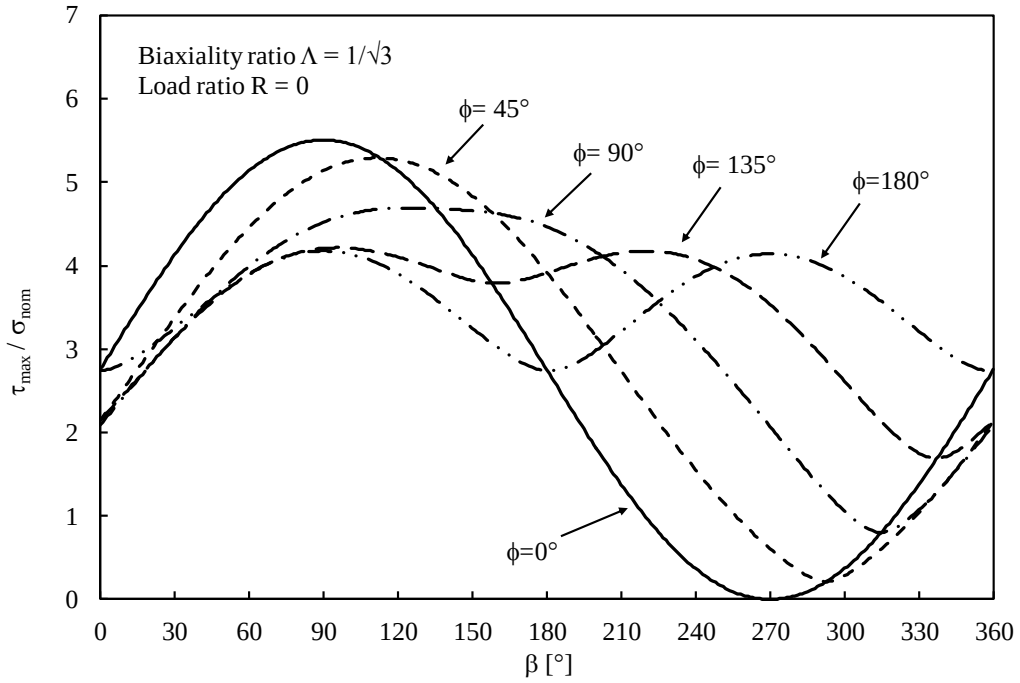

Figure 7.3.10. Variation of the maximum tangential stress on the critical coordinate θ during an entire loading cycle for different phase displacements. Case R=0, Λ=1/√3.

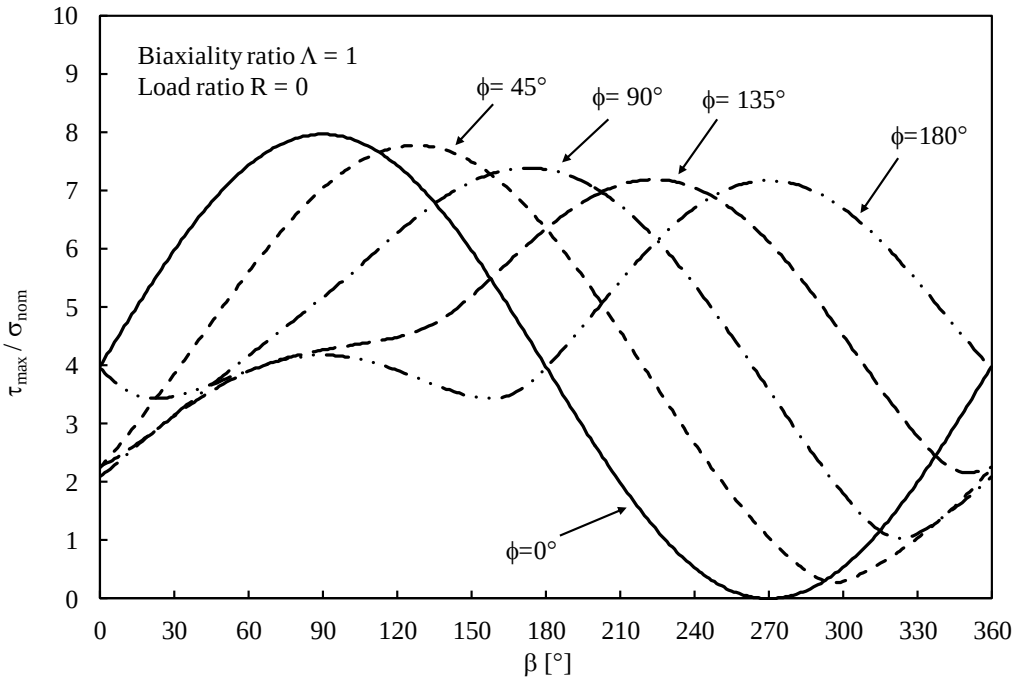

Figure 7.3.11. Variation of the maximum tangential stress on the critical coordinate θ during an entire loading cycle for different phase displacements. Case R=0, Λ=1.

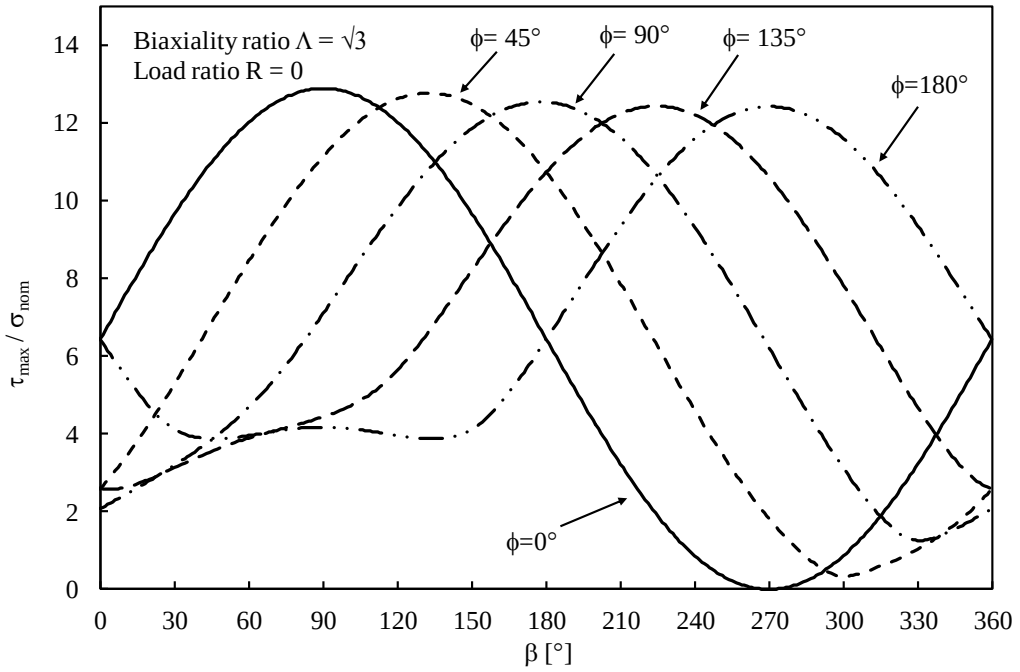

Figure 7.3.12. Variation of the maximum tangential stress on the critical coordinate θ during an entire loading cycle for different phase displacements. Case R=0, Λ=√3.

The following two figures represent a sort of summary diagrams with the aim of quantifying the damaging effect due to the phase angle on a sharply V-notched component subjected to multi-axial fatigue loading. The first figure (Figure 7.3.13) shows the averaged maximum shear stress normalised by the maximum value computed for a fixed biaxiality ratio in the case of a fully reversed cycle. It can be seen that for all the five considered cases the critical configuration is reached for ϕ=90°. The in phase loading is always the less damaging configuration, however it becomes comparable to the case ϕ= 90° when the biaxiality ratio increases. In the cases corresponding to lower values of Λ, the in phase loading is about 13% less damaging with respect to the case ϕ=90°, while the difference between in phase and out of phase loading reduces to 6% for higher values if the biaxiality ratio. Dealing with a load ratio equal to 0, the critical phase angle, as visible from Figure 7.3.14, corresponds to the out of phase configuration (ϕ=180°) while the in phase loading is about 22% less damaging in the case of low biaxiality ratios. The difference between in phase and out of phase loading reduces to 12-13% for higher values of Λ. Moving from ϕ=0° to ϕ=180 the effect of the phase angle becomes less detrimental but not negligible.

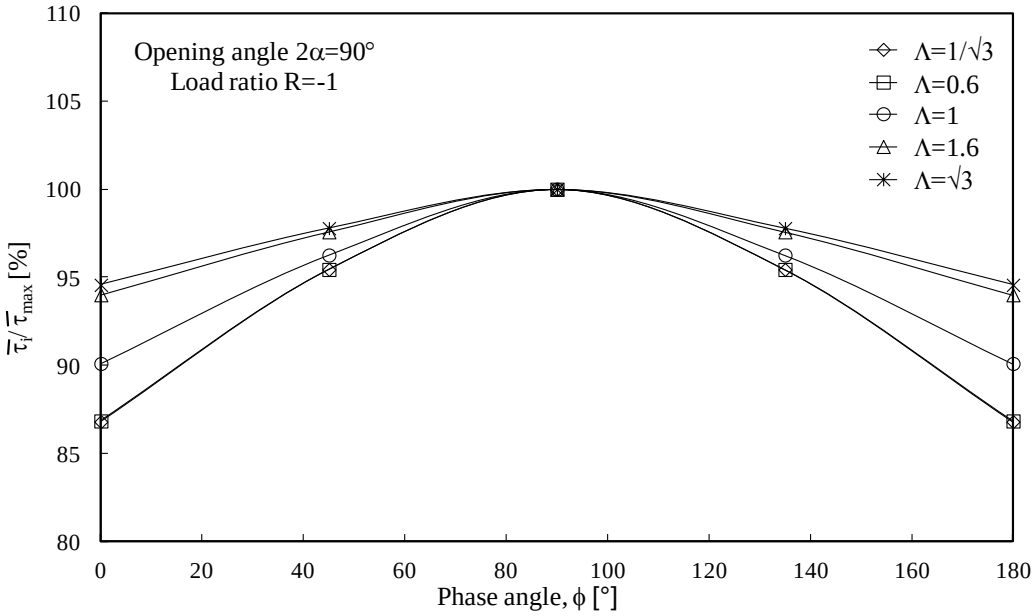

Figure 7.3.13. Summary of the phase angle effect for different biaxiality ratios in the case of R=-1.

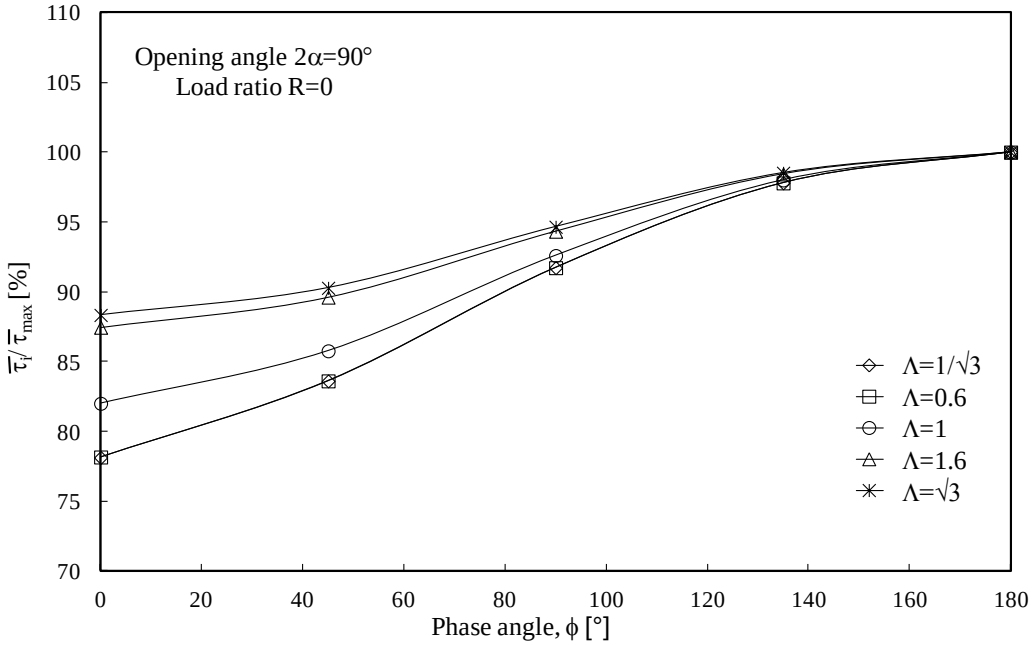

Figure 7.3.14. Summary of the phase angle effect for different biaxiality ratios in the case of R=0.

Being conscious that the out-of-phase loading is still an open problem in fatigue design and that the approach summarised here is only a simplified method developed under linear elastic hypotheses, there are some recent experimental results which confirm the slight penalizing effect at least for severely notched specimens under multiaxial loading (Berto et al. 2011c, Berto and Lazzarin 2011, Berto et al. 2014). When the notch becomes blunt (see Berto et al. 2014) the effect of out-of-phase is negligible. As explained above this is a general tendency that could be influenced by the mechanical/fatigue properties of the tested material, by many non-linear effects which could be important in the crack nucleation and propagation under non-proportional loadings and also by the material characteristic length or control volume size with respect to the notch radius. Figures 7.3.15 and 7.3.16 report two examples taken from Berto et al. (2011c) and Berto et al. (2014). In Figure 7.3.15 data from 39NiCrMo3 steel under in-phase and out-of-phase loadings are summarized (Berto et al. 2011c). The notch tip radius was equal to 0.1 mm. In Figure 7.3.16 data from 40CrMoV13.9 notched specimens are summarized (Berto et al. 2014). The notch tip radius was constant and equal to 1 mm. The notch opening angle was equal to 90° for 39NiCrMo3 and for 40CrMoV13.9 steels. For both materials the penalizing effect due to out-of-phase is usually evident even it is also clear that for the same material the behaviour could be influenced by the nominal load ratio as taken into account by the analytical frame proposed here as well as by the biaxiality ratio ($\lambda=\tau/\sigma$). These effects can be also different at low and high cycle fatigue due to the influence of the non-linear effects occurring during the tests. It is also evident that in Figure 17 for R=0 the effect of out-of-phase is more evident than for R=-1 in agreement with the proposed analytical frame and with Figures 7.3.13 and 7.3.14.

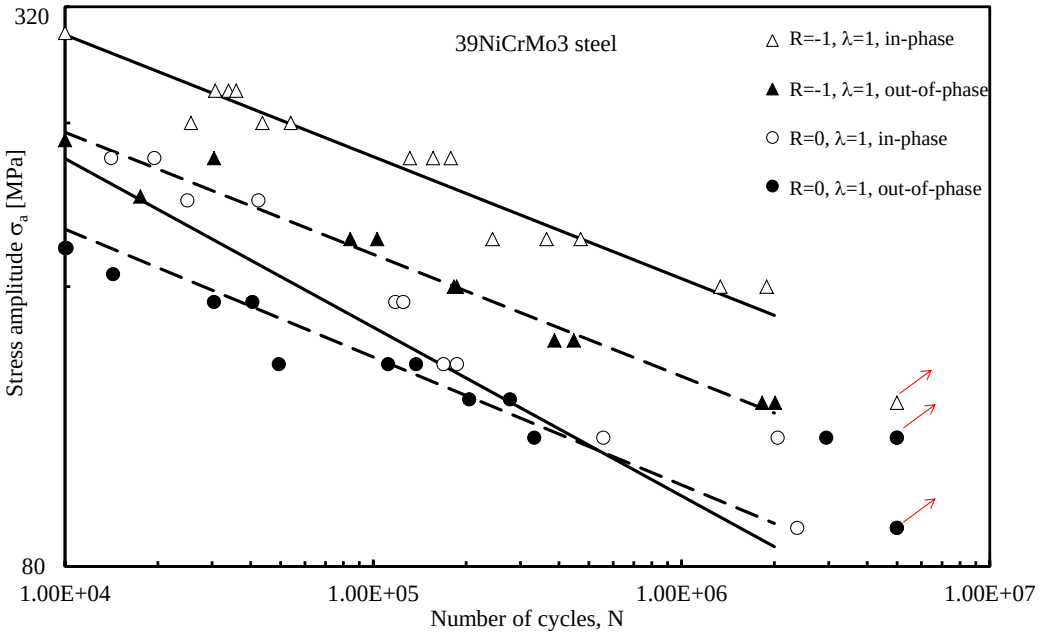

Figure 7.3.15. Fatigue data taken from Berto et al. (2011).

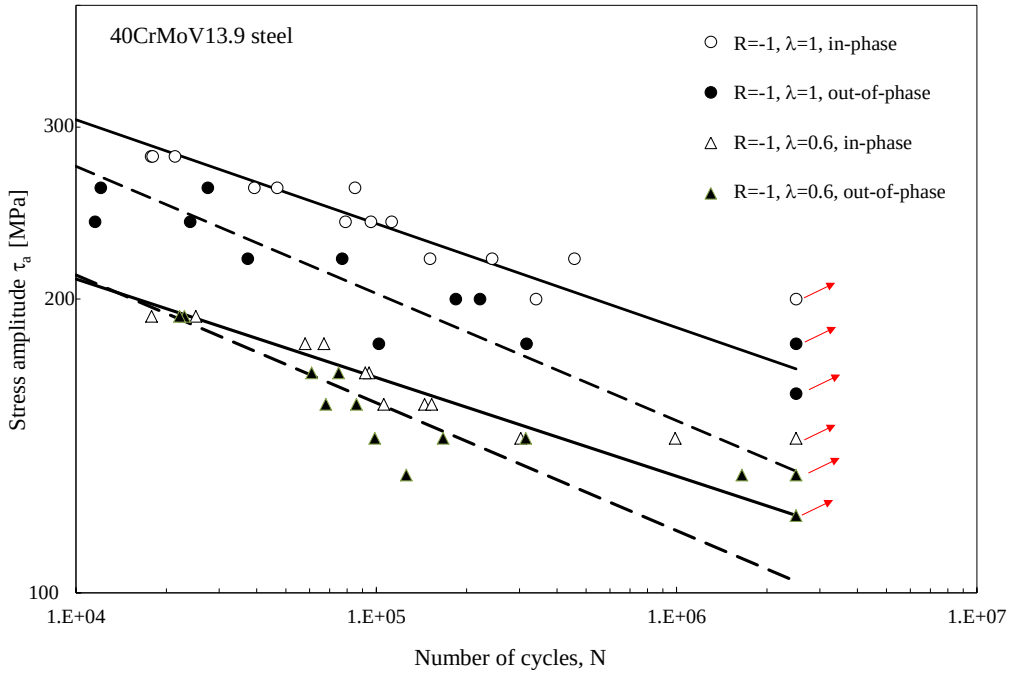

Figure 7.3.16. Fatigue data taken from Berto et al. (2013).

To conclude, it can be also said that in a recent review (Susmel 2013) of the most widely adopted multiaxial fatigue criteria is carried out discussing the main issues to calibrate the adopted design criterion being the used information usually derived from the fatigue strength under both pure uniaxial and pure torsional

fatigue loading. The complex fatigue response of metallic materials to multiaxial loading paths requires for calibration some information which can be obtained only by running the appropriate experiments. Unfortunately, because of a lack of both time and resources, very often, structural engineers are requested to perform the multiaxial fatigue assessment by guessing the necessary fatigue properties. In this complex scenario, initially, the nowadays available empirical rules suitable for estimating fatigue strength under both pure axial and pure torsional fatigue loading have been reviewed (Susmel 2013).

Under proportional loading, the empirical rules reviewed in that paper can confidently be used to perform the multiaxial fatigue assessment, this holding true in the presence of both zero and non-zero superimposed static stresses. On the contrary, under non-proportional loading, the use of such rules can result in a non-conservative fatigue design. This work is a first trial to solve this problem.

7.4 Discrimination of the phase displacement effect by means of energetic assumptions

This brief paragraph focuses on the research of a discriminating parameter dealing with the phase effect between applied load amplitudes on multiaxial fatigue, considering energetic assumptions. The same geometries already analysed in the previous sections will be studied.

The analytical relation describing the strain energy at a particular point of coordinates (r,θ) and at a certain machine angle (β) of the fatigue cycle can be written as:

$$W(r,\theta,\beta)=\frac{1}{2E}\left[\sigma_{rr}^2(r,\theta,\beta)+\sigma_{\theta\theta}^2(r,\theta,\beta)+\sigma_{zz}^2(r,\theta,\beta)-2\nu\cdot\left(\sigma_{rr}(r,\theta,\beta)\cdot\sigma_{\theta\theta}(r,\theta,\beta)+\right.\right.$$
$$\left.\left.+\sigma_{\theta\theta}(r,\theta,\beta)\cdot\sigma_{zz}(r,\theta,\beta)+\sigma_{rr}(r,\theta,\beta)\cdot\sigma_{zz}(r,\theta,\beta)\right)+2(1+\nu)\left(\tau_{r\theta}^2(r,\theta,\beta)+\tau_{\theta z}^2(r,\theta,\beta)+\tau_{rz}^2(r,\theta,\beta)\right)\right] \quad (7.4.1)$$

Where all the stress components can be obtained from Eqs. (7.2.1-7.2.6).

By implementing a particular routine furnishing the most damaging point in terms of strain energy in the vicinity of the notch tip, the behaviour of this particular parameter over one loading cycle has been obtained.

The value of the strain energy obtained at a particular distance r (0.28 mm) and in the critical angle θ can be expressed as:

$$W(\beta)=\frac{1}{2E}\left[\sigma_{rr}^2(\beta)+\sigma_{\theta\theta}^2(\beta)+\sigma_{zz}^2(\beta)-2\nu\cdot\left(\sigma_{rr}(\beta)\cdot\sigma_{\theta\theta}(\beta)+\right.\right.$$
$$\left.\left.+\sigma_{\theta\theta}(\beta)\cdot\sigma_{zz}(\beta)+\sigma_{rr}(\beta)\cdot\sigma_{zz}(\beta)\right)+2(1+\nu)\left(\tau_{r\theta}^2(\beta)+\tau_{\theta z}^2(\beta)+\tau_{rz}^2(\beta)\right)\right] \quad (7.4.2)$$

In this formulation the stress components vary only as a function of the machine angle β.

Figure 7.4.1 shows the trend of the strain energy during one loading cycle in the particular case of a load ratio equal to -1 and a biaxiality ratio equal to 1. As already remarked in the case of the maximum shear stress based analysis, an in-phase loading generates a behaviour ranging from zero to an absolute maximum value. The introduction of a phase displacement between the applied loads generates an increasing of the minimum value of the instantaneous strain energy and at the same time a decrement of the maximum value, obtaining a sinusoidal function with a narrower amplitude the bigger becomes the phase displacement.

By following the same procedure reported in the previous sections, the strain energy has been averaged during an entire loading cycle in order to search a particular discriminating effect of the phase displacement.

Figure 7.4.2 demonstrates that, both in the case of load ratio equal to -1 or 0, the strain energy averaged during one loading cycle holds a constant value varying the phase displacement between the applied loads. In conclusion, a procedure based on energetic assumptions proved to be unsuitable for the discrimination of the phase effect on multiaxial fatigue.

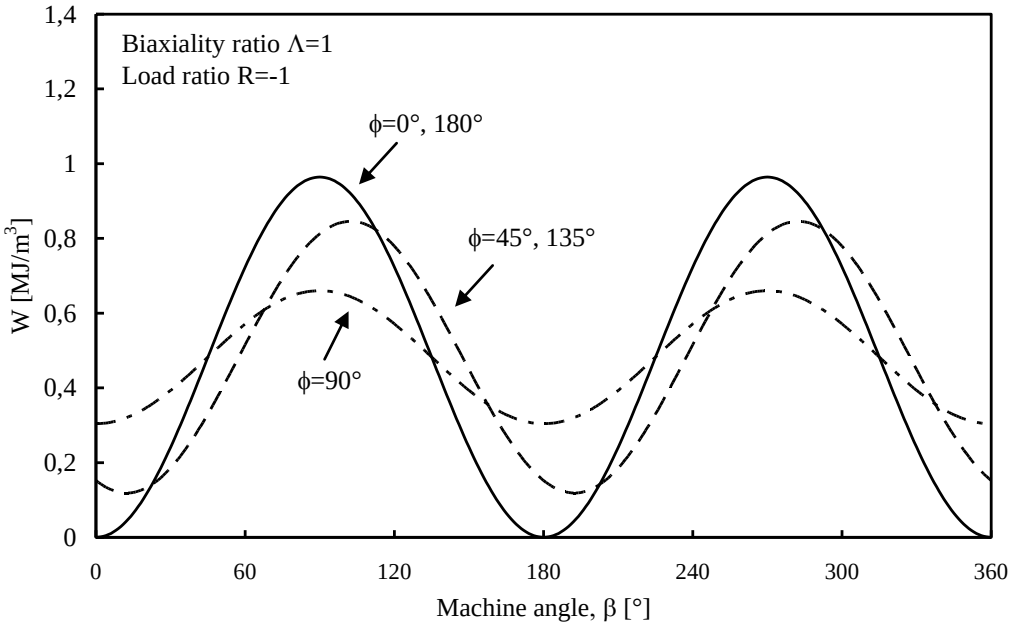

Figure 7.4.1. Variation of the strain energy on the critical coordinate θ during an entire loading cycle for different phase displacements. Case R=-1, Λ=1.

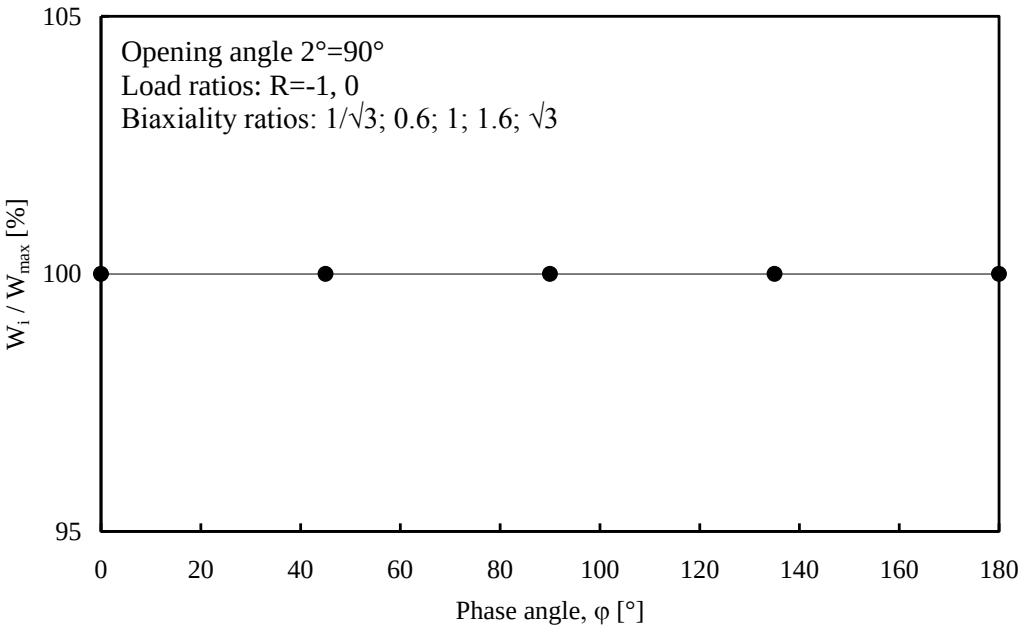

Figure 7.4.2. Summary of the phase angle effect for different biaxiality ratios in the case of R=0 and R=-1 by means of energetic assumptions.

7.5 Conclusions

The present chapter deals with the investigation of the effect of the phase angle on sharp V-notched components subjected to multi-axial fatigue. This is still an open problem and very challenging issue. The possible detrimental influence of the phase angle is often related to the arising of non linear effects contemplated on the cyclic plasticity theory, as suggests by many papers in the literature.

Being conscious of the material dependent non-linear effects just mentioned and the simplified assumption of the herein proposed approach, this work tries to explain the phase angle effect only focusing on the linear elastic stress field ahead of the notch. The parameter considered critical in the present study is the maximum shear stress averaged over an entire loading cycle. The analogy of the present model with the critical plane approach is only the consideration of a shear stress as a critical parameter. On the other hand substantial differences exist between the present approach and those based on critical planes. The main difference with the critical plane approach is that in the present work, due to the fact that sharp notches are considered, the critical point is not known a priori and its determination is based on the maximization of the critical parameter.

All in all 4500 different analyses have been carried out considering different load ratios, biaxiality ratios and phase angles. A dedicate software has been implemented in order to compute the averaged maximum shear stress on different inclinations with respect to the notch bisector line. It has been found that the location on which the averaged parameter reaches its maximum value is far from the notch bisector line and it acts at a circumferential coordinate ranging between 70° and 90° depending on the loading conditions. Considering an entire cycle on the critical angle, the maximum shear stress ranges from a value equal to zero to an absolute maximum in the case of in-phase loading. Introducing a phase angle it has been noted that the peak values decrease while the valley values increase, resulting in a mean effect more damaging for the component.

In more detail, it has been shown that in the case of a fully reversed multi-axial fatigue loading the most damaging configuration is the 90° out of phase loading with a decreasing of the fatigue strength between 6 and 15% with respect to the in-phase loading. The influence of the phase angle is more pronounced for lower

values of the biaxiality ratio. A similar behaviour has been observed for a load ratio equal to 0 being in this case, the most damaging configuration at ϕ=180°. The reduction of the fatigue strength has been estimated between 15 and 28%. Also in this case, the influence of the phase angle is more pronounced for lower values of the biaxiality ratio.

The phase displacement effect has been investigated also by means of energetic assumptions. A strain energy criterion averaged over one loading cycle proved to be unsuitable for this particular analysis, In fact, by varying the applied load amplitudes the value of the averaged strain energy on the critical point in the vicinity of the notch tip results to be constant.

8

Cyclic plasticity on notched components: 3D effects and energetic considerations

8.1 Basic concepts on cyclic plasticity

A cyclic plasticity model is used to be defined by three main different functions describing the three critical parts of the plastic evolution of a particular material:

- The yield function is the boundary surface of the problem. Considering the three domensional stress space, the yield function is the locus of points which divides the linear elastic behavior (within the surface) and the elastic plastic behavior (on the surface);
- The flow rule is the particular relation describing the increment/decrement of plastic strain during a load increment/decrement;
- The hardening rule defines the translation/expansion of the boundary yield surface during a cyclic loading. It establishes the movement of the yield surface within the three dimensional stress space.

8.1.1 Yield function

During a cyclic loading the material is assumed to follow an elastic stress-strain relation without plastic strains until the stresses satisfy the yield condition. The two most used conditions are due to Tresca and von Mises (Figure 8.1.1). Considering the hydrostatic axis as reference axis and the π plane represents in the figure, the elliptical boundary surface on Cartesian coordinate system, described by von Mises, becomes a circular boundary surface in the deviatoric stress space. The radius of the new circumferential surface is equal to $\sqrt{2}k$ that is a

characteristic value varying from material to material, where k denotes the yield stress in simple shear.

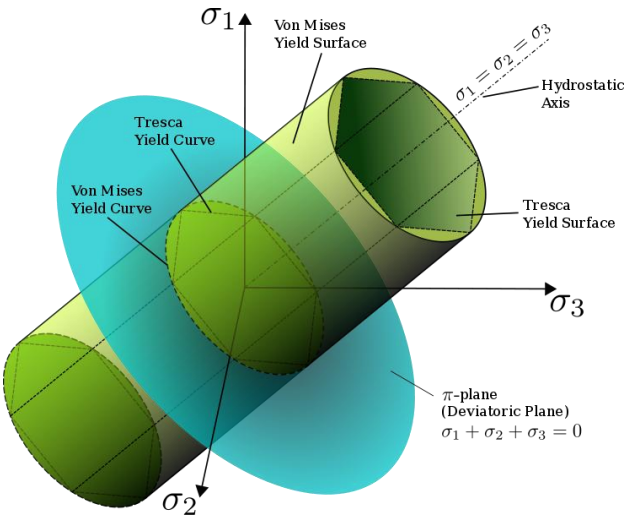

Figure 8.1.1. Schematic representation of Tresca and von Mises criterion (figure from Wikipedia.com)

In order to better describe the material behavior during a cyclic plasticity problem the backstress tensor, α, representing the center of the boundary yield surface has been introduced (see Figure 8.1.2). The backstress permits to instantaneously monitor the yield condition by taking in consideration the movement of the limiting surface during the whole loading cycle. In the next sessions the particular yield stress condition used in this chapter will be described.

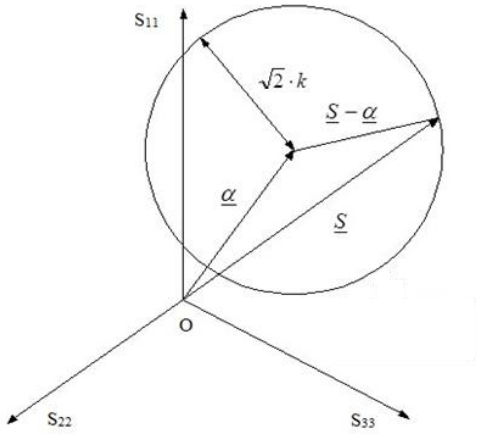

Figure 8.1.2. Representation of yield surface and backstress (figure from Jiang and Sehitoglu 1996).

8.1.2 Flow rule

The flow rule relates the increment of plastic strain to the respectively increment of stress. The most commonly rule used for metals is the associated flow rule or the normality condition (Drucker 1951). According to this rule one can say that the plastic strain increment is collinear with the instantaneous exterior normal to the yield surface.
Mathematically the flow rule can be expressed as:

$$d\varepsilon_{ij}^{P} = \frac{1}{h}\left\langle dS_{ij} n_{ij} \right\rangle n_{ij} \tag{8.1.1}$$

Where < > denotes the McCauley brackets:

$$\left\langle dS_{ij} n_{ij} \right\rangle = \begin{cases} 0, & dS < 0 \\ dS, & dS \geq 0 \end{cases} \tag{8.1.2}$$

This implies that plastic strain is reached only in presence of a loading condition and not during the unloading part of the cycle.
Parameters n and h represent the unit exterior normal and the instantaneous plastic modulus function respectively.

8.1.3 Hardening rule

Generally all the cyclic plasticity models use the above mentioned yield criterion and flow rule, thus an hardening rule distinguishes one plasticity model from another. An hardening rule specifies how the yield surface changes during a loading cycle fatigue.

Isotropic hardening

This type of hardening rule simulates an homothetic expansion of the yield surface in all directions (see Figure 8.1.3). This means that an increase of the plastic strain causes an increase of the linear elastic domain. In the case of stress

controlled cyclic loading the use of an isotropic hardening rule implies linear completely elastic deformations after the first fatigue cycle.

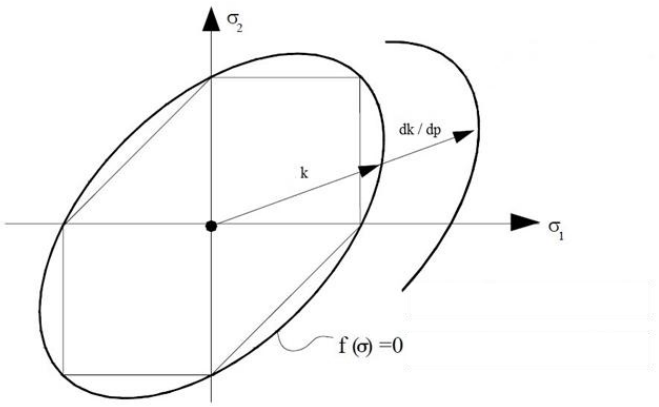

Figure 8.1.3. Schematic representation of isotropic hardening (figure from Jiang and Sehitoglu 1996)

Kinematic hardening

The kinematic hardening model is used to consider the Bauschinger effect. It consists on a reduction of the yield strength in compression when the material is loaded over its tensional yield strength limit. The critical surface in this case does not change in shape or size but it has the possibility to move through the stress space (see Figure 8.1.4).

The movement of the center of the yield surface is called backstress and it represents the range between the centers of two consecutive steps of the yield surface during a loading cycle.

Kinematic hardening model produces a stabilized cyclical response after the first loading cycle. For this reason this type of hardening rule is the most used dealing with fatigue problems.

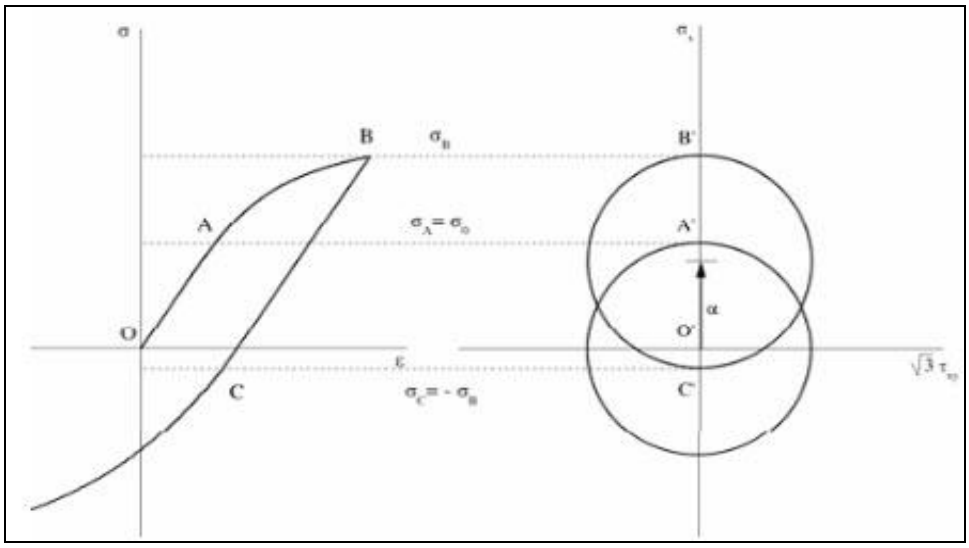

Figure 8.1.4. Schematic representation of kinematic hardening. Movement of the yield surface into the stress space.

8.2Introduction on chapter's aim

Failure against fatigue of engineering components is often related to the presence of stress raisers like defects, cracks or different shaped notches. It is well known that the stress arising in the proximity of these points may exceed the yielding limit of the material. The full elastic-plastic stress and strain fields ahead of notches can be assessed by using complex non linear finite element analyses that, however, result in consuming precious time or monetary resources by engineers and industries. For these reasons, simplified methods that approximate the actual elastic–plastic notch-tip material behaviour are frequently preferred in practical engineering applications. One of the most important works on the evaluation of the elastic-plastic stress state at the tip of a notch is due to Neuber (1961), which proposed a general rule able to obtain the stress-strain concentration factors for uniaxial static and cyclic loading. Dealing with energetic assumptions, Molski and Glinka (1981) stated that the strain energy density distribution in the plastic zone ahead of a notch tip is the same as that determined under a pure elastic stress–strain solution, adopting this as the basis of the ESED criterion. During the last years extensions of the above mentioned criteria have been developed in order to refine the assessment of the actual state of stress and strain ahead of a notch under

simple and complex loading configurations, among the others Topper et al. (1969), Hoffmann and Seeger (1985), Moftakar et al. (1995), Elliyn and Kujawski (1989), Singh et al. (1996), Ye et al. (2004-2008), Zappalorto and Lazzarin (2009-2010). In particular Ye et al.. (2004-2008), making use of thermodynamics assumptions, considered the influence of the stored energy during the loading history as a fundamental parameter for the calculation of the actual stress-strain at the tip of a notch. With this aim a new modified approach, which confines the two milestones as limiting cases of the same problem, has been presented. In particular Ye proved that the two above mentioned methods give the same results when considering the dissipated energy as a negligible parameter.

Uniaxial and multiaxial fatigue loads generate a variable complex state of stress at the tip of a rounded notch. In order to take into account this particular effect, incremental approximate formulations have been developed establishing energetic equilibrium conditions between the components of stress and strain acting at the notch tip (Elliyn and Kujawski 1989, Moftakar et al. 1995, Singh et al. 1996).

The incremental approximate procedure make use of constitutive relations of the cyclic incremental plasticity theory that is composed of three main parts: 1) The von Mises yield criterion is the most used in fatigue problems. 2) The flow rule (or normality condition) presented by Drucker (1960) is used to combine the increment of plastic strain with the related increment of stress. 3) The hardening rule is the part that distinguishes one plasticity model to another. In the case of fatigue problems the kinematic hardening rule is the most used because of the inner ability to simulate the Bauschinger effect during cyclic loading. Prager (1955) proposed the first linear hardening formulation able to take into account the above mentioned effect. This particular rule allows the yield surface to move into the stress space without changing in shape or size. Armstrong and Frederick (1966) presented the first non linear relation introducing a recovery term associated to a strain memory effect. Different extensions of the A-F rule have been proposed in the last years (see among the others Bower 1987, Bower and Johnson 1989, Ohno-Wang 1991). Chaboche (1979,1987) expressed for the first time a non linear kinematic hardening rule in the form of an expansion of M backstress parts, each one following the Armstrong-Frederick relation. Chaboche

model has been adopted by many finite element codes in order to obtain the actual behaviour of the material subjected to fatigue loading. A new A-F type model has been presented by Jiang and Sehitoglu (1996a, 1996b) aiming to account for the ratcheting effect during an asymmetric loading cycle.

Many contributions dealing with fatigue plasticity problems have been developed in the last years addressing different fields of applications. Jiang and Xu (2001) studied the problem of a plate with a central hole and a shaft with a circumference groove subjected to proportional and non proportional loading, implementing an approximate incremental method and comparing the results with some cyclic FE analyses. Ye et al. (2004-2008) made use of the incremental procedure in order to develop the modified ESED method. The new approach was first calibrated with experimental results obtained by uniaxial fatigue tests on flat specimens weakened by different notch geometries (2004) and then extended to the multiaxial fatigue of notched components (2008). Foletti and Desimone (2007) used a dedicated algorithm based on cyclic plasticity in order to address the problem of the residual stresses in rolling contact fatigue obtaining a very good agreement with respect to much more time consuming non linear FE analyses. Qiu et al. (2009) made use of the incremental procedure in order to investigate the non-Masing behaviour of 16MnR steel. Automotive problems related to wheel radial fatigue tests and rear axles strength have been addressed by Firat et al. (2009) and Firat (2011) which used a cyclic plasticity model aiming to obtain the actual stress and strain state at the focal points of the components in exam. Gao et al. (2010) conducted tension–compression, torsion, and axial-torsion fatigue experiments on notched shaft specimens made of 16MnR steel comparing the fatigue life with those obtained by provisional analyses based on incremental cyclic plasticity.

As already mentioned, the incremental cyclic plasticity has been used in order to address plane or axy-symmetric problems but it has never been coupled with three dimensional effect arising at the tip of a notched component. An extended review on the 3D linear elastic stress distribution ahead of the notch tip can be found in (Pook 2013) where the developments over the past 50 years leading up to the current state of the art are described. All the three conditions of loads have been addressed concluding that three-dimensional effects are sometimes ignored in

situations where they might be important for the strength of components. In particular, the application of a remote Mode II loading induces a coupled Mode O (out-of-plane) singularity at the tip of a crack (Harding et al. 2010). The authors investigated the parameters influencing the intensity of this new singularity and demonstrated the relevance of this new singular mode to practical problems, as i.e., welded lap joints. Berto et al. (2011a) extended the study of three dimensional effects on sharp notched components, largely ignored in the past. Dealing with rounded notch geometries, Lazzarin and Zappalorto (2012), Berto et al. (2012a) and Berto and Marangon (2013), demonstrated that also when the notch root radius is different from zero, the out-of-plane mode continues to exist, and its intensity depends on the notch radius and the plate thickness. A new stress field theory for plates of finite thickness has been proposed in (Zappalorto and Lazzarin 2013) using two different functions able to take into account the plane and the out-of-plane notch problem both in the case of sharp and rounded notches.

Aiming to relate the incremental cyclic plasticity to the three-dimensional effects arising in the vicinity of the notch tip, this chapter first focuses on the calibration of the incremental cyclic plasticity with plane and axy-symmetric problems of notched members subjected to uniaxial and multiaxial cyclic loadings. Subsequently, the procedure will be extended for the first time to the investigation of the three dimensional effects arising at the tip of a rounded notch by considering the presence of a small scale yielded area ahead the notch tip. 3D flat specimens weakened by different geometries and subjected to cyclic Mode I and Mode II loading will be investigated by comparing the analytical results obtained from a modification of the incremental routine with cyclic elastic-plastic FE analyses.

8.3Analytical frame

Recently Ye et al. (2004) proposed a unified expression to estimate the elastic-plastic stress/strain state at the tip of a rounded notch both in the case of static and cyclic uniaxial loading. The general expression can be written as follows:

$$K_t^2 \Delta\sigma^e \Delta\varepsilon^e = \Delta\sigma\ \Delta\varepsilon\ + \Delta W_q(\Delta\sigma, \Delta\varepsilon\ ) \tag{8.3.1}$$

where K_t is the theoretical (elastic) stress concentration factor, $\Delta\sigma^e$ and $\Delta\varepsilon^e$ are the remotely applied nominal stress and strain ranges and $\Delta\sigma$ and $\Delta\varepsilon$ denote the notch-tip elastic plastic stress and strain ranges. ΔW_q is, instead, the dissipated energy during one loading cycle. The approach considers the energy stored within the specimen during the loading as a damaging parameter. The Neuber's rule (Neuber 1961) and the ESED approach (Molski and Glinka 1981) can be obtained as particular cases of the above mentioned criterion.

Ye also introduced the so called "energy dissipation coefficient" in order to obtain a physical relationship between the plastic strain energy density and the dissipated energy during one loading cycle:

$$C_q = \frac{\Delta W_q}{\Delta W_p} = \frac{1 - 2n'}{1 + n'} \tag{8.3.2}$$

In Eq.(8.3.2) ΔW_p is the total plastic strain energy density during one loading cycle and n' is the strain hardening exponent of the material took into account.

Moving from a uniaxial to a multiaxial state of stress/strain, the use of K_t is no longer sufficient because it is linked only to the normal stress component acting at the notch tip, thus a more general formulation of Eq. (8.3.1) is needed. This problem can be overcome by introducing the "hypothetical notch tip stress and strain" (Ellyin and Kujawski 1989 and Singh et al. 1996) which allows to define an equilibrium equation for each component of stress/strain acting at the tip of a rounded notch. The governing equation is:

$$\Delta\sigma_{ij}^e \Delta\varepsilon_{ij}^e = \Delta\sigma_{ij}\Delta\varepsilon_{ij} + C_q \Delta W_p(\Delta\sigma_{ij}, \Delta\varepsilon_{ij}) \tag{8.3.3}$$

The subscripts "ij" denote the different components of stress and strain involved in the problem.

When the proposed expression is applied to estimate the notch-tip stress and strain field of a generic cyclic loading a proper incremental form should be developed:

$$\sigma_{ij}^{e}\delta\varepsilon_{ij}^{e}+\varepsilon_{ij}^{e}\delta\sigma_{ij}^{e}=(1+C_q)\sigma_{ij}\delta\varepsilon_{ij}+(1-C_q)\varepsilon_{ij}\delta\sigma_{ij} \tag{8.3.4}$$

The prefix δ denotes a small but finite increment and the implicit summation rule is applied. Gao et al. (2010) modified Eq.(8.3.4) by introducing, within the formulation, the reference state parameter defined by Chu (1995b).

$$\left(\sigma_{ij}^{e}-\sigma_{ij}^{e(0)}\right)\delta\varepsilon_{ij}^{e}+\left(\varepsilon_{ij}^{e}-\varepsilon_{ij}^{e(0)}\right)\delta\sigma_{ij}^{e}=(1+C_q)\left(\sigma_{ij}-\sigma_{ij}^{(0)}\right)\delta\varepsilon_{ij}+(1-C_q)\left(\varepsilon_{ij}-\varepsilon_{ij}^{(0)}\right)\delta\sigma_{ij} \tag{8.3.5}$$

The superscript "0" represents the reference state of the particular component of stress/strain. When a reversal point of a component occurs, the reference states of the components are updated to the corresponding stress and strain at the reversal point.

For the sake of simplicity, in this work, all the equations taking the form of Eq. (8.3.5) will be named "energy equations".

Once the linear elastic components of stress and strain are known, each energy equation presents two unknowns: the elastic-plastic component of stress and the related elastic-plastic component of strain. Thus every energy equation has to be coupled with the corresponding constitutive equation.

According to the theory of small deformations, an incremental component of strain can be written as the sum of an elastic part ($\delta\varepsilon^{e}_{ij}$) and a plastic contribution ($\delta\varepsilon^{p}_{ij}$) as follows:

$$\delta\varepsilon_{ij}=\delta\varepsilon_{ij}^{e}+\delta\varepsilon_{ij}^{p} \tag{8.3.6}$$

The elastic part of strain is governed by the well known Hooke's law:

$$\delta\varepsilon_{ij}^{e} = \frac{\delta\sigma}{2G} - \frac{\nu}{E}\delta\sigma_{kk}\delta_{ij} \tag{8.3.7}$$

where G is the shear modulus, E is the Young's modulus, ν the Poisson's ratio, δ_{ij} the Kronecker delta and σ_{kk} the hydrostatic component of stress.

The incremental plastic part of strain can be described by using the cyclic plasticity theory which can be comprehensively described by the introduction of a proper yield criterion, a flow rule and an hardening rule which will be illustrated in the following.

The yield function represents the locus of points that divides the linear elastic behaviour (within the boundary) and the elastic plastic behaviour (boundary surface). In the case of cyclic loading the von Mises yield criterion is the most used. The material is thought to follow the elastic behaviour with totally absence of plastic deformation until the stress components satisfy the yield condition:

$$f = \sqrt{(S_{ij} - \alpha_{ij})(S_{ij} - \alpha_{ij})} - \sqrt{2}k = 0 \tag{8.3.8}$$

Where S_{ij} is the deviatoric stress, α_{ij} is the deviatoric backstress (center of the yield surface) and k is the yield stress in simple shear.

When the yield condition is satisfied, the normality flow rule has to be applied in order to describe the increment of plastic strain behaviour during a loading cycle. Mathematically:

$$d\varepsilon_{ij}^{p} = \frac{1}{h}\langle dS_{ij}n_{ij}\rangle n_{ij} \tag{8.3.9}$$

Where the symbol "< >" denotes the McCauley brackets (i.e. $\langle x\rangle = (x + |x|)/2$).

n_{ij} is the unit exterior normal to the yield surface which is calculated using the following formula:

$$n_{ij} = \frac{S_{ij} - \alpha_{ij}}{\left\| S_{ij} - \alpha_{ij} \right\|} \tag{8.3.10}$$

and h is the plastic modulus function that will be described later.

Finally, the hardening rule deals with the definition of the translation/expansion of the boundary yield surface within the stress space. In engineering practice the kinematic hardening rule is the most used in the case of cyclic loading, being it able to account for the Bauschinger effect. In particular, in the generic case of a multiaxial state of stress/strain, the non linear kinematic hardening rule gives the most accurate results. In this case, the yield surface is allowed only to move within the stress space but not to homotetically expand or contract. Aiming only to simplify the implementation of the incremental routine for the determination of the elastic-plastic state of stress/strain, the Jiang-Sehitoglu's (1996a-1996b) non linear kinematic hardening has been used for the calculations. The formulation of the plastic modulus function and of the i-th part of the backstress can be written as follows:

$$h = \sum_{i=1}^{M} c^{(i)} \cdot \left(r^{(i)} - \left(\frac{\left\| \alpha^{(i)} \right\|}{r^{(i)}} \right)^{\chi^{(i)}} \alpha^{(i)} : n \right) \delta p \tag{8.3.11}$$

$$\delta\alpha^{(i)} = c^{(i)} \cdot r^{(i)} \left(n - \left(\frac{\left\| \alpha^{(i)} \right\|}{r^{(i)}} \right)^{\chi^{(i)}+1} \frac{\alpha^{(i)}}{\left\| \alpha^{(i)} \right\|} \right) \delta p \tag{8.3.12}$$

Where ":" denotes a scalar vector and δp is the equivalent plastic strain increment which can be computed as:

$$\delta p = \sqrt{\frac{2}{3} \left(\delta\varepsilon_{ij}^{p} : \delta\varepsilon_{ij}^{p} \right)} \tag{8.3.13}$$

Parameters $c^{(i)}$, $r^{(i)}$ and $\chi^{(i)}$ are "ad-hoc" material coefficients. The superscript "i" denotes the ith part of the incremental backstress. In fact, according to Chaboche (1979-1987), the total backstress can be thought of as composed by M additive parts:

$$\delta\alpha = \sum_{i=1}^{M} \delta\alpha^{(i)} \tag{8.3.14}$$

The Jiang-Sehitoglu's model is able to take into account a non constant ratcheting decay phenomena. In the case of cyclic loading with load ratio R= -1, considered for all the analyses in this work, this phenomena can be neglected. Thus the parameter $\chi^{(i)}$ in Eqs.(8.3.11, 8.3.12), which controls the ratchetting rate decay can be set equal to zero (Jiang and Kurath 1996). This allows one to obtain the initial Chaboche model (1979-1987) by means of Jiang-Sehitoglu coefficients. The Chaboche model, however, is able to take into account a constant ratchetting rate decay.

The procedure for the determination of the material coefficients $c^{(i)}$, $r^{(i)}$ and $\chi^{(i)}$ is extensively described in (Jiang and Kurath 1996). It is based on a multilinearization of the plastic part of the cyclic stabilised curve of the material. When M couple of (σ,ε^p) on the SCC curve are known, the evaluation of the i-th material parameters is straightforward and equal to:

$$c^{(i)} = \sqrt{\frac{2}{3}}\frac{1}{\varepsilon^p} \tag{8.3.15}$$

$$r^{(i)} = \frac{2}{3}\frac{H_{(i)} - H_{(i+1)}}{c^{(i)}} \tag{8.3.16}$$

Being:

$$H_{(i)} = \frac{\sigma_{(i)} - \sigma_{(i-1)}}{\varepsilon^{p}_{(i)} - \varepsilon^{p}_{(i-1)}} \tag{8.3.17}$$

Many contributions on this topic deal with axy-symmetric components weakened by circumferential rounded notches and subjected to a multiaxial remote loading (Ye et al. 2008, Gao et al. 2010, Firat et al. 2009, Firat 2011). Only few contributions deal with plane 2D specimens weakened by rounded notches (Sethuraman et al. 2004, Ye et al. 2004). In this work, the use of the incremental cyclic plasticity theory combined with the "energy equations" will be first calibrated analysing plane and axy –symmetric components and then extended to the evaluations of three-dimensional effects at the tip of rounded notches. In the case of 3D flat specimens subjected to tensile loading it is well known that the stress concentration factor decreases moving through the thickness of the specimen (Pook 2013). In addiction, the application of a remote cyclic in-plane shear load induces a local multiaxial state of stress at the tip of the notch. Many contributions on this topic explain that, at the pointed notch tip, under linear elastic conditions a new singularity called "Out of plane mode" arises in addiction to the Mode II (Harding et al. 2010, Berto et al. 2011, Lazzarin and Zappalorto 2012, Berto et al. 2012a, Berto and Marangon 2013). The so called "O Mode" holds zero value at the mid plane of the specimen, reaches a maximum value approaching to the free surface and then falls to zero at the free surface. The new applied procedure will be used to analyse these phenomena under cyclic elastic-plastic behaviour, providing different hysteresis loops moving through the thickness of the specimen.

Six different combinations of specimen geometries and applied loads have been studied in this work. In the following the elastic-plastic systems to be solved, in order to obtain the full stress/strain state at the tip of a rounded notch during one loading cycle, are reported.

Tensile loading – Plane stress

Consider the Cartesian coordinate system centred at the tip of a rounded notch (Figure 8.3.1). In the case of a remote tensile loading applied to a very thin plate, four equations (three constitutive equation and one energy equation) are needed for the determination of the elastic-plastic stress/strain state at the tip of the notch:

$$\begin{cases} \left(\sigma_{yy}^{e}-\sigma_{yy}^{e(0)}\right)\delta\varepsilon_{yy}^{e}+\left(\varepsilon_{yy}^{e}-\varepsilon_{yy}^{e(0)}\right)\delta\sigma_{yy}^{e}=(1+C_q)\left(\sigma_{yy}-\sigma_{yy}^{(0)}\right)\delta\varepsilon_{yy}+(1-C_q)\left(\varepsilon_{yy}-\varepsilon_{yy}^{(0)}\right)\delta\sigma_{yy} \\ \delta\varepsilon_{xx}=\delta\sigma_{yy}\left(-\frac{1}{3h}n_{xx}^{2}+\frac{2}{3h}n_{xx}n_{yy}-\frac{1}{3h}n_{xx}n_{zz}-\frac{\nu}{E}\right) \\ \delta\varepsilon_{yy}=\delta\sigma_{yy}\left(-\frac{1}{3h}n_{xx}n_{yy}+\frac{2}{3h}n_{yy}^{2}-\frac{1}{3h}n_{yy}n_{zz}+\frac{1}{E}\right) \\ \delta\varepsilon_{zz}=\delta\sigma_{yy}\left(-\frac{1}{3h}n_{xx}n_{zz}+\frac{2}{3h}n_{yy}n_{zz}-\frac{1}{3h}n_{zz}^{2}-\frac{\nu}{E}\right) \end{cases} \tag{8.3.18}$$

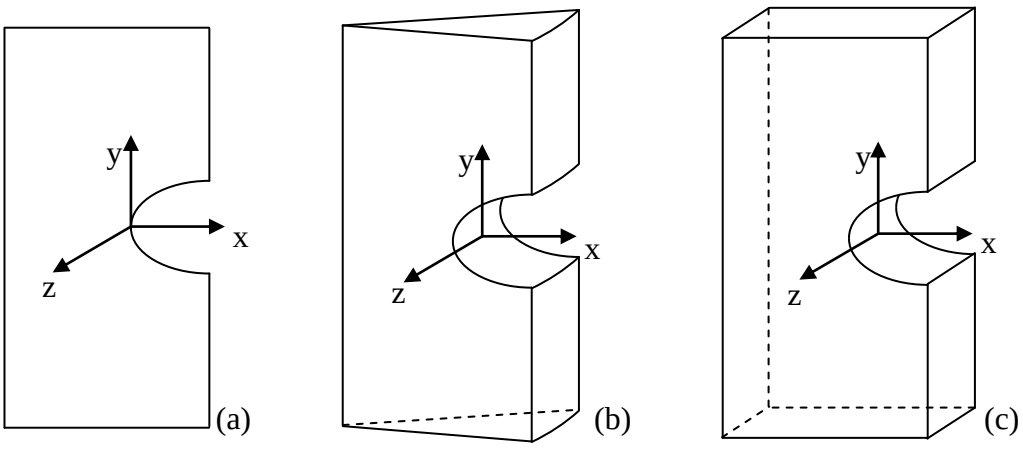

Figure 8.3.1. Cartesian coordinate systems in the case on 2D-problems (a), axy-symmetric problems (b), 3D-problems (c).

Tensile loading – Plane strain

In the case of plane strain conditions, the following four relations are needed for the determination of the elastic plastic stress/strain state:

$$\begin{cases} \left(\sigma^{e}_{yy}-\sigma^{e(0)}_{yy}\right)\delta\varepsilon^{e}_{yy}+\left(\varepsilon^{e}_{yy}-\varepsilon^{e(0)}_{yy}\right)\delta\sigma^{e}_{yy}=(1+C_q)\left(\sigma_{yy}-\sigma^{(0)}_{yy}\right)\delta\varepsilon_{yy}+(1-C_q)\left(\varepsilon_{yy}-\varepsilon^{(0)}_{yy}\right)\delta\sigma_{yy} \\ \delta\sigma_{zz}=\nu_{pl}\cdot\sigma_{yy} \\ \delta\varepsilon_{xx}=\delta\sigma_{yy}\left(-\dfrac{1+\nu_{pl}}{3h}n^{2}_{xx}+\dfrac{2-\nu_{pl}}{3h}n_{xx}n_{yy}-\dfrac{1-2\nu_{pl}}{3h}n_{xx}n_{zz}-\dfrac{\nu}{E}(1+\nu)\right) \\ \delta\varepsilon_{yy}=\delta\sigma_{yy}\left(-\dfrac{1+\nu_{pl}}{3h}n_{xx}n_{yy}+\dfrac{2-\nu_{pl}}{3h}n^{2}_{yy}-\dfrac{1-2\nu_{pl}}{3h}n_{yy}n_{zz}+\dfrac{1-\nu^{2}}{E}\right) \end{cases} \tag{8.3.19}$$

Where ν_{pl} is equal to 0.5 and it is named plastic Poisson's ratio.

Pure torsion loading – Axy-symmetric specimen

The case of a pure torsion loading consists in two different equations governing the problem, in fact, at the notch tip, only the "yz" component of stress/strain acts.

$$\begin{cases} \left(\sigma^{e}_{yz}-\sigma^{e(0)}_{yz}\right)\delta\varepsilon^{e}_{yz}+\left(\varepsilon^{e}_{yz}-\varepsilon^{e(0)}_{yz}\right)\delta\sigma^{e}_{yz}=(1+C_q)\left(\sigma_{yz}-\sigma^{(0)}_{yz}\right)\delta\varepsilon_{yz}+(1-C_q)\left(\varepsilon_{yz}-\varepsilon^{(0)}_{yz}\right)\delta\sigma_{yz} \\ \delta\varepsilon_{yz}=\left(\dfrac{2}{h}n^{2}_{yz}+\dfrac{1+\nu}{E}\right)\cdot\delta\sigma_{yz} \end{cases} \tag{8.3.20}$$

In this case the Cartesian coordinate system has been hold in order to simplify the calculation. It has been assumed the tip of the notch belonging to the "xy" plane

Multiaxial loading – Axy-symmetric specimen

The general case of an axy-symmetric specimen subjected to multiaxial loading has been faced by many researchers (Ye et al. 2008, Gao et al. 2010, Firat et al. 2009, Firat 2011). For the sake of completeness the governing equation will be presented.

$$
\begin{cases}
\left(\sigma_{yy}^{e}-\sigma_{yy}^{e(0)}\right)\delta\varepsilon_{yy}^{e}+\left(\varepsilon_{yy}^{e}-\varepsilon_{yy}^{e(0)}\right)\delta\sigma_{yy}^{e}=(1+C_q)\left(\sigma_{yy}-\sigma_{yy}^{(0)}\right)\delta\varepsilon_{yy}+(1-C_q)\left(\varepsilon_{yy}-\varepsilon_{yy}^{(0)}\right)\delta\sigma_{yy} \\
\left(\sigma_{zz}^{e}-\sigma_{zz}^{e(0)}\right)\delta\varepsilon_{yy}^{e}+\left(\varepsilon_{zz}^{e}-\varepsilon_{zz}^{e(0)}\right)\delta\sigma_{zz}^{e}=(1+C_q)\left(\sigma_{zz}-\sigma_{zz}^{(0)}\right)\delta\varepsilon_{zz}+(1-C_q)\left(\varepsilon_{zz,(z)}-\varepsilon_{zz}^{(0)}\right)\delta\sigma_{zz} \\
\left(\sigma_{yz}^{e}-\sigma_{yz}^{e(0)}\right)\delta\varepsilon_{yy}^{e}+\left(\varepsilon_{yz}^{e}-\varepsilon_{yz}^{e(0)}\right)\delta\sigma_{yz}^{e}=(1+C_q)\left(\sigma_{yz}-\sigma_{yz}^{(0)}\right)\delta\varepsilon_{yz}+(1-C_q)\left(\varepsilon_{yz,(z)}-\varepsilon_{yz}^{(0)}\right)\delta\sigma_{yz} \\
\delta\varepsilon_{xx}=\dfrac{n_{xx}}{3h}\Big(-\left(\delta\sigma_{yy}+\delta\sigma_{zz}\right)n_{xx}+\left(2\delta\sigma_{yy}-\delta\sigma_{zz}\right)n_{yy} \\
\qquad\qquad +\left(2\delta\sigma_{zz}-\delta\sigma_{yy}\right)n_{zz}+6\delta\sigma_{yz}n_{yz}\Big)-\dfrac{\nu}{E}\left(\delta\sigma_{yy}+\delta\sigma_{zz}\right) \\
\delta\varepsilon_{yy}=\dfrac{n_{yy}}{3h}\Big(-\left(\delta\sigma_{yy}+\delta\sigma_{zz}\right)n_{xx}+\left(2\delta\sigma_{yy}-\delta\sigma_{zz}\right)n_{yy} \\
\qquad\qquad +\left(2\delta\sigma_{zz}-\delta\sigma_{yy}\right)n_{zz}+6\delta\sigma_{yz}n_{yz}\Big)+\dfrac{1}{E}\left(\delta\sigma_{yy}-\nu\delta\sigma_{zz}\right) \\
\delta\varepsilon_{zz}=\dfrac{n_{zz}}{3h}\Big(-\left(\delta\sigma_{yy}+\delta\sigma_{zz}\right)n_{xx}+\left(2\delta\sigma_{yy}-\delta\sigma_{zz}\right)n_{yy} \\
\qquad\qquad +\left(2\delta\sigma_{zz}-\delta\sigma_{yy}\right)n_{zz}+6\delta\sigma_{yz}n_{yz}\Big)+\dfrac{1}{E}\left(\delta\sigma_{zz}-\nu\delta\sigma_{yy}\right) \\
\delta\varepsilon_{yz}=\dfrac{n_{yz}}{3h}\Big(-\left(\delta\sigma_{yy}+\delta\sigma_{zz}\right)n_{xx}+\left(2\delta\sigma_{yy}-\delta\sigma_{zz}\right)n_{yy} \\
\qquad\qquad +\left(2\delta\sigma_{zz}-\delta\sigma_{yy}\right)n_{zz}+6\delta\sigma_{yz}n_{yz}\Big)+\dfrac{1+\nu}{E}\delta\sigma_{yz}
\end{cases}
\tag{8.3.21}
$$

Tensile loading – Three dimensional plate

In the case of a flat specimen with finite thickness and weakened by a rounded notch, five unknowns are present at the notch tip, two components of stress (σ_{yy} and σ_{zz}) and three components of strain (ε_{xx}, ε_{yy}, ε_{zz}), thus five different equations should be used. The present work, as explained above, permits to evaluate the behaviour of every different component of stress/strain through the thickness of the plate, only by furnishing a relation describing the trend of the stress concentration factor along the z coordinate (see Figure8.3.1). The problem is governed by the following equations:

$$
\begin{cases}
\left(\sigma^{e}_{yy,(z)}-\sigma^{e(0)}_{yy,(z)}\right)\delta\varepsilon^{e}_{yy}+\left(\varepsilon^{e}_{yy,(z)}-\varepsilon^{e(0)}_{yy,(z)}\right)\delta\sigma^{e}_{yy} \\
\qquad =(1+C_q)\left(\sigma_{yy,(z)}-\sigma^{(0)}_{yy,(z)}\right)\delta\varepsilon_{yy}+(1-C_q)\left(\varepsilon_{yy,(z)}-\varepsilon^{(0)}_{yy,(z)}\right)\delta\sigma_{yy} \\
\left(\sigma^{e}_{zz,(z)}-\sigma^{e(0)}_{zz,(z)}\right)\delta\varepsilon^{e}_{yy}+\left(\varepsilon^{e}_{zz,(z)}-\varepsilon^{e(0)}_{zz,(z)}\right)\delta\sigma^{e}_{zz} \\
\qquad =(1+C_q)\left(\sigma_{zz,(z)}-\sigma^{(0)}_{zz,(z)}\right)\delta\varepsilon_{zz}+(1-C_q)\left(\varepsilon_{zz,(z)}-\varepsilon^{(0)}_{zz,(z)}\right)\delta\sigma_{zz} \\
\delta\varepsilon_{xx}=\dfrac{n_{xx}}{3h}\left(-\left(\delta\sigma_{yy,(z)}+\delta\sigma_{zz,(z)}\right)n_{xx}+\left(2\delta\sigma_{yy,(z)}-\delta\sigma_{zz,(z)}\right)n_{yy}\right. \\
\qquad \left.+\left(2\delta\sigma_{zz,(z)}-\delta\sigma_{yy,(z)}\right)n_{zz}\right)-\dfrac{\nu}{E}\left(\delta\sigma_{yy,(z)}+\delta\sigma_{zz,(z)}\right) \\
\delta\varepsilon_{yy}=\dfrac{n_{yy}}{3h}\left(-\left(\delta\sigma_{yy,(z)}+\delta\sigma_{zz,(z)}\right)n_{xx}+\left(2\delta\sigma_{yy,(z)}-\delta\sigma_{zz,(z)}\right)n_{yy}\right. \\
\qquad \left.+\left(2\delta\sigma_{zz,(z)}-\delta\sigma_{yy,(z)}\right)n_{zz}\right)+\dfrac{1}{E}\left(\delta\sigma_{yy,(z)}-\nu\delta\sigma_{zz,(z)}\right) \\
\delta\varepsilon_{zz}=\dfrac{n_{zz}}{3h}\left(-\left(\delta\sigma_{yy,(z)}+\delta\sigma_{zz,(z)}\right)n_{xx}+\left(2\delta\sigma_{yy,(z)}-\delta\sigma_{zz,(z)}\right)n_{yy}\right. \\
\qquad \left.+\left(2\delta\sigma_{zz,(z)}-\delta\sigma_{yy,(z)}\right)n_{zz}\right)+\dfrac{1}{E}\left(\delta\sigma_{zz,(z)}-\nu\delta\sigma_{yy,(z)}\right)
\end{cases}
\tag{8.3.22}
$$

Where the subscript "(z)" denotes the through the thickness Cartesian coordinate.

Shear in-plane loading – Three dimensional plate

The application of a remote in plane shear loading causes, at the tip of a rounded notch, the presence of a non-negligible out of plane component of stress due to three dimensional effects (Harding et al. 2010, Berto et al. 2011a, Lazzarin and Zappalorto 2012, Berto et al. 2012a, Berto and Marangon 2013). With the aim to emphasise this effect, in this work will be studied a flat specimen with finite thickness and weakened by a rounded notch characterised by an opening angle equal to 120°. It is well known that the singularity tied to the remote shear loading disappears for opening angle higher than 102°. Thus in the studied case, at the tip of the notch there will be only the presence of the out of plane singularity (Berto and Marangon 2013). By knowing the through the thickness behaviour of the stress concentration factor related to the O mode (K_o), the new proposed procedure permits to obtain the cyclic stress/strain acting at the notch tip along the z coordinate. The equation governing the problem are the following:

$$\begin{cases} \left(\sigma^{e}_{yz,(z)}-\sigma^{e(0)}_{yz,(z)}\right)\delta\varepsilon^{e}_{yz}+\left(\varepsilon^{e}_{yz,(z)}-\varepsilon^{e(0)}_{yz,(z)}\right)\delta\sigma^{e}_{yz} \\ \qquad\qquad =(1+C_q)\left(\sigma_{yz,(z)}-\sigma^{(0)}_{yz,(z)}\right)\delta\varepsilon_{yz}+(1-C_q)\left(\varepsilon_{yz,(z)}-\varepsilon^{(0)}_{yz,(z)}\right)\delta\sigma_{yz} \\ \delta\varepsilon_{yz}=\left(\frac{2}{h}n^{2}_{yz}+\frac{1+\nu}{E}\right)\cdot\delta\sigma_{yz} \end{cases} \tag{8.3.23}$$

Procedure flow chart

In order to represent the local behaviour of the stress/strain components acting at the tip of a rounded notch during one loading cycle, an incremental procedure based on the incremental cyclic plasticity has been implemented in Wolfram Mathematica®. The applied procedure accurately follows the chart presented in Gao et al. (2010). Following only the fundamental steps are quoted:

- Obtain the linear elastic stress/strain at the notch tip at step i-th by knowing the stress concentration factor of the notch;
- Get the increment of linear elastic stress/strain components between step i-th and i+1-th;
- Obtain the hypothetical linear elastic stress/strain at the notch tip at step i+1-th by assuming no plastic deformations;
- Check the yield condition (Eq.8) and the positivity of the flow rule (Eq.9);
- Even if only one of the conditions is not satisfied, the hypothetical linear elastic stress/strain behaviour will be the real behaviour at the tip of the notch; the obtained solutions will be the i-th variable at the next incremental step;
- If, instead, both the conditions are satisfied, plastic deformations will be induced at the tip of the notch;
- Compute the plastic modulus function (Eq.11) after obtaining the material coefficients (Eq.15,16,17);
- Compute the real stress/strain behaviour by solving the elastic-plastic system of equations depending on the case studied (Eq. 18-23); the obtained solutions will be the i-th variable at the next incremental step;
- Calculate the increment of equivalent plastic deformation (Eq.13) and then the tensor describing the incremental deviatoric backstress (Eq.12,14);
- Update the input values of the M backstress parts;
- Return to begin and start the next step.

8.4 Material characterisation and FE models construction

The following material properties have been used for the FE analyses:

- Young's modulus, E= 194700 MPa;
- Poisson's ratio, ν= 0.3;
- Fatigue strength coefficient, K'= 2250 MPa;
- Cyclic strain hardening coefficient, n'= 0.337;

These values correspond to the mechanical behaviour of an AISI 304L steel as reported in Meneghetti and Ricotta (2012). In addition, the stress defining the upper limit of purely elastic strains is named σ* and is equal to 160 MPa. Knowing this particular value, the quantification of the yield stress in simple shear, k, is straightforward.
By applying the von Mises criterion:

$$k = \frac{\sigma^*}{\sqrt{3}} = 92.4\,\mathrm{MPa} \tag{8.4.1}$$

The material has been thought to obey to a linear elastic behaviour up to σ* and then to a Ramberg-Osgood representation:

$$\varepsilon = \begin{cases} \dfrac{\sigma}{E} & \text{when } \sigma < \sigma^* \\ \dfrac{\sigma}{E} + \left(\dfrac{\sigma - \sigma^*}{K'} \right)^{\frac{1}{n'}} & \text{when } \sigma \geq \sigma^* \end{cases} \tag{8.4.2}$$

As already explained in the previous section, the characterisation of the material behaviour in the case of the incremental procedure consists on the multilinearisation of the plastic part of the SCC (stabilised cyclic curve), following the guidelines explained in (Jiang and Kurath 1996). The Jiang-Sehitoglu's material parameters have been determined using Eqs. (8.3.15-8.3.17).

As already remarked, the parameters $\chi^{(i)}$ have been set equal to zero, thus neglecting ratchetting phenomena for this study.

The results obtained from the solution of the incremental procedure have been compared with a bulk of numerical analyses carried out with the FE software Ansys®. The Chaboche material model routine has been used in order to simulate the material cyclic behaviour. Different from the incremental procedure, in the case of FE analyses the plastic part of the material SCC needs to be described using a multiparametric function according to the following expression (Imaoka 2008):

$$\sigma - \sigma^{*} = \sum_{i=1}^{j} \frac{C_i}{\gamma_i} \cdot \tanh\left(\gamma_i \cdot \varepsilon^{p}\right) \tag{8.4.3}$$

where C_i and γ_i are material parameters to be obtained from a dedicated fitting routine. In this work, eleven different parameters have been furnished to the FE software (j=5), namely five couples (C_i, γ_i) and k. Another example of the use of the Chaboche routine in Ansys can be found in Kulkarny et al. (2004) dealing with the study of the ratchetting phenomena in piping materials.

Then, aiming to simulate the cyclic fatigue loading applied to a specimen, a particular APDL routine has been implemented. This procedure also permits to obtain the components of stress/strain acting at the notch tip that will be compared with the results obtained from the incremental cyclic plasticity frame.

In both cases the simplified material curves accurately match the actual behaviour of the used material. All the parameters employed in the analyses are listed in Table 8.4.1.

Table 8.4.1. Jiang-Sehitoglu's and Chaboche's material parameters.

	J-S Material Parameters		Chaboche Material Parameters	
(i)	c	r	C	γ
1	127407.9	28.9	1100000	9000
2	9782.9	33.0	80500	510
3	2522.5	31.9	20000	48
4	929.5	33.3	480	20
5	440.9	35.0	450	1
6	222.5	39.5		
7	123.1	43.1		
8	70.8	66.5		
9	27.2	109.2		
10	12.4	314.4		

In order to investigate the accuracy of the results obtained from the incremental cyclic plasticity procedure presented in 8.3, several 2D or 3D FE analyses have been carried out with the software Ansys®, using four node solid elements for 2D analyses and eight node solid elements for three-dimensional models.
In more details, the following notched geometries have been studied:

- 2D flat specimen weakened by a circular hole and by a blunt U notch subjected to a tension-compression fatigue loading, both under plane stress and plane strain conditions (see Figures8.4.1 a, b);
- An axy-symmetric specimen weakened by a circumferential semicircular notch subjected to a pure torsion and to a tension-torsion fatigue loading (Figure 8.4.1 c);

- A flat specimen of finite thickness (3D analysis) weakened by a circular hole, by a blunt U notch and by a rounded V-notch subjected to a tension-compression fatigue loading (Figures 8.4.1 a, b, d);
- A flat specimen of finite thickness (3D analysis) weakened by a rounded V notch subjected to a pure in-plane shear fatigue loading (Figure 8.4.1 d);

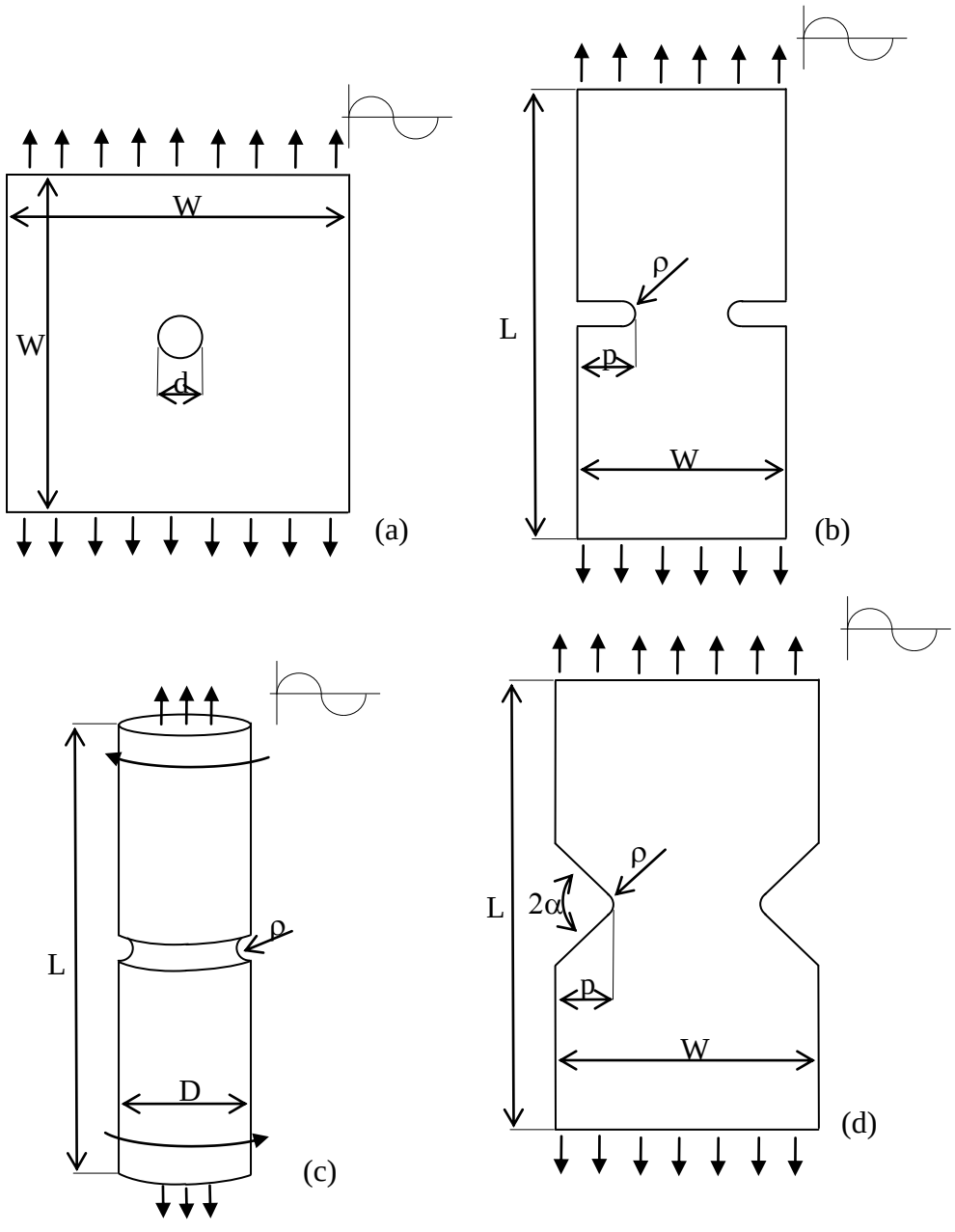

Figure 8.4.1. Tested geometries: plate weakened by a circular hole (a), blunt U-notch (b), axy-symmetric U-notched specimen (c), plate weakened by a rounded V-notch (d)

8.5 Results and discussions

The different acting hysteresis loops obtained from the incremental cyclic plasticity procedure and from the cyclic FE analyses will be compared hereafter, considering initially the two-dimensional cases above mentioned and then extending the analysis to 3D axy-symmetric components. Finally the tri-dimensional stress distribution effects arising at the tip of a rounded notch in a thick plate subjected to a tension-compression and a in-plane shear fatigue loading will be investigated.

The applied nominal load amplitudes have been chosen in order to guarantee a state of small scale yielding on the neighbourhood of the notch tip. This condition is necessary to ensure the validity of the incremental procedure based on cyclic plasticity, being one of its basic hypothesis.

The load ratio has been set equal to -1 for all the processed analyses.

8.5.1 Stress/strain state at the tip of a rounded notch - plane stress conditions

The attention has been initially focused on the case of a very thin flat specimen weakened by a circular hole and by a blunt U notch (plane stress conditions).

A circular hole with diameter, d, equal to 10 mm in a plate of ligament W= 200 mm has been taken into account for first (see Figure 8.4.1 a). The nominal stress amplitude of the tension-compression cycle has been chosen equal to 0.8 times σ^*, namely 128 MPa.

In this case only one hysteresis loop, related to σ_{yy} and ε_{yy}, can be used as a basis of comparison (see Figure8.5.1).

From the figure it can be seen a satisfactory agreement between the analytical incremental procedure and FE cyclic analyses. The transient behaviour of the material is identical for both the cases, whereas a slight distinction between the two curves can be observed on the lower bounds of the hysteresis loops. This slight deviation can be thought of as due to a numerical inaccuracy of the incremental cyclic procedure induced by an increment of the hypothetical elastic stresses and strains not small enough.

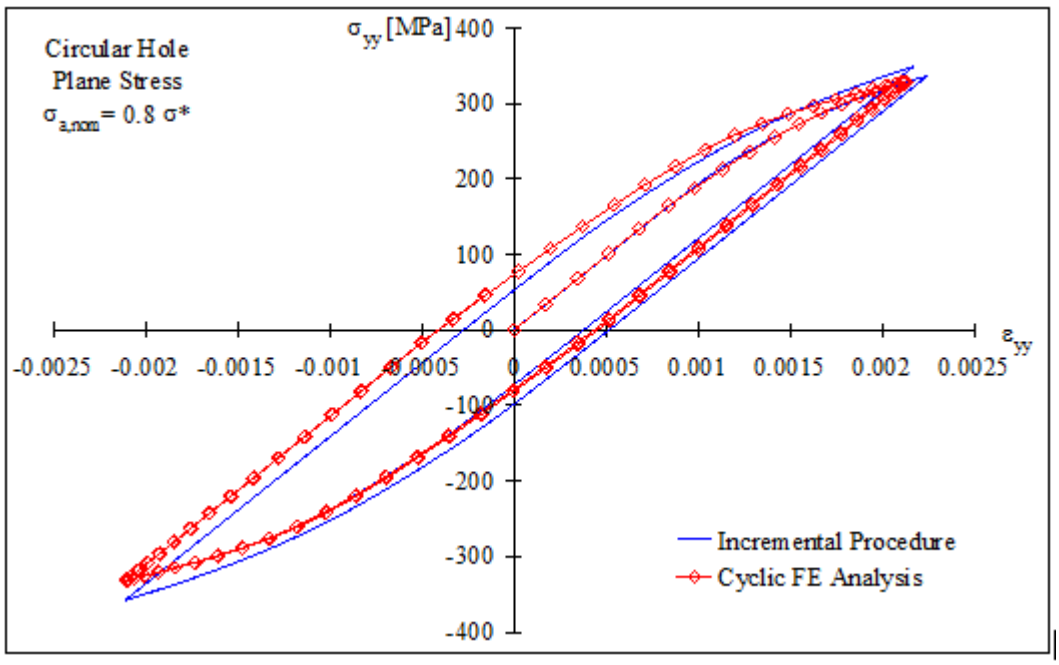

Figure 8.5.1. σ_{yy}-ε_{yy} hysteresis loop at the notch tip. Plain stress conditions. Circular hole.

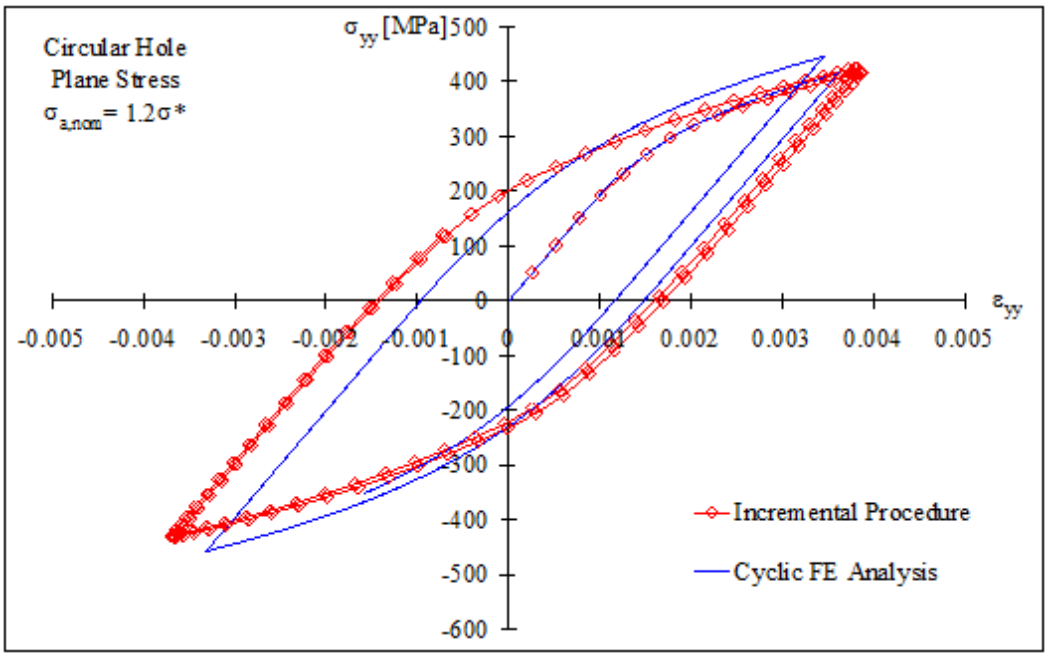

Figure 8.5.2. σ_{yy}-ε_{yy} hysteresis loop at the notch tip. Plain stress conditions. Circular hole.

By increasing the applied amplitude load to a $\sigma_{a,nom} = 1.2\ \sigma^*$ (See Figure8.5.2) the deviation between the two considered procedure slightly increases, probably due to the occurrence of state of large plasticity ahead of the notch tip, thus the small scale yielding conditions being no longer satisfied.

In order to investigate the effect of the local notch geometry on the accuracy of the results, a flat specimen weakened by U notched geometries with different notch root radii have been analysed (ρ= 4 and 1 mm). The notch dept, p, has been kept constant and equal to 15 mm. Obviously, moving towards a sharper configuration, identical loading conditions result in an increase of the plastic zone ahead of the notch tip. However, as it can be seen from Figures 8.5.3 and 8.5.4, the agreement between analytical and numerical results remains satisfactory for a nominal load stress amplitude equal to 0.8 σ^*.

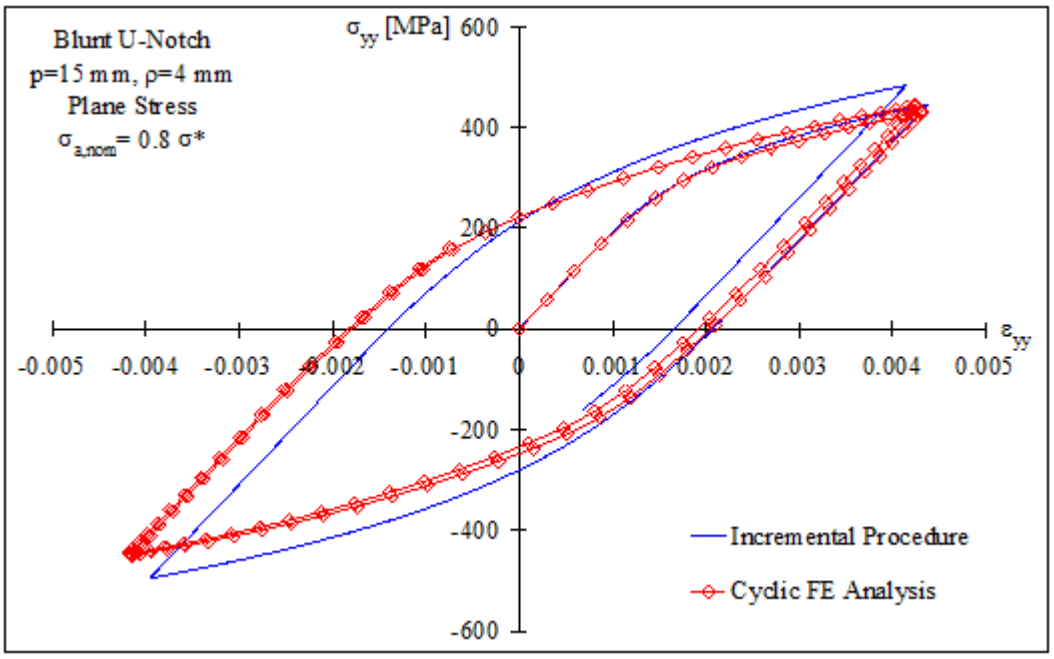

Figure 8.5.3. σ_{yy}-ε_{yy} hysteresis loop at the notch tip. Plain stress conditions. Blunt U-notch, ρ=4 mm.

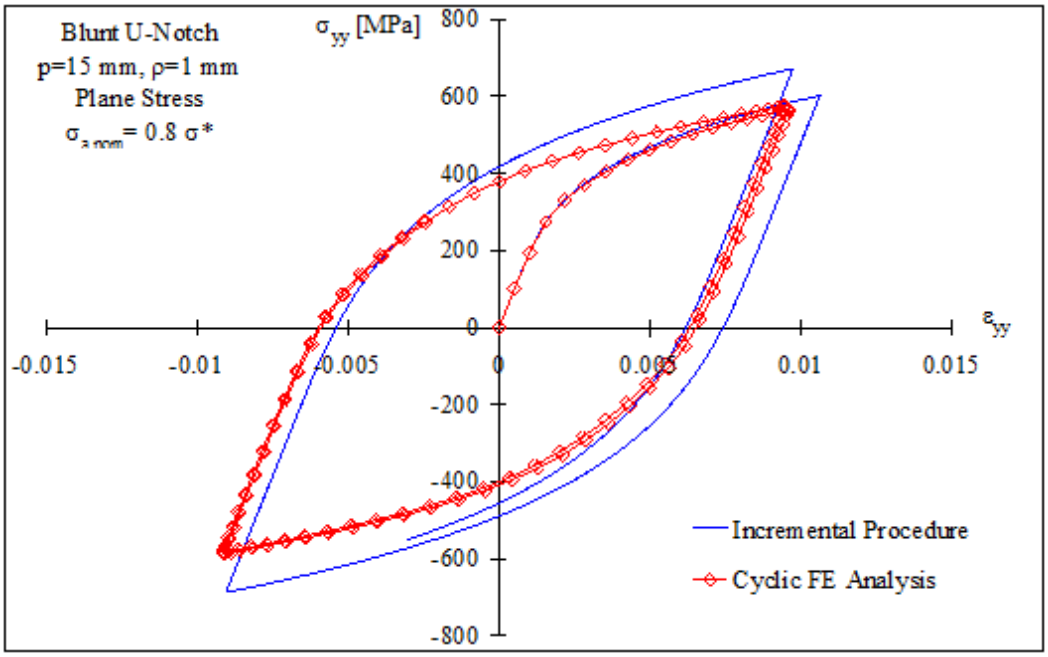

Figure 8.5.4. σ_{yy}-ε_{yy} hysteresis loop at the notch tip. Plain stress conditions. Blunt U-notch, ρ=1 mm.

8.5.2 Stress/strain state at the tip of a rounded notch - plane strain conditions

It is well known that under plane strain conditions the amount of plasticity at the notch tip neighbours is less pronounced than under plane stress. Accordingly, in this section the same geometries studied under plane stress have been analysed under plane strain conditions. The incremental system of equations (Eq. 8.3.19) has been used in order to obtain the results from the incremental procedure. Results are presented in Figures (8.5.5-8.5.7). The agreement is evident. It is worth to be underlined that, with respect to the plane stress conditions, in this case the plastic hysteretic energies are slightly lower.

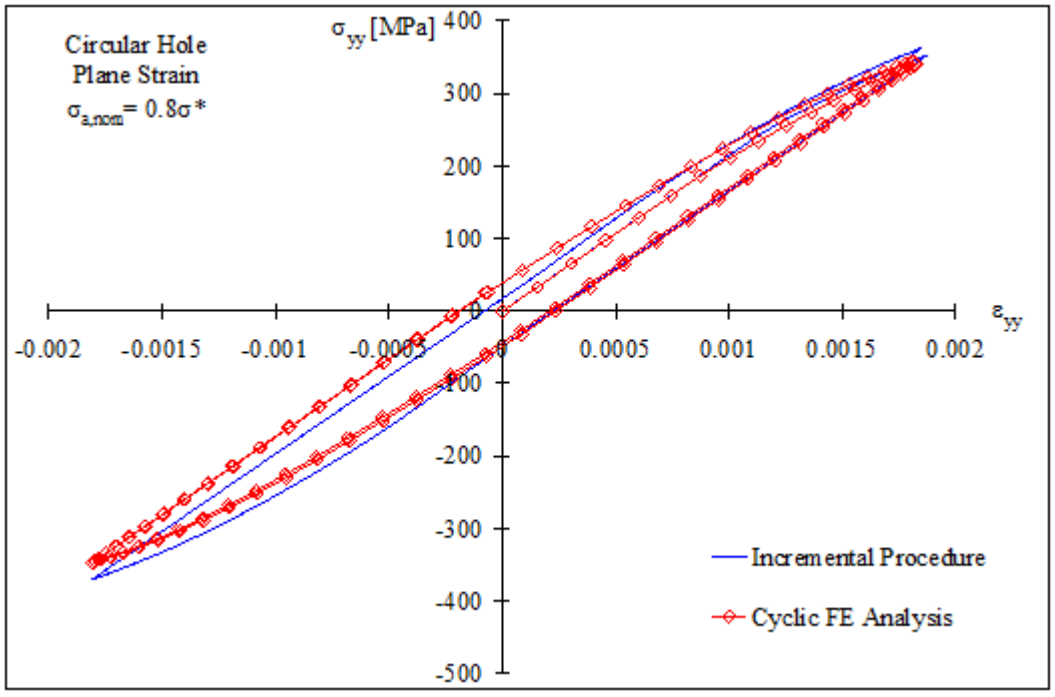

Figure 8.5.5. σ_{yy}-ε_{yy} hysteresis loop at the notch tip. Plain stress conditions. Circular hole.

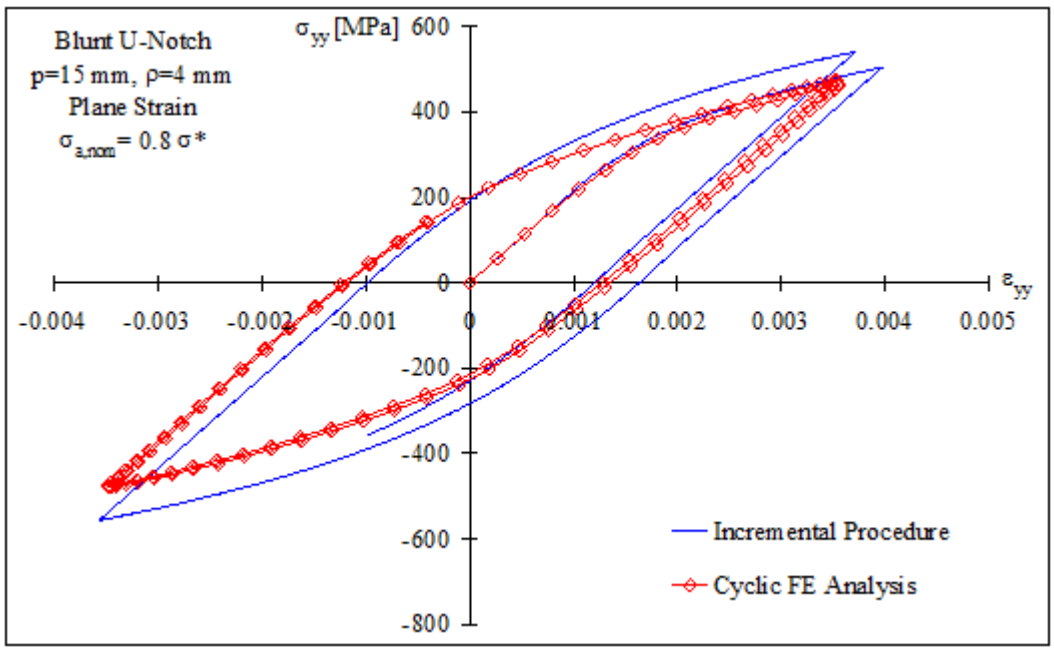

Figure 8.5.6. σ_{yy}-ε_{yy} hysteresis loop at the notch tip. Plain stress conditions. Blunt U-notch, ρ=4 mm.

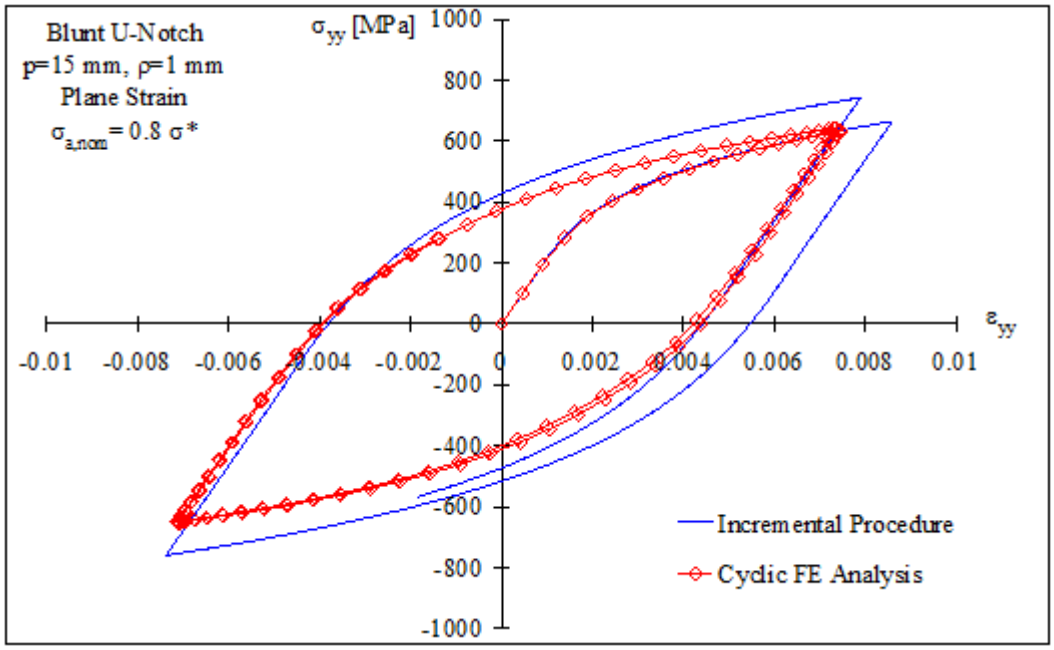

Figure 8.5.7. σ_{yy}-ε_{yy} hysteresis loop at the notch tip. Plain stress conditions. Blunt U-notch, ρ=1 mm.

8.5.3 Stress/strain state at the tip of a rounded notch - pure torsion fatigue loading

An axy-symmetric specimen weakened by a circumferential notch with ρ=4 mm has been considered. The overall geometry of the specimen is shown in Figure 8.4.1 c. With reference to the Cartesian coordinate system shown in Figure 8.3.1 b, only one hysteresis loop is present at the notch tip, that is tied to the "yz" shear components of stress and strain. Dealing with the incremental plasticity procedure, the system of equation defined by Eq. (8.3.20) has been solved. The FE analyses have been carried out by considering larger cyclic incremental step with respect to the previous analyses, because the analysis of a torque loaded specimen requires three-dimensional models, with a much more higher number of degrees of freedom with respect to a simple 2D analysis.

The nominal shear amplitude remotely applied to the specimen has been set equal to 0.5 times the yield stress in simple shear, k. This choice is tied to the arising of a more extended plastic area ahead of the notch tip with respect to a tension-compression cyclic loading.

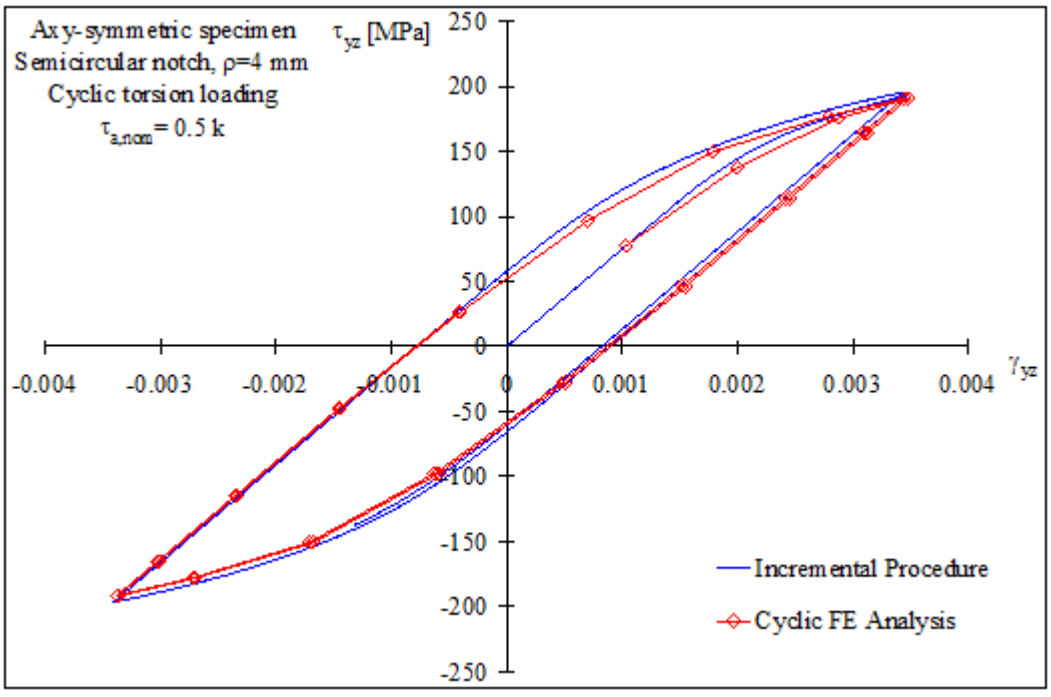

Figure 8.5.8. τ_{yz}-γ_{yz} hysteresis loop at the notch tip. Pure torsion. Axy-symmetric specimen weakened by a blunt U-notch, ρ=4 mm.

Figure 8.5.8 shows the comparison between analytical and numerical results. It is worth nothing that the agreement is again satisfactory, with a percentage difference lower than 3%.

8.5.4 Stress/strain state at the tip of a rounded notch - multiaxial fatigue

The same specimen considered in the previous case has been subjected to a multiaxial tension-torsion loading. Considering the Cartesian coordinate system in Figure 8.3.1 b, three different hysteresis loops act at the notch tip: in fact both the normal components "yy" and "zz" of stress/strain synergistically act in addition to the shear "yz" component. However, the "zz" component is negligible and has not been considered. The nominal tensile amplitude loading and the torsion amplitude have been set equal to 0.5 σ* and 0.38 k respectively. This choice ensures a small scale yielding condition at the notch tip. The comparisons between analytical and FE analyses are presented in Figures (8.5.9, 8.5.10). A good correlation has been obtained. Dealing with the computational time, the incremental procedure proved to be about 10 times faster then an elastic plastic cyclic FE analysis with an average level of accuracy. The difference ranges between ±10%.

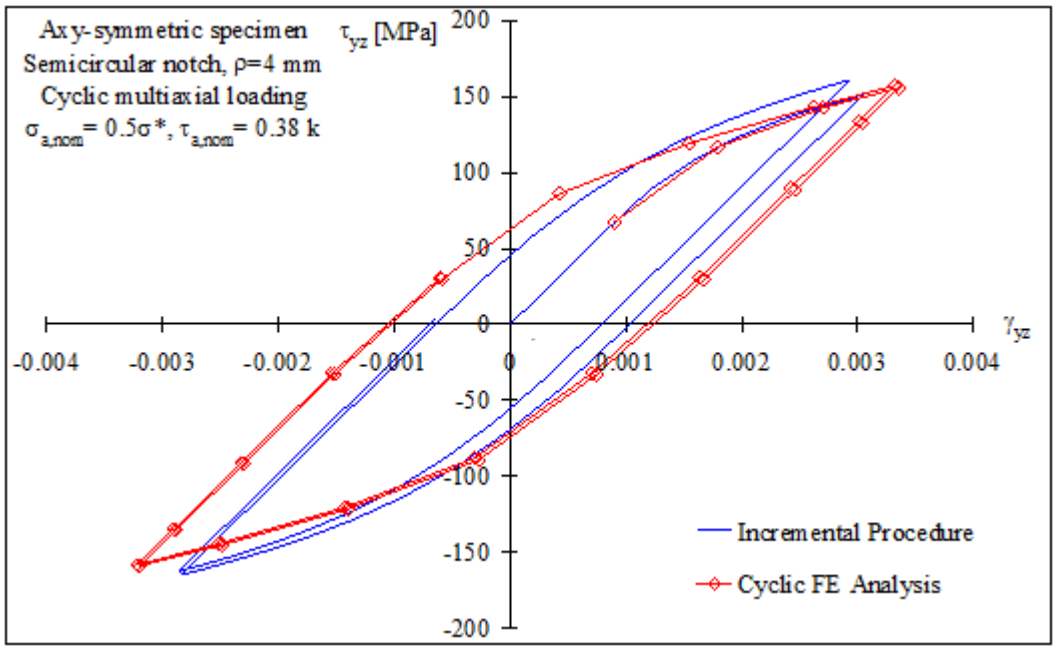

Figure 8.5.9. τ_{yz}-γ_{yz} hysteresis loop at the notch tip. Multiaxial loading. Axy-symmetric specimen weakened by a blunt U-notch, ρ=4 mm.

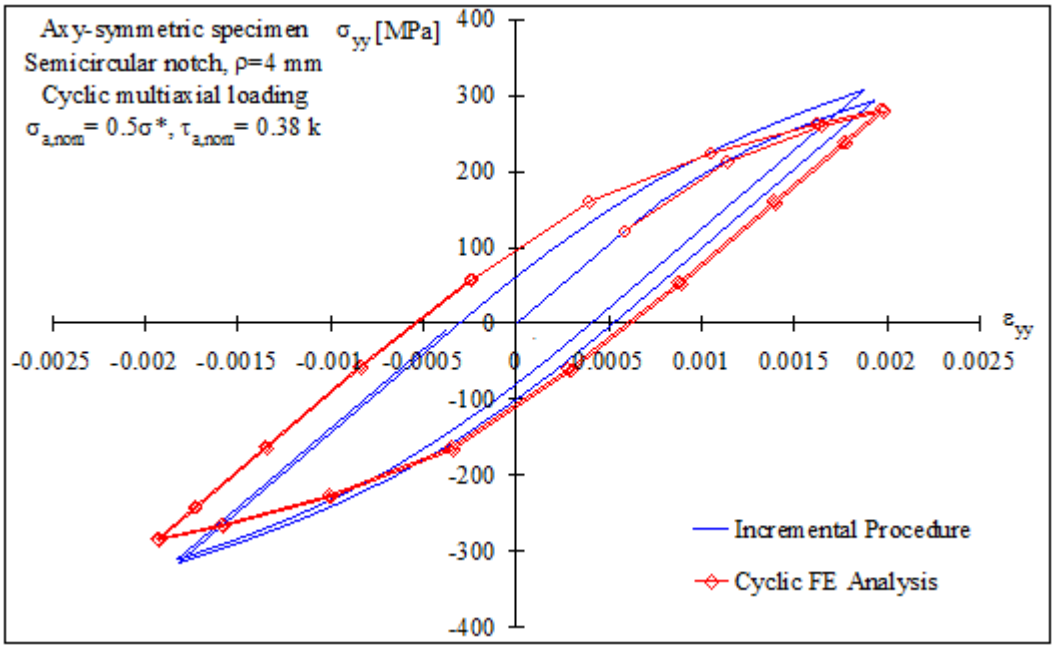

Figure 8.5.10. σ_{yy}-ε_{yy} hysteresis loop at the notch tip. Multiaxial loading. Axy-symmetric specimen weakened by a blunt U-notch, ρ=4 mm.

8.5.5 Stress/strain state at the tip of a rounded notch – 3D analysis, uniaxial fatigue, tensile loading

Dealing with a three-dimensional thick plate weakened by different rounded notches and subjected to a cyclic tension-compression loading, a biaxial state of stress/strain is induced at the notch tip. In particular, through the plate thickness the stress concentration factors related to the acting stress components reduce while moving from the mid plane to the free surface (i.e. see Figure 8.5.11 in the case of a blunt U-notch).

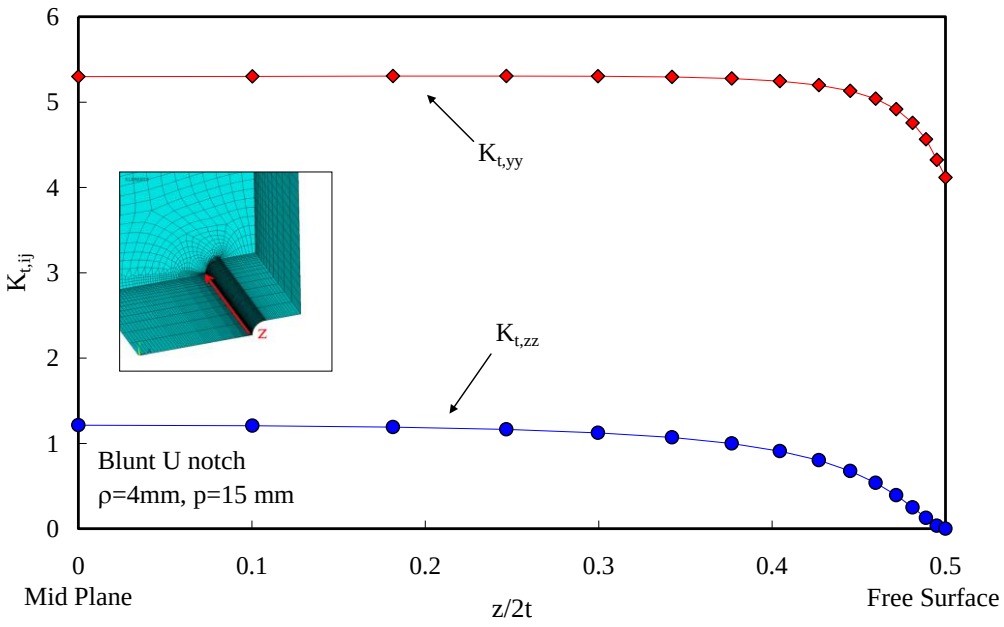

Figure 8.5.11. Stress concentration factors through-the-thickness of the plate at the notch tip. Tensile case.

In this work, the incremental procedure based on the cyclic plasticity has been extended for the first time to the investigation of the three dimensional effects arising at the notch tip. Starting from the equations describing the linear elastic through-the-thickness variations of the “yy” and “zz” stress concentration factors (obtainable with a much easier 3D linear elastic FE analysis), the new incremental routine allows us to obtain the whole elastic-plastic stress/strain state at the tip of the notch.

As a first example, a three dimensional flat specimen weakened by a circular hole has been considered, with d=10 mm, W=200 mm and thickness of the plate (2t) equal to 40 mm. The applied uniaxial fatigue loading amplitude has been set equal to 0.8 times σ*, in order to guarantee a small scale yielding condition at the notch tip. Figures 8.5.12, 8.5.13 and 8.5.14 show the "yy" hysteresis loop at the mid plane, at a coordinate z/2t=0.25mm and on the free surface of the specimen. A comparison has been made with the results obtained from a 3D cyclic FE analysis as already done for the problems investigated in the previous sections. As expected, the hysteresis loop tends to become smaller moving from the mid plane to the free surface of the specimen, following the behaviour of the related stress concentration factor. The hysteresis loop tied to the "zz" component has not reported, being it negligible.

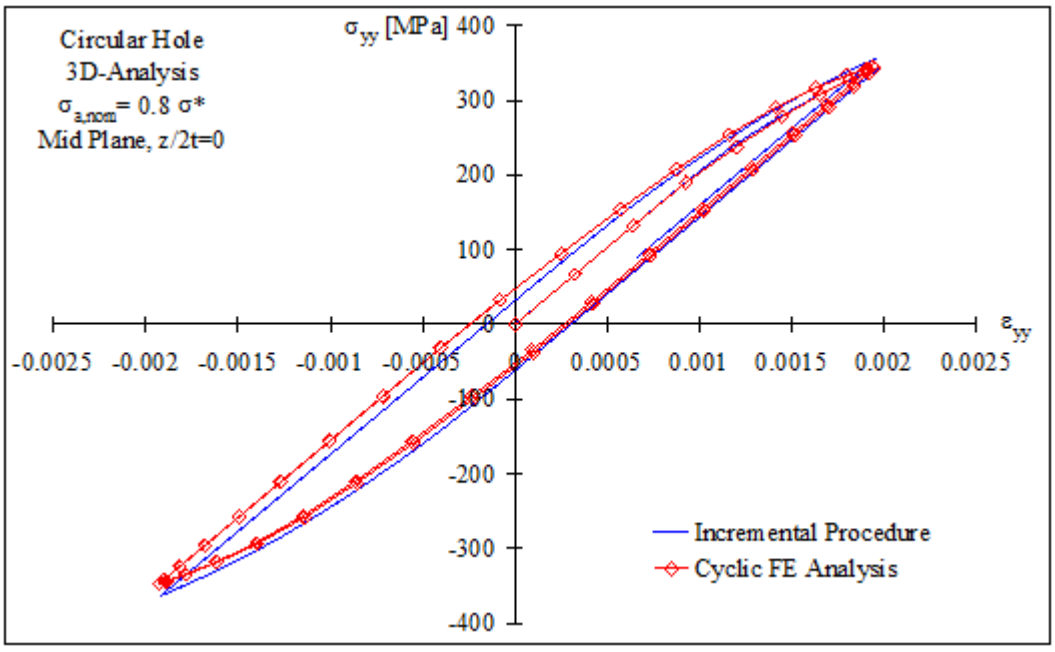

Figure 8.5.12. σ_{yy}-ε_{yy} hysteresis loop at the notch tip on the mid plane of the plate. Uniaxial cyclic tensile loading. Three-dimensional analysis. Circular hole.

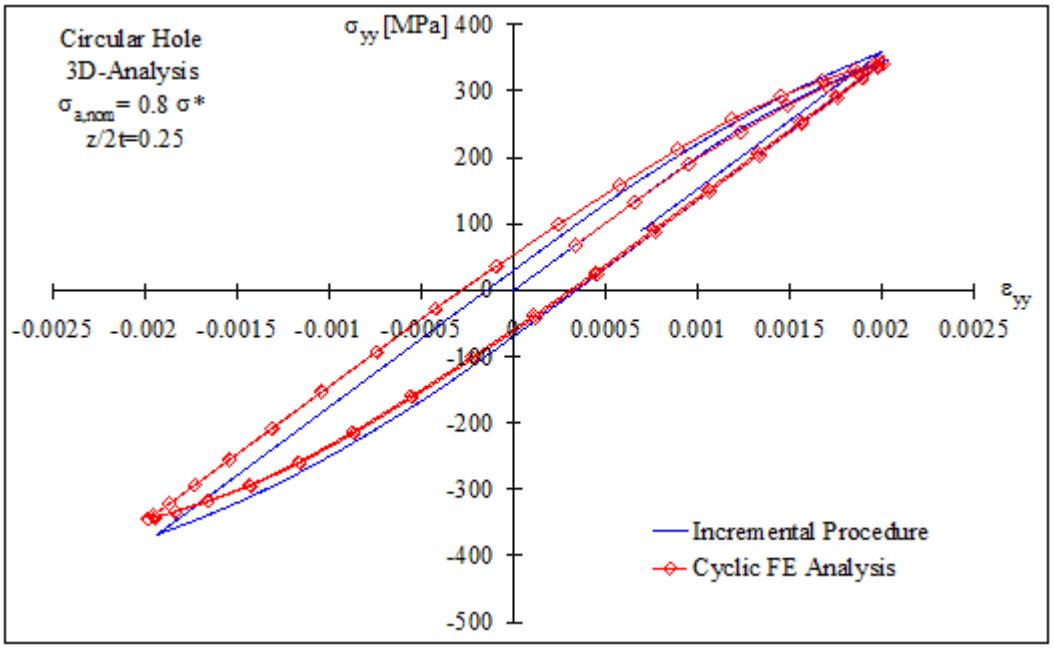

Figure 8.5.13. σ_{yy}-ε_{yy} hysteresis loop at the notch tip on the plane equal to z/2t=0.25 of the plate. Uniaxial cyclic tensile loading. Three-dimensional analysis. Circular hole.

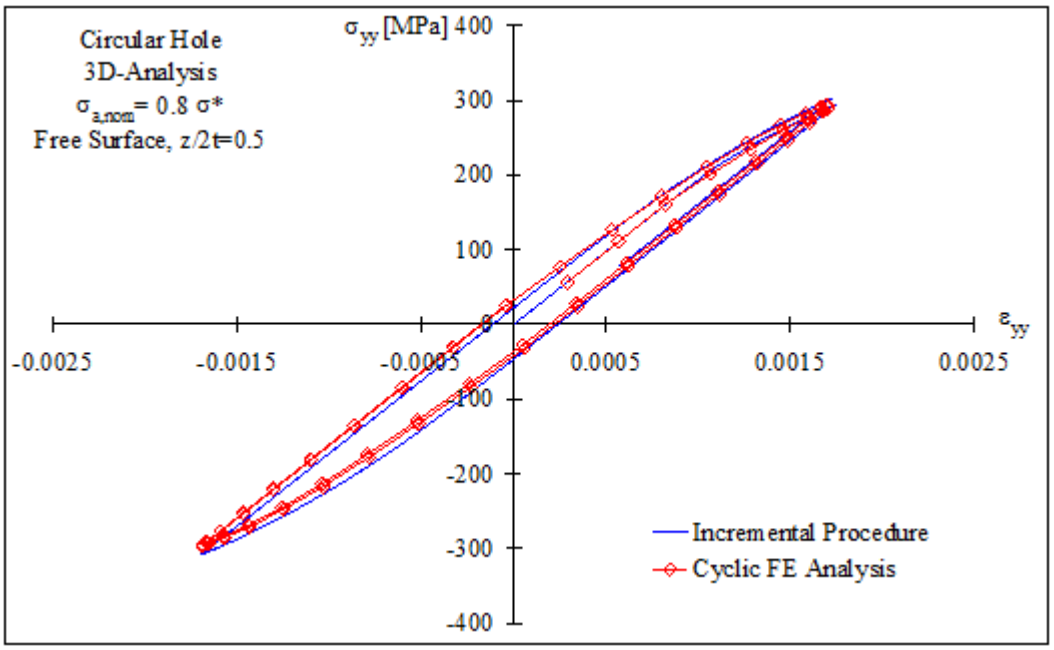

Figure 8.5.14. σ_{yy}-ε_{yy} hysteresis loop at the notch tip on the free surface of the plate. Uniaxial cyclic tensile loading. Three-dimensional analysis. Circular hole.

The second studied case is a flat specimen with a thickness (2t) equal to 40 mm weakened by a blunt U notch characterised by a radius at the notch tip equal to 4 mm and a notch depth of 15 mm. The load is the same that has been applied in the

previous investigation. Once again Figures 8.5.15, 8.5.16 and 8.5.17 demonstrates that the hysteresis loop related to "yy" component, follows the stress concentration factor behaviour. A very good correlation has been obtained between analytical and numerical FE results.

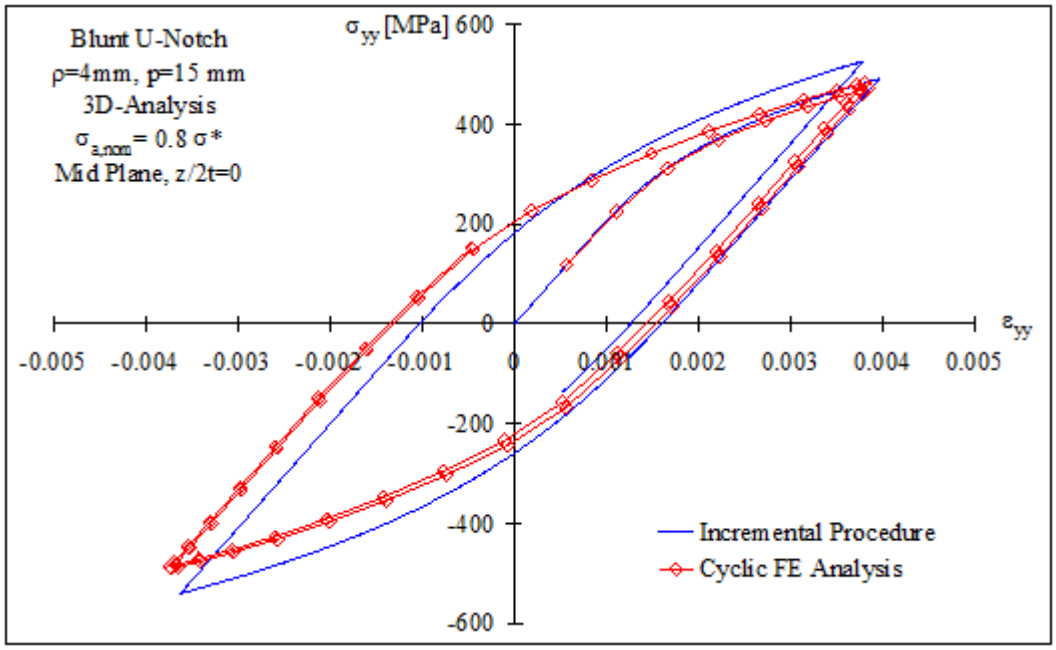

Figure 8.5.15. σ_{yy}-ε_{yy} hysteresis loop at the notch tip on the mid plane of the plate. Uniaxial cyclic tensile loading. 3D analysis. Blunt U-notch, ρ=4mm.

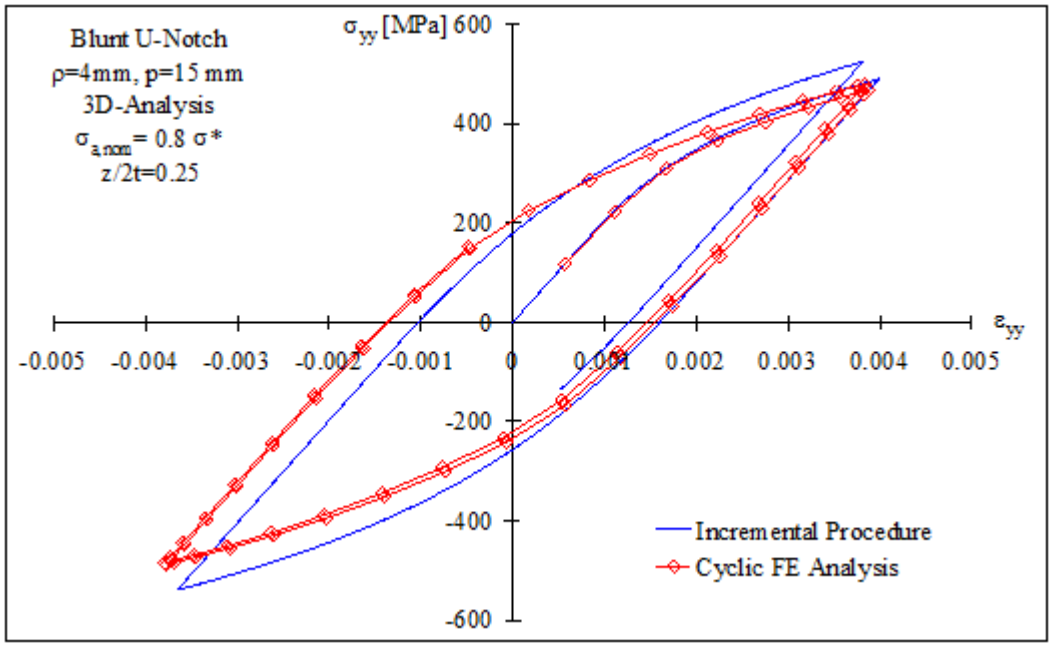

Figure 8.5.16. σ_{yy}-ε_{yy} hysteresis loop at the notch tip on the plane equal to z/2t=0.25 of the plate. Uniaxial cyclic tensile loading. 3D analysis. Blunt U-notch, ρ=4mm.

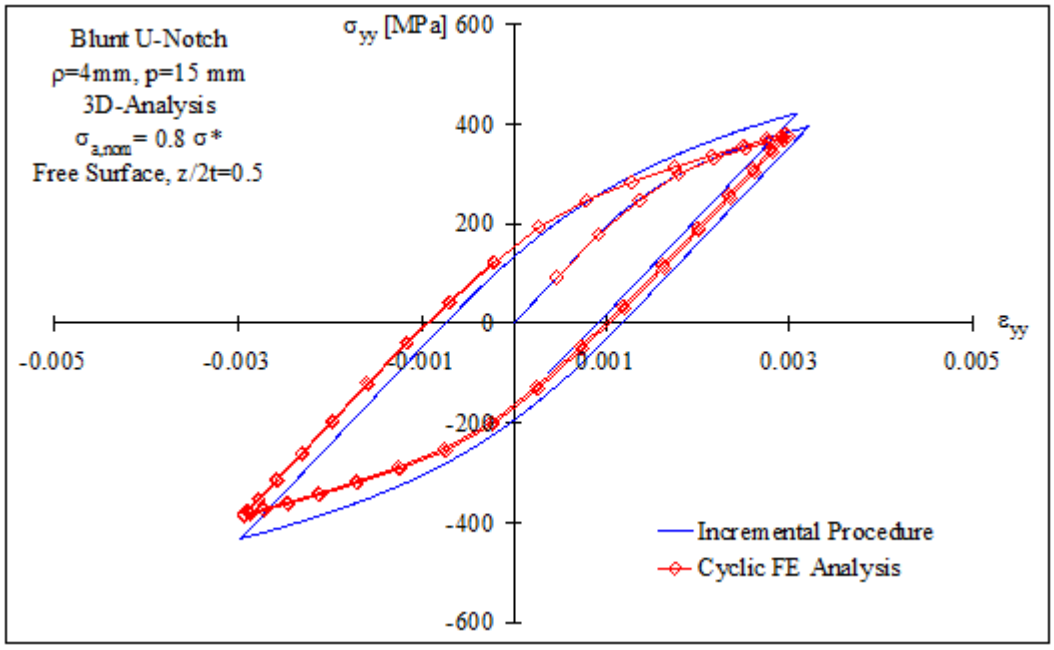

Figure 8.5.17. σ_{yy}-ε_{yy} hysteresis loop at the notch tip on the free surface of the plate. Uniaxial cyclic tensile loading. 3D analysis. Blunt U-notch, ρ=4mm.

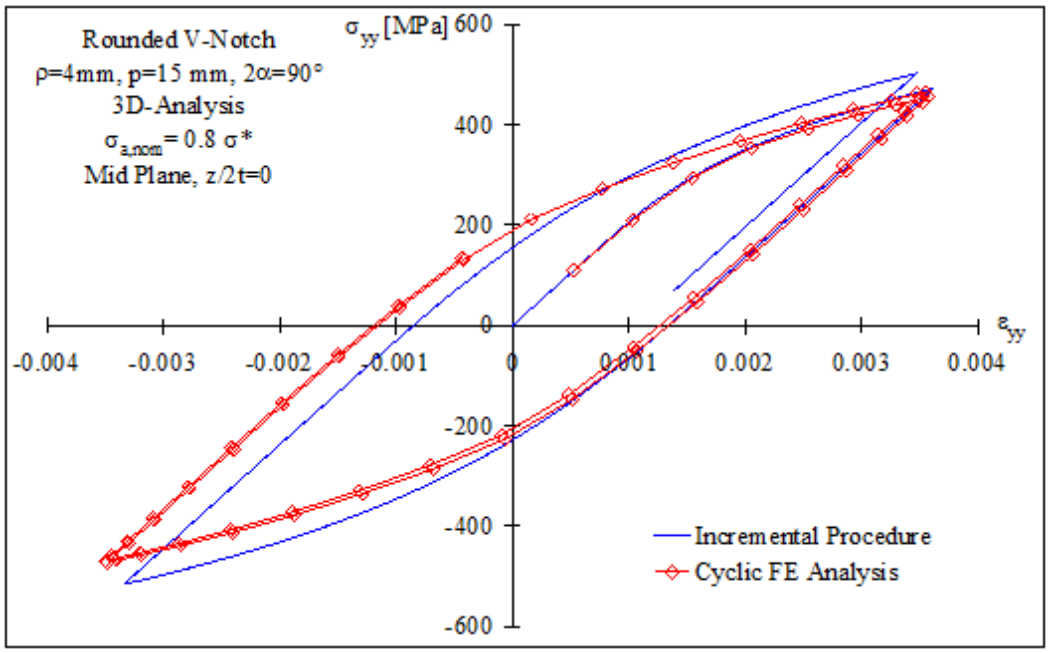

Figure 8.5.18. σ_{yy}-ε_{yy} hysteresis loop at the notch tip on the mid plane of the plate. Uniaxial cyclic tensile loading. 3D analysis. Rounded V-notch, ρ=4mm, 2α=90°.

Finally, a flat specimen weakened by a rounded V-notch with an opening angle $2\alpha=120°$, a notch root radius ρ = 4 mm and a notch depth p= 15 mm has been studied. The specimen has been loaded with a uniaxial fatigue loading characterised by an amplitude equal to 0.8 times σ^*. As in the previous case, only the hysteresis loop tied to the prevailing component of stress and strain has been taken into account. Figures 8.5.18, 8.5.19 and 8.5.20 show, once again, a very good correlation between analytical results and cyclic FE analyses on different normalised "z" coordinates, in fact, approaching to the free surface of the specimen the hysteresis loop becomes smaller than that related to the mid plane.

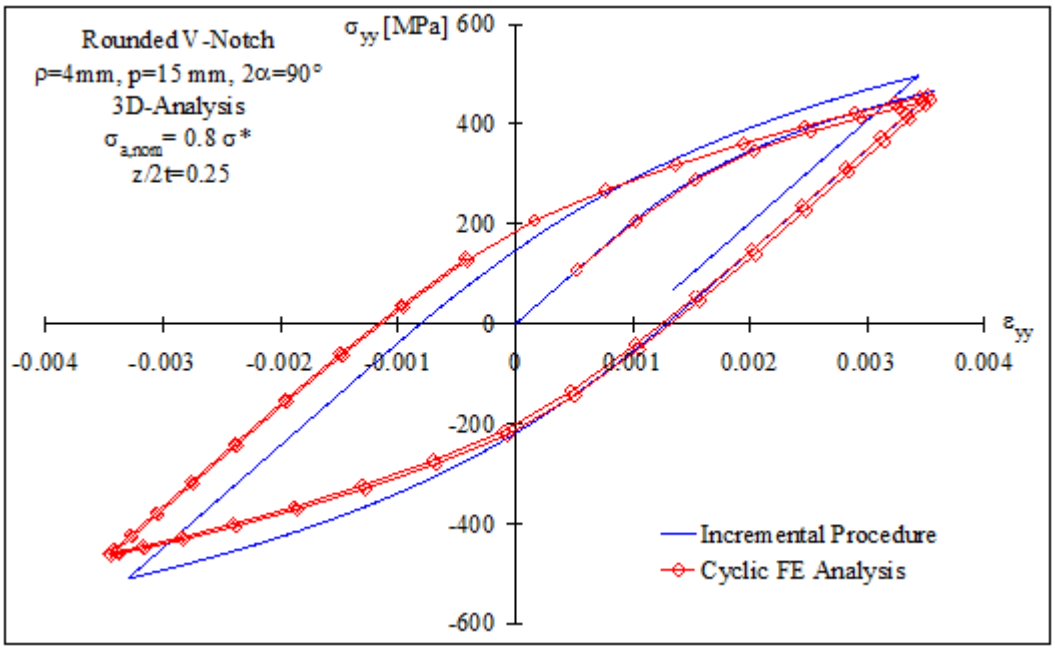

Figure 8.5.19. σ_{yy}-ε_{yy} hysteresis loop at the notch tip on the plane equal to z/2t=0.25 of the plate. Uniaxial cyclic tensile loading. 3D analysis. Rounded V-notch, ρ=4mm, $2\alpha=90°$.

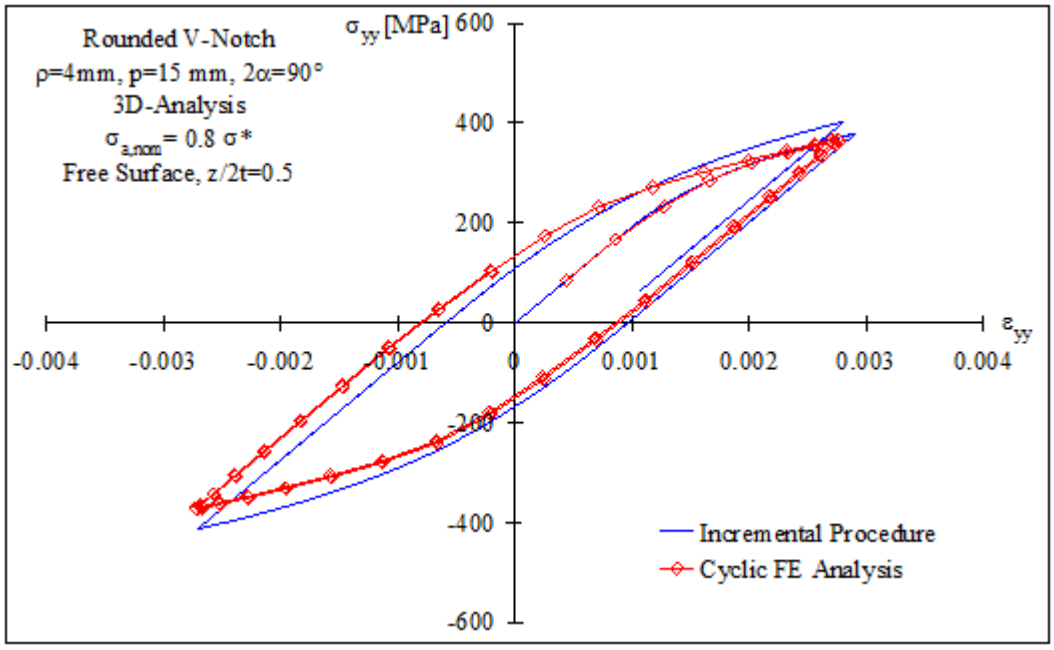

Figure 8.5.20. σ_{yy}-ε_{yy} hysteresis loop at the notch tip on the free surface of the plate. Uniaxial cyclic tensile loading. 3D analysis. Rounded V-notch, ρ=4mm, 2α=90°.

8.5.6 Stress/strain state at the tip of a rounded notch – 3D analysis, uniaxial fatigue, shear loading

A thick plate weakened by a rounded V notch (2α= 120°) and loaded under in-plane shear has been considered in order to extend the cyclic plasticity to the study of the out of plane effects. As already explained in section 8.2, if a notched specimen of finite thickness is subjected to a remote Mode II loading, an out of plane component of stress (comparable to a Mode III stress component) arises at the notch tip. This particular effect is strictly related to the contraction/expansion of the specimen due to the Poisson's ratio. As exhaustively reported in literature (Pook 2013), the concentration of the stress tied to the applied load vanishes for opening angle greater than 102°, leaving only the out of plane component of stress/strain acting at the notch tip. The so called O-mode follows the through-the-thickness behaviour shown in Figure 8.5.21. In particular, the out of plane effect ($K_{t,yz}$) does not act on the mid plane and on the free surface of the specimen, while it increases its intensity moving towards the free surface, reaching its maximum

value at a coordinate z/2t=0.46 (for the case taken into account) and then it drops to zero.

In order to obtain a non negligible yielded area at the notch tip neighbours, a very high nominal shear in-plane amplitude has been applied. As it can be noted, the intensity of the out of plane effect is equal to 0.6 times the nominal applied load near to the free surface. For this reasons the nominal in-plane shear amplitude has been set equal to 5k.

By providing the equations describing the linear elastic through-the-thickness variation of the "yz" stress concentration factors (obtainable with a simple 3D linear elastic FE analysis), the new incremental routine is able to obtain the whole elastic-plastic stress/strain behaviour at the tip of a rounded notch in the 3D plate.

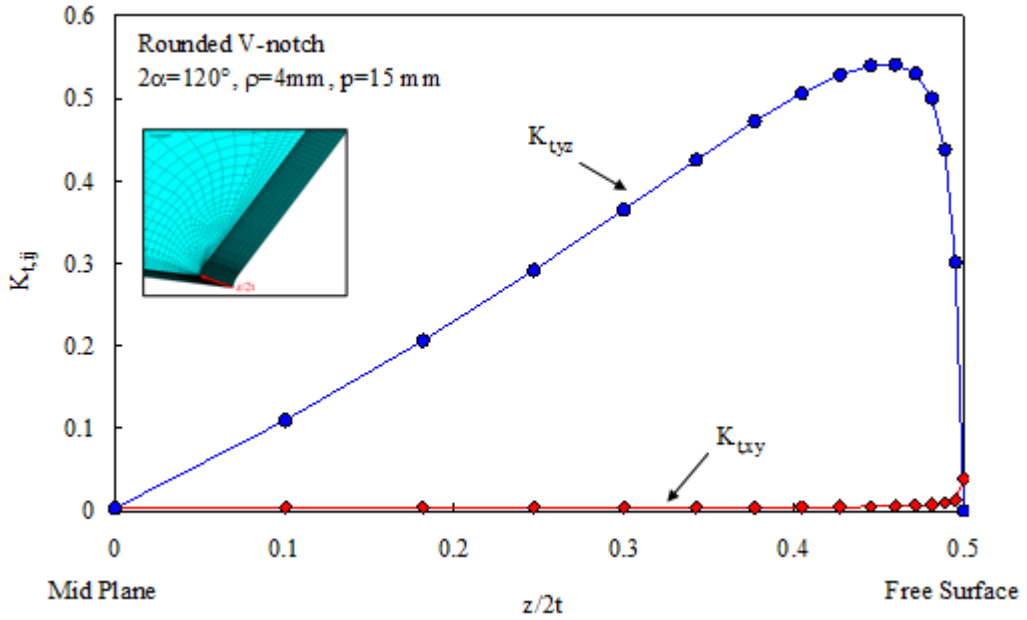

Figure 8.5.21. Stress concentration factors through-the-thickness of the plate at the notch tip. In-plane shear case.

In particular, three different through-the-thickness coordinates (z/2t) have been chosen to compare the incremental procedure and the FE cyclic elastic-plastic results. Figures 8.5.22, 8.5.23 and 8.5.24 show a very good correlation between analytical and FE results. Figure 8.5.22 shows the "yz" hysteresis loop at a coordinate z/2t=0.25, in the increasing branch of the curve representing the through-the-thickness behaviour of the out of plane stress concentration factor. It

is worth noting that, in this particular case, the yield condition has been just satisfied and the plastic strains are still very low.

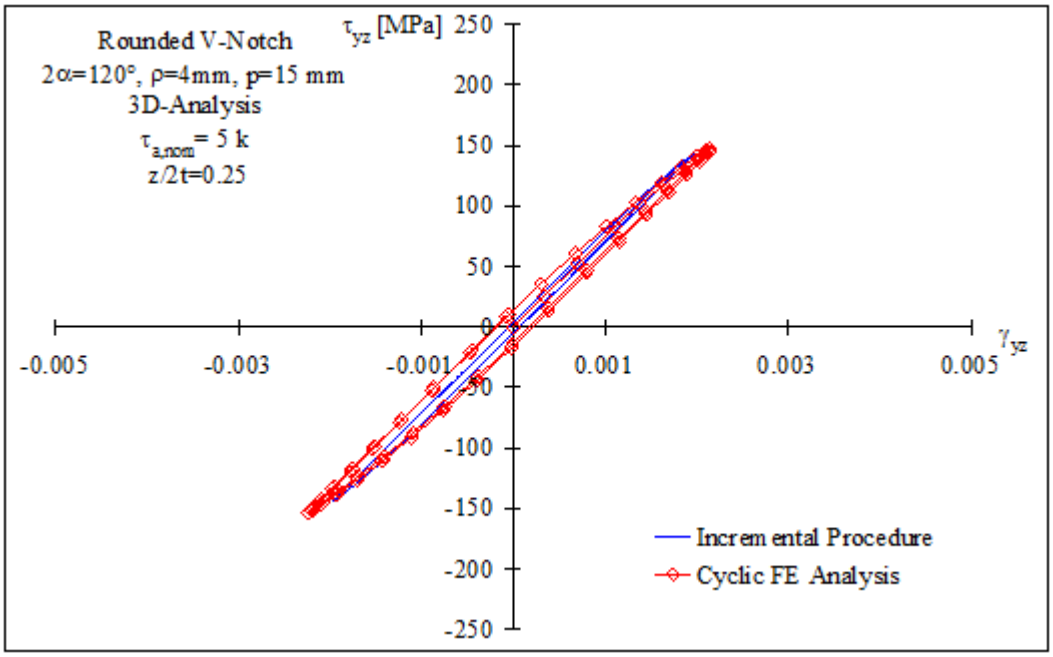

Figure 8.5.22. τ_{yz}-γ_{yz} hysteresis loop at the notch tip on the plane equal to z/2t=0.25 of the plate. Uniaxial cyclic in-plane shear loading. 3D analysis. Rounded V-notch, ρ=4mm, 2α=120°.

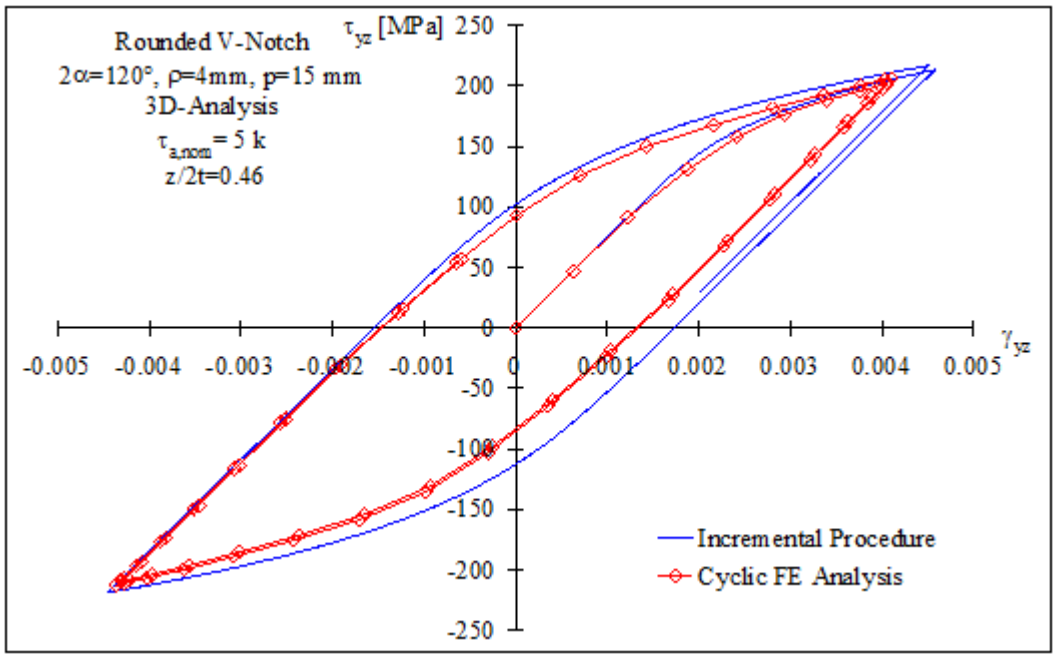

Figure 8.5.23. τ_{yz}-γ_{yz} hysteresis loop at the notch tip on the plane equal to z/2t=0.46 of the plate. Uniaxial cyclic in-plane shear loading. 3D analysis. Rounded V-notch, ρ=4mm, 2α=120°.

Moving from the mid plane to the free surface, the $K_{t,yz}$ reaches its maximum value at a coordinate z/2t=0.46 (see Figure8.5.23). In this case a very dilated hysteresis loop is present, documenting an extended yielded area near the notch tip. A low difference can be observed between analytical and numerical results but it can be stated that the modified incremental procedure is sensitive to the three dimensional effects induced by the application of an in-plane shear loading.

Approaching the free surface, the out of plane stress concentration factor decreases, equating zero at z/2t=0.5 (see Figure8.5.21). Accordingly, the area subtended by the "yz" hysteresis loop quickly decreases up to vanishing on the free surface.

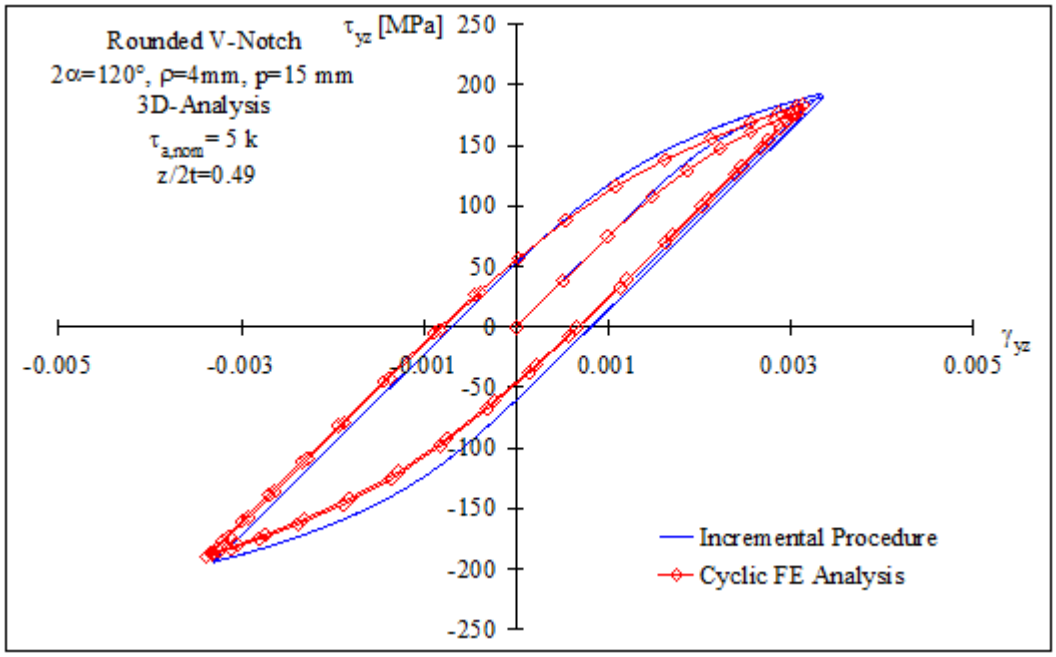

Figure 8.5.24. τ_{yz}-γ_{yz} hysteresis loop at the notch tip on the plane equal to z/2t=0.49 of the plate. Uniaxial cyclic in-plane shear loading. 3D analysis. Rounded V-notch, ρ=4mm, 2α=120°.

8.6 A link between cyclic plasticity and the averaged SED criterion

The criterion based on the evaluation of the strain energy density (SED) over a control volume surrounding the tip of a sharp or rounded notch has been presented and accurately described in some recent contributions (Lazzarin and Zambardi 2001, Lazzarin and Berto 2005a). The strength properties of brittle components weakened by different types of notch were uniquely obtained both in the case of static and cyclic loading. The control volume for the evaluation of the SED adapts itself as a function of the notch geometry and in particular of the notch root radius ρ and the notch opening angle 2α (See chapter 2). The critical radius R_c, expressed as the measure along the notch bisector line starting from the notch tip, depends only on the material properties and not on the notch geometry. The particular crescent shape volume presented in Lazzarin and Berto (2005a) varies from notch geometry to notch geometry following the next formulations:

$$q = \frac{2\pi - 2\alpha}{\pi} \tag{8.6.1}$$

$$r_0 = \frac{q-1}{q}\rho \tag{8.6.2}$$

In the past, the SED criterion has been already used in order to find a correspondence between linear elastic and elastic-plastic behaviour. In particular the relation between linear elastic and elastic-plastic notch stress intensity factors has been obtained under plane stress and plane strain conditions and also under torsion (Lazzarin and Zambardi 2001, Lazzarin and Zappalorto 2008-2011).

In this work, a link between the averaged SED criterion and the area subtended by the hysteresis loops tied to the different components of stress/strain acting at the notch tip, obtained by the incremental cyclic plasticity, has been investigated.

The averaged strain energy density over the crescent shape volume has been evaluated with some static FE elastic-plastic analyses provided in Ansys®. In all the cases taken into account the static applied load has been set equal to the nominal amplitude of the cyclic loading considered in the incremental procedure.

The values of the averaged SED have been obtained for three different critical radius (R_c=0.1, 0.2 and 0.3 mm) in order to investigate the influence on the outputs of this fundamental parameter and in addition to ensure the stability of the comparison method.

The area subtended by the hysteresis loops related to one loading cycle, has been carried out by a numerical integration routine. In this work, it has been thought that only the synergetic presence of a component of stress with the related component of strain causes a damaging effect. This leads to neglect the action of, for instance, the "xx" component of strain. In fact, because of equilibrium conditions, the related component of stress holds zero value at the tip of a rounded notch (See Figure 8.3.1).

In order to obtain a correlation between the SED and area of the acting hysteresis loops, four different analyses have been carried out. In particular the problem of a cyclic tension-compression loading in the case of plane stress, plane strain and generic three-dimensional conditions, and of a multiaxial (tension-torsion) loading have been addressed. In all the studied cases, a specimen weakened by a blunt U notch with a radius at the notch tip (ρ) equal to 1 mm has been considered. The notch depth (p) was set equal to 15 mm in the case of a flat specimen and equal to 6 mm for the axy-symmetric specimen (See Figure 8.4.1). The load ratio has been considered always equal to – 1. The material taken into account is the same than that used for the analyses in section 8.5, namely AISI 304L steel.

Several analyses have been carried out with different nominal load amplitudes in order to evaluate the evolution of parameter C_m, defined as the ratio between the value of the averaged SED and the area of the hysteresis loop acting at the notch tip (SED/A_{hl}).

The problem of a very thin flat specimen weakened by a blunt U notch has been addressed initially. Results are shown in Figure 8.6.1, where it is evident that, for high values of the nominal applied stress, C_m tends to an asymptotic constant value. For low loads, instead, the link between the SED and the area of the hysteresis loop is more complex. Accordingly, for high loads, the area subtended by the hysteresis loop can be directly determined from the SED value through a multiplicative factor (C_m). This behaviour holds true for all the three considered

control volumes and as it can be seen from Figure 8.6.1, it diminishes increasing the value of the critical radius. Thus, obtaining the exact critical radius related to the material taken into account, the plastic strain hysteresis energy can be easily obtained by means of a static FE analysis.

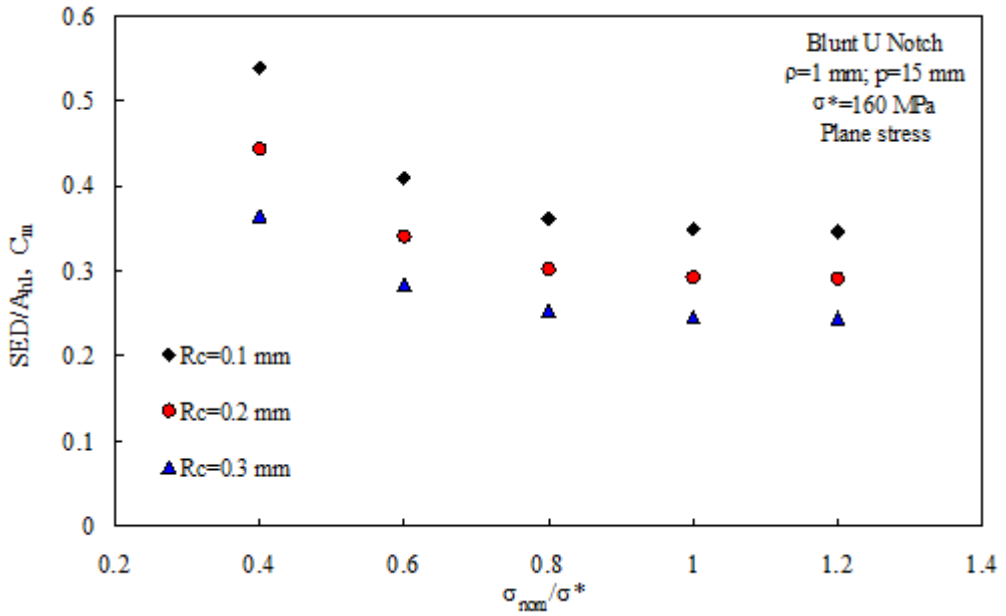

Figure 8.6.1. Cm correlation factor trend for different applied load amplitudes. Blunt U-Notch, ρ=1 mm. Plane stress case.

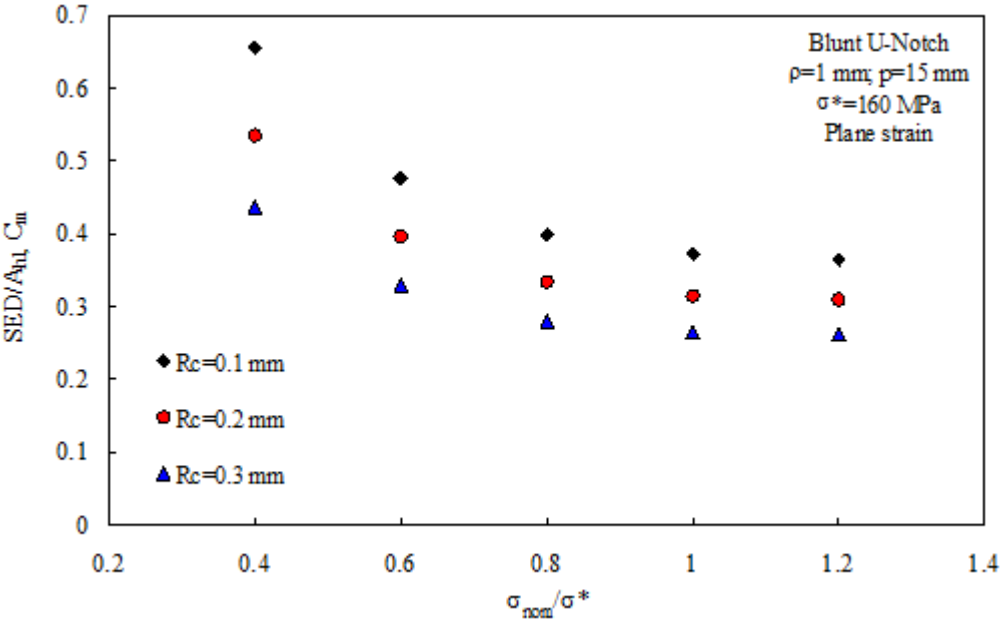

Figure 8.6.2. Cm correlation factor trend for different applied load amplitudes. Blunt U-Notch, ρ=1 mm. Plane strain case.

The same analyses have been carried out for a very thick plate (plane strain conditions). Results shown in Figure8.6.2 make it evident that a plateau value exists at high applied loads, namely when a non negligible amount of plasticity is present at the notch tip. A correlation can be observed for all the three considered R_c and its value, as expected, is similar to that obtained from the plane stress analysis.

Since plane stress and plane strain conditions are only "plane idealisation", the investigation has been extended to the 3D problem of a thick plate weakened by a U shaped notch and subjected to a tension-compression cyclic loading (Figure 8.4.1b). At the tip of the notch two different couples of stress and strain components act ((σ_{yy}, ε_{yy}) and (σ_{zz}, ε_{zz})). However only the hysteresis loop area tied to the "yy" component has been taken into account, being that related to the "zz" component almost negligible (less than 1%).

It is worth mentioning again that, in a thick plate with a rounded notch, the maximum notch tip stress varies with the through-the-thickness coordinate and, in turn, a variation of C_m might be present, as well. Accordingly, the correlation factor, C_m, has been determined on the mid plane (z/2t=0) and on the free surface of the specimen (z/2t=0.5) (See Figure 8.6.3 and 8.6.4).

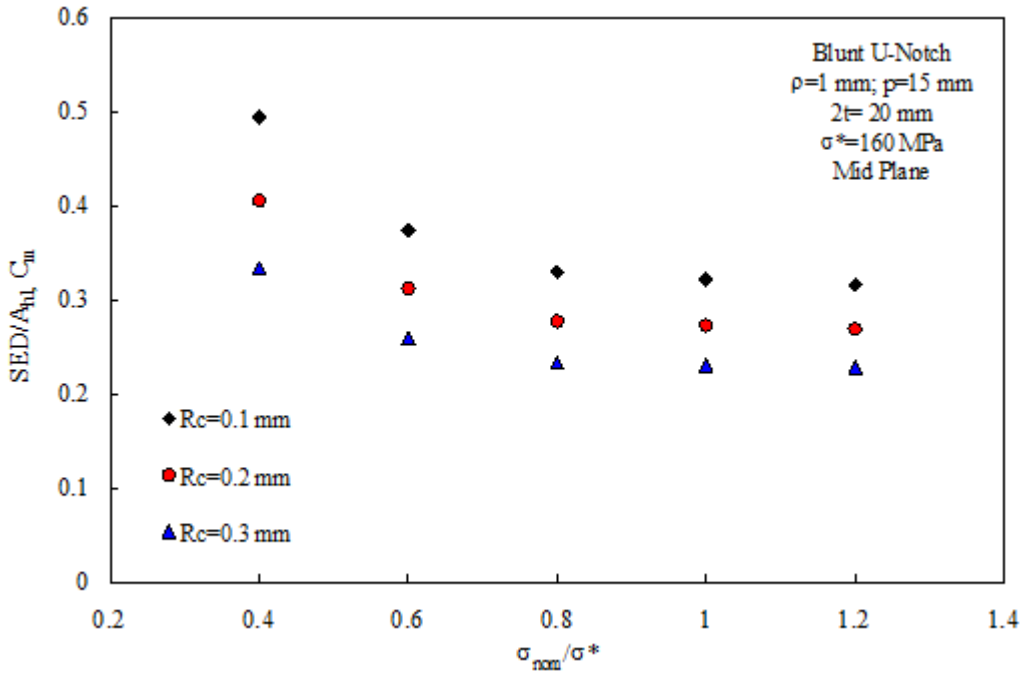

Figure 8.6.3. Cm correlation factor trend for different applied load amplitudes. Blunt U-Notch, ρ=1 mm. Three dimensional analysis. Mid plane of the plate.

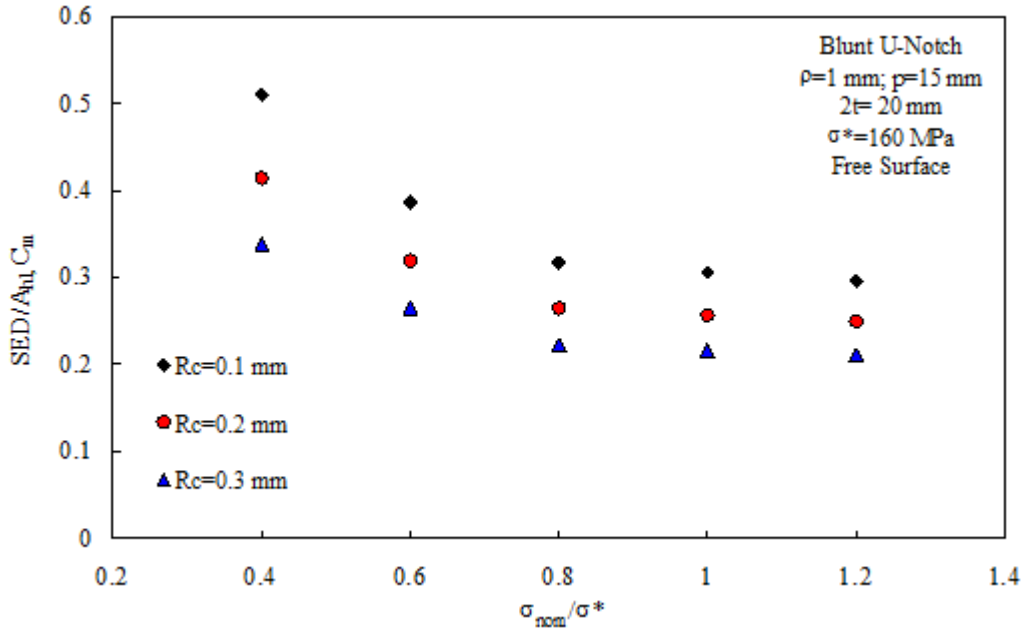

Figure 8.6.4. Cm correlation factor trend for different applied load amplitudes. Blunt U-Notch, ρ=1 mm. Three dimensional analysis. Free surface of the plate.

It is also interesting to discuss the through-the-thickness variation of the correlation factor for a critical radius equal to 0.3 mm (Figure8.6.5). It is worth noting that the parameter holds an almost constant value moving from the mid plane to the free surface of the specimen for different nominal applied loads.

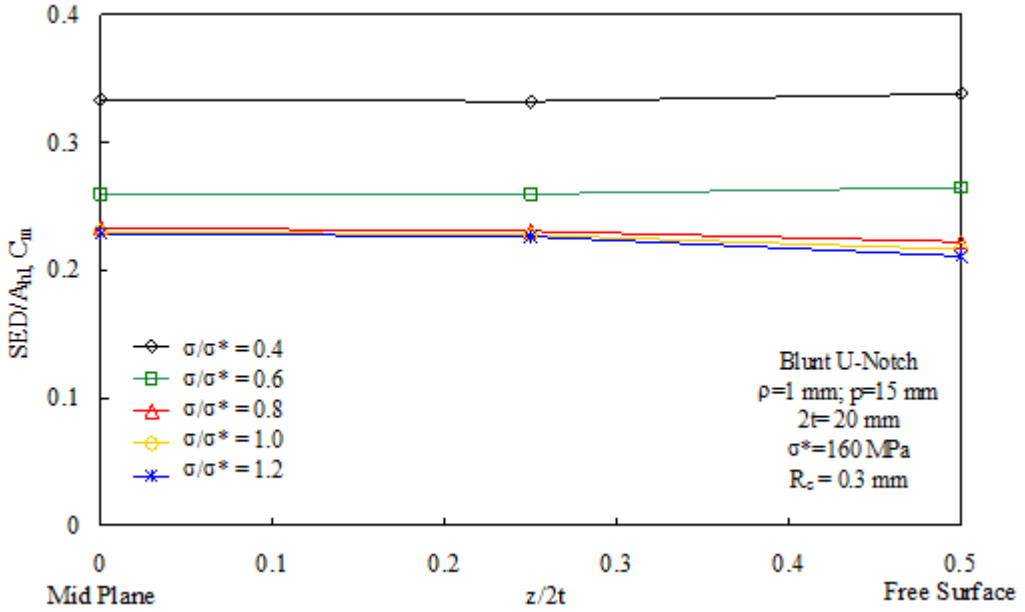

Figure 8.6.5. Cm correlation factor trend through the plate thickness for different applied load amplitudes. Blunt U-Notch, ρ=1 mm. Three dimensional analysis.

The last addressed problem is an axy-symmetric specimen weakened by a circumferential U notch under combined cyclic tension-torsion loading. Three couples of stress/strain act at the notch tip, in particular the normal components "yy" and "zz" and the shear component "yz". Being the values of the hysteresis loop areas comparable, the total area has been thought as the sum of them. The trend of the correlation factor is shown in Figure 8.6.6 for different applied loads, where the parameter σ_{eq} is the nominal equivalent von Mises stress. It is evident that the results are similar to those discussed for the previous cases.

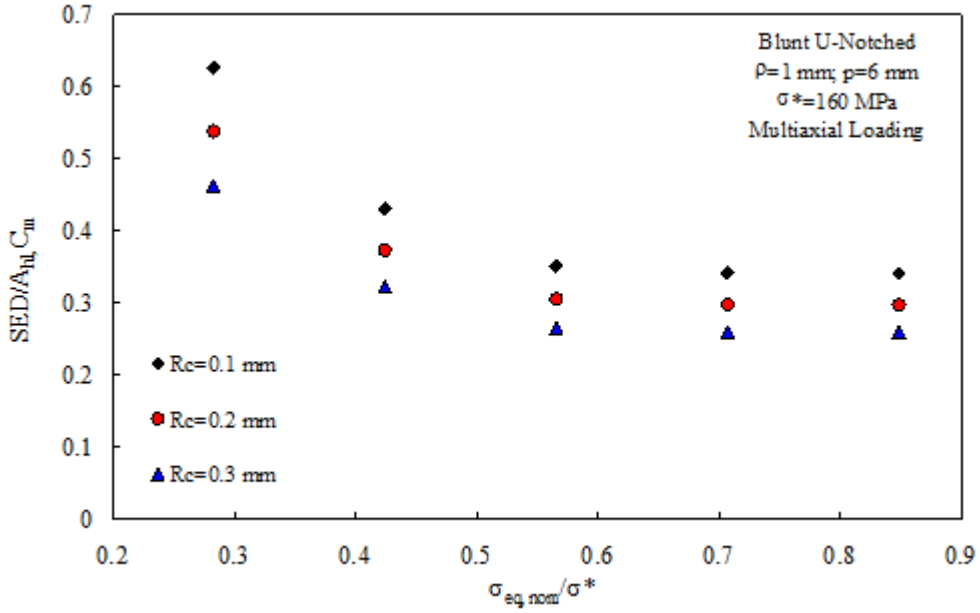

Figure 8.6.6. Cm correlation factor trend for different applied load amplitudes. Axy-symmetric specimen. Blunt U-Notch, ρ=1 mm. Three dimensional analysis. Multiaxial loading.

8.7 Conclusions

A modification of the incremental cyclic plasticity procedure has been presented aiming to extend the investigation to the three dimensional effects arising at the tip of a rounded notch subjected to different loading configurations. The incremental procedure has been initially validated with a number of plane analyses (plane stress and plane strain conditions). Then, the problem of an axy-symmetric specimen weakened by a circumferential notch under pure torsion and combined tension-torsion loading has been addressed. In both cases the theoretical

predictions have been compared with FE elastic-plastic analyses showing a very good agreement.

Subsequently, the problem has been extended to the three dimensional effects arising at the notch tip considering plates of finite thickness weakened by different notch geometries, such as a circular hole, a blunt notch and a rounded V-shaped notch.

The through-the-thickness variation of the stress concentration factors, as obtained by a linear elastic static FE analysis, have been included into the incremental cyclic procedure in order to consider the triaxial nature of the problem. By doing so, the actual stress/strain state on different through-the-thickness coordinates has been evaluated and compared with three dimensional elastic plastic FE analyses, exhibiting a very good agreement. The results prove that the 3D effects related to the presence of a finite thickness of the plate cannot be neglected *a priori* either in linear elastic problems or in the presence of a yielded area ahead of the notch tip.

Conclusions

The present PhD dissertation dealt with linear and non-linear structural analysis of notched components by means of local energy approaches. In particular the validity of the averaged SED criterion has been investigated by considering notched components weakened by different geometrical discontinuities and subjected to various loading histories. Three-dimensional effects arising in the vicinity of the tip of a notch, multiaxial static and cyclic loadings have been investigated taking also into account some particular effects tied to the phase displacement between the applied loads and non-linear effects induced by low cycle fatigue loadings, trying to extend the averaged SED criterion to the above mentioned problems.

The research activity has been substantially divided in three different research topics. In particular, the first topic dealt with the application of the averaged strain energy density criterion over a control volume (Lazzarin and Zambardi 2001) on mechanical components weakened by sharp and blunt notches and subjected to static and cyclic loadings. With the aim to validate the SED criterion, several finite element analyses on notched components have been carried out. Two-dimensional and three-dimensional analyses have been compared to theoretical solutions or experimental data, showing the soundness of the approach. In particular the SED criterion permitted to assess the static critical load in the case of notched specimens made of isostatic graphite subjected to mixed mode monotonic loading and the fatigue strength of notched components in 40CrMoV13.9 steel in the case of uniaxial and multiaxial in-phase and out-of-phase loadings. Moreover, after the investigation of the out-of-plane effects induced by a remotely applied Mode II loading on three-dimensional notched specimens, it has been underlined the inherent ability of the criterion to take into account the coupled mode arising in the vicinity of the notch tip due to the

Poisson's effect in the case of the presence of particular boundary conditions applied to the notch profile.

Taking advantage of some results obtained in the case of cyclic analyses, the second research topic dealt with the presentation of a new proposal able to discriminate the effect tied to the phase displacement between the applied loads on sharp V-notched components subjected to multiaxial loadings. This analytical activity made use of the Cardano formulation (1545) in order to obtain the maximum tangential stress acting in the vicinity of the notch tip. Results demonstrated that a severe notch geometry coupled with an out-of-phase multiaxial loading could lead to a more critical condition for the overall strength of the component. This phenomenon instead is not noticed in the case of un-notched or blunt notched components. A brief investigation of the phase displacement effect has been carried out also in terms of energetic assumptions. In this case, however, an energy based approach reveals to be not effective for the discrimination of the phase angle effects.

The third research topic dealt with the implementation of a dedicate software able to obtain the actual stress/strain state at the tip of a rounded notch subjected to low cycle fatigue. This particular loading configuration leads to the presence of a non negligible yielded area in the proximity of the notch tip. After a deep study on the cyclic plasticity theory (as formalised by Prager 1955, Armstrong and Frederick 1966, Chaboche 1979-1987, Jiang-Sehitoglu 1996a-1996b) and on the simplified methods for the determination of the actual stress/strain state at the tip of a rounded notch (Neuber 1961, Molski and Glinka 1981, Ye 2004-2008), an incremental procedure based on a energetic balance able to model the actual cyclic material behaviour (yield criterion, flow rule, hardening rule) has been developed and implemented using a commercial calculus software.

Initially, the obtained results have been compared with those presented in the previous scientific literature and, subsequently, the procedure has been extended for the first time to the study of the three dimensional effects arising at the notch tip. By furnishing the elastic out-of-plane through-the-thickness stress concentration factor acting at the tip of a rounded notch, the actual cyclic stress/strain through-the-thickness distributions have been obtained. Theoretical

results have been compared to a number of non-linear cyclic finite element analyses showing a satisfactory agreement. Finally, a new correlation factor between the plastic hysteresis energy and the elastic-plastic averaged strain energy density within a control volume has been found in order to extend the averaged SED criterion to the cyclic plasticity. The analyses reveal a link between the two energetic parameters when the yielded area ahead of the notch is not negligible, namely when applying non negligible loading amplitudes.

Bibliography

Abazadeh, B., Chakherlou, T.N., Farrahi, G.H., Alderliesten, R.C. (2013) Fatigue life estimation of bolt clamped and interference fitted-bolt clamped double shear lap joints using multiaxial fatigue criteria. Materials and Design, 43, 327–336.

Armstrong, P.J, Frederick, C.O. (1966) A mathematical representation of the multiaxial Bauschinger effect. Report RD/B/N 731, Central Electricity Generating Board .

Atzori, B., Lazzarin, P., Meneghetti, G. (2003) Fracture mechanics and notch sensitivity. Fatigue and Fracture of Engineering Materials and Structures, 26, 257-267.

Atzori, B., Berto, F., Lazzarin, P., Quaresimin, M. (2006) Multiaxial fatigue behaviour of a severely notched carbon steel. International Journal of Fatigue, 28, 485-493.

Ayatollahi, M.R., Torabi, A.R. (2010a) Brittle fracture in rounded-tip V-shaped notches. Materials and Design, 31, 60-67.

Ayatollahi, M.R., Torabi, A.R. (2010b) Determination of mode II fracture toughness for U shaped notches using Brazilian disc specimen. International Journal of Solids and Structures, 47, 454–465.

Ayatollahi, M.R., Torabi, A.R. (2010c) Investigation of mixed mode brittle fracture in rounded-tip V-notched components. Engineering Fracture Mechanics, 77, 3087–3104.

Ayatollahi, M.R., Torabi, A.R. (2010d) Tensile fracture in notched polycrystalline graphite specimens. Carbon, 48, 2255–2265.

Ayatollahi, M.R., Nejati, M. (2011) An over-deterministic method for calculation of coefficients of crack tip asymptotic field from finite element analysis. Fatigue and Fracure of Engineering Materials and Structures, 34, 159–176.

Ayatollahi, M.R., Berto, F., Lazzarin, P. (2011) Mixed mode brittle fracture of sharp and blunt V-notches in polycrystalline graphite. Carbon, 49, 2465-2474.

Bagherifard, S., Fernandez-Pariente, I., Ghelichi, R., Guagliano, M. (2013) Fatigue behavior of notched steel specimens with nanocrystallized surface obtained by severe shot peening. Materials and Design, 45, 497–503.

Bai-ping, D., Nian, L. (1989) The influence of microstress on the effective fatigue threshold. International Journal of Fatigue, 11, 43-50.

Bai-ping, D., Nian, L., Hui-jiu, Z. (1989) Factors influencing the effective fatigue threshold ΔKeff,th. International Journal of Fatigue, 9, 43-49.

Banvillet, A., Palin-Luc, T., Lasserre, S. (2003) A volumetric energy based high cycle multiaxial fatigue criterion. International Journal of Fatigue, 26, 755–769.

Barati, E., Alizadeh, Y. (2011) A numerical method for evaluation of J-integral in plates made of functionally graded materials with sharp and blunt V-notches. Fatigue and Fracture of Engineering Materials and Structures, 34, 1041–1052.

Barati, E., Alizadeh, Y., Aghazadeh, J., Berto, F. (2010a) Some new practical equations for rapid calculation of J-integral in plates weakened by U-notches under bending. Materials and Design, 31, 2964-2971.

Barati, E., Aghazadeh Mohandesi, J., Alizadeh, Y. (2010b) The effect of notch depth on J-integral and critical fracture load in plates made of functionally graded aluminum–silicone carbide composite with U-notches under bending. Materials and Design, 31, 4686-4692.

Bažant, Z.P., Estenssoro, L.F. (1979) Surface singularity and crack propagation. International Journal of Solids and Structures, 15, 405-426.

Benthem, J.P. (1977) State of stress at the vertex of a quarter-infinite crack in a half-space. International Journal of Solids and Structures, 13**,** 479–492.

Berto, F., Lazzarin, P. (2007) Relationships between J-integral and the strain energy evaluated in a finite volume surrounding the tip of sharp and blunt V-notches. International Journal of Solids and Structures, 44, 4621-4645.

Berto, F., Lazzarin, P. (2009) A review of the volume-based strain energy density approach applied to V-notches and welded structures. Theoretical and Applied Fracture Mechanics 52, 183-194.

Berto, F., Ayatollahi, M.R. (2011) Fracture assessment of Brazilian disc specimens weakened by blunt V-notches under mixed mode loading by means of local energy. Materials and Design, 32, 2858-2869.

Berto, F., Barati, E. (2011) Fracture assessment of U-notches under three point bending by means of local energy density. Materials and Design, 32, 822-830.

Berto, F., Lazzarin, P. (2011) Fatigue strength of structural components under multi-axial loading in terms of local energy density averaged on a control volume. International Journal of Fatigue, 33, 1055-1065.

Berto F., Marangon C. (2013) Three-dimensional effects in finite thickness plates weakened by rounded notches and holes under in-plane shear. Fatigue and Fracture of Engineering Materials and Structures 36, 1139–1152.

Berto, F., Lazzarin, P. (2013) Recent developments in brittle and quasi-brittle failure assessment of engineering materials by means of local approaches. Materials Science and Engineering R: Reports 2013, In press, Doi: 10.1016/j.mser.2013.11.001.

Berto, F., Lazzarin, P., Wang, C.H. (2004) Three-dimensional linear elastic distributions of stress and strain energy density ahead of V-shaped notches in plates of arbitrary thickness. International Journal of Fracture, 127, 265-282.

Berto, F., Lazzarin, P., Gomez, F.J., Elices, M. (2007) Fracture assessment of U-notches under mixed mode loading: Two procedures based on the 'equivalent local mode I' concept. International Journal of. Fracture, 148, 415-433.

Berto, F., Croccolo, D., Cuppini, R. (2008) Fatigue strength of a fork-pin equivalent coupling in terms of the local strain energy density. Materials and Design, 29, 1780–1792.

Berto, F., Lazzarin, P., Kotousov, A., Harding, S. (2011a) Out-of-plane singular stress fields in V-notched plates and welded lap joints induced by in-plane shear load conditions. Fatigue and Fracture of Engineering Materials and Structures, 34, 291-304.

Berto, F., Lazzarin, P., Kotousov, A. (2011b) On higher order terms and out-of-plane singular mode. Mechanics of Materials, 43, 332-341.

Berto, F., Lazzarin, P., Yates, J. (2011c) Multiaxial fatigue of V-notched steel specimens: a non-conventional application of the local energy method. Fatigue and Fracture of Engineering Materials and Structures, 34, 921–943.

Berto, F., Lazzarin, P., Kotousov, A. (2011d) On the Presence of the Out-of-Plane Singular Mode Induced by Plane Loading With K(II) = K(I)=0. International Journal of Fracture, 167, 119-126.

Berto, F., Lazzarin, P., Kotousov, A., Pook, L.P. (2012a) Induced out-of-plane mode at the tip of blunt lateral notches and holes under in-plane shear loading. Fatigue and Fracture of Engineering Materials and Structures, 35, 538-555.

Berto, F., Lazzarin, P., Ayatollahi, M.R. (2012b) Brittle fracture of sharp and blunt V-notches in isostatic graphite under torsion loading. Carbon, 50, 1942-1952.

Berto, F., Lazzarin, P., Marangon, C. (2012c) Brittle fracture of U-notched graphite plates under mixed mode loading. Materials and Design, 41, 421-432.

Berto, F., Lazzarin, P., Kotousov, A., Pook, L.P. (2013a) On Scale Effect in Plates Weakened by Rounded V-Notches and Subjected to In-Plane Shear Loading. International Journal of Fracture 180, 111–118.

Berto, F., Kotousov, A., Lazzarin, P., Pegorin, F. (2013b) On a Coupled Mode at Sharp Notches Subjected to Anti-Plane Loading. European Journal of Mechanics A/Solids, 38, 70-78.

Berto, F., Campagnolo, A., Elices, M., Lazzarin, P. (2013c) A synthesis of polymethylmethacrylate data from U-notched specimens and V-notches with end holes by means of local energy. Materials and Design, 49, 826-833.

Berto, F., Lazzarin, P., Marangon, C. (2014) Fatigue strength of notched specimens made of 40CrMoV13.9 under multiaxial loading. Materials and Design, 54, 57-66.

Bower, A.F. (1987) Some aspects of plastic flow, residual stress and fatigue due to rolling and sliding contact. PhD dissertation, Emmanuel college, Department of engineering, University of Cambridge.

Bower A. F., Johnson K.L. (1989) The influence of strain hardening on cumulative plastic deformation in rolling and sliding line contact. Journal of the Mechanics and Physics of Solids, 37, 471-493.

Brahtz, J.H.A. (1933) Stress Distribution in a Reentrant Corner. Transactions of

the American Society of Mechanical Engineers, 55, 31-37.

Brown, M.W., Miller, K.J. (1973) A theory for fatigue under multi-axial stress–strain conditions. In: Proceedings of the institute of mechanical engineers, 187, 745–756.

Capetta, S., Tovo, R., Taylor, D., Livieri, P. (2011) Numerical evaluation of fatigue strength on mechanical notched components under multi-axial loadings. International Journal of Fatigue, 33, 661-671.

Cardano, G. (1545) Ars magna or The Rules of Algebra, Dover (published 1993).

Carpinteri, An., Spagnoli, A. (2001) Multiaxial high-cycle fatigue criterion for hard metals. International Journal of Fatigue, 23, 135-145.

Carpinteri, An., Spagnoli, A., Vantadori, S. (2009) Multiaxial fatigue life estimation in welded joints using the critical plane approach. International Journal of Fatigue, 31, 188-196.

Chaboche, J.L. (1987) Cyclic plasticity modelling and ratchetting effects. Proceedings of the second international conference on constitutive laws for engineering materials: Theory and applications, Tucson, Arizona, Desal et al., Eds. Elsevier 47-58.

Chaboche, J.L. (1991) On some modifications of kinematic hardening to improve the description of ratchetting effects. International Journal of Plasticity, 7, 661-687.

Chaboche, J.L., Dang Van, K., Cordier, G. (1979) Modelization of the strain memory effect on the cyclic hardening of the 316 stainless steel. Structural Mechanical in Reactor Technology, Transaction of the 5th International Conference on Structural Mechanics in Reactor Technology, Div.L, Berlin, L11/3.

Chen, D.H., Ozaki, S. (2008) Investigation of failure criteria for a sharp notch. International Journal of Fracture, 152, 63–74.

Cheng, C., Niu, Z., Recho, N., Hou, H. (2013) Analyse the role of the non-singular stress in brittle fracture by BEM coupled with eigen-analysis. Fatigue and Fracture of Engineering Materials and Structures, 36, 416–426.

Christopher, C.J., James, M.N., Patterson, E.A., Tee K.F. (2007) Towards a new model of crack tip stress fields. International Journal of Fracture, 148, 361–371.

Christopher, C.J., James, M.N., Patterson, E.A., Tee, K.F. (2008) A quantitative evaluation of fatigue crack shielding forces using photoelasticity. Engineering Fracture Mechanics, 75, 4190-4199.

Chu C.C. (1995a) Fatigue damage calculation using the critical plane approach. Journal of Engineering Materials and Technology ASME, 117, 41-49.

Chu, C.C. (1995b) Incremental multiaxial Neuber correction for fatigue analysis. SAE International Journal of Materials and Manufacturing, 104, 595–602.

Coker, E.G., Filon, L.N.G. (1931) A Treatise on Photoelasticity. Cambridge University Press.

Colombo, C., Vergani, L. (2010) A numerical and experimental study of crack tip shielding in presence of overloads. Engineering Fracture Mechanics, 77, 1644-1655.

Colombo, C., Du, Y., James, M.N., Patterson, E.A., Vergani, L. (2010) On crack tip shielding due to plasticity-induced closure during an overload. Fatigue and Fracture of Engineering Materials and Structures, 33, 766–777.

Creager, M., Paris, P.C. (1967) Elastic field equations for blunt cracks with reference to stress corrosion cracking. International Journal of Fracture Mechanics, 3, 247-252.

Cristofori, A., Benasciutti, D., Tovo, R. (2011) A stress invariant based spectral method to estimate fatigue life under multiaxial random loading. International Journal of Fatigue, 33, 887–899.

Doquet, V., Ben Ali, N., Constantinescu, A., Boutillon, A. X. (2013) Fracture of a borosilicate glass under triaxial tension. Mechanics of Materials, 57, 15-29.

Döring, R., Hoffmeyer, J., Seeger, T., Vormwald, M. (2006) Short fatigue crack growth under non-proportional multi-axial elastic–plastic strains. International Journal of Fatigue, 28, 972-982.

Drucker, D.C. (1960) Plasticity in structural mechanics. Proceeding of the First Symposium on Naval Structural Mechanics. Goodier and Hoff, Eds., Pergamon, Macmillan, New York. 331-350.

Dunn, M.L., Suwito, W., Cunningham, S. (1997) Stress intensities at notch singularities. Engineering Fracture Mechanics, 57, 417-430.

Ellyin, F. (1989) Cyclic strain energy density as a criterion for multiaxial fatigue failure. Brown, Miller, editors. Biaxial and Multiaxial Fatigue, 3. London: EGF Publication; 571–583.

Ellyin, F. (1997) Fatigue damage, crack growth and life prediction. Edmonton: Chapman and Hall.

Ellyin, F., Kujawski, D. (1989) Generalization of notch analysis and its extension to cyclic loading. Engineering Fracture Mechanics, 32, 819–826.

Erdogan, F., Sih, C.G. (1963) On the crack extension in plates under plane loading and transverse shear. Journal of Basic Engineering, 85, 528-534.

Esnault, J.B., Doquet, V., Massin, P. (2013) A three-dimensional analysis of fatigue crack paths in thin metallic sheets, International Journal of Fatigue, in press, http://dx.doi.org/10.1016/j.ijfatigue.2013.03.015.

Ewing, J.A., Humfrey, J.C. (1903) The fracture of metals under repeated alterations of stress. Philosophical Transactions of The Royal Society - A, 200, 241-253.

Fadle, J. (1941) Die Selbstspannungs-Eigenwertfunktionen der quadratischen Scheibe. Ing.-Arch. 11, 125-148.

Fatemi, A., Kurath, P.P. (1988) Multiaxial fatigue life prediction under the influence of mean stresses. ASME Journal of Engineering Materials and Technology, 110, 380-388.

Fatemi, A., Socie, D.F. (1988) A critical plane approach to multiaxial fatigue damage including out-of-phase loading. Fatigue and Fracture of Engineering Materials and Structures, 11, 149-165.

Fatemi, A., Shamsaei, N. (2011) Multiaxial fatigue: An overview and some approximation models for life estimation. International Journal of Fatigue, 33, 948-958.

Filippi, S., Lazzarin, P., Tovo, R. (2002). Developments of some explicit formulas useful to describe elastic stress fields ahead of notches in plates. International Journal of Solids and Structures, 39, 4543-4565.

Firat, M. (2011) A computer simulation of four-point bending fatigue of a rear axle assembly. Engineering Failure Analysis, 18, 1049–1057.

Firat, M., Kozan, R., Ozsoy, M., Mete, O.H. (2009) Numerical modeling and simulation of wheel radial fatigue tests. Engineering Failure Analysis, 16, 1533–1541.

Foletti, S., Desimone, H. J. (2007) A semi-analytical approach for two-dimensional rolling/sliding contact with applications to shakedown analysis. Wear. 262, 850-857.

Forsyth, P.J.E. (1961). Proceedings of the crack propagation symposium. Cranfield: The College of Aeronautics, 1, 76–94.

Gao, Z., Qiu, B., Wang, X., Jiang, Y. (2010) An investigation of fatigue of a notched member. International Journal of Fatigue, 32, 1960-1969.

Ghasemnejad, H., Aboutorabi, A. (2011) Cohesive zone modeling (CZM) in prediction of delamination failure in laminated composite structures. Journal of Material Science and Engineering, 5, 61-64.

Gillemot, L.F. (1965) Brittle fracture of welded materials. Commonwealth Welding Conference C.7., 353.

Gillemot, L.F., Czoboly, E., Havas, I. (1985) Fracture mechanics applications of absorbed specific fracture energy: notch and unnotched specimens. Theoretical and Applied Fracture Mechanics, 4, 39-45.

Glinka, G. (1985) Calculation of inelastic notch-tip strain-stress histories under cyclic loading. Engineering Fracture Mechanics, 22, 839-854.

Glinka, G., Wang, G., Plumtree, A. (1995) Mean stress effects in multi-axial fatigue. Fatigue and Fracture of Engineering Materials and Structures, 18, 755–764.

Gogotsi, G.A. (2003) Fracture toughness of ceramics and ceramic composites. Ceramics International, 7, 777-884.

Gómez, F.J., Elices, M. (2003) A fracture criterion for sharp V-notched samples. International Journal of Fracture, 123, 163–175.

Gómez, F.J., Elices, M., Valiente, A. (2000) Cracking in PMMA containing U-shaped notches. Fatigue and Fracture of Engineering Materials and Structures, 23, 795–803.

Gomez, F.J., Guinea, G.V., Elices, M (2006) Failure criteria for linear elastic materials with U-notches. International Journal of Fracture, 141, 99–113.

Gómez, F.J., Elices, M., Berto, F., Lazzarin, P. (2007) Local strain energy density to assess the static failure of U-shaped notches in plates under mixed mode loading. International Journal of Fracture, 145, 29-45.

Gómez, F.J., Elices, M., Berto, F., Lazzarin, P. (2008) A generalized notch stress intensity factor for U-notched components loaded under mixed mode. Engineering Fracture Mechanics, 75, 4819–4833.

Gómez, F.J., Elices, M., Berto, F., Lazzarin, P. (2009a) Fracture of V-notched specimens under mixed mode (I+II) loading in brittle materials. International Journal of Fracture, 159, 121–135.

Gómez, F.J., Elices, M., Berto, F., Lazzarin, P. (2009b) Fracture of U-notched specimens under mixed mode experimental results and numerical predictions. Engineering Fracture Mechanics, 76, 236–249.

Gross, R., Mendelson, A. (1972) Plane Elastostatic Analysis of V-Notched Plates. International Journal of Fracture Mechanics, 8, 267-272.

Harding, S., Kotousov, A., Lazzarin, P., Berto, F. (2010) Transverse singular effects in V-shaped notches stressed in mode II, International Journal of Fracture, 164, 1-14.

Hartranft, R.J., Sih, G.C. (1968) Effect of plate thickness on the bending stress distribution around through cracks. Journal of Mathematical Physics, 47, 276–291.

Hartranft, R.J., Sih, G.C. (1969) The use of eigenfunction expansions in general solution of three-dimensional crack problems. Journal of applied Mathematics and Mechanics, 19, 23.

Hartranft, R.J., Sih, G.C. (1970) An approximate three-dimensional theory of plates with application to crack problems. International Journal of Engineering Science, 8, 711–729.

Hartranft, R.J., Sih, G.C. (1973) Alternating method applied to edge and surface crack problems. Method of Analysis and Solutions to Crack Problems, 1, G.C. Sih (Ed.), Noordhoff International Publishing, the Netherlands.

Hertel, O., Vormwald, M. (2011) Short-crack-growth-based fatigue assessment of notched components under multi-axial variable amplitude loading. Engineering Fracture Mechanics, 78, 1614-1627.

Hoffmann, M., Seeger, T. (1985) A generalized method for estimating multiaxial elastic–plastic notch stresses and strains. ASME Journal of Engineering Materials and Technology, 107, 250–260.

Huang, C.S. (2004) Corner stress singularities in a high-order plate theory. Computers and Structures, 82, 1657-1669.

Imaoka, S., (2008) Uniaxial and biaxial ratchetting in piping materials-experiments and analysis. Memo Number STI0805A, ANSYS Release 12.0.1.

James, M.N. (2013) Fractographic insights into cracking mechanisms and microstructure. Fatigue and Fracture of Engineering Materials and Structures, 36, 851-860

James, M.N., Lu, Y., Christopher, C.J., Patterson, E.A. (2013a) Crack path support for deformation mechanisms in fatigue of polycarbonate, Engineering Fracture Mechanics, 108, 89-97

James, M.N., Christopher, C.J., Lu, Y., Patterson, E.A. (2013b) Local crack plasticity and its influences on the global elastic stress field. International Journal of Fatigue, 46, 4-15.

Jasper, T.M. (1923) The value of the energy relation in the testing of ferrous metals at varying ranges and at intermediate and high temperature. Philosophical Magazine, 46, 609–627.

Jiang, Y. (1994) Cyclic plasticity with an emphasys on ratchetting. PhD dissertation, College of Engineering, University of Illinois at Urbana Champagne.

Jiang, Y. (2000) A fatigue criterion for general multi-axial loading. Fatigue and Fracture of Engineering Materials and Structures, 23, 19–32.

Jiang, Y., Kurath, P. (1996) Characteristics of Armstrong-Frederick Type Plasticity Model. International Journal of Plasticity, 12, 387–415.

Jiang, Y., Sehitoglu, H. (1996a) Modeling of cyclic ratchetting plasticity: part I: development of constitutive equations. ASME Journal of Applied Mechanics, 63, 720–725.

Jiang, Y., Sehitoglu, H. (1996b) Modeling of cyclic ratcheting plasticity, part II: comparison of model simulations with experiments. ASME Journal of Applied Mechanics, 63, 726–733.

Jiang, Y., Xu, B. (2001) Deformation analysis of notched components and assessment of approximate method. Fatigue and Fracture of Engineering Materials and Structures, 24, 729–740.

Jiang, Y., Feng, M. (2004) Modeling of fatigue crack propagation. Journal of Engineering Materials and Technology – ASME, 126, 77–86.

Jiang, Y., She, C., Yu, P., Guo, W. (2011) Three-dimensional stress concentrations at circular pin holes in clearance-fit lugs. Fatigue and Fracture of Engineering Materials and Structures, 34, 573–580.

Jin, Z.H., Batra, R.C. (1997) A crack at the interface between a Kane-Mindlin plate and a rigid substrate. Engineering Fracture Mechanics, 57, 343-354.

Kane, T.R., Mindlin, R.D. (1956) High frequency extensional vibrations of plates. Journal of Applied Mechanics, 23, 277–283.

Kattekola, B., Ranjan, A., Basu, S. (2013) Three dimensional finite element investigations into the effects of thickness and notch radius on the fracture toughness of polycarbonate. International Journal of Fracture, 181, 1-12.

Khan, S.M.A., Merah, N., Adinoyi, M.J. (2013) 3D effects on crack front core regions, stress intensity factors and crack initiation angles. International Journal of Solids and Structures, 50, 1449-1459.

Knésl Z. (1991) A criterion of V-notch stability. International Journal of Fracture, 48, 79-83.

Kotousov, A. (2007) Fracture in plates of finite thickness. International Journal of Solids and Structures, 44, 8259-8273.

Kotousov, A., Wang, C.H. (2002) Three-dimensional stress constraint in an elastic plate with a notch. International Journal of Solids and Structures, 39, 4311-4326.

Kotousov, A., Lew, Y.T. (2006) Stress singularities resulting from various boundary conditions in angular corners of plates of arbitrary thickness in extension. International Journal of Solids and Structures, 43, 5100– 5109.

Kotousov, A., Lazzarin, P., Berto, F., Harding, S. (2010) Effect of the thickness on elastic deformation and quasi-brittle fracture of plate components. Engineering Fracture Mechanics, 77, 1665-1681.

Kotousov, A., Berto, F., Lazzarin, P., Pegorin, F. (2012) Three dimensional finite element mixed fracture mode under anti-plane loading of a crack, Theoretical and Applied Fracture Mechanics, 62, 26-33.

Kulkarni, S.C., Desai, Y.M., Kant, T., Reddy, G.R., Prasad, P., Vaze, K.K., Gupta, C. (2004) Uniaxial and biaxial ratchetting in piping materials - experiments and analysis. International Journal of Pressure Vessels and Piping, 81, 609-617.

Łagoda, T., Macha, E., Bedkowski, W. (1999) A critical plane approach based on energy concepts: application to biaxial random tension-compression high-cycle fatigue regime. International Journal of Fatigue, 21, 431-443.

Lazzarin, P., Tovo, R. (1996). A unified approach to the evaluation of linear elastic stress fields in the neighborhood of cracks and notches. International Journal of Fracture, 78, 3-19.

Lazzarin, P., Zambardi, R. (2001) A finite-volume-energy based approach to predict the static and fatigue behaviour of components with sharp V-shaped notches. International Journal of Fracture, 112, 275-298.

Lazzarin, P., Susmel, L. (2003) A stress-based method to predict lifetime under multiaxial fatigue loadings. Fatigue and Fracture of Engineering Materials and Structures, 26, 1171-1187.

Lazzarin, P., Berto, F. (2005a) Some expressions for the strain energy in a finite volume surrounding the root of blunt V-notches. International Journal of Fracture, 135, 161-185.

Lazzarin, P., Berto, F. (2005b) From Neuber's elementary volume to Kitagawa and Atzori's diagrams: an interpretation based on local energy. International Journal of Fracture, 135, 33-38.

Lazzarin, P., Filippi, S. (2006) A generalised stress intensity factor to be applied to rounded V-shaped notches. International Journal of Solids and Structures, 43, 2461–2478.

Lazzarin, P., Berto, F. (2008) Control volumes and strain energy density under small and large scale yielding due to tensile and torsion loading. Fatigue and

Fracture of Engineering Materials and Structures, 31, 95-107.

Lazzarin, P., Zappalorto, M. (2012) A three-dimensional stress field solution for pointed and sharply radiused V-notches in plates of finite thickness, Fatigue and Fracture of Engineering Materials and Structures, 35, 1105-1119.

Lazzarin, P.; Lassen, T.; Livieri, P. (2003) A notch stress intensity approach applied to fatigue life predictions of welded joints with different local toe geometry. Fatigue and Fracture of Engineering Materials and Structures, 26, 49-58.

Lazzarin, P., Sonsino, C.M., Zambardi, R. (2004) A notch stress intensity approach to assess the multiaxial fatigue strength of welded tube-to-flange joints subjected to combined loadings. Fatigue and Fracture of Engineering Materials and Structures, 27, 127-140.

Lazzarin, P., Zappalorto, M., Yates, J.R. (2007) Analytical study of stress distributions due to semi-elliptic notches in shafts under torsion loading, International Journal of Engineering Science, 45, 308-328.

Lazzarin, P., Berto, F., Gomez, F.J, Zappalorto, M. (2008a) Some advantages derived from the use of the strain energy density over a control volume in fatigue strength assessments of welded joints. International Journal of Fatigue, 30, 1345-1357.

Lazzarin, P., Livieri, P., Berto, F., Zappalorto, M. (2008b) Local strain energy density and fatigue strength of welded joints under uniaxial and multiaxial loading. Engineering Fracture Mechanics, 75, 1875-1889.

Lazzarin, P., Berto, F., Radaj, D. (2009a) Fatigue-relevant stress field parameters of welded lap joints: pointed slit tip compared with keyhole notch. Fatigue and Fracture of Engineering Materials and Structures, 32, 713-735.

Lazzarin, P., Berto, F., Elices, M., Gómez, J. (2009b) Brittle failures from U- and V-notches in mode I and mixed, I+II, mode. A synthesis based on the strain energy density averaged on finite size volumes. Fatigue and Fracture of Engineering Materials and Structures, 32, 671–684.

Lazzarin, P., Berto, F., Zappalorto, M. (2010) Rapid calculations of notch stress intensity factors based on averaged strain energy density from coarse meshes: Theoretical bases and applications. International Journal of Fatigue, 32, 1559-1567.

Lazzarin, P., Zappalorto, M., Berto, F. (2011) Generalised stress intensity factors for rounded notches in plates under in-plane shear loading. International Journal of Fracture, 170, 123-144.

Lazzarin, P., Berto, F., Ayatollahi, M. R. (2013a) Brittle failure of inclined key-hole notches in isostatic graphite under in-plane mixed mode loading. Fatigue and Fracture of Engineering Materials and Structures, 36, 942-955.

Lazzarin, P., Berto, F., Atzori, B. (2013b) A synthesis of data from steel spot welded joints of reduced thickness by means of local SED. Theoretical and Applied Fracture Mechanics, 63-64, 32-39.

Li, A., Zhao, J., Wang, D., Gao, X., Tang, H. (2013) Three-point bending fatigue behavior of WC–Co cemented carbides. Materials and Design, 45, 271–278.

Li, J., Zhang, Z.P., Sun, Q., Li, C.W. (2011) Multi-axial fatigue life prediction for various metallic materials based on the critical plane approach. International Journal of Fatigue, 33, 90-101.

Lin, B., Mear, M.E., Ravi-Chandar, K. (2010) Criterion for initiation of cracks under mixed-mode I + III loading. International Journal of Fracture, 165, 175-188.

Liu, J., Nie, A., Dong, C., Wang, P., Wang, H., Fu, M., Yang, W. (2011) Grain boundary structure dependent fracture in nanocrystalline Au films. Materials Letters 65, 2769–2771.

Liu, K.C. (1993) A method based on virtual strain energy parameters for multi-axial fatigue life prediction. Advances in Multi-axial Fatigue, ASTM STP 1191 (eds K.J. Miller and D.L. McDowell) ASTM, West Conshohocken, PA; 67–84.

Lomakin, E.V., Zobnin, A.I., Berezin, A.V. (1975) Finding the fracture toughness characteristics of graphite materials in plane strain. Strength of Materials, 7, 484–487.

Macha, E., Sonsino, C.M. (1999) Energy criteria of multiaxial fatigue failure. Fatigue and Fracture of Engineering Materials and Structures, 22, 1053–1070.

Matvienko, Y.G., Morozov, E.M. (2004) Calculation of the energy J-integral for bodies with notches and cracks. International Journal of Fracture, 125, 249–261.

Matvienko, Y.G., Shlyannikov, V.N., Boychenko N.V. (2013) In-plane and out-of-plane constraint parameters along a three-dimensional crack-front stress field under creep loading. Fatigue and Fracture of Engineering Materials and Structures, 36, 14–24.

Mehran, S., Rouhi, S., Ramzani, B., Barati, E. (2012) Fracture analysis of functionally graded materials with U- and V-notches under mode I loading using the averaged strain-energy density criterion, Fatigue and Fracture of Engineering Materials and Structures, 35, 614–627.

Meneghetti, G., Ricotta, M. (2012) The use of the specific heat loss to analyse the low- and high-cycle fatigue behaviour of plain and notched specimens made of a stainless steel. Engineering Fracture Mechanics, 81, 2–16.

Moftakhar, A., Buczynski, A., Glinka, G. (1995) Calculation of elasto-plastic strains and stresses in notches under multiaxial loading. International Journal of Fracture, 70, 357–372.

Molski, K., Glinka, G. (1981) A method of elastic–plastic stress and strain calculation at a notch root. Materials Science and Engineering, 50, 93–100.

Nakamura, T., Parks, D.M. (1988) Three-dimensional stress field near the crack front of a thin elastic plate. Journal of Applied Mechanics, 55, 805–813.

Nakamura, T., Parks, D.M. (1989) Antisymmetrical 3-D stress field near the crack front of a thin elastic plate. International Journal of Solids and Structures 25, 1411-1426.

Neuber, H. (1958) Kerbspannungslehre, Springer-Verlag (2nd edition), Berlin.

Neuber, H. (1961) Theory of stress concentration for shear-strained prismatic bodies with arbitrar nonlinear stress–strain law. Journal of Applied Mechanics (Trans. ASME), 28, 544–549.

Nian, L., Bai-ping, D., Hui-jiu, Z. (1984) On the relationship between fatigue limit, threshold and microstructure of a low-carbon Cr-Ni steel. International Journal of Fatigue, 6, 89-94.

Nian, L., Bai-ping, D. (1995) The effect of low-stress high cycle fatigue on the microstructure and fatigue threshold of a 40 Cr steel. International Journal of Fatigue, 17, 43-48.

Nieslony, A., Sonsino, C.M. (2008) Comparison of some selected multiaxial fatigue assessment criteria. LBF Report, FB-234.

Nui, L.S., Chehimi, C., Pluvinage, G. (1994) Stress field near a large blunted tip V-notch and application of the concept of the critical notch stress intensity factor (NSIF) to the fracture toughness of very brittle materials. Engineering Fracture Mechanics, 49, 325-335.

Ohno, N., Wang, J.D. (1991) Non linear kinematic hardening rule: proposition and application to ratchetting problems. Structural Mechanical in Reactor Technology, Transaction of the 11th International Conference on Structural Mechanics in Reactor Technology, Shibata, L22/1.

Palin-Luc, T., Lasserre, S. (1998) An energy based criterion for high cycle multiaxial fatigue. European Journal of Mechanics A/Solids, 17, 237–251.

Panin, S.V., Byakov, A.V., Grenke, V.V., Shakirov, I.V., Yussif, S.A.K. (2010) Multiscale monitoring of localized plastic strain evolution stages in notched aluminum AA 2024 alloy tension specimens by acoustic emission and television-optical techniques. Physical Mesomechanics, 13, 203-211.

Panin, V.E., Panin, A.V., Sergeev, V.P., Shugurov, A.R. (2007) Scaling effects in structural-phase self-organization at the “thin film-substrate” interface. Physical Mesomechanics, 10, 117-128.

Panin, V.E., Elsukova, T.F., Egorushkin, V.E., Vaulina, Yu, O., Pochivalov, Yu, I. (2008) Nonlinear wave effects of curvature solitons in surface layers of high-purity aluminum polycrystals under severe plastic deformation. II. The role of boundary conditions, interfaces, and nonequilibrium of a deformed state. Physical Mesomechanics, 11, 299-307.

Papadopoulos, G.A., Paniridis, P.I. (1988) Crack initiation from blunt notches under biaxial loading. Engineering Fracture Mechanics, 31, 65–78.

Park, J., Nelson, D. (2000) Evaluation of an energy-based approach and a critical plane approach for predicting constant amplitude multiaxial fatigue life. International Journal of Fatigue, 22, 23-39.

Pippan, R., Zelger, C., Gach, E., Bichler, C., Weinhandl, H. (2011) On the mechanism of fatigue crack propagation in ductile metallic materials. Fatigue and Fracture of Engineering Materials and Structures, 34, 1-16.

Pook, L.P. (1985) The fatigue crack direction and threshold behaviour of mild steel under mixed mode I and III loading. International Journal of Fatigue, 7, 21-

30.

Pook, L.P. (1992) A note on corner point singularities. International Journal of Fracture, 53, 3-8.

Pook, L.P. (1994) Some implications of corner point singularities. Engineering Fracture Mechanics, 48, 367-378.

Pook, L.P. (2000a) Finite element analysis of corner point displacements and stress intensity factors for narrow notches in square sheets and plates. Fatigue and Fracture of Engineering Materials and Structures, 23, 979–992.

Pook, L.P. (2000b) Crack profiles and corner point singularities. Fatigue and Fracture of Engineering Materials and Structures, 23, 141-150.

Pook, L.P. (2003) A finite element analysis of cracked square plates and bars under antiplane loading. Fatigue and Fracture of Engineering Materials and Structures, 26, 533-541.

Pook, L.P. (2013) A fifty year retrospective review of three dimensional effects at cracks and sharp notches. Fatigue and Fracture of Engineering Materials and Structures. 36, 699-723.

Pook, L.P., Sharples, J.K. (1979) The mode III fatigue crack growth threshold for mild steel. International Journal of Fracture, 15, 223-226.

Prager, W. (1955) The theory of plasticity: a survey of recent achievements. Institution of Mechanical Engineers, London. 169, 41-57.

Priel, E., Yosibash, Z., Leguillon, D. (2008) Failure initiation of a blunt V-notch tip under mixed mode loading. International Journal of Fracture, 149, 143-173.

Qian, J., Hasebe, N. (1997) Property of Eigenvalues and eigenfunctions for an interface V-notch in antiplane elasticity. Engineering Fracture Mechanics, 56, 729-734.

Qiu, B., Gao, Z., Wang, X. (2009) Fatigue life prediction of notched components based on multiaxial local stress-strain approach. PVP2009-78002, 183-189, Prague, Czech Republic.

Radaj, D., Berto, F., Lazzarin, P. (2009) Local fatigue strength parameters for welded joints based on strain energy density with inclusion of small-size notches. Engineering Fracture Mechanics, 76, 1109-1130.

Radaj, D., Lazzarin, P., Berto, F. (2009) Fatigue assessment of welded joints under slit-parallel loading based on strain energy density or notch rounding. International Journal of Fatigue, 31, 1490-1504.

Reis, L., Li, B., de Freitas, M. (2009) Crack initiation and growth path under multi-axial fatigue loading in structural steels. International Journal of Fatigue, 31, 1660-1668.

Ritchie, R.O. (1988) Mechanisms of fatigue crack propagation in metals, ceramics and composites: Role of crack tip shielding. Materials Science and Engineering A-Structures, 103, 15-28.

Saintier, N., Palin-Luc, T., Bénabes, J., Cocheteux, F. (2013) Non-local energy

based fatigue life calculation method under multiaxial variable amplitude loadings. International Journal of Fatigue, 54, 68-83.

Sethuraman, R., Gupta, S.V. (2004) Evaluation of notch root elasto-plastic stress–strain state for general loadings using an elastic solution. International Journal of Pressure Vessels and Piping, 81, 313–325.

Seweryn, A. (1994) Brittle fracture criterion for structures with sharp notches. Engineering Fracture Mechanics, 47, 673-681.

Seweryn, A., Molski, K. (1996) Elastic stress singularities and corresponding generalized stress intensity factors for angular corners under various boundary condition. Engineering Fracture Mechanics, 55, 529-556.

Seweryn, A., Lucaszewicz, A. (2002) Verification of brittle fracture criteria for elements with V-shaped notches. Engineering Fracture Mechanics, 69:1487–1510.

She, C., Guo, W. (2007) Three-dimensional stress concentrations at elliptic holes in elastic isotropic plates subjected to tensile stress. International Journal of Fatigue, 29, 330-335.

Sih, G.C. (1974) Strain-energy-density factor applied to mixed mode crack problems. International Journal of Fracture, 10, 305-321.

Sih, G.C. (2007) Multiscaling in molecular and continuum mechanics: interaction of time and size from macro to nano. Springer, Dordrecht, 2007.

Sih, G.C. (2009a) Crack tip mechanics based on progressive damage of arrow: Hierarchy of singularities and multiscale segments. Theoretical and Applied Fracture Mechanics, 51, 11-32.

Sih, G.C. (2009b) Ideomechanics of transitory and dissipative systems associated with length, velocity, mass and energy. Theoretical and Applied Fracture Mechanics, 51, 149-160.

Sih, G.C. (2010) Mesomechanics of energy and mass interaction for dissipative systems. Physical Mesomechanics, 13, 233-244.

Sih, G.C., Ho, J.W. (1991) Sharp notch fracture strength characterized by critical energy density. Theoretical and Applied Fracture Mechanics, 16, 179-214.

Sih, G.C., Tang, X.S. (2005a) Scaling of volume energy density function reflecting damage by singularities at macro-, meso- and microscopic level. Theoretical and Applied Fracture Mechanics, 43, 211-231.

Sih, G.C., Tang, X.S. (2005b) Equilibrium mechanics model of multiscaling by segmentation: Asymptotic solution for macro-meso-micro damage in anti-plane shear deformation, Theoretical and Applied Fracture Mechanics, 44, 1-15.

Singh, M.N.K., Glinka, G., Dubey, R.N. (1996) Elastic–plastic stress–strain calculation in notched bodies subjected to non-proportional loading. International Journal of Fracture, 76, 39–60.

Smith, R.N., Watson, P., Topper, T.H. (1970) A stress–strain function for the fatigue of metal. Journal of Materials, 5, 767–778.

Socie, D., Marquis, G. (2000) Multi-axial fatigue. Warrendale (PA): Society of Automotive Engineers.

Sousa, R.A., Castro, J.T.P., Lopes, A.A.O., Martha, L.F. (2013) On improved crack tip plastic zone estimates based on T-stress and on complete stress fields. Fatigue and Fracture of Engineering Materials and Structures, 36, 25–38.

Strandberg, M. (2002) Fracture at V-notches with contained plasticity. Engineering Fracture Mechanics, 69, 403-415.

Susmel, L. (2009) Multi-axial notch fatigue. Woodhead publishing, Cambridge.

Susmel, L. (2010) Estimating fatigue lifetime of steel weldments locally damaged by variable amplitude multiaxial stress fields. International Journal of Fatigue, 32, 1057-1080

Susmel, L., Taylor, D. (2012) A critical distance/plane method to estimate finite life of notched components under variable amplitude uniaxial/multiaxial fatigue loading. International Journal of Fatigue, 38, 7-24.

Tanaka, K. (2012) Small crack propagation in multiaxial notch fatigue. International Conference on Crack Paths.

Tanaka, K., Akiniwa, Y., Yu, H. (1999) The propagation of a circumferential fatigue crack in medium-carbon steel bars under combined torsional and axial loadings. In: Mixed-Mode Crack Behaviour, ASTM 1359 (eds KJ Miller and DL McDowell), West Conshohocked, PA, 295-311.

Tang, X.S., Sih, G.C. (2005) Weak and strong singularities reflecting multiscale damage: Micro-boundary conditions for free–free, fixed–fixed and free–fixed constraints, Theoretical and Applied Fracture Mechanics, 43, 5-62.

Terres, M.A., Sidhom, H. (2012) Fatigue life evaluation of 42CrMo4 nitrided steel by local approach: Equivalent strain-life-time. Materials and Design, 33, 444–450.

Terres, M.A., Laalai, N., Sidhom, H. (2012) Effect of nitriding and shot-peening on the fatigue behavior of 42CrMo4 steel: Experimental analysis and predictive approach. Materials and Design, 35, 741–748.

Timoshenko, S.P., Goodier, J.N. (1970) Theory of elasticity, 3rd Edition. McGraw-Hill, New York.

Tong, J., Yates, J.R., Brown, M.W. (1986) Some aspects of fatigue thresholds under mode III and mixed mode and I loadings. International Journal of Fatigue, 18, 279-285.

Topper, T.H., Wetzel, R.M., Morrow, J. (1969) Neuber's rule applied to fatigue of notched specimens. Journal of Materials, 4, 200–209.

Wang, H., Nie, A., Liu, J., Wang, P., Yang, W., Chen, B., Liu, H., Fu, M. (2011) In situ TEM study on crack propagation in nanoscale Au thin films. Scripta Materialia, 65, 377–379.

Williams, M.L. (1952). Stress singularities resulting from various boundary conditions in angular corners of plate in extension. Journal of Applied Mechanics,

19, 526-528.

Yamauchi, Y., Nakano, M., Kishida, K., Okabe, T. (2001) Measurement of mixed-mode fracture toughness for brittle materials using edge-notched half-disk specimen. Zairyo/ Journal of the Society of Materials Science (Japan), 50, 224–229.

Yang, W., Freund, L.B. (1985) Transverse shear effects for through-cracks in an elastic plate. International Journal of Solids and Structures, 21, 977–994.

Yang, J., Wang, G.Z., Xuan, F. Z., Tu, S. T. (2013) Unified characterisation of in-plane and out-of-plane constraint based on crack-tip equivalent plastic strain. Fatigue and Fracture of Engineering Materials and Structures, 36, 504-514.

Ye, D., Matsuoka, S., Suzuki, N., Maeda, Y. (2004) Further investigation of Neuber's Rule and the equivalent strain energy density (ESED) method. International Journal of Fracture, 26, 447-455.

Ye, D., Hertel, O., Vormwald, M. (2008) A unified expression of elastic–plastic notch stress–strain calculation in bodies subjected to multiaxial cyclic loading. International Journal of Solids and Structures, 45, 6177-6189.

Yosibash, Z., Bussiba, A., Gilad, I. (2004) Failure criteria for brittle elastic materials. International Journal of Fracture, 125, 307–333.

Yosibash, Z., Priel, E., Leguillon, D. (2006) A failure criterion for brittle elastic materials under mixed-mode loading. International Journal Fracture, 141, 291–312.

Yu, H.C., Tanaka, K., Akiniwa, Y. (1998) Estimation of torsional fatigue strength of medium carbon steel bars with circumferential crack by the cyclic resistance-curve method. Fatigue and Fracture of Engineering Materials and Structures, 21, 1067-1076.

Yu, P., Guo, W., She, C., Zhao, J. (2008) The influence of Poisson's ratio on thickness-dependent stress concentration at elliptic holes in elastic plates. International Journal of Fatigue, 30, 165–171.

Zacharopoulos, D.A. (2004) Stability analysis of crack path using the strain energy density. Theoretical and Applied Fracture Mechanics, 41, 327-337.

Zappalorto, M., Lazzarin, P. (2009) A new version of the Neuber rule accounting for the influence of the notch opening angle for out-of-plane shear loads. International Journal of Solids and Structures, 46, 1901-1910.

Zappalorto, M., Lazzarin, P. (2010) A unified approach to the analysis of nonlinear stress and strain fields ahead of mode III-loaded notches and cracks. International Journal of Solids and Structures, 47, 851-864.

Zappalorto, M., Lazzarin, P. (2013) Three-dimensional elastic stress fields ahead of notches in thick plates under various loading conditions. Engineering Fracture Mechanics, 108, 75–88.

Zappalorto, M., Lazzarin, P., Yates, J.R. (2008) Elastic stress distributions for hyperbolic and parabolic notches in round shafts under torsion and uniform

antiplane shear loadings. International Journal of Solids and Structures, 45, 4879-4901.

Zappalorto, M., Lazzarin, P., Filippi, S. (2010) Stress field equations for U and blunt V-shaped notches in axisymmetric shafts under torsion. International Journal of Fracture, 164, 253-269.

Zheng, M., Zhou, G., Zacharopoulos, D.A., Kuna, M. (2001) Crack initiation behavior in StE690 Steel characterized by strain energy density criterion. Theoretical and Applied Fracture Mechanics, 36, 141-145.

Ringraziamenti

I miei primi ringraziamenti vanno di cuore al Prof. Lazzarin, per aver creduto nelle mie capacità nel corso di tutto il mio percorso accademico. Dopo la tesi triennale e la specialistica sotto la Sua supervisione, ora è arrivata anche la tesi di Dottorato, direi che non ci siamo fatti mancare nulla. Scherzi a parte, La ringrazio per la sua attenta e competente supervisione e per tutti i momenti passati assieme anche solo a parlare di calcio o ciclismo, o a berci "un'ombra" in compagnia.

Ringrazio Filippo per i quattro anni passati fianco a fianco sia nei momenti di divertimento che in quelli di tensione lavorativa. Ti ringrazio per avermi coinvolto e supportato durante i lavori svolti assieme e per avermi spinto a scegliere il percorso di dottorato. Probabilmente se non ci fossi stato tu non sarei qui a scrivere questi ringraziamenti.

Ringrazio tutti i miei colleghi dottorandi, i tecnici di laboratorio, i docenti, i tesisti, con cui è stato un piacere scherzare e condividere momenti belli e brutti. Non sto qui ad elencarvi tutti sennò mi servirebbero probabilmente due pagine. Ringrazio in particolare i ragazzi dell'ufficio dottorandi, Marco, Paolo, Pasquale, Stefano, Alessandro, Lucio, Reza, Giacomo. Con voi questi tre anni sono stati davvero uno spasso.

Ora, non vogliatemene, ma un Ringraziamento (con la R maiuscola) va a Michele e Alberto, amici prima che colleghi, compagni di tutto, di scherzi ben riusciti e mal riusciti, di nervosismi e rabbia, di risate, di aiuti reciproci, di prese in giro, di depressione e euforia, di seratone pazzesche passate assieme, di thè, caffè e partitine. Grazie perché la vostra fiducia nei miei confronti è stata totale, come del resto la mia nei vostri. Grazie per il supporto che mi avete dato, alla fine posso dire che col vostro aiuto è tutto giusto, anche il risultato!

Un ringraziamento particolare va a Bibo e Ciambo, amici di una vita, perché stare con voi è come ricaricare le pile. E se magari non ce lo diciamo mai, perché tra uomini funziona così, sappiate che vi voglio un gran bene. Grazie anche a Anna, Toby, Giulia, Principe e Angela, ai Tusi del calcetto e agli amici Troglo.

Un grosso ringraziamento va a Mamma, Papà e Martina perché sono cosciente che ce ne vuole di pazienza per sopportarmi. Grazie per averci creduto e per aver sposato da subito il mio progetto. Grazie per avermi fatto ragionare nei momenti difficili. Alla fine posso dire di essere arrivato in fondo. Ora meglio andare a lavorare….

L'ultimo ringraziamento, ma forse davvero il più sentito, va a Chiara. Perché comunque tu ci sei, perché riesci a farmi sentire una persona importante. *Perché arrivi in punta di piedi ma sei rivoluzione. Perché mi hai preso e mi hai reso qualcosa di migliore…Questo castello con la sua regina vive ed ogni cosa sorride*…

Grazie

Christian